MICROWAVE AND MILLIMETER-WAVE INTERACTION WITH TERRAIN

by

Yang Du

A dissertation submitted in partial fulfillment
of the requirements for the degree of
Doctor of Philosophy
(Electrical Engineering)
in The University of Michigan
2003

Doctoral Committee:

Professor Fawwaz T. Ulaby, Chairperson
Assistant Research Scientist Adib Nashashibi
Associate Professor Christopher S. Ruf
Professor Kamal Sarabandi

This work is dedicated to my family.

ACKNOWLEDGEMENTS

I am indebted to my advisor, Professor Fawwaz T. Ulaby, for his continuous financial support, academic guidance and encouragement. I am grateful to Dr. Adib Nashashibi, a talented experimentalist and perfectionist, who has readily assisted, guided and encouraged me through the whole course.

I thank my committee members, Professor Kamal Sarabandi and Professor Christopher S. Ruf, for their insightful criticisms and suggestions that have greatly improved the quality of this thesis.

Dr. Roger DeRoo has aligned substantially my research work at the early stage through his vast knowledge and enthusiasm in the tenet of remote sensing. Dr. Leland Pierce has helped me out numerous times of subtle computer intricacies. Dr. Valdis Liepa, Mr. Craig Dobson, Dr. Josef Kellndorfer, Dr. Mark Casciato and Professor Tony England were all very helpful in deepening my understanding of the subjects.

Countless interactions with many graduate students at and outside the Radiation Laboratory (RadLab) never failed to establish an important inflow of ideas, suggestions, solutions and corrections.

Finally, I want to thank the RadLab staff, specifically Patti Wolfe, Susan C. Charnley, Karen Kirchner and Mary Eyler for their professional assistance.

TABLE OF CONTENTS

CHAPTER

LIST OF FIGURES

Figure

LIST OF TABLES

Table

CHAPTER I

Introduction

1.1 Overview

Microwave and millimeter wave (MMW) remote sensing have become important tools for the extraction of biophysical or hydrological information about the imaged scene from the remotely sensed data, which may otherwise be difficult, if not impossible, to obtain. Microwave sensors are also used for target detection, either alone or in conjunction with electro-optical sensors.

To develop better understanding of the scattering mechanisms responsible for the observed sensor response, it is imperative to construct an extensive database of microwave and MMW measurements for numerous combinations of the terrain conditions and the sensor attributes such as frequency, incidence angle and so on, as well as to develop theoretical or semi-empirical models. Undoubtedly such a database will serve as a solid ground for deepening our understanding of scattering phenomenon and as a testbed for the models to be built. The more features provided by the measurements that can be successfully addressed by the models, the stronger will be the motivation for such measurements. Even though an extensive number of investigation have been conducted over the past 30 years, "gray areas" still exists in terms of our understanding of microwave and millimeter-wave interaction with natural media.

These deficiencies are attributed to constraints associated with limited resources or technology-related constraints.

The rapid developments in measurements at microwave and MMW wavelengths and in correlated scattering phenomenology serve to challenge and inspire modellers. At the microwave and MMW scale, many natural targets to be sensed are random media. Although statistically uniform in most cases, they can produce appreciable variations as the antenna footprint moves from spot to spot. Any successful model needs to relate the observed statistical properties of the response to the physical structure of the medium. It also requires to identify and faithfully account for the underlying scattering mechanisms, in particular for a dense medium where multiple scattering effects cannot be ignored.

In the literature tremendous efforts have been made in building suitable models, which mainly fall in one of three categories: 1) field-based full wave theory; 2) energy based radiative transfer theory (RT); 3) empirical or semi-empirical models. Each has its own share of strengths and weaknesses. In brief, 1) the full wave method is formulated on a rigorous theoretical basis, such as Maxwell's equations or some derivation therefrom, including IEM (integral equation method) and EBC (extended boundary condition), but the encountered analytical difficulties more often than not lead inevitably to a cluster of assumptions requiring that either a direct simplification is made or a well-established asymptotic framework is adopted in order to attack the problem at hand. Quite understandably, this method often resorts to numerical simulation, such as the frequently used Monte-Carlo simulation, which presupposes knowledge of the essential statistical properties of the medium, a presumption not always true. 2) RT concentrates on the propagation and scattering of electromagnetic intensity in the inhomogeneous medium. Conventional RT assumes that the scatterers are in the far field of each other, hence the scattered fields are independent. This independence assumption provides flexibility in use, but may also be deficient in predicting power. A mixture variant has emerged where the general framework of RT is retained, but in conjunction with the use of field-based calculations of the extinction coefficient. Examples of this approach include the quasi-crystalline-approximation (QCA) and the quasi-crystalline-approximation-coherent potential (QCA-CP). In general, the RT framework has the advantage of being able to treat complex media more easily and consistently than the field approach. A variation on the traditional RT model, the dense medium radiative transfer theory (DMRT), has been developed to treat dense media, but it is limited to nonabsorptive scatterers. 3) Empirical or semi-empirical models use the measured data for their construction, which is quite convenient but the applicability of such models is limited to the conditons associated with the measured data.

It is the interplay of modeling effort and measurements and the tradeoff between modeling rigorousness and flexibility as well as consistency that motivates the work presented in this thesis. It includes an effort to plan and carry out some extensive measurements to fill in certain “gray areas” of the measurement database at MMW wavelength, to trace the connections among the scattering mechanisms underlying a number of important scattering phenomena at microwave and MMW wavelengths, and to build predictive models by choosing a suitable framework and constructing a detailed structure and incorporating mechanisms into the models.

1.2 Outline

In Chapter II, the topic of sensitivity to soil moisture for vegetation-covered land by active and passive sensors at L band is revisited. At such a low microwave frequency, for the usually encountered vegetation covers such as grass and soybean, which are electrically small in dimension, the conventional RTE can be used to study the scattering mechanisms.

In Chapter III we examine the radar response of a soybean canopy. The scattering mechanism becomes more complex for a soybean canopy at C band. The independent scattering assumption for conventional RTE does not hold strictly; the interaction among scatterers are addressed in the literature by either the inclusion of higher order scattering components [15] or the application of antenna array-like treatment [115]. Though both provide higher fidelity in accounting for the underlying scattering mechanism, the former is computationally demanding, while the latter necessitates the introduction of a new set of parameters to describe the geometrical and positional properties of the constituents of a soybean plant. If an inversion algorithm is to be developed for extracting water content, biomass, rough surface rms height and soil moisture from the L, C bands measurements of soybean at 45° incidence, we can hardly use the high order scattering approach due to its complexity, nor can we use the antenna array -like approach due to the limited measurement data available for inversion. Rather, assuming the adoption of the conventional RTE technique, we endeavor to best characterize the dependence of the volume extinction coefficient κ_e and the phase matrix $\mathbf{P}$, two critical input parameters to RTE, upon the water content to the biomass. Chapter III addresses all the relevant issues and provides discussions of the inversion results.

When the sensor frequency moves from the microwave to the millimeter-wave regime, the scattering mechanism becomes even substantially more complicated, mainly due to the dense medium nature of many natural media such as snow. For dry snow, the conventional RTE can be used, in conjunction with QCA, for studying the backscatter due to the relative simplicity of the air-ice mixture approach. However, RTE and QCA provide different characterizations of the propagation properties of the dry snow media, which calls for reconciliation of the two approaches. This issue is addressed in Chapter IV, along with the modeling performance. Further discussion is also provided on the impact of snow particle shape and surface roughness upon the backscatter.

Yet when snow becomes wet, as frequently encountered in diurnal observations, the QCA approach for determining the volume extinction coefficient κ_e collapses due to the severe violation of its assumptions. Encouraged by the success of conventional RTE when applied to other dense media [56], the conventional RTE was adopted for wet snow in our study. adopted. This treatment is addressed in Chapter V where we incorporated thermodynamic information in the application of the model to explain diurnal observations.

So far the main focus has been on the incoherent power of the scattered field. Such treatment is insufficient when it comes to the characterization of a communication channel, where the interference statistics assume a considerably important role. In such cases, an electric-field based study is necessary and is given in Chapter VI. At 35 GHz, a simple Kirchhoff model is used for scattering from rough surfaces. Based on it, a four-ray model is constructed to help interpret the observed backward interference pattern. Moreover, to infer the forward scattering behavior from the backward one, an equivalence relation between forward and backward scattering is established. However, when the surface is very rough, or covered by some vegetation such as grass, the backward interference pattern tends to disintegrate, even for a moderate number of independent samples. This calls for techniques that can address both the coherent and incoherent components of the scattered field from a rough surface directly. IEM is one such candidate, but it cannot be applied directly in its current form because it assumes uniform plane wave incidence. Such an approximation may not be valid or appropriate for calculating the forward scattered field. Hence, the IEM formulation is revisited in Chapter VII wherein the antenna electric-field pattern is incorporated in the calculation of the field intercepted by the receive antenna.

In summary, the contributions described in this thesis are:

1. Evaluation of the sensitivity to soil moisture for both active and passive sensors at L band. This evaluation brings to a conclusion a long disputed issue. Implementation of the MIMICS model [106] is extended to the passive case.

2. Development of an inversion algorithm for extracting water content, biomass, rough surface rms height and soil moisture from the L, C band measurements of soybean at 45° incidence. This treatment illustrates how a sound scattering model can be constructed for inversion by incorporating information provided by complicated microwave scattering models such as MIMICS.

3. Characterization and extensive measurements of MMW backscatter from snow at near grazing incidence. These new measurements enhanced the data base significantly. Moreover, they are used to validate the scattering models in this study.

4. Development of a MMW snow backscatter model for the response as a function of incidence angle at near grazing incidence. This treatment illustrates how the conventional RTE can be used in conjunction with QCA for studying the backscatter from a dense medium such as dry snow through the proposed

reconciliation technique. The study also examines the effect of snow particle shape and surface roughness upon the backscatter.

5. Development of a MMW snow backscatter model for the diurnal pattern at near grazing incidence. This treatment illustrates how, for a wet snow where dense media techniques are hard to apply, the conventional RTE can be used successfully by incorporating thermodynamic information.

6. Characterization and measurements of the backscatter receiver-height interference pattern at 35 GHz over different types of terrain. It provides the first set of measurements for such a configuration in the literature and sheds light on how the backscatter interference pattern varies with terrain type.

7. Development of a model to interpret the observed interference pattern. This treatment illustrates how a simple single scattering based four-ray model can effectively capture the major scattering mechanisms underlying the measurements.

8. Establishment of the equivalence between the backscatter and forward scattering interference patterns. This treatment provides a means to characterize the forward scattering channel without having to do bistatic measurements.

9. Extension of the conventional IEM model for rough surface scattering to incorporate antenna pattern. Driven by the absence of calibration, this treatment extends the conventional IEM to more general settings.

CHAPTER II

Sensitivity To Soil Moisture For Vegetation Covered Land By Active and Passive Microwave Sensors

2.1 Introduction

Active and passive microwave approaches to sensing soil moisture share certain physical processes, but they are also markedly different insofar as the quantities they sense and the image products they generate. Numerous papers, and indeed books, have been published on the theory of radar scattering from a soil surface, with and without vegetation cover, as well as on analyses of experimental observations and system imaging considerations (references [3,4,7,25,26,30,73,80,86,94,96,104] comprise a representative sample). Similar studies have been reported for the passive-microwave case [18, 48–51, 84, 100, 114], but only one serious study has been conducted to date in which the active and passive approaches were inter-compared with respect to their relative sensitivities to change in soil moisture content under vegetation-covered conditions [35]. The comparison study, which was published over a decade ago, provided useful and interesting results but the geometrical models it used in characterizing the vegetation cover were somewhat simplistic. This chapter represents a focused revisit of the comparison question. This portion of the work has been published in [28]. The study considers only a single set of wave parameters for both active and passive simulations (L-band, incidence angle $\theta = 30°$, and an h-polarized antenna), but considers three types of cover: (a) a hypothetical layers of Rayleigh particles, (b) a grass-like vegetation layer, and (c) a canopy of soybean plants.

2.2 Soil-Moisture Sensitivity

In this study we ignore atmospheric effects, terrain slope and imaging and calibration issues. We assume we have a pair of sensors, a radar and a radiometer, both pointed at a soil surface at an incidence angle of 30°. Both instruments operate at 1.5 GHz and use identical horizontally polarized antennas. The soil is covered with a layer of vegetation characterized by an optical depth τ and an albedo ω, as well as other geometrical properties specific to the particular vegetation cover under consideration.

We shall start with two bare surfaces, one characerized by a relatively smooth interface and the other is a medium rough interface (Section 3). Appropriate surface scattering and emission models are then used to calculate the e_0 and the backscattering coefficient σ_0° as a function of the soil volumetric moisture content m_v. (The zero subscirpt of e_0 and σ_0° denotes that these quantitites pertain to the bare-soil case.) The radiometric and radar bare-soil moisture sensitivities are then defined as follows:

$$E_0 = \frac{\partial e_0}{\partial m_v} \ , \tag{2.1}$$

$$S_0 = \frac{\partial \sigma_0^\circ}{\partial m_v} \ , \tag{2.2}$$

where σ_0° is in m^2/m^2. For reasons that we will discuss later, we will also examine the behavior of the logarithmic radar sensitivity S_0^{dB}, defined as:

$$S_0^{\mathrm{dB}} = \frac{\partial \sigma_0^\circ(\mathrm{dB})}{\partial m_v}, \tag{2.3}$$

where $\sigma_0^\circ(\mathrm{dB}) = 10 \log \sigma_0^\circ$.

For the vegetation-covered case, we shall denote the emissivity and backscattering coefficient by e and σ°, and the corresponding soil- moisture sensitivities are defined as

$$E(\tau, \omega) = \frac{\partial e(m_v, \tau, \omega)}{\partial m_v} \tag{2.4}$$

$$S(\tau, \omega) = \frac{\partial \sigma^\circ(m_v, \tau, \omega)}{\partial m_v}\ . \tag{2.5}$$

where τ is the optical depth. When σ° is expressed in dB, the correspoinding logarithmic sensitivity is denoted $S^{\mathrm{dB}}(\tau, \omega)$.

In this chapter we attempt to answer the following questions:

1. Is the relative radiometric sensitivity $E(\tau)/E_0 \leq 1$ always true, and does it decrease monotonically with increasing optical thickness τ?

2. Is the relative radar sensitivity $S(\tau)/S_0 \leq 1$ always true, and does it decrease montonically with increasing optical thickness τ? The same question applies to $S^{\mathrm{dB}}/S_0^{\mathrm{dB}}$.

3. How does the albedo of the vegetation medium affect $E(\tau)/E_0$ and $S(\tau)/S_0$?

4. Does vegetation cover have a greater or lesser influence on the radiometric sensitivity compared with its influence on the radar sensitivity to soil moisture?

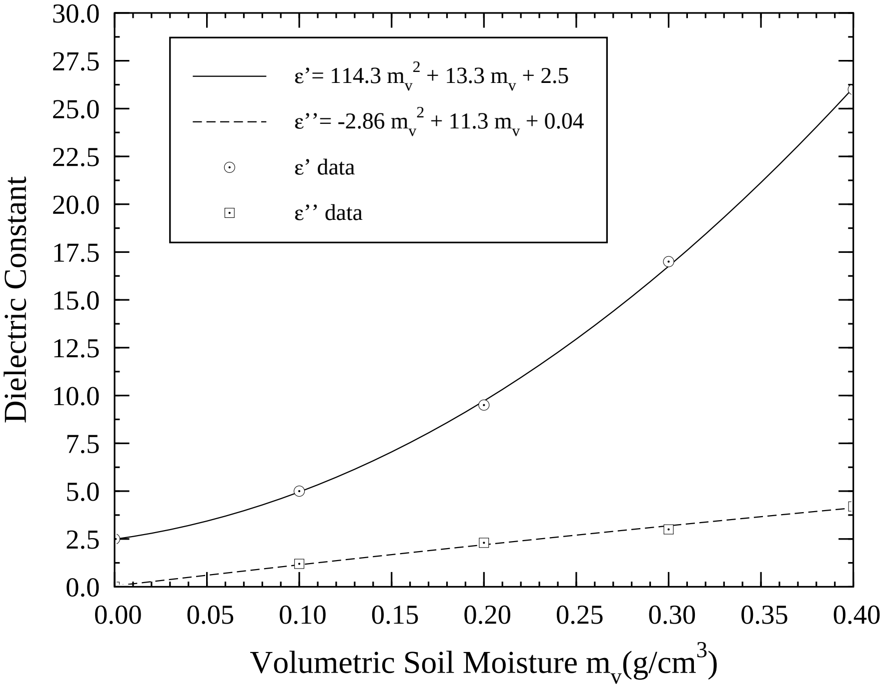

Figure 2.1: Dielectric constant of silt clay soil at 1.4 GHz. The data points are from the measurements rerported in Ulaby et al. [104] and the curves are second-order polynomial fits.

2.3 Bare Surface Models

To insure credibility of the results and conclusions realized by this study, it is important that we choose our soil surface and vegetation cover parameters and our emission and scattering models with as much realism as possible. To this end we will choose a silt loam soil with 30.6% sand, 55.9% silt, and 13.5% clay, for which its measured dielectric constant [[104], Appendix E] can be approximated by the quadratic expressions:

$$\epsilon' = 114.3m_v^2 + 13.3m_v + 2.5, \tag{2.6}$$

$$\epsilon'' = -2.86m_v^2 + 11.3m_v + 0.04, \tag{2.7}$$

as illustrated by the plots in Figure 2.1. The corresponding variation of the Fresnel reflectivity with m_v at an incidence angle of 30° is shown in Figure 2.2 for horizontal

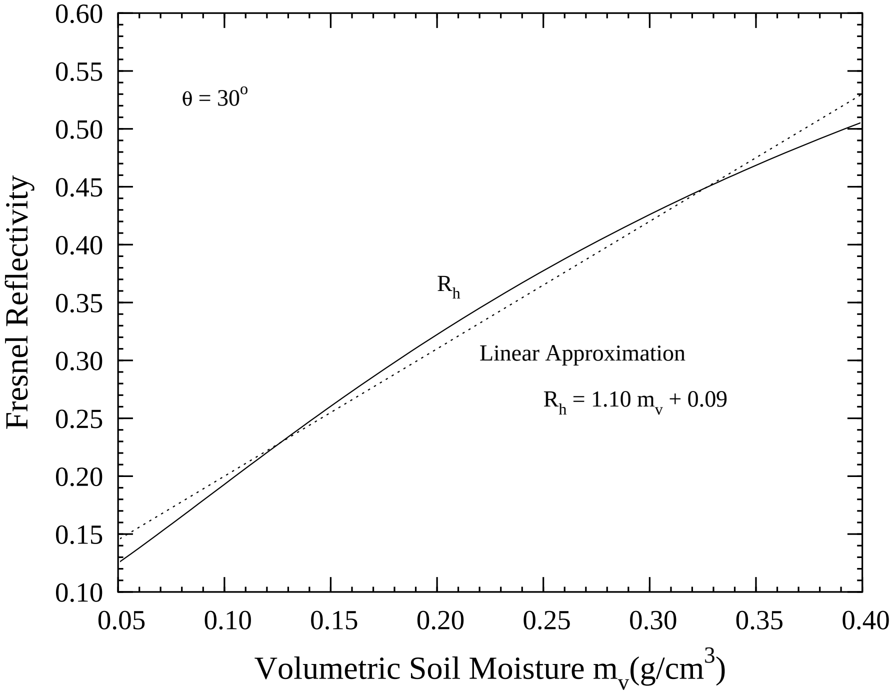

Figure 2.2: Calculated horizontal-polarization Freznel reflectivity at 30° versus soil moisture (solid curve), and its linear approximation (dashed).

polarization. We note that R_h exhibits an approximately linear dependence on m_v and it is given by

$$R_h = 1.10 m_v + 0.09 \tag{2.8}$$

Since surface roughness is an important parameter, we wanted to choose more than one surface, and we wanted the surfaces to be characterized by high quality radar measurments and, if possible, appropriate scattering models. According to the study reported by Oh et al. [73], one of the relatively smooth surfaces (whose surface profile was measured by a laser ranging system) was characterized by an exponential correlation function with a correlation length $\ell = 8.6$ cm and a rms height $s = 0.4$ cm. Furthermore, it was reported that the measured backscatter showed excellent agreement with calculations based on the small perturbation model. In the same study a medium rough surface with $s = 1.12$ cm and $\ell = 6.4$ cm was also measured by the laser profiler and the radar system. The parameters of the smoother surface place it well within the range of validity of the small penturbation model, and for the medium rough surface, its ks $= 2\pi s/\lambda = 0.35$ is just oustide the usually accepted boundary of 0.3, but we will use the small penturbation model anyway because the measured angular behavior of σ° is in close agreement with the model calculation.

2.3.1 Emission

According to the mdoel introduced by Choudhury et al. [18], the horizontally polarized emissivity of a randomly rough surface with *rms* height s is given by

$$e_0 = 1 - R_h' \tag{2.9}$$

where

$$R_h' = R_h \exp[-(2ks'\cos\theta)^2], \tag{2.10}$$

where R_h is the Fresnel refelctivity for horizontal polarization, $k = 2\pi/\lambda$, and s' is an "effective" *rms* height of the surface. Based on the empirical relationship proposed by Choudhury et al. [18] between s and s', we determined that $s' = 0$ for our smooth surface ($s = 0.4$ cm) and $s' = 0.14$ cm for our medium rough surface ($s = 1.12$cm). Hence, at $\lambda = 20$ cm, and $\theta = 30^\circ$, we have the following emissivity models for the bare soil surfaces:

<u>Smooth Surface</u> ($s = 0.4$ cm):

$$\begin{aligned} e_0 &= 1 - R_h \\ &= 0.91 - 1.10 m_v \end{aligned} \tag{2.11}$$

<u>Medium Rough Surface</u> ($s = 1.12$ cm):

$$\begin{aligned} e_0 &= 1 - 0.9945 R_h \\ &= 0.91 - 1.09 m_v \end{aligned} \tag{2.12}$$

If the surface temperature is T_0, the brighness temperature of the surface is

$$T_B = e_0 T_0. \tag{2.13}$$

2.3.2 Backscatter

For a surface characterized by an exponential height correlation function, the small-perturbation model expression for σ_0° is given by [73]

$$\sigma_0^\circ = \frac{4k^4 s^2 \ell^2 R_h}{[1 + 2(k\ell \sin\theta)^2]^{3/2}}. \tag{2.14}$$

For our two surfaces, Eq. 2.14 reduces to:

<u>Smooth Surface</u>:

$$\sigma_0^\circ = 0.046 R_h. \tag{2.15}$$

<u>Medium Rough Surface</u>:

$$\sigma_0^\circ = 0.381 R_h \tag{2.16}$$

2.4 Vegetation Models

2.4.1 Emission

The vector radiative transfer equation for emission by an inhomogeneous medium is given by [[104], Chapter 13]:

$$\frac{d\mathbf{T}_c(\hat{\mathbf{s}})}{ds} = -\boldsymbol{\kappa}_e(\hat{\mathbf{s}})\mathbf{T}_c(\hat{\mathbf{s}}) + \boldsymbol{\kappa}_a T_0 + \iint_{4\pi} \mathbf{P}(\hat{\mathbf{s}}, \hat{\mathbf{s}}')\mathbf{T}_c(\hat{\mathbf{s}}')\, d\Omega', \tag{2.17}$$

where

$\mathbf{T}_c(\hat{\mathbf{s}})$ = brightness temperature vector of the canopy, for propagation along $\hat{\mathbf{s}}$,

$\boldsymbol{\kappa}_e$ = extinction matrix of the canopy, along $\hat{\mathbf{s}}$,

$\boldsymbol{\kappa}_a$ = absorption vector of the canopy, along $\hat{\mathbf{s}}$

$\mathbf{P}(\hat{\mathbf{s}}, \hat{\mathbf{s}}')$ = phase matrix of the canopy, for incidence along $\hat{\mathbf{s}}'$ and scattering along $\hat{\mathbf{s}}$.

T_0 = physical temperature of the vegetation medium.

Upon specifying the sizes and orientation distributions of the vegetation elements, and their dielectric properties, we can apply available techniques [94,104] to obtain values for $\boldsymbol{\kappa}_e, \boldsymbol{\kappa}_a$, and $\mathbf{P}(\hat{\mathbf{s}}, \hat{\mathbf{s}}')$ for all directions $\hat{\mathbf{s}}$ and $\hat{\mathbf{s}}'$. Equation 2.17 can then be solved either numerically or iteratively to obtain a value for $\mathbf{T}_c^+(\theta)$, the brightness temperature of the canopy at a point above the canopy, representing the energy emitted at an angle θ relative to the zenith. In this study, we shall use the iterative approach because (1) for the canopies we plan to examine, the albedo of the canopy is sufficiently small that the iterative technique provides results that are within a few percentage points of those obtained through numerical calculations, and (2) the form of the iterative solution is such that each term represents a specific emission/scattering mechanism, thereby facilitating the analysis.

If we (a) split the brightness temperature vector $\mathbf{T}_c(\hat{\mathbf{s}})$ into an upward-moving component $\mathbf{T}_c^+$ and a downward-moving component $\mathbf{T}_c^-$, (b) assume the ground surface to be quasi-specular with respect to bistatic reflection of downward propagating energy (R_h' given by Eq. 2.10 is used instead of R_h), (c) denote $z = -d$ as the soil surface and $z = 0$ as the top of the canopy, and (d) apply appropriate boundary conditions at the air-vegetation boundary (diffuse) and at the vegetation-soil boundary (plane interface), the first-order solution of Eq. 2.17 takes the following form:

$$\mathbf{T}_c^+ = \mathbf{T}_1 + \mathbf{T}_2 + \mathbf{T}_3 + \mathbf{T}_4 + \mathbf{T}_5 + \mathbf{T}_6 + \mathbf{T}_7, \tag{2.18}$$

where the various contributions are represented symbolically in Figure 2.3. We note that the first three terms of Eq. 2.18 comprise the zero-order solution, which ignore scattering in the vegetation medium (except for its contribution to extinction). These terms include $\mathbf{T}_1$, the direct soil emission, attenuated by passage through the canopy; $\mathbf{T}_2$, the direct, upward, self-emitted contribution of the canopy; and $\mathbf{T}_3$,

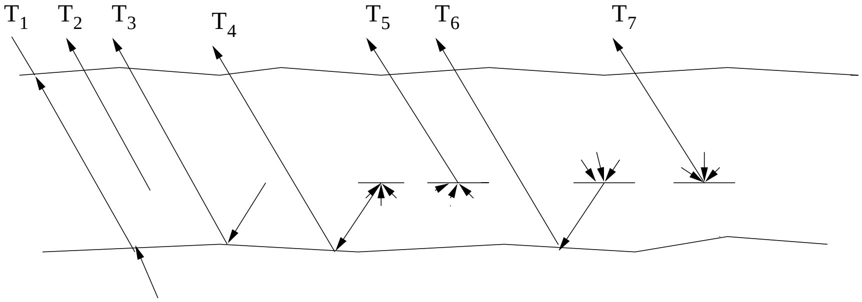

Figure 2.3: The first-order radiative transfer solution for emission consists of seven contributions, of which the first three belong to the zero-order solution.

the downward, self- emitted energy that gets reflected by the soil surface. For media with azimuthal symmetry and for which the orientation distribution of the scattering elements is symmetrical with respect to the horizontal plane, the zero-order solution for horizontal polarization takes the simple form [104]:

$$T_c^+ = \Upsilon(1 - R_h')T_0 + (1 - \Upsilon)\kappa_a T_0 + R_h' \Upsilon(1 - \Upsilon)k_a T_0 \tag{2.19}$$

where

$$\begin{aligned} \Upsilon &= \text{one-way canopy transmissivity} \\ &= \exp(-\tau \sec\theta), \\ \tau &= \kappa_e d = \text{optical thickness.} \end{aligned}$$

Terms $\mathbf{T}_4$ through $\mathbf{T}_7$ in Eq. 2.18 represent single-scattering contributions and are contributed by the first-order iteration upon using the zero-order solution as a source function. As shown in the report version of this study [27], for canopies with scattering albedo $\omega < 0.1$, the emission is dominated by the zero-order terms.

2.4.2 Backscatter

For backscatter, the vector radiative transfer equation assumes a form similar to Eq. 2.10; if we ignore the self-emission term $\boldsymbol{\kappa}_a T_0$ in Eq. 2.17 and replace $\mathbf{T}_c$ with the specific intensity $\mathbf{I}$, we have:

$$\frac{d\mathbf{I}(\hat{\mathbf{s}})}{ds} = -\boldsymbol{\kappa}_e \mathbf{I}(\hat{\mathbf{s}}) + \iint_{4\pi} \mathbf{P}(\hat{\mathbf{s}}, \hat{\mathbf{s}}')\mathbf{I}(\hat{\mathbf{s}}')d\Omega' \tag{2.20}$$

We use MIMICS [106] to obtain a first-order solution for $\mathbf{I}(\theta)$ at a point above the canopy, from which we can obtain an expression for the horizontally polarized backscattering coefficient σ°:

$$\sigma^\circ(\theta) = 4\pi \cos\theta \; I_h(\theta). \tag{2.21}$$

where I_h is the horizontal-polarization element of the vector $\mathbf{I}$.

If we define $\hat{\mathbf{s}} = (\theta, \phi)$ as the backscatter direction of interest, $-\hat{\mathbf{s}} = (\pi - \theta, \phi)$, $\hat{\mathbf{o}} = (\theta, \pi + \phi)$, and $-\hat{\mathbf{o}} = (\pi - \theta, \phi + \pi)$, the first-order solution can be expressed as follows:

$$\begin{aligned}
\sigma^\circ &= \sigma_1^\circ + \sigma_2^\circ + \sigma_3^\circ + \sigma_4^\circ + \sigma_5^\circ \\
&= \Upsilon^2\sigma_0^\circ + \frac{2\pi\cos\theta}{\kappa_e}(1-\Upsilon^2)P_{22}(\hat{\mathbf{s}}, -\hat{\mathbf{o}}) + 4\pi\Upsilon^2 R_h P_{22}(\hat{\mathbf{s}}, \hat{\mathbf{o}})\frac{\tau}{\kappa_e} \\
&\quad + 4\pi\Upsilon^2 R_h P_{22}(-\hat{\mathbf{s}}, -\hat{\mathbf{o}})\frac{\tau}{\kappa_e} + \frac{2\pi\cos\theta}{\kappa_e}\Upsilon^2 R_h^2(1-\Upsilon^2)P_{22}(-\hat{\mathbf{s}}, \hat{\mathbf{o}}),
\end{aligned} \tag{2.22}$$

where P_{22} is the element of the phase matrix corresponding to hh polarization, its first argument denotes the direction of energy scattered by the vegetation volume and the second argument denotes the direction of incidence upon it, and σ_0° is the bare-soil backscattering coefficient given by Eq. 2.14. The physical mechanisms corresponding to contributions σ_1° through σ_5° are diagrammed in Figure 2.4.

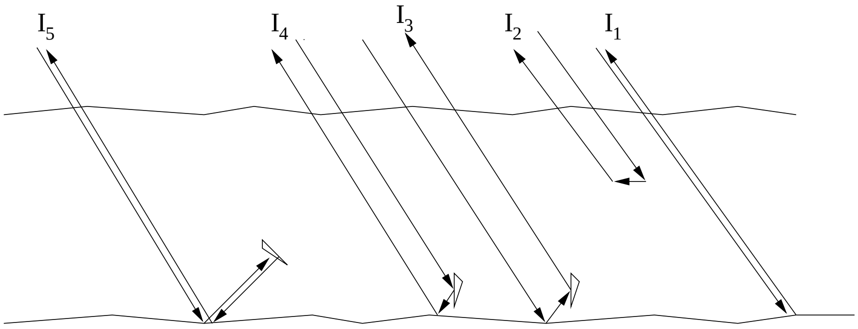

Figure 2.4: The first-order solution for backscatter consists of five contributions.

2.5 Case Studies

In Section 2 of this chapter, we posed four questions. The first two deal with the variation of the relative radiometric and radar sensitivities, E/E_0 and S/S_0, with optical thickness τ and the third question pertains to the dependence these sensitivities might have on the scattering albedo ω. In this section we will answer these questions through graphical presentations. The interested reader may also want to refer to our analytical solutions, which are available in Appendices A to C of the technical report version of this study [27]. Both approaches lead to the following conclusions:

1. $E/E_0 \leq 1$ is always true.

2. With σ° expressed in (m^2/m^2), $S/S_0 \leq 1$ is not always true; for relatively smooth surfaces there are situations for which $S/S_0 > 1$.

3. With σ° expressed in dB, $\mathrm{S}^{\mathrm{dB}}/\mathrm{S}_0^{\mathrm{dB}} \leq 1$ is always true.

4. Over the range $0.07 \leq \omega \leq 0.15$, the radiometric and radar sensitivities are essentially insensitive to ω.

The final question of Section 2 seeks to compare the relative soil moisture sensitivities of passive and active microwave sensing techniques. To answer this and the preceding questions we will consider three types of canopies: (a) an "imaginary" canopy made up of Rayleigh spheres, (b) a grass-like canopy, and (c) a soybeans canopy. The Rayleigh canopy is included because it has a simple phase matrix, making the analysis easy to understand, and it also serves as a precursor to the grass and soybeans canopies.

In all three case, the ground surface is assumed to have the dielectric and roughness properties described in Section 3. All plots and results are for 1.5 GHz, $\theta = 30°$, h-polarized emission and hh-polarized backscatter.

2.5.1 Rayleigh Canopy

Smooth Soil Surface

For a canopy comprised of Rayleigh spheres, the emission and backscatter are governed by m_v of the surface, and the albedo ω and optical thickness τ of the overlying layer. Expressions for the elements of the phase matrix of a Rayleigh particle, which are available in Tsang et al. [[94], pp. 155-158], were used to compute the extinction matrix $\boldsymbol{\kappa}_e$ and the absorption vector $\boldsymbol{\kappa}_a$ according to the definitions given in Tsang et al. [[94], pp. 140-148]. Figures 2.5 and Figure 2.5.1 depict

the variations of the canopy emissivity e and backscattering coefficient σ° with m_v for each of five values of τ, all computed for the smooth soil surface and a vegetation albedo $\omega = 0.1$. In preparation for a forthcoming discussion regarding the use of

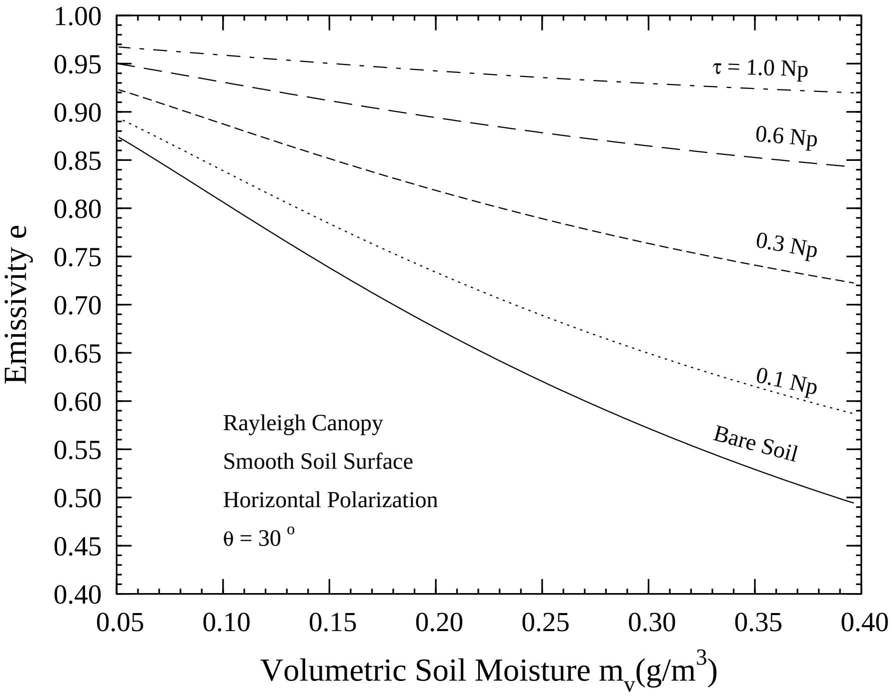

Figure 2.5: Plots of (a) e versus m_v, (b) σ^0 (m^2/m^2) versus m_v, and (c) σ^0 (dB) versus m_v, all for a Rayleigh canopy over a smooth surface

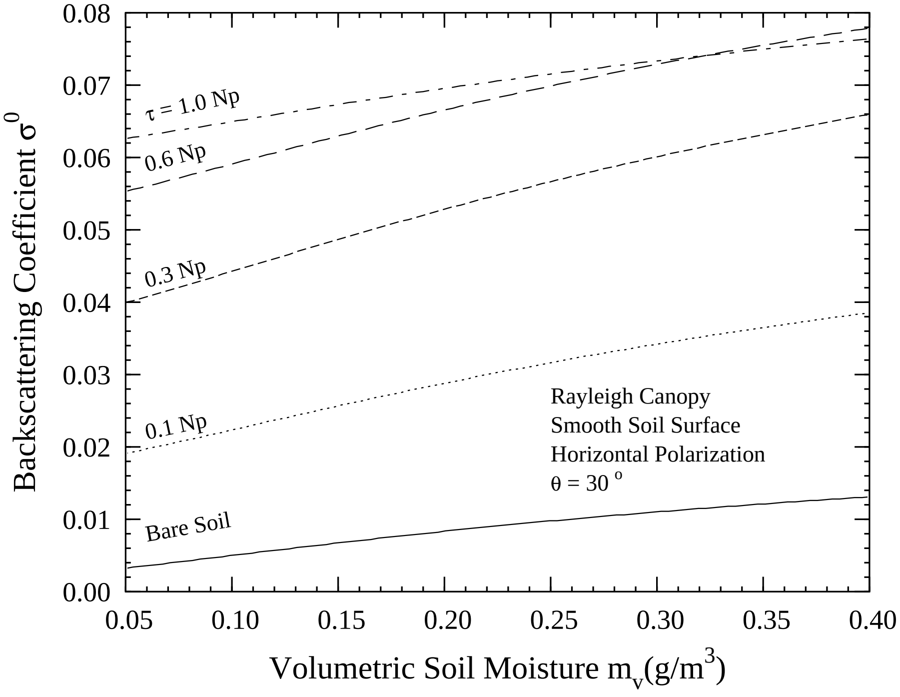

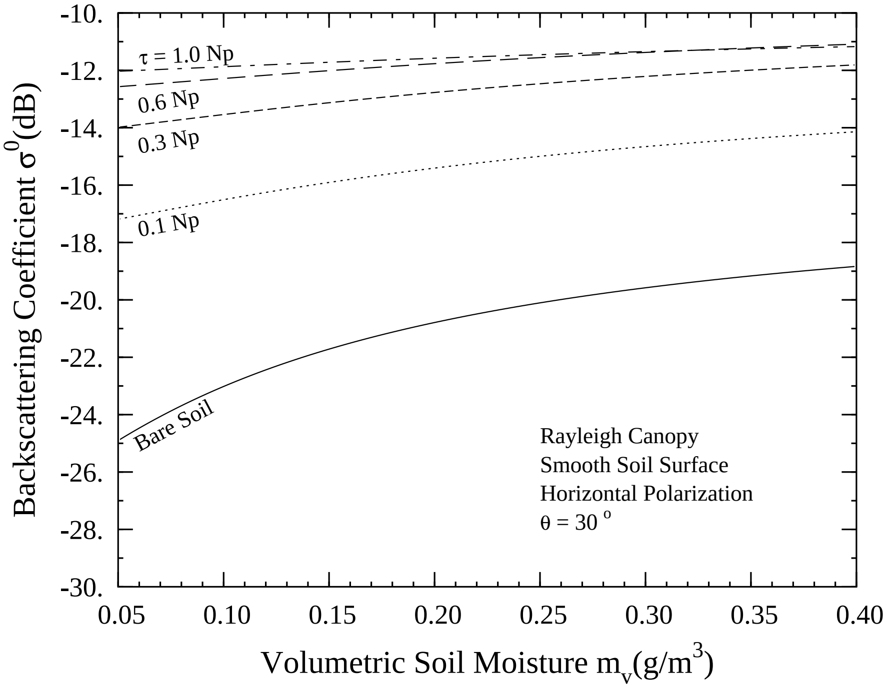

dB scale to express σ°, the plots of σ° shown in Figure 2.5.1 are shown in dB in Figure 2.5.1. In each figure, the curve labeled τ=0 corresponds to the bare-soil case. Even though the curves shown in Figure 5 are not straight lines, we will linearize them by determining the best linear fit to equally spaced points across the 0.05 to 0.4 g/cm^3 range of m_v. We decided to start at 0.05 g/cm^3 instead of at 0 because in practice soil moisture rarely drops below 0.05 g/cm^3. ¿From the slopes of these lines, we will obtain representative values of E_0, S_0, and S_0^{dB} for the bare-soil sensitivities and E, S, and S^{dB} for each value of τ.

This process will allow us to generate the plots shown in Figure 2.6 for the relative sensitivities, E/E_0, S/S_0, and $S^{\mathrm{dB}}/S_0^{\mathrm{dB}}$, as functions of τ. These curves indicate that for this Rayleigh canopy, the normalized radiometric sensitivity decreases monotonically with increasing τ. The addition of vegetation reduces the soil-emission contribution and increases the self emission by the vegetation. The radar case is not so simple. The curve for S/S_0, corresponding to σ° expressed in natural units of m^2/m^2, exhibits an increase with increasing τ up to a maximum of

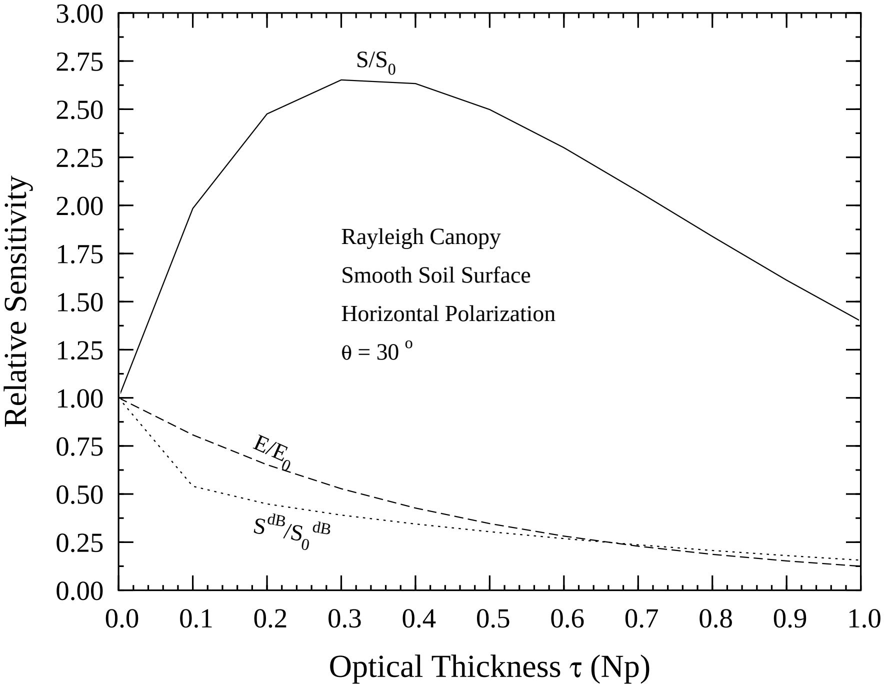

Figure 2.6: Plots of the relative sensitivities $E/E_0, S/S_0$, and $S^{\mathrm{dB}}/S_0^{\mathrm{dB}}$ versus τ for a Rayleigh canopy over a smooth surface.

2.6 at $\tau = 0.3$ Np, and then it reverses direction and decreases with τ, and if we were to continue the plot beyond $\tau = 1$ Np, the curve would have continued its decreasing trend towards zero for τ very large. Although somewhat unusual, this "sensitivity enhancement" behavior is explainable in terms of the variations of the individual σ° terms in Eq. 2.22 with m_v and τ. In the range between $\tau = 0$ and $\tau = 0.3$ Np, the addition of vegetation (increasing τ) reduces the soil moisture sensitivity of the direct soil-backscatter term σ_1°, but it increases the contributions of terms $\sigma_3^\circ, \sigma_4^\circ$, and σ_5°, all of which are proportional to R_h or R_h^2, and hence to m_v. This process continues as τ is increased until a point is reached beyond which attenuation effects overtake the "enhancement" effect, thereby causing the relative sensitivity S/S_0 to decrease with τ. This sensitivity enhancement behavior is not unique to the conditions of the Rayleigh canopy and underlying soil surface associated with Figure 5 and

Figure 2.6; the overall pattern of S/S_0 shown in Figure 6 was also observed for the grass and soybean canopies (of the next two subsections), and over a modest range of scattering albedo (0.07 to 0.15), but in all cases the soil surface was the same, namely the smooth surface described by Eq. 2.15. As we will see later, when the same examination was conducted for a vegetation canopy over the medium rough surface, no sensitivity enhancement effect was observed.

Next, we should consider the dB case. We usually express σ° in dB because: (1) the dB scale serves to compress its range (when we plot σ° versus incidence angle, it often varies over several orders of magnitude), and (2) the precision associated with experimental measurements is governed by Rayleigh fading statistics [99] which exhibit the behavior of multiplicative noise; the confidence interval associated with a measurement of σ° is proportional to σ° itself, whereas when σ° is expressed in dB, the confidence interval is independent of the value of σ° itself [[104], pp. 1818-1819]. If we use the chain rule, (3) can be rewritten as

$$\begin{aligned} S^{\mathrm{dB}} &= \frac{\partial \sigma^\circ(\mathrm{dB})}{\partial m_v} \\ &= \frac{\partial(10\log\sigma^\circ)}{\partial m_v} = \frac{10\log e}{\sigma^\circ}\ \frac{\partial\sigma^\circ}{\sigma m_v} \qquad (2.23) \\ &= \frac{4.34}{\sigma^\circ}\ S. \end{aligned}$$

Because σ° increases with increasing τ faster than the rate at which S increases with τ (over the range between 0 and 0.3 Np), S^{dB} exhibits the monotonically decaying pattern shown in Figure 2.6 over the entire range of τ.

Medium Rough Soil Surface

Upon repeating the process described in the preceding subsection, but only changing the soil surface to that described by Eq. 2.12 for emission and by Eq. 2.16 for

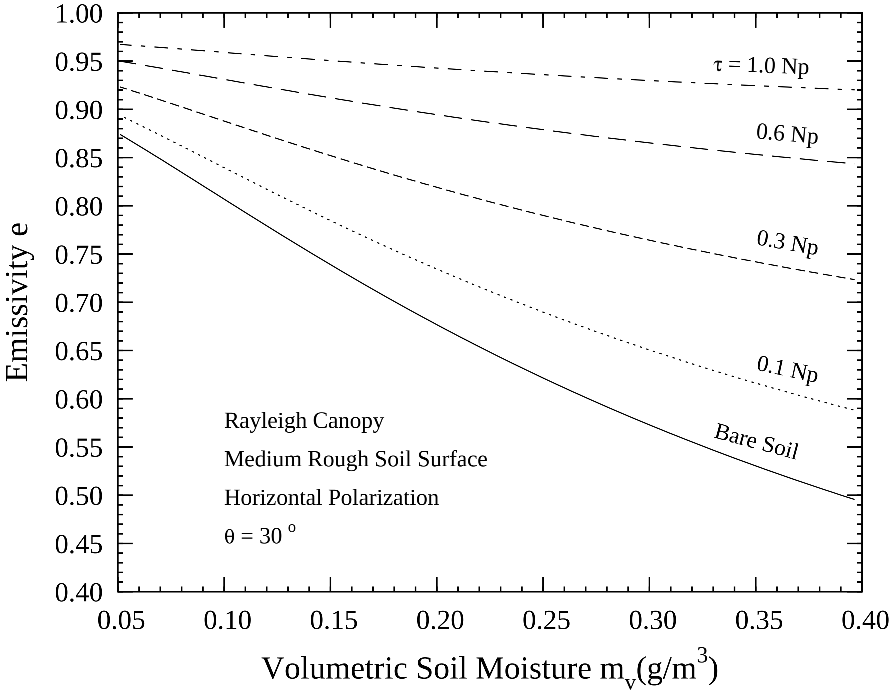

Figure 2.7: Plots of (a) e versus m_v, (b) σ^0 ($\mathrm{m}^2/\mathrm{m}^2$) versus m_v, and (c) σ^0 (dB) versus m_v, all for a Rayleigh canopy over a medium rough surface.

backscatter,

we obtain the emissivity and backscatter responses shown in Figure 2.7 and the corresponding relative sensitivity curves shown in Figure 2.8. We observe that:

(a) $E/E_0 \leq S/S_0$, which means that soil masking by the vegetation layer is more pronounced in the case of emission than for backscatter,

(b) S/S_0 no longer exhibits the sensitivity enhancement effect observed earlier for the canopy over the smooth soil surface (Figure 2.6), and

(c) S/S_0 is only slightly larger than $S^{\mathrm{dB}}/S_0^{\mathrm{dB}}$.

2.5.2 Grass Canopy

The grass canopy is modeled as a collection of circular cylinders whose axes are oriented in accordance with an empirically determined probability density function

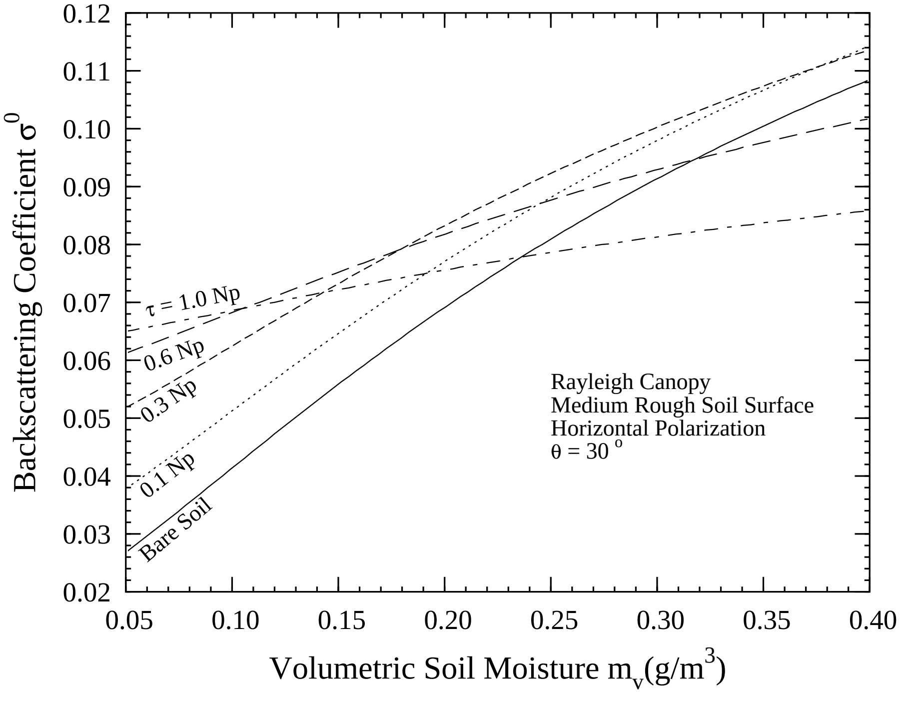
Backscattering Coefficient σ^0
Volumetric Soil Moisture $m_v(g/m^3)$
0.12
0.11
0.10
0.09
0.08
0.07
0.06
0.05
0.04
0.03
0.02
0.05
0.10
0.15
0.20
0.25
0.30
0.35
0.40
τ = 1.0 Np
0.6 Np
0.3 Np
0.1 Np
Bare Soil
Rayleigh Canopy
Medium Rough Soil Surface
Horizontal Polarization
θ = 30 °

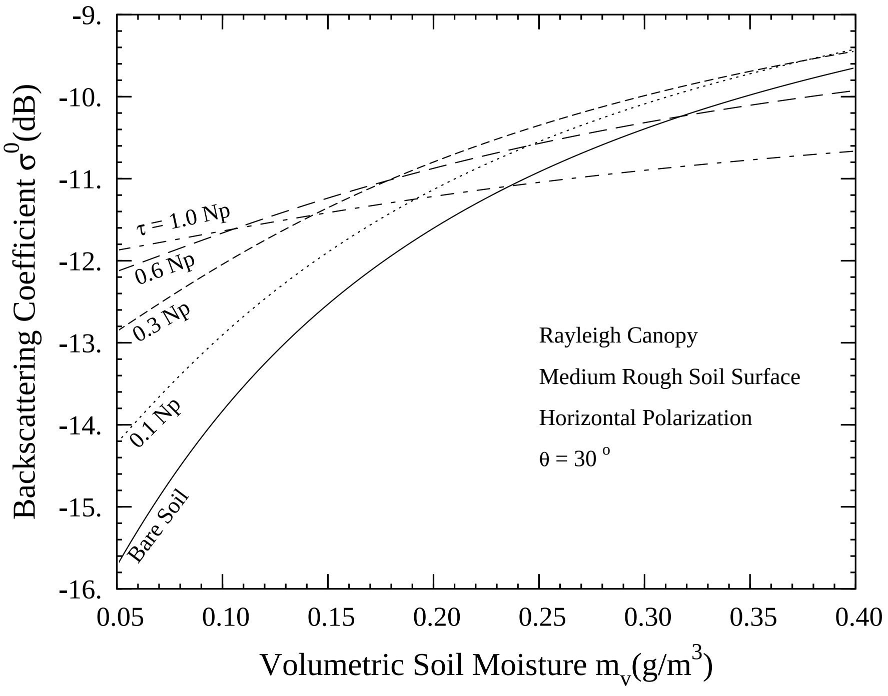
Backscattering Coefficient σ^0(dB)
Volumetric Soil Moisture $m_v(g/m^3)$
-9.
-10.
-11.
-12.
-13.
-14.
-15.
-16.
0.05
0.10
0.15
0.20
0.25
0.30
0.35
0.40
τ = 1.0 Np
0.6 Np
0.3 Np
0.1 Np
Bare Soil
Rayleigh Canopy
Medium Rough Soil Surface
Horizontal Polarization
θ = 30 °

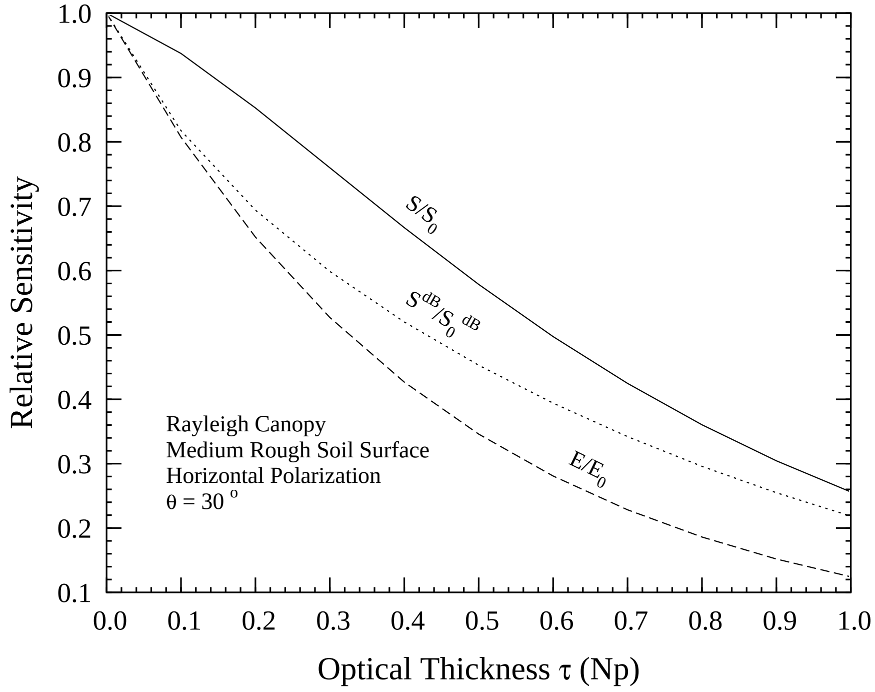

Figure 2.8: Plots of the relative sensitivities $E/E_0, S/S_0$, and $S^{\mathrm{dB}}/S_0^{\mathrm{dB}}$ versus τ for a Rayleigh canopy over a medium rough surface.

which can be described approximately by the pdf given in Table 2.1 where θ is the angle between the axis of the cylinder and the zenith direction. The emission and backscatter calculations were performed as a function of canopy height from zero to 30 cm, with 30 cm corresponding to a dry biomass of 1 kg/m^2. Using the information given in Table 2.1, we obtain the following expressions for the extinction matrix $\boldsymbol{\kappa}_e$ and the absorption vector $\boldsymbol{\kappa}_a$:

$$\boldsymbol{\kappa}_e = \begin{pmatrix} 2.70 & 0 & -4\times10^{-8} & 1.29\times10^{-7} \\ 0 & 3.08 & -4\times10^{-8} & 1.29\times10^{-7} \\ -8\times10^{-8} & -8\times10^{-8} & 2.89 & -0.71 \\ -2.6\times10^{-7} & -2.5\times10^{-7} & 0.71 & 2.89 \end{pmatrix} \tag{2.24}$$

$$\boldsymbol{\kappa}_a = \begin{bmatrix} 2.575 \\ 2.860 \\ -1.60 \times 10^{-7} \\ 3.83 \times 10^{-12} \end{bmatrix} \tag{2.25}$$

We note that in view of the azimuthal symmetry of the orientations of the vegetation elements, $\boldsymbol{\kappa}_e^+ = \boldsymbol{\kappa}_e^- = \boldsymbol{\kappa}_e$ and a similar statement applies to $\boldsymbol{\kappa}_a$. The albedo for horizontal polarization is given by

$$\omega = 1 - \frac{\kappa_{a_2}}{\kappa_{e_{22}}} = 1 - \frac{2.86}{3.08} = 0.07. \tag{2.26}$$

Of the two surface roughnesses discussed in Section 3, the medium rough surface is the more typical as a surface underlying a grass canopy. Hence, all the calculations displayed

in Figure 2.9 and Figure 2.10 were performed for that case. The key observation to note is that the soil-masking effect of the grass cover is about the same for emission and backscatter (Figure 2.10).

The plots shown in Figure 2.10 were generated for a grass canopy with an albedo $\omega = 0.07$. Similar calculations were also carried out for $\omega = 0.1$ and 0.15. Comparison of the three cases revealed that S/S_0, $S^{\mathrm{dB}}/S_0^{\mathrm{dB}}$ and E/E_0 are all essentially insensitive to ω over the indicated range [27]; the variation with ω was less than 3% for $\tau < 0.3$Np and less than 10% for τ as large as 0.9 Np. For values of ω significantly larger than 0.15, the first-order iterative solutions for e and σ° would no longer provide accurate results.

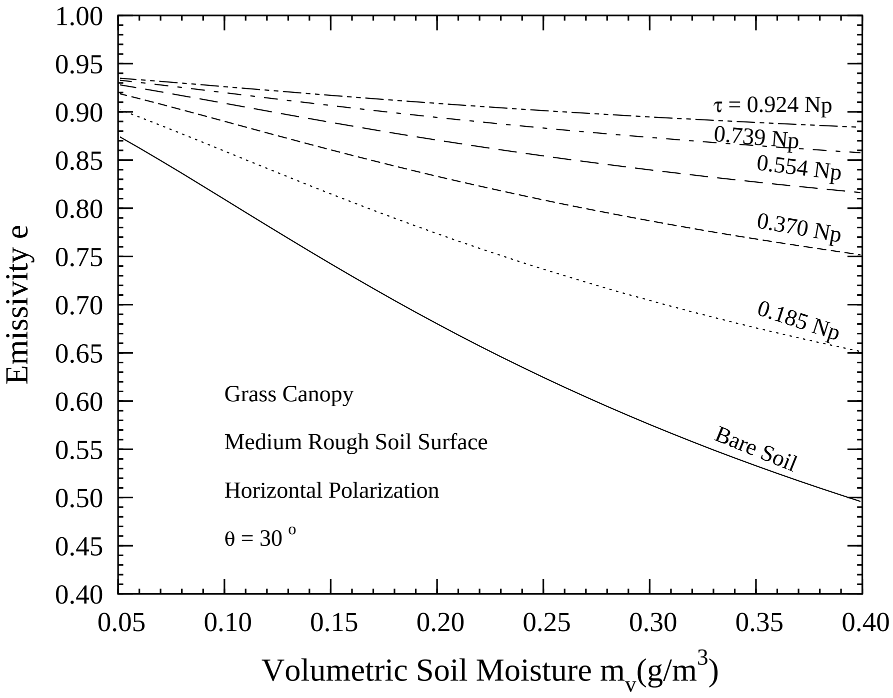

Figure 2.9: Plots of (a) e versus m_v and (b) $\sigma^0(\mathrm{m}^2/\mathrm{m}^2)$ versus m_v both for a grass canopy over a medium rough surface.

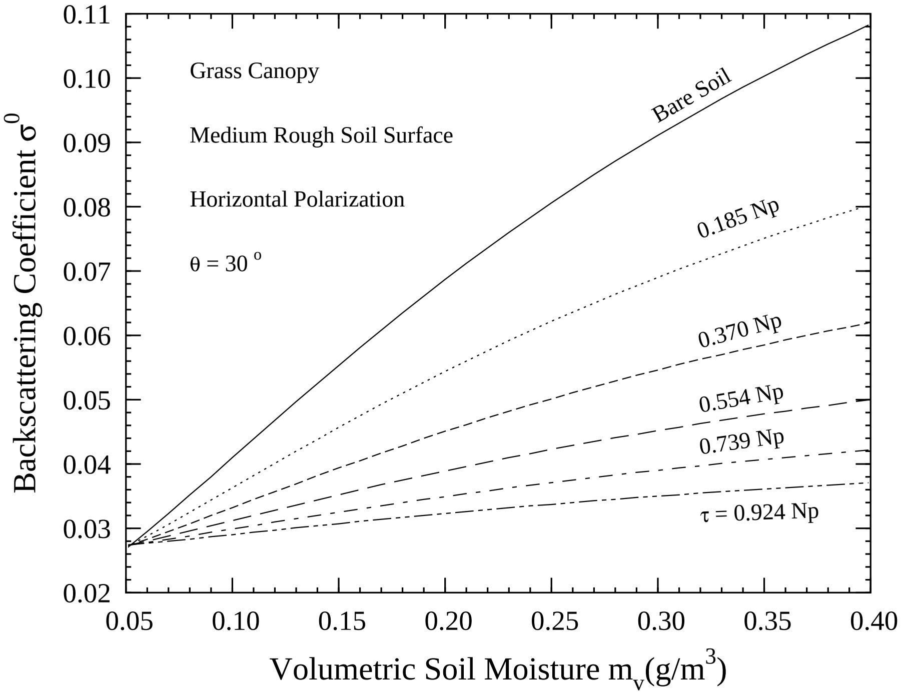

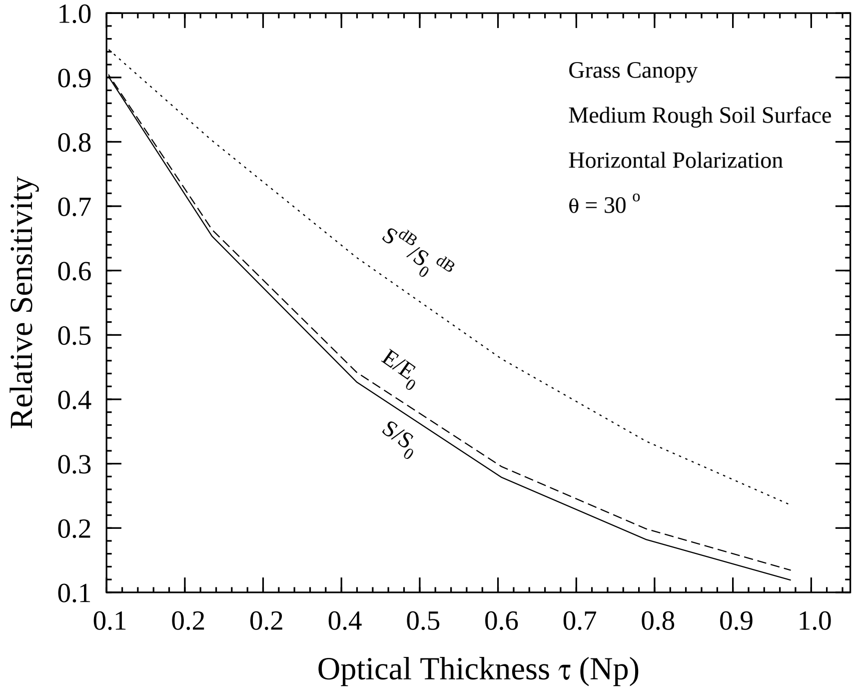

Figure 2.10: Plots of the relative sensititivies E/E_0, S/S_0 and S_0^{dB}versus τ for a grass canopy over a medium rough surface.

2.5.3 Soybean Canopy

The soybean canopy is modeled as a collection of leaves and branches, with the leaves modeled as flat dielectric disks and the branches as straight, circular dielectric cylinders. The canopy parameters, including the pdfs of the leaf and cylinder orientations (which are approximations to measured distributions), are given in Table 2.1. The calculations were performed as a function of canopy height up to a maximum height of 60 cm. When the canopy reaches that height, the dry biomass is 0.7 kg/m^2 for the leaves and 1.0 kg/m^2 for the branches. For the specified parameters, the extinction matrix and absorption coefficient vector are:

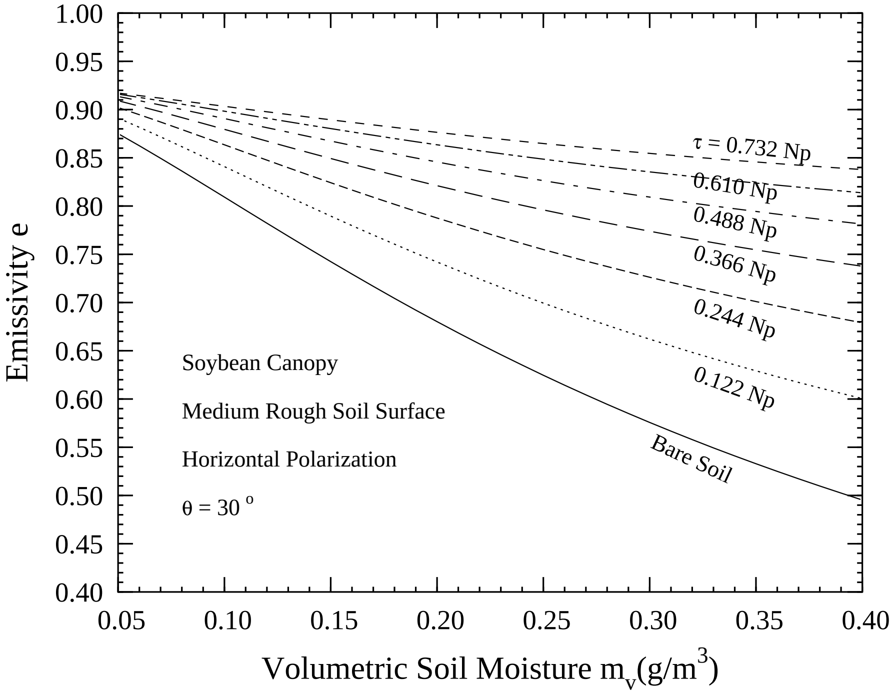

Figure 2.11: Plots of (a) e versus m_v and (b) $\sigma^0(\mathrm{m}^2/\mathrm{m}^2)$ versus m_v both for a soybean canopy over a medium rough surface.

$$\boldsymbol{\kappa}_e = \begin{pmatrix} 1.11 & 0 & 1.13\times10^{-8} & -6.64\times10^{-8} \\ 0 & 1.228 & 9.79\times10^{-9} & 7.13\times10^{-10} \\ 1.95\times10^{-8} & 2.26\times10^{-8} & 1.16 & -0.19 \\ 1.42\times10^{-7} & -1.33\times10^{-7} & 0.19 & 1.16 \end{pmatrix} \tag{2.27}$$

$$\boldsymbol{\kappa}_a = \begin{bmatrix} 1.03 \\ 1.10 \\ 4.23\times10^{-8} \\ 1.30\times10^{-7} \end{bmatrix}. \tag{2.28}$$

For horizontal polarization, $\omega = 0.1$, and over the height range of 0 to 60 cm, τ varies between 0 and 0.72 Np.

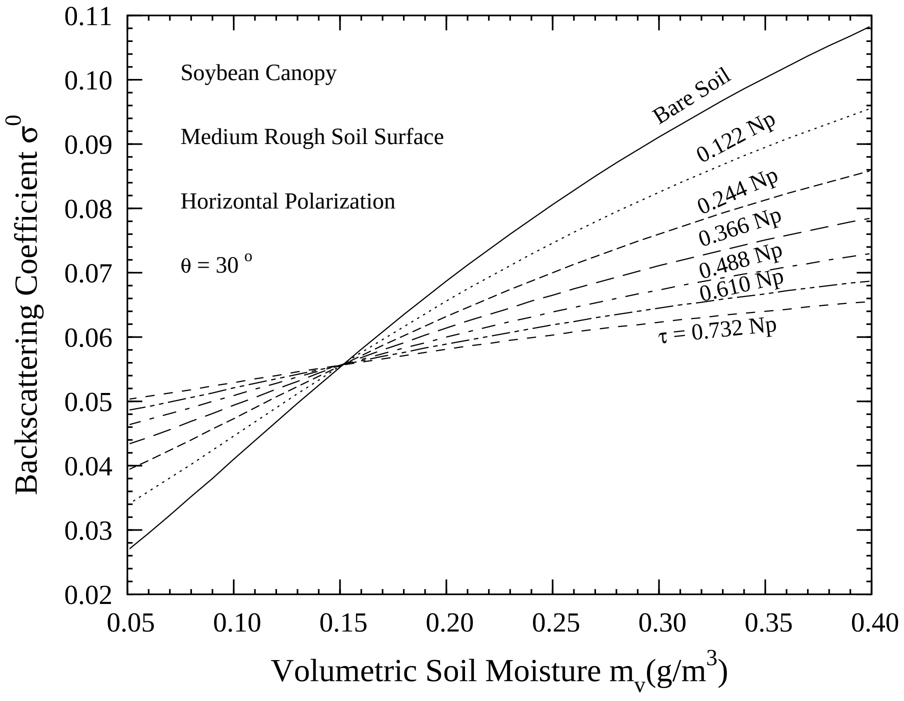

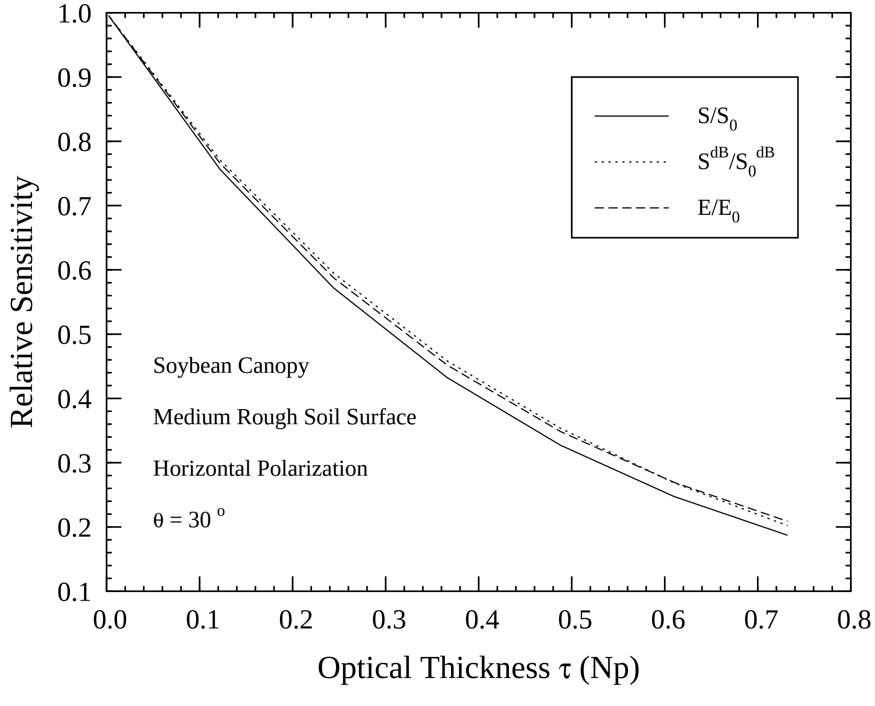

Figure 2.12: Plots of the relative sensititivities E/E_0, S/S_0 and $S^{\mathrm{dB}}/S_0^{\mathrm{dB}}$ versus τ for a soybean canopy over a medium rough surface

The results for soybeans are given in Figure 2.11 and Figure 2.12, and the conclusion is the same: The reduction in soil-moisture sensitivity caused by the vegetation cover is essentially the same for emission and backscatter (Figure 2.12).

2.6 Conclusion

Using realistic emission and scattering models, together with appropriate models for the soil surface and vegetation canopy, this study evaluated the L-band active and passive microwave responses to soil moisture and vegetation optical thickness for three types of vegetation. The conclusions drawn from this study are:

(1) For all canopy conditions and soil surfaces, the relative soil-moisture radiometric sensitivity, $E(\tau)/E_0$, decreases approximately exponentially with increasing optical thickness of the vegetation cover. Furthermore, over the range of albedo values characteristic of vegetation canopies at 1.5 GHz, $E(\tau)/E_0$ is essentially insensitive to changes in ω.

(2) With σ° expressed in ($\mathrm{m}^2/\mathrm{m}^2$), the variation of the relative soil-moisture radar sensitivity, $S(\tau)/S_0$, with τ depends on the roughness of the underling soil surface. For a smooth surface with rms height of 0.4 cm, $S(\tau)/S_o$ increases with τ up to a maximum value exceeding 2.5 (at τ=0.3 Np) and then decreases with further increase in τ. In contrast, for a medium rough surface with s = 1.12 cm (or greater), $S(\tau)/S_0$ behaves in a manner similar to that of $E(\tau)/E_0$.

(3) Except for the special case of a smooth soil surface, the radar and radiometric sensitivities exhibited comparable reductions due to vegetation cover.

Table 2.1: Properties of grass and soybean canopies

Grass

Grass density = 109160 needles/m^2

Needle diameter = 0.18 cm

Needle length = 6 cm

Dry density of needle naterial = 0.2gcm^3

Volumetric moisture = 0.8 g/cm^3

Orientation distribution = plagiophile $(p(\theta) = \frac{3}{4}\sin^3\theta, \quad 0 \le \theta \le \pi)$

Soybean

(1) Leaves

Leaf density = 9794 leaves/m^2

Leaf thickness = 0.026 cm

Leaf diameter = 5 cm

Dry density of leaf material = 0.2 g/cm^3

Volumetric moisture = 0.8 g/cm^3

Leaf orientation = plagiophile

(2) Secondary branches

Branch density = 999 branches/m^2

Branch diameter = 0.3 cm

Branch length = 20 cm

Dry density of branch material = 0.2 g/cm^3

Volumetric moisture = 0.8 g/cm^3

Brand orientation = plagiophile

CHAPTER III

A Semi-Empirical Backscattering Model at L-band and C-band for a Soybean Canopy with Soil Moisture Inversion

3.1 Introduction

The preceding chapter addresses the topic of sensitivity to soil moisture for vegetation covered land by active and passive sensors at L band is revisited. At such frequency, for the usually encountered vegetation covers such as grass and soybean, which are electrically small in dimension, the conventional RTE can be used to study the scattering mechanisms.

The scattering mechanism becomes more complex for a soybean canopy at C band. The independent scattering assumption for conventional RTE does not hold strictly; the interaction among scatterers are addressed in the literature by either the inclusion of higher order scattering components [83] [16] or the application of antenna array-like treatment [115] [12]. Though both provide higher fidelity in accounting for the underlying scattering mechanism, the former is computationally demanding, while the latter necessitates the introduction of a new set of parameters to describe the geometrical and positional properties of the constituents of a soybean plant. If an inversion algorithm is to be developed for extracting water content, biomass, rough surface rms height and soil moisture from the L, C bands measurements of soybean at 45° incidence, we can hardly use the high order scattering approach due to its complexity, nor can we use the antenna array -like approach due to the limited measurement data available for inversion. Rather, assuming the adoption of the conventional RTE technique, we endeavor to best characterize the dependence of the volume extinction coefficient κ_e and the phase matrix $\mathbf{P}$, two most critical input to RTE, upon the water content to the biomass.

For bare-soil surfaces, the backscattering coefficient, σ^0, is strongly dependent on the roughness and the moisture content of the soil surface layer [74,75,95]. Given two or more radar channels (such as simultaneous multi-polarization or multi-frequency observations), it is possible to estimate the volumetric moisture content, m_v, with good precision. Specifically, when multi-polarized L-band observations were used, the precision of the retrieved moisture was about 3.2% [95]. The data included observations made by a truck-mounted radar, by the JPL airborne AirSAR system, and by SIR-C.

This chapter addresses the vegetation-covered case for a soybeans canopy. This portion of the work has been published in [23]. The first part describes the test site and data acquisition process. It is then followed with an analysis of the "direct problem", namely matching the measured data to a backscatter model. Then it ends with the development of a regression-based inversion algorithm (inverse problem) that predicts soil moisture content and vegetation biomass on the basis of multi-channel radar observations as input.

3.2 Experimental Measurements

The measurements reported in this study were conducted during the summer of 1996 at the Long-Term Ecological Research (LTER) site of the Kellogg Biological Station in Hickory Corners, Michigan. Three primary types of vegetation canopies were chosen for measurement: corn, which represents agricultural fields in which a stem or stalk is a dominant feature at microwave frequencies; soybeans and alfalfa, which represent agricultural fields that lack a dominant stem; and a field which had lain fallow for many years and is now populated with many native grasses. The present study will address the soybean observations only.

The radar backscatter measurements were made by a truck mounted radar system. All measurements were made at an incidence angle of 45° and at a range of 12-m in a fully polarimetric mode at both L-band (1.25 GHz) and C-band (5.4 GHz). Calibration accuracy is estimated at ± 0.5 dB for the copolarized backscattering coefficients, σ^0_{vv} and σ^0_{hh}, ± 1.0 dB for the cross-polarized backscattering coefficient, σ^0_{hv}, and ±15° for phase difference between polarizations.

To reduce signal-fading variations of the backscattered signal, multiple measurements of the same target were performed under the same radar parameters (frequency, polarization and angle of incidence), but with a translation or rotation of the radar antennas. The figure of merit for the reduction of fading is the number of independent samples, which is the product of the number of independent samples per spatial sample (due to frequency averaging) and the number of spatial samples measured. For each measurement reported in this study, the number of independent samples is 205 at L-band and 157 at C-band.

The radar measurements and associated canopy and soil observations were com-

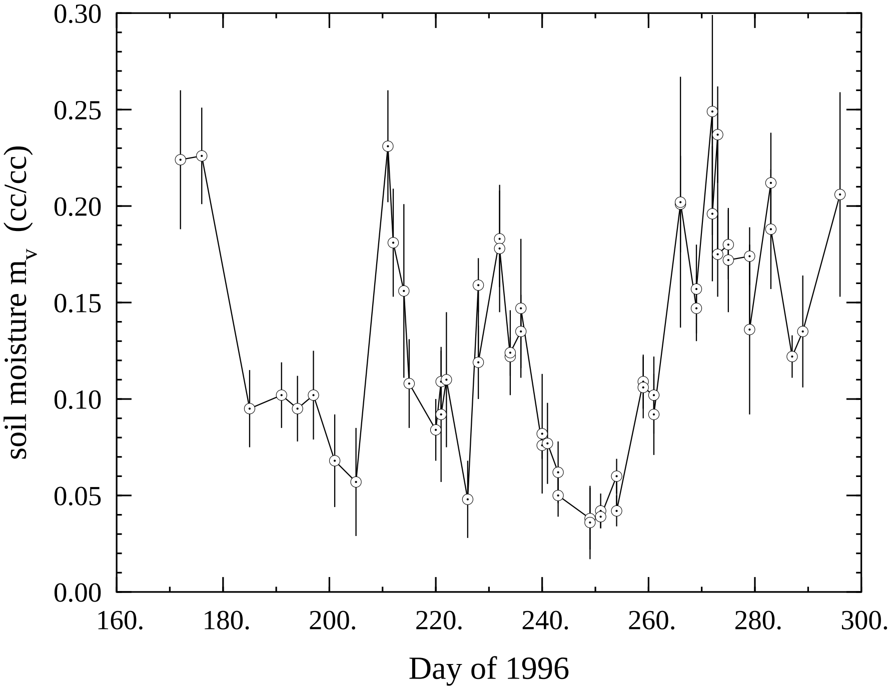

Figure 3.1: Variation of the soil moisture under the soybean canopy.

menced on 20 June 1996 and were completed on 26 October. A total of 57 data sets were acquired, covering a wide range of conditions, extending from 0.02 kg/m^2 to 0.97 kg/m^2 in vegetation water mass, 3% to 26% in volumetric soil moisture, and 12 cm to 63 cm in canopy height. The variation of the moisture in the soybean fields measured in the growing season of 1996 is shown in Figure 3.1.

3.3 Backscatter Model

The Michigan Microwave Canopy Scattering (MIMICS) model was developed several years ago for predicting the backscatter from forest stands [64, 97]. We shall adopt the basic structure of the model for characterizing the backscatter from soybeans, but we shall delete the scattering component associated with ground-trunk scattering because the architecture of a soybean plant does not have a vertical stalk. Hence, σ^0_{pq}, the pq-polarized backscattering coefficient (where p and q are each either

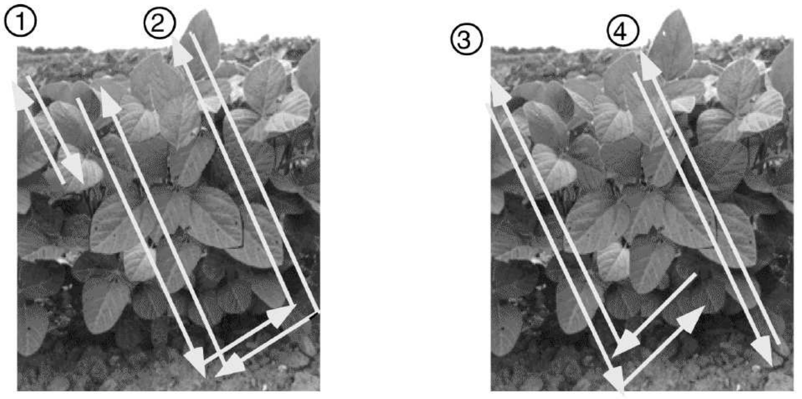

Figure 3.2: Scattering mechanisms considered in this chapter for soybean canopies.

v or h polarization) of the canopy may be expressed as:

$$\sigma^0_{pq} = \sigma^0_{pq_1} + \sigma^0_{pq_2} + \sigma^0_{pq_3} + \sigma^0_{pq_4}, \tag{3.1}$$

where each component represents a scattering mechanism, as illustrated in Figure 3.2, particular pq-polarization configuration, these components are:

σ^0_1 = direct backscatter contribution from the canopy,

σ^0_2 = combined ground–canopy and canopy–ground forward scattering contribution,

σ^0_3 = ground–canopy–ground scattering contribution

σ^0_4 = direct backscatter contribution of the underlying soil surface (including two-way attenuation by the canopy).

The expressions for the four components are:

$$\sigma^0_{pq_1} = \frac{\sigma_{pq_1}\cos\theta}{\kappa_p + \kappa_q}\left(1 - T_p T_q\right), \tag{3.2}$$

$$\sigma^0_{pq_2} = 2T_p T_q(\Gamma_p + \Gamma_q)h\sigma_{pq_2} \tag{3.3}$$

$$\sigma^0_{pq_3} = \sigma^0_{pq_1} T_p T_q \Gamma_p \Gamma_q \tag{3.4}$$

$$\sigma^0_{pq_4} = \sigma^0_{pqs} T_p T_q, \tag{3.5}$$

where:

σ_{pq_1} = backscatter cross section per unit volume of the leaves and stems, ($\mathrm{m}^2/\mathrm{m}^3$),

σ_{pq_2} = bistatic cross section per unit volume of the leaves and stems, ($\mathrm{m}^2/\mathrm{m}^3$),

κ_p = p-polarized extinction coefficient of vegetation canopy, (Np/m),

T_p = p-polarized one-way transmissivity of the canopy,

$= e^{-\kappa_p h \sec\theta}$,

h = canopy height, m

Γ_p = p-polarized reflectivity of ground surface,

$= \Gamma_{po} \exp\left[-(2ks\cos\theta)^2\right]$

Γ_{po} = Fresnel reflectivity of a specular surface,

k $= 2\pi/\lambda$,

s = rms height of ground surface, (m)

σ^0_{pqs} = backscattering coefficient of soil surface in the absence of vegetation cover.

3.3.1 Soil Surface Model

For the soil surface, we adopt the semi-empirical model developed by Oh *et al.*, which was first introduced in 1992 [74] and then improved in a later study in 1994 [75]. The soil backscattering coefficient is given by:

$$\sigma^0_{vvs} = \frac{g\cos^3\theta}{\sqrt{p}}\left[\Gamma_v(\theta) + \Gamma_h(\theta)\right] \tag{3.6}$$

$$\sigma^0_{hhs} = p\,\sigma^0_{vvs} \tag{3.7}$$

$$\sigma^0_{hvs} = q\,\sigma^0_{vvs} \tag{3.8}$$

where

$$p = \frac{\sigma^0_{hhs}}{\sigma^0_{vvs}} = \left[1 - \left(\frac{2\theta}{\pi}\right)^{(0.314/\Gamma_0)} \cdot \exp(-ks)\right]^2 \tag{3.9}$$

$$q = \frac{\sigma^0_{hvs}}{\sigma^0_{vvs}} = 0.25\sqrt{\Gamma_0}(0.1 + \sin^{0.9}\theta)[1 - e^{-(1.4-1.6\Gamma_0)ks}] \tag{3.10}$$

$$g = 0.7\left[1 - e^{-0.65(ks)^{1.8}}\right], \tag{3.11}$$

$$\Gamma_0 = \left|\frac{\sqrt{\epsilon_s} - 1}{\sqrt{\epsilon_s} + 1}\right|^2, \tag{3.12}$$

$$\Gamma_{ho}(\theta) = \left|\frac{\cos\theta - \sqrt{\epsilon_s - \sin^2\theta}}{\cos\theta + \sqrt{\epsilon_s - \sin^2\theta}}\right|^2 , \tag{3.13}$$

$$\Gamma_{vo}(\theta) = \left|\frac{\epsilon_s\cos\theta - \sqrt{\epsilon_s - \sin^2\theta}}{\epsilon_s\cos\theta + \sqrt{\epsilon_s - \sin^2\theta}}\right|^2 , \tag{3.14}$$

and ϵ_s is the relative complex dielectric constant of the soil:

$$\epsilon_s = \epsilon'_s - j\epsilon''_s. \tag{3.15}$$

The incidence angle θ is in radians and the models used for relating ϵ'_s and ϵ''_s to m_v, the volumetric soil moisture content, are given in Hallikainen *et al.* [41]. According to field tests, the soil was 51% sand and 13% clay.

The effect of soil surface roughness comes into the picture not only in terms of the direct soil backscatter component, σ^0_{pq4}, but also in terms of forward scattering by the soil surface, σ^0_{pq2} and σ^0_{pq3}; the p-polarized Fresnel surface reflectivity, Γ_{po}, is reduced by the exponential factor $[-(2ks\cos\theta)^2]$.

3.3.2 Vegetation Model

Next, we shall find the form of the functional dependence of the electromagnetic parameters of the vegetation, namely $\sigma_{pq1}, \sigma_{pq2}$, and κ_p, to the area density of vegetation water mass, m_w (kg/m^2). We start with the extinction coefficient κ_p. For a given canopy, we expect κ to be a function of (a) the canopy architecture, and (b) the

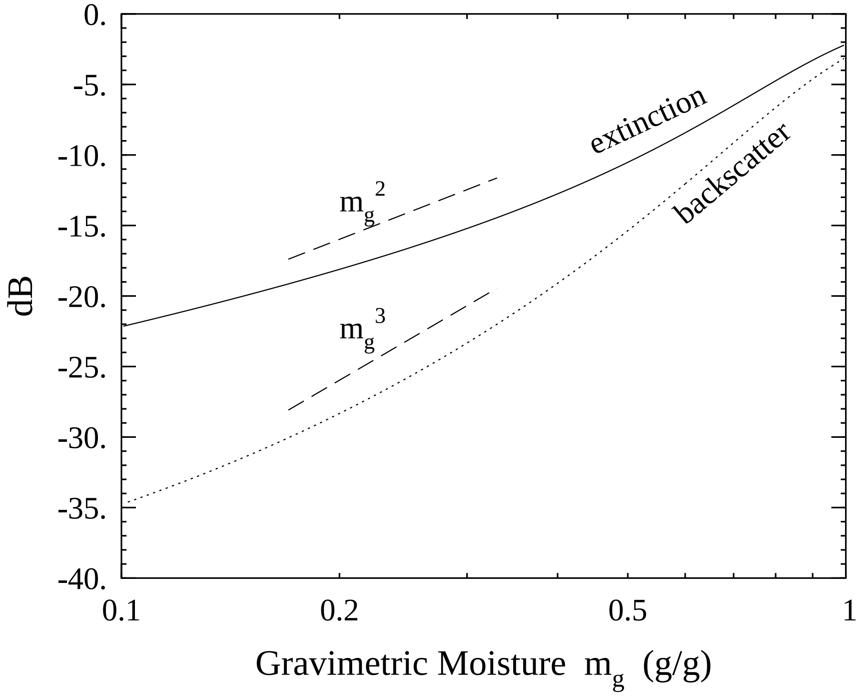

Figure 3.3: Dependence of the extinction and backscatter cross section of a single leaf upon its gravimetric moisture, after [85]. The vertical scale is normalized with respect to an equivalent perfectly conducting leaf of the same geometry. The extinction displays an approximately m_g^2 dependence while the backscatter displays an approximately m_g^3 dependence. The dashed line segments show perfect m_g^2 and m_g^3 dependence.

dielectric constant, ϵ_v, of the vegetation material. By canopy architecture, we mean the shapes, orientations, and sizes of the canopy constituents (defined relative to the wavelength λ), the incidence angle θ, and the wave polarization, p. Even though the extinction cross-section of an individual leaf or branch may exhibit a strong dependence on its orientation relative to the incident beam, we shall assume that the extinction coefficient κ_p- which is an ensemble average over the probability distribution characterizing the shapes, sizes, and orientations of leaves and branches$-$ is independent of direction, which is a reasonable assumption for a canopy like soybeans. The dielectric constant of a vegetation material, ϵ_v, is strongly dependent on its moisture content. According to a study reported by Senior *et al.* [85], which included both a theoretical model and experimental verification, the extinction cross-section of a vegetation leaf (where first normalized to the extinction cross-section of a perfectly conductive leaf of the same size) varies approximately linearly with the gravimetric moisture m_g, when both quantities are expressed on a logarithmic scale. The gravimetric moisture m_g is the ratio of the mass of water in the leaf (wet weight - dry weight) to the total mass of the leaf (wet weight). Figure 3.3 is a reproduction of their results for the gravimetric moisture range between 0.1 and 0.9. The approximately linear response with a slope of approximately 2 (on a log-log scale) suggests that the extinction cross-section of a leaf may be expressed as:

$$\sigma^e = a_o m_g^2, \tag{3.16}$$

where a_o is a constant. Thus, for a canopy containing, on average, N leaves per m^3, the extinction coefficient becomes

$$\kappa_p = N a_o m_g^2 \quad (\mathrm{Np/m}). \tag{3.17}$$

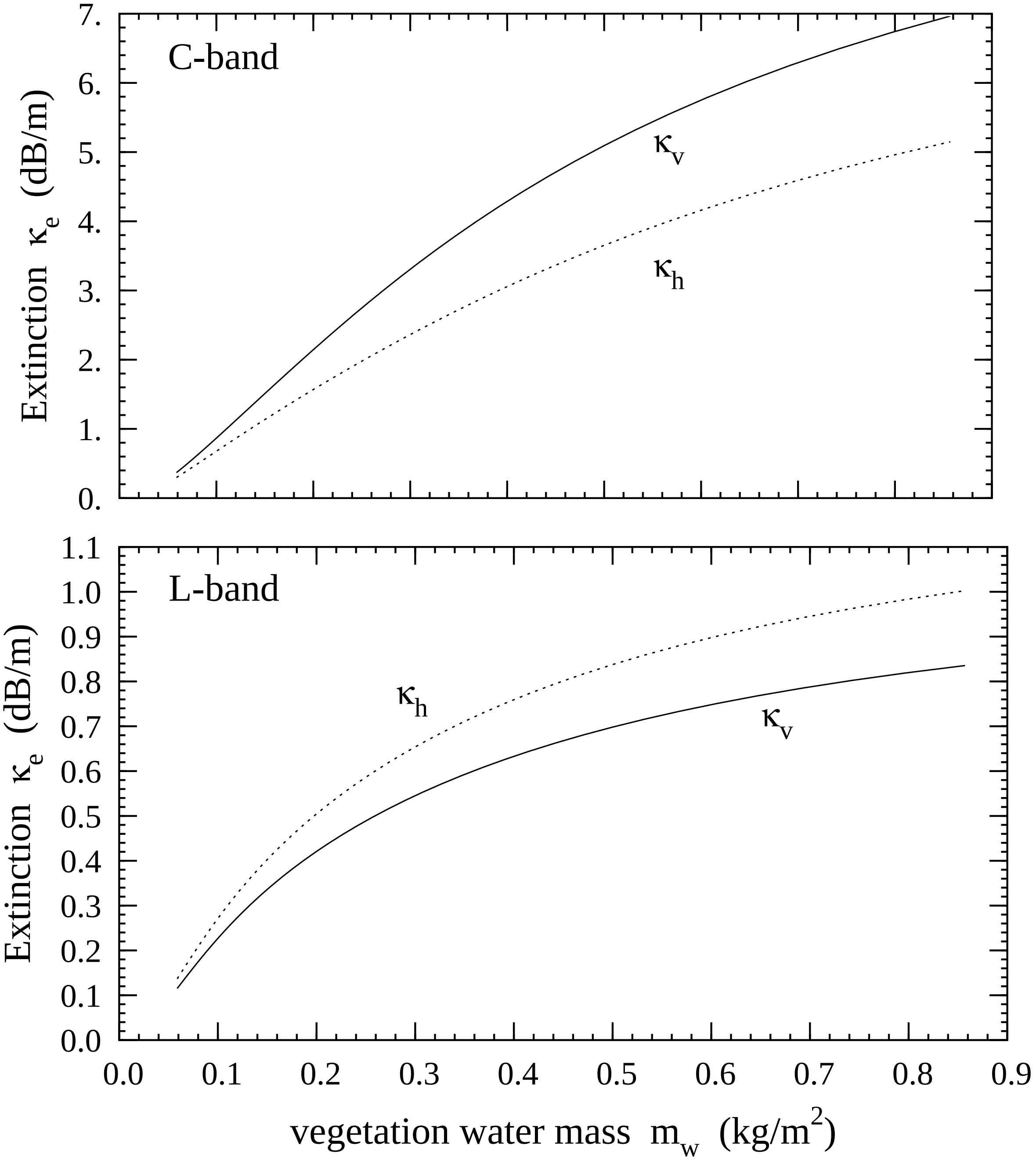

Figure 3.4: Dependence of the extinction on the area density of vegetation water mass in leaves and stems at C-band and L-band. Whereas the extinction exhibits a strong frequency dependence, all of the extinction rates are approximately proportional

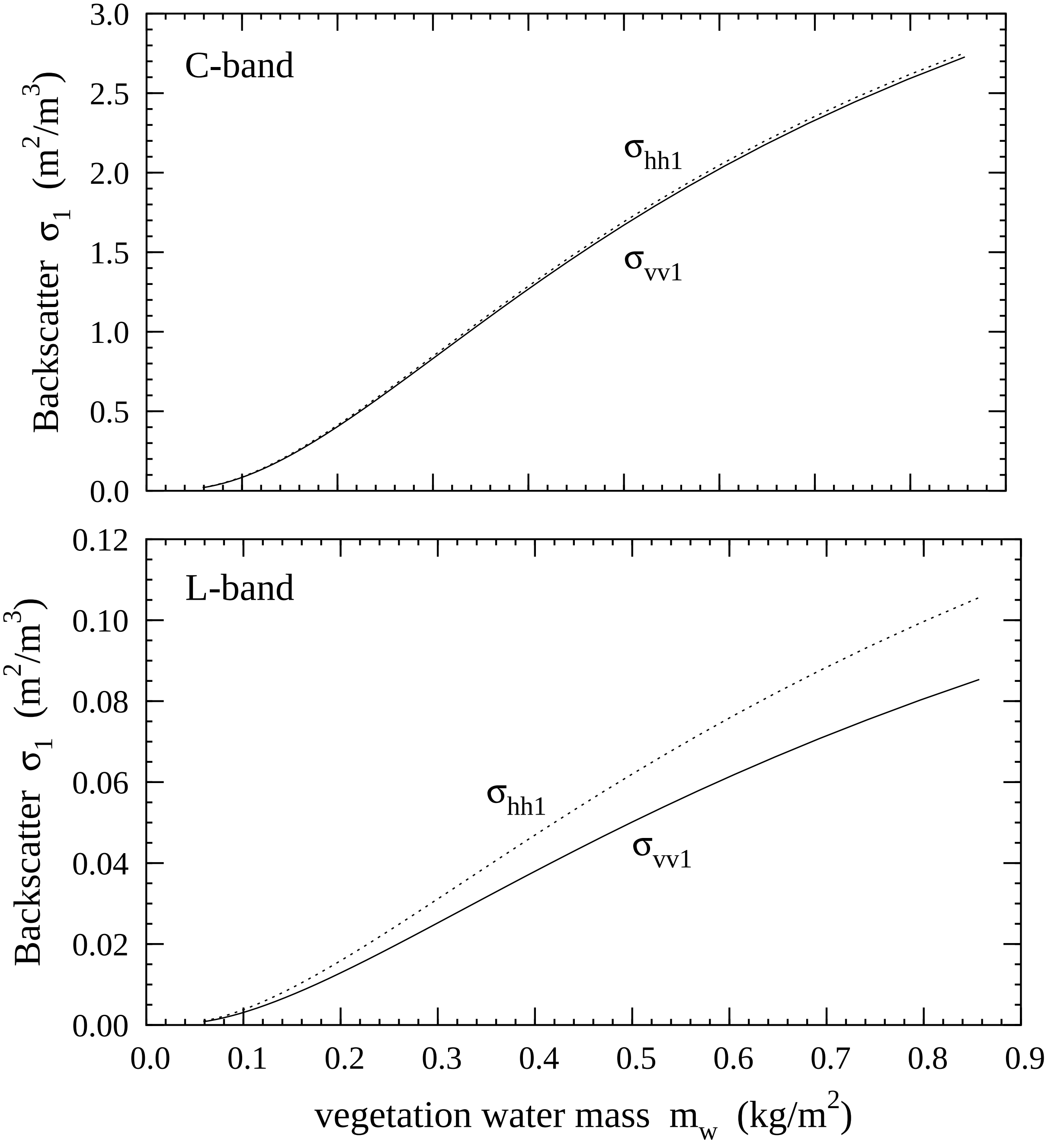

Figure 3.5: Dependence of the backscatter RCS per unit volume on the area density of vegetation water mass in leaves and stems at C-band and L-band. Both VV and HH exhibit a dependence which is roughly proportional to m_w.

The results of Senior *etal.* also suggest that the backscatter is proportional m_g^3. But these conclusions are valid only for the restrictive case where the leaves are oriented to backscatter specularly from the surface of the leaves. For the more complicated and more realistic case of a broad distribution of orientations of leaves, and including stems, the MIMICS radiative transfer model [64, 97] was used to find the extinction and backscatter averaged over the shape, size and orientation distributions of the detailed soybean vegetation parameters as provided in [17, 43, 71]. The results of these calculations for L-band and C-bands are shown in Figures 3.4 and 3.5. It was found that for both VV and HH polarizations, the mean extinction was proportional to $\sqrt{m_w}$, where m_w is the area density of vegetation water mass in kg/m^2. The MIMICS model calculations for the mean backscatter, shown in Figure 3.5, exhibit a linear dependence on m_w. MIMICS model calculations for the backscatter and bistatic phase matrices indicate that this linear dependence on m_w is appropriate for both the backscatter and bistatic canopy scattering terms in the radiative transfer model.

The curves in Figures 3.4 can be described with more faithful but more complicated dependencies on m_w, such as $\ln m_w$ or $b_1\left(\frac{1-m_w/b_2}{1+m_w/b_2}\right)$. Nonetheless, the fact that the curves themselves are based on a vegetation model developed for forest canopies and that the formulas found here are used in the semi-empirical model below only to tie the dependence of the vegetation moisture to extinction and/or volume backscattering, these more complicated dependencies are not justified. Indeed, we have tried other formulations for the dependence of extinction and scattering on m_w, and the semi-empirical model goodness-of-fit values were either insignificantly different or somewhat worse than those reported below. Therefore, the extinction is assumed to be proportional to $\sqrt{m_w}$ and the scattering is proportional to m_w.

3.3.3 A semi-empirical forward scattering model

Combining the first order radiative transfer solution of eqn. (3.1) with the results of the study of the dependence of the scattering and extinction on the vegetation water mass, we obtain the following equation to which the data must be fit:

$$\sigma^0_{pq} = a_{bias}\left(\frac{\sigma_{pq_1}\cos\theta}{2\kappa_{pq}}\left(1 - T^2_{pq}\right)\left(1 + T^2_{pq}\Gamma_p\Gamma_q\right) + T^2_{pq}\left(2(\Gamma_p + \Gamma_q)h\sigma_{pq_2} + \sigma^0_{pqs}\right)\right) \tag{3.18}$$

where

$$\sigma_{pq_1} = a_2 m_w/h \tag{3.19}$$

$$\sigma_{pq_2} = a_3 m_w/h \tag{3.20}$$

$$\kappa_{pq} = a_4\sqrt{m_w/h} \tag{3.21}$$

$$T_{pq} = e^{-\kappa_{pq}h\sec\theta} \tag{3.22}$$

and the remaining symbols $(h, \theta, \Gamma_p, \Gamma_q, \sigma^0_{pqs})$ retain their definitions from the previous section. The units of a_2 and a_3 are in RCS per kilogram of vegetation moisture, and a_4 is in Nepers per root kilogram of vegetation moisture per root meter of canopy height.

With the form of the scattering equation known, and a set of parameters either known (θ, λ, p, q) or measured $(\sigma^0_{pq}, h, m_w, m_g, m_v)$, the task of obtaining a semi-empirical forward scattering model becomes that of finding the unknown parameters $(a_{bias}, a_2, a_3, a_4, s)$ keeping in mind the fixed relationships between some of these parameters. The measured parameters, radar backscatter and soil moisture, are combined with interpolated values for the vegetation parameters (water mass, height and leaf gravimetric moisture) and inserted into a program which searches for the least squares error between the predicted backscatter and the measured backscatter, by varying the free parameters over their valid range in discrete steps. When a close fit is found, a Levenberg-Marquardt algorithm [78] is implemented which finds a local minimum of the error with respect to all the free parameters at once. The set of free parameters which provides the global minimum to the error is chosen as the set of free parameters most likely to represent the scattering mechanisms observed. This process is done independently for each frequency and polarization pair.

To determine the rms surface height of the soil, our radar measurements were divided into two sets. The first set consists of two days of polarimetric measurements made early in the season, before substantial biomass accumulated on the plants. The semi-empirical soil surface scattering model of Oh *et al.* [75] was used on the C-band measurements of this set to invert the soil roughness, and a value of $s = 2.8$ cm was obtained. The L-band measurements lead to a similar roughness value. This is a mid-range value for the data used by Oh *et al.*, and is consistent with our photographic record. The remaining measurements, excluding those made after harvest, constitute the second set, and were used for finding the forward and inverse models described below.

For C-band, the normalized roughness value of $ks = 3.2$ indicates that the reflection from the ground at this frequency would be insignificantly small. Nonetheless, the Levenberg-Marquardt algorithm attempts to find a best fit of the model to the data and reports that the bistatic scattering in the canopy is on the order of 50 dB in excess of the backscattering in the canopy. This numerical compensation for the large ks value is physically inappropriate, and so for C-band we have forced σ_{pq2} to be equal to σ_{pq1} (that is, $a_3 = a_2$). At L-band, however, the normalized roughness is much more modest at $ks = 0.74$, and all the parameters have been allowed to vary independently for the minimization algorithm.

Freq	Pol	a_2	a_3	a_4	bias	rms error	max error	P
		m^2/kg	m^2/kg	$Np/(kg/m)^{1/2}$	dB	dB	dB	%
C	HH	0.151	$= a_2$	0.341	2.50	0.71	1.79	23
C	VV	0.170	$= a_2$	0.484	3.47	0.73	1.82	16
C	HV	0.051	$= a_2$	0.948	5.16	0.55	1.26	84
L	HH	0.0	0.132	0.126	3.39	0.81	1.38	1.5
L	VV	0.0025	0.0605	0.0	4.78	0.62	1.81	49
L	HV	0.0	0.0351	0.125	5.06	0.70	1.95	15

Table 3.1: Best fit free parameters for semi-empirical soybean model.

We have included in equation (3.18) a bias factor, a_{bias}, because, without it, the data could not be accurately described by the model. The usual suspects, namely calibration and measurement errors, have been investigated, but we have not located any source of error. It is possible that the semi-empirical soil surface scattering model of Oh *et al.*, developed for bare soils, may not be directly applicable to a surface under a growing crop. Also, rain may significantly alter the soil roughness over the course of the growing season. For any of these reasons, the bias value may not be appropriate for other data sets. Nonetheless, the existence of an arbitrary but constant bias does not alter the objectives or the conclusions of this chapter.

The free parameters that were found to provide the best fit for the set of soybean measurements are shown in Table 3.1. The rms error and maximum error are given in dB. The goodness-of-fit measure P represents the statistical level required to reject the model, or, in other words, the probability that a repetition of the measurements would result in a worse fit to the model, assuming that this model and the values of these parameters are correct. The measure P takes into account the known or assumed errors in the measurements, while the rms error or maximum error measures do not. Values of P greater than approximately 5% indicate that a more complicated model is unlikely to provide a better fit to the data. The low value of P for L-band HH indicates that the model is not a very good representation of the observations. The reason the fit for L-band VV-polarization is better than HH may be due to the fact the numerical fitting algorithm has a better chance of finding a good fit for some values of the free parameters for VV. This is because Γ_v, the V-polarized ground reflectivity, has a larger dynamic range due to the variation in soil moisture, m_v, than does Γ_h.

While the free parameters for each polarization and frequency are derived independently of each other, certain known relationships exist between them. The extinction parameter, a_4, while not independent of polarization, should be only weakly sensitive to polarization, but should be much higher for C-band than for L-band. The canopy scattering terms, a_2 and a_3, should also be much higher for C-band than L-band. Within a given frequency and polarization, it is expected that the bistatic scattering from the canopy would be stronger than backscattering, and so $a_3 > a_2$. While we have essentially turned off the bistatic term at C-band because of the rough ground, at L-band the bistatic term so dominates the backscatter that the best fit parameters for backscatter are zero for two polarizations. Otherwise, all of these expectations are realized in the values of the free parameters derived.

An analysis of the contributions from the mechanisms described in Figure 3.2 for the mature soybean canopy show that the ground-canopy-ground scattering interaction described by σ^0_{pq3} in equation (3.4) is negligible for all polarizations and both frequencies investigated. From the parameters for C-band VV and HH backscatter in Table 3.1, the direct ground backscatter, as attenuated by the canopy, is comparable to the crown backscatter, the only other significant contribution. This somewhat surprising result that the direct ground may contribute so much may be a consequence of the fact that on the particular fields measured the row spacing was 30 inches, which, coupled with the dry summer, resulted in a canopy with significant discontinuities. For C-band HV polarization, the direct backscatter from the crown dominates.

The predicted dominant scattering mechanism is polarization dependent at L-band. For VV polarization, zero attenuation provided the best fit to the observations, and as a result the direct backscatter from the ground dominates the terms from the canopy. For HH polarization, the direct ground and crown–ground terms are comparable, while for HV the crown–ground interaction term is most important. For both HH and HV at L-band, the algorithm estimated no direct crown backscatter contribution, but considering the relative strengths of the direct crown and crown–ground terms for VV polarization, it is not too surprising that the algorithm could not accurately quantify the weaker mechanism from the data. Similarly, the weak extinction at L-band results in a best fit prediction of no extinction for VV polarization.

Ulaby and Wilson [98] report direct measurements of attenuation through a soybean crop at L-band and C-band. In addition to measurements of a full soybean canopy at an incidence angle of 52° and perpendicular to the rows, they also defoliated the plants and repeated the measurement, to determine the relative contributions to extinction due to leaves and stems. Table 3.2 shows their measurements for the one way full canopy losses, with the results of applying equation (3.21) to the ground truth reported in their paper for comparison. The H-polarized predic-

Freq	Pol	measured	predicted
C	H	3.1 ± 0.5 dB	2.3 dB
L	H	0.7 ± 0.4 dB	0.85 dB
C	V	9.9 ± 1.6 dB	3.3 dB
L	V	2.6 ± 0.5 dB	0 dB

Table 3.2: Comparison of measurements by Ulaby and Wilson [98] and for one-way extinction through a full soybean canopy.

tions compare very favorably with their measurements. Their measurements for V-polarization are higher, while our model falls short of these observations. Their defoliation experiments lead to a conclusion that the stems dominate the V-polarized extinction but only contribute about 50% of the H-polarized extinction at L- and C-bands. Our largest measured water mass density in the stems is one fourth of theirs. Thus, while our derived H-polarized extinction appears to extrapolate nicely to a healthy canopy, the same cannot be said for our V-polarized extinction expressions.

Comparisons of the semi-empirical model calculations with the measured data are shown Figures 3.6 and 3.7.

3.4 Inversions

The objective of the exercise is not to simply understand how the backscattering from a crop such as soybeans depends on scientifically and commercially important quantities like soil moisture and biomass, but to use the measurements of backscatter to determine estimates of these important quantities. This section outlines the approaches used to invert the semi-empirical model developed in the previous section.

As a first step, the desired invertible quantities, namely soil moisture and vege-

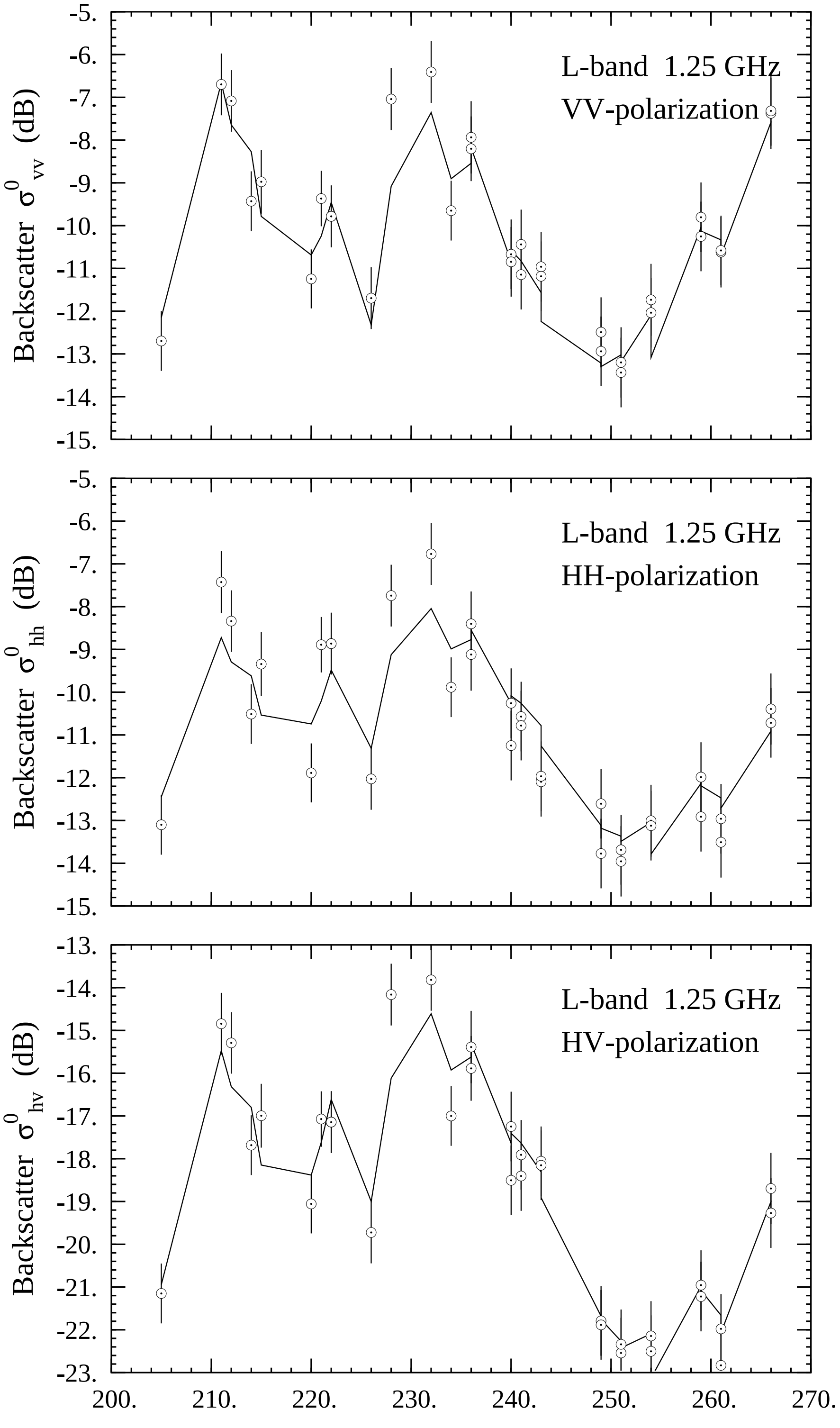

Figure 3.6: Comparison of the semi-empirical model to the measured data at L-band. The angle of incidence is fixed at 45° and the look direction relative to the row direction was also fixed at 45°.

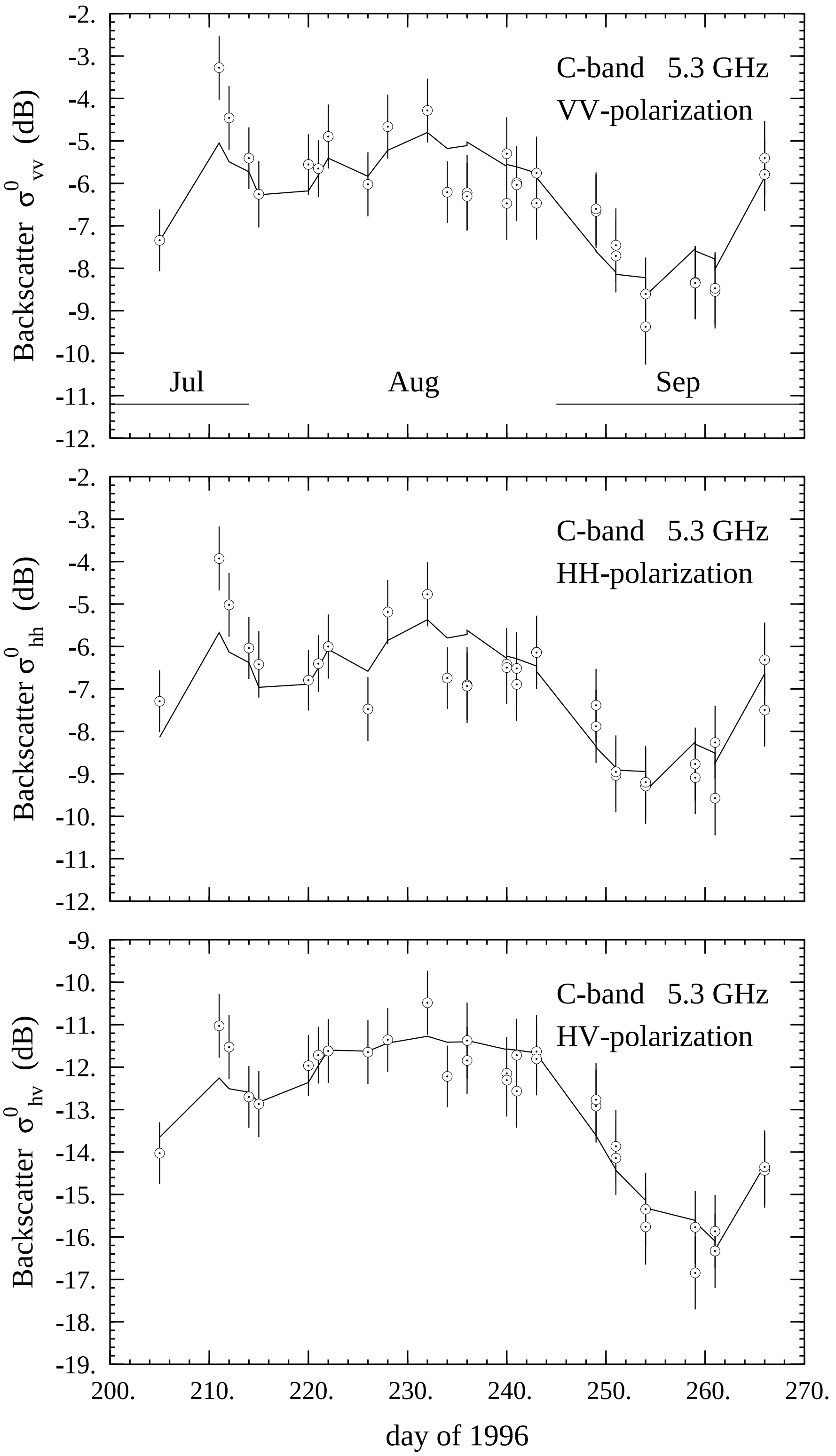

Figure 3.7: Comparison of the semi-empirical model to the measured data at C-band. The angle of incidence is fixed at 45° and the look direction relative to the row direction was also fixed at 45°.

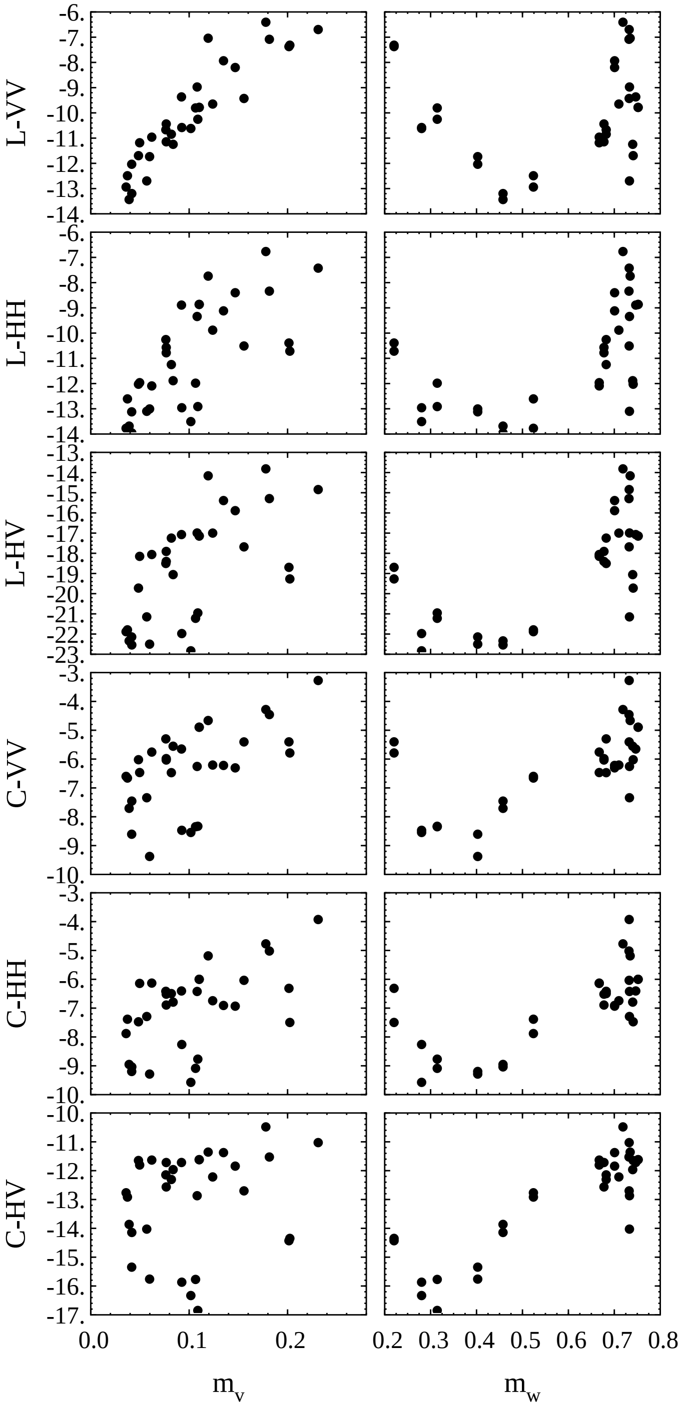

Figure 3.8: Visual results of the regression of the measured soil moisture m_v, left column, the area density of the vegetation water mass m_w, right column, and the six radar channels. Only L-band VV shows a strong direct correlation with m_v.

tation water mass, are regressed against the six radar channels (L-band and C-band, each with VV, HH, and HV), as shown graphically in Figure 3.8. The fifteen combinations of ratios of those radar channels were similarly regressed against m_v and m_w. The vast majority of these regressions show very poor correlation between the radar quantity and the desired parameter, but a few show modest correlations. The single channel with the best correlation with soil moisture is, not surprisingly, L-band VV polarization, since the relatively long wavelength permits substantial penetration of the canopy and the vertically polarized Fresnel reflection coefficient of the surface is sensitive to soil moisture. For all polarizations, L-band has a much higher dynamic range than C-band, and much larger measurement to measurement variation. For the three L-band polarizations, VV is most faithfully described by the forward model.

The channel ratio with the best correlation to soil moisture is the L-band cross-pol to C-band cross-pol ratio. The L-band cross-pol data has a slightly larger dynamic range than does either co-pol, and the C-band cross-pol has the smallest sensitivity of all channels measured to soil moisture. This particular combination provides the large dynamic range of the L-band measurements to soil moisture with a correction for vegetation water mass provided by the C-band channel.

The channel ratio with the best correlation to vegetation water mass is L-band cross-pol to L-band VV-polarization. The best fits to our measured data, together with the root-mean-squared error and the regression coefficients, for each of these physical quantities are given by

$$\frac{\sigma^0_{L-HV}}{\sigma^0_{C-HV}} = 1.9360 m_v^{0.8237} \tag{3.23}$$

with

$$rmse \;=\; 3.25\%$$

$$R^2 = 0.633$$

$$\frac{\sigma^0_{L-HV}}{\sigma^0_{L-VV}} = 0.2510 m_w^{1.0277} \tag{3.24}$$

with

$$\begin{aligned} rmse &= 0.0678 \text{ kg/m}^2 \\ R^2 &= 0.867 \end{aligned} \tag{3.25}$$

In these equations, σ^0 is given in RCS per unit area (m^2/m^2). Figures 3.9 and 3.10 show the resultant inversion of our measured data for the soil moisture and vegetation water mass. Ferrazzoli *et al.* [31] have also found that L-band cross-pol to be an important predictor of vegetation biomass for crops.

While the regression for vegetation water mass in (3.24) is quite good, the use of (3.23) for inversion is less than ideal. The single channel with the highest sensitivity to soil moisture is the L-band VV-polarization, as is evident from Figures 3.6 and 3.7. The following equations show the linear regression of this channel, together with two combinations of channel ratios which improve the correlation significantly.

$$m_v = 0.3489 + 0.0244\sigma^0_{L-VV} \tag{3.26}$$

with

$$\begin{aligned} rmse &= 2.13\% \\ R^2 &= 0.842 \end{aligned} \tag{3.27}$$

$$m_v = 0.2338 + 0.0244\sigma^0_{L-VV} - 0.0142\left(\sigma^0_{C-HV} - \sigma^0_{C-VV}\right) \tag{3.28}$$

with

$$\begin{aligned} rmse &= 1.75\% \\ R^2 &= 0.898 \end{aligned} \tag{3.29}$$

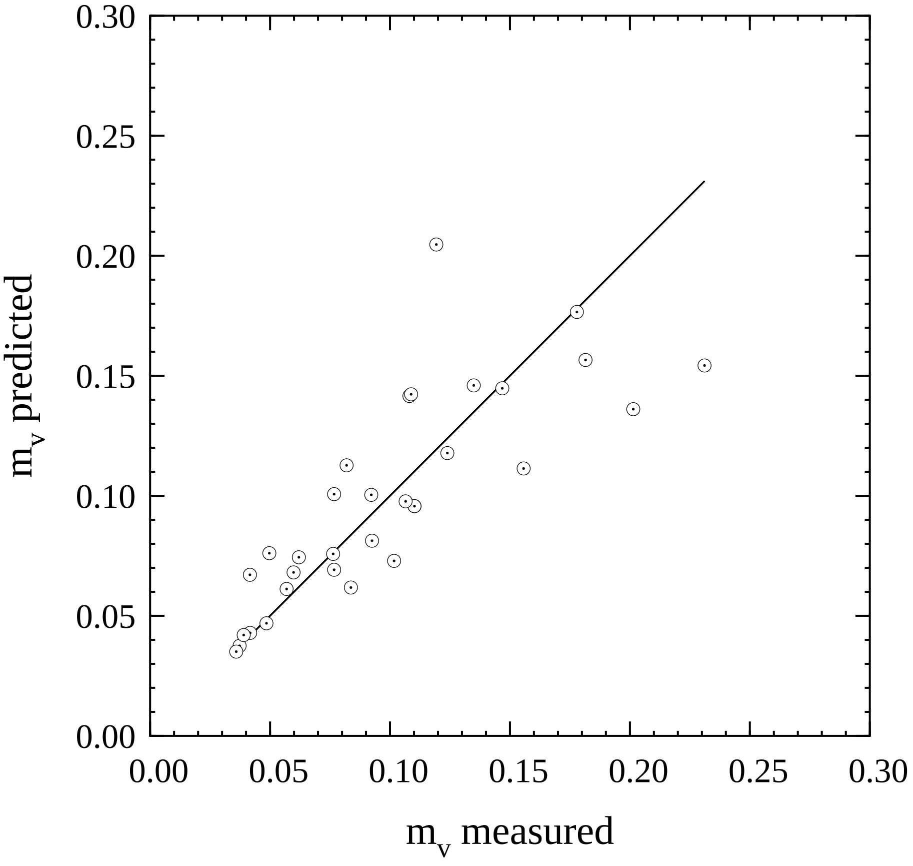

Figure 3.9: Comparison of the measured soil moisture with inverted soil moisture derived from both L-band and C-band cross-polarization radar measurements.

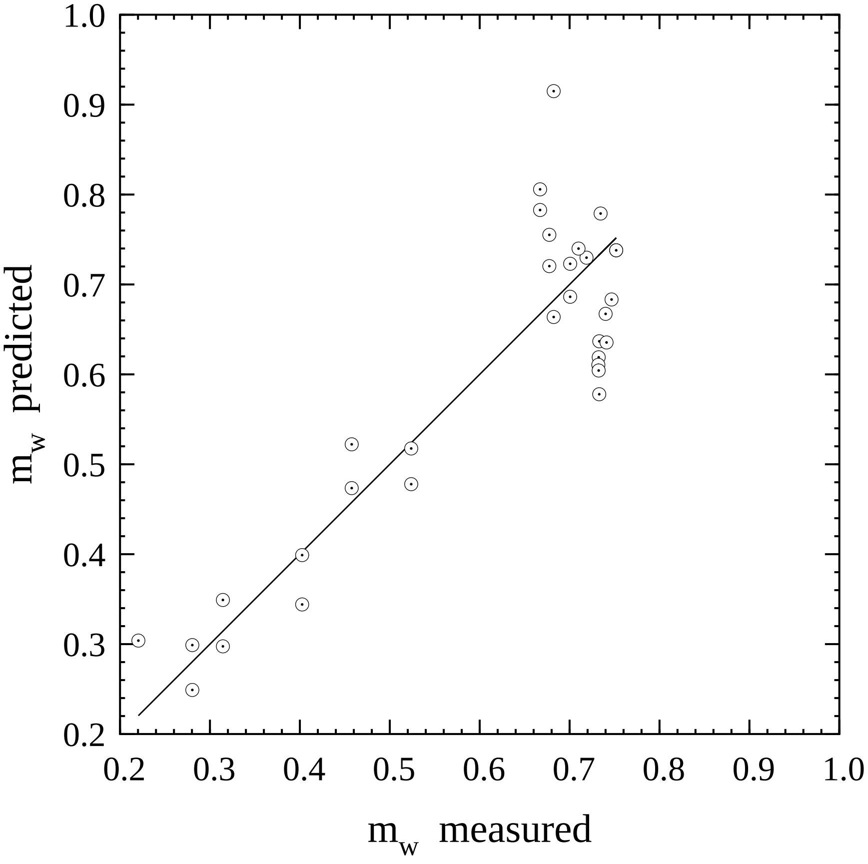

Figure 3.10: Comparison of the measured vegetation water mass with inverted vegetation water mass derived from both L-band VV- and cross-polarization radar measurements.

$$m_v = 0.2483 + 0.0272\sigma^0_{L-VV} - 0.0139\left(\sigma^0_{C-HV} - \sigma^0_{C-VV}\right) - 0.0063\left(\sigma^0_{L-HV} - \sigma^0_{C-HV}\right) \tag{3.30}$$

$$\begin{aligned} rmse &= 1.72\% \\ R^2 &= 0.904 \end{aligned} \tag{3.31}$$

In these equations, σ^0 is given in dB.

Use of L-band VV-polarization alone is an improvement over the exclusive use of the L-band to C-band cross-pol ratio, but it is improved with the inclusion of the C-band cross-to-co-pol ratio, which is essentially a correction for the dependence of L-band VV on the vegetation water mass. Further inclusion of L-band to C-band cross-pol ratio provides negligible improvement in the correlation. Figure 3.11 shows the improved inversion of our measured data for the soil moisture using equation (3.28).

3.5 Conclusions

A series of measurements of the radar backscatter from soybeans is reported. The soybeans fields were located at the Kellogg Biological Station in Hickory Corners, MI, USA. The series of 57 measurements on these fields commenced on 20 June 1996 and were completed on 26 October 1996. Each measurement was fully polarimetric at both L-band and C-band, made at an incidence angle of 45° and also at 45° with respect to the crop row structure, and contains a minimum of 157 independent samples. With each measurement is a set of soil core samples used to determine the volumetric soil moisture; several destructive samples over the growing season were used to obtain measures of the above-ground biomass, including the area density of vegetation water mass. Measurements from the center of this period, when the

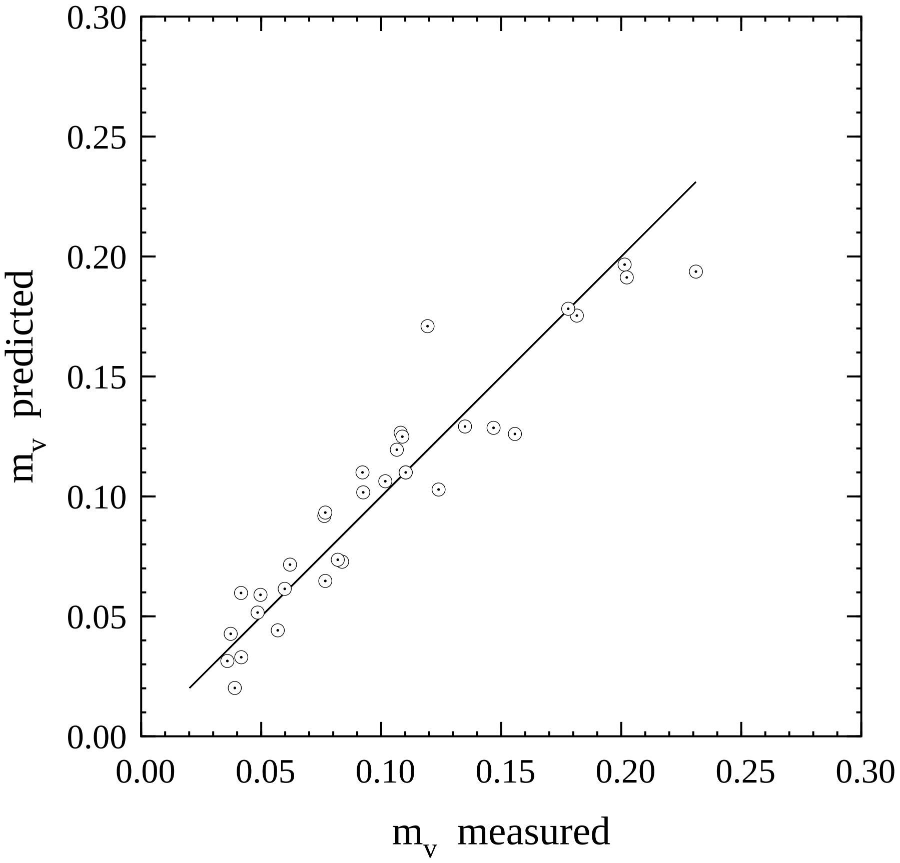

Figure 3.11: Comparison of the measured soil moisture with inverted soil moisture derived from radar measurements using equation (3.28).

soybean biomass was not negligible, were used to create a semi-empirical forward scattering model. This forward scattering model is based on the first-order radiative transfer solution, akin to MIMICS, used for the prediction of forest backscatter. Four parameters are determined from the data: two for scattering from the leaves and one for extinction through the canopy, and one for the rough ground. Another parameter for describing the rough ground backscatter, the effective rms surface height, was independently determined from radar measurements early in the growing season; these measurements are not included in the dataset used to fit the radiative transfer model. A slightly modified semi-empirical model proposed by Oh *et al.* [75] is used for direct backscatter from the ground in the forward scattering model. The four parameters are determined independently for each frequency and polarization; very good fits to the model are achieved for all polarizations at C-band and for VV-polarization at L-band.

Subsets of the measured data in frequency and polarization are used to obtain inversion models. For a measure of the biomass, a combination of L-band VV-polarization and HV-polarization was found to have the highest correlation to the area density of vegetation water mass, with a regression coefficient $R^2 = 0.867$ and a root-mean-square error of 0.0678 kg/m^2. Numerous polarizations and frequencies, singly or in combination, can be used to invert for soil moisture. The use of cross-polarized backscattering at both L-band and C-band for soil moisture inversion, first reported here, provides an adequate measure for the soil moisture. L-band VV-polarized backscatter, however, is the single channel with the largest dynamic range due to soil moisture changes and simultaneously well-described by the forward scattering model. Its use, in conjunction with the C-band cross- to co-polarized ratio as a correction for biomass effects, yields a regression against volumetric soil moisture with root-mean-square error of 1.75% and a regression coefficient of $R^2 = 0.898$.

CHAPTER IV

MMW Measurements and Modeling of Snow Backscatter at Near Grazing Incidence

4.1 Introduction

The study of MMW backscattering of snow at near grazing incidence is very important for both military applications, such as target detection, and for civilian applications such as vehicle road condition warning systems [61]. Of particular interest are the angular and diurnal behaviors [60] [102] [11].

Radar backscatter of snow has been extensively measured at millimeter wavelengths at incidence angles less than 70- degrees at both 35 and 95 GHz. The majority of these measurements were conducted in the 1980's and early 1990's by the University of Michigan and the University of Massachusetts [102] [107] [65]. Both of these institutions were under contract with the Army Research Office to characterize the polarimetric backscatter response of snow at millimeter wavelengths and several reports and papers were published in their efforts. In addition to the two major programs just mentioned, Professor Martti Hallikainen of the Helsinki University of Technology has also made significant research into the character of snow at millimeter wavelengths, but from the point of view of passive remote sensing (radiometry) rather than active (radar) [40] [59].

To extend our understanding of snow backscatter to the near grazing incidence angular range, the millimeter-wave diurnal and angular backscattering response of snow was obtained at near grazing incidence during the winter measurement campaigns of 1999 and 2000. Carefully planned measurements were undertaken, resulting in over 300 data points for 1999 and over 500 for 2000, including measurements at both 35 and 95 GHz [22]. In addition, extensive ground truth data, including temperature, water content in the snow pack, snow thickness and snow surface roughness were collected. Numerous photographs of snow slices were also taken to assist the characterization of snow particles in terms of shape and size.

Due to the limited space in this thesis, we will discuss few data sets that represent the typical MMW backscatter response of snow at near grazing incidence with respect to the angular dependence and diurnal pattern. The backscatter response of each case will provide us full appreciation of its unique salient features, and bring to attention the subtle issues to be addressed in modeling.

Furthermore, although both are dense medium at MMW wavelength, dry snow and wet snow are to a substantial degree different topologically, hydrologically and electrically from each other, hence call for distinct treatments. In this regard, the rest of this chapter is devoted to the modeling of the angular backscatter pattern, leaving the study of the diurnal pattern to the next chapter.

The interactions among snow particles represent a challenging ongoing research topic [90] [37] [112]. Techniques for studying snow behavior in the literature can be categorized into three types: 1) the conventional radiative transfer method (CRT) [93] [58]; 2) the dense medium radiative transfer theory (DMRT) [90] [91]; 3) a mixture of the above [60]. CRT assumes independent scattering, an assumption that has been challenged both theoretically and experimentally [112] for dense media. On the other side, in the derivation of DMRT, the independent scattering assumption is completely discarded, and a rigorous procedure is adopted such that the first moment of the field is treated using QCA-CP (quasi-crystalline approximation with coherent potential) while the second moment of the field is treated with the ladder approximation of correlated scatterers [90]. Energy is exactly conserved. Yet this technique is highly restricted in application due to its very assumptions: the scatterer must be non-absorptive, small and spherical. Nonabsorptiveness is needed to establish Eq.6 in [90], the foundation of the whole derivation, while smallness and sphericity are needed to arrive at Eqs. 10-12 in the same paper. Recognizing the restrictions, in [92], the authors compromise energy conservation and multiple scattering of the incoherent wave by using QCA as opposed to QCA-CP, and using the Born approximation as opposed to the ladder approximation in [90], respectively. Based on the same consideration, we will use QCA in our model.

The third method, reported by Kuga *et al.* [60], is a mixed one. It uses either QCA or QCA-CP to calculate κ_e, while uses Rayleigh scatterers to calculate the phase matrix $\mathbf{P}$, a procedure that implies the independent-scatterers assumption [60]. Doing so calls for some mechanism to reconcile the disparate assumptions embedded in the treatment of κ_e and $\mathbf{P}$, which are ignored in [60]. As we shall see, failing to reconcile these assumptions may lead to severe performance degradation. In this study, we will use the third method (mixture between CRT and DMRT) while reconciling the disparate assumptions in the treatment of κ_e and $\mathbf{P}$ using a novel technique as described in detail in section 4.3.

Moreover, in the third method, there is a subtle issue that is associated with the interpretation of κ_e as obtained from QCA or QCA-CP. If the scatterer is non-absorptive, then there is no ambiguity: $\boldsymbol{\kappa}_e = \boldsymbol{\kappa}_s$, in other words, the extinction is solely caused by scattering. Yet in the case where the scatterer is absorptive, $\boldsymbol{\kappa}_e$ as obtained from QCA or QCA-CP bears two contradictory interpretations: a) one regards it as only representing the scattering part, so it is actually $\boldsymbol{\kappa}_s$, and we need to add $\boldsymbol{\kappa}_a$ to it to obtain the total extinction coefficient [60]; and b) the other regards it as representing the total extinction rate [112], hence to obtain the scattering coefficient $\boldsymbol{\kappa}_s$, we need to subtract from it $\boldsymbol{\kappa}_a$. Taking a close look at the mathematical foundations of QCA or QCA-CP, we find that the latter is the correct interpretation and will be used in our method.

Characterization of the shapes of snow particles plays an important role in any modeling effort. For reasons listed in the next chapter, it is both natural and pertinent to approximate the ice particles as spheroids with some orientational distribution. This treatment is conceptually simple yet it is computationally demanding, especially if QCA is used to calculate the volume extinction coefficient.

To attain the advantages of assuming spheroidal particles while simultaneously dealing with the computational demand, a new intuitive strategy is proposed in this study that dichotomizes the treatments of the shapes of snow particles such that the snow particles are treated as spheres with certain effective size in calculating $\boldsymbol{\kappa}_e$ and as spheroids in calculating $\mathbf{P}$. The former is because the snow particles, though nonspherical in nature, tend to follow a uniform distribution in orientation [19], which leads to an extinction coefficient independent of polarization, an inherent property of spherical scatterers [93]. The latter is because the scattering pattern depends on size and orientation and is important for cross polarization calculations [32].

The roughness present at the air-snow interface surface will attenuate both the specific intensity transmissivity and reflectivity at this interface, will provide direct surface backscatter, and will cause shadowing effect. For the direct surface backscatter, we will use the Kirchhoff stationary-phase approximation to model it as in [108]; for the shadowing correction, we will use the technique as described in [69].

The rest of this chapter is organized as follows. In section 4.2, MMW measurement of snow backscatter at near grazing incidence will be introduced. Some typical MMW backscatter response with respect to the angular dependence and diurnal pattern will be presented. Section 4.3 describes modeling of MMW snow angular backscatter at near grazing incidence. Section 4.4 provides comparison between model and measurements of dry snow.

4.2 MMW Measurements of Snow Backscatter at Near Grazing Incidence

The radar backscatter response of snow, in general, is a function of two different sets of parameters: the radar system parameters and the physical and electrical parameters of snow. The radar system parameters include center frequency, incidence angle, and transmitter and receiver polarization combinations. The snow parameters include snow density as a function of depth, particle size distribution and shape, surface roughnesses at upper and lower interfaces, moisture, thermodynamic condition within the snow layer and salinity. As mentioned earlier, little data, if any, was available prior to 1999 of MMW radar backscatter response of snow at near-grazing incidence with proper ground truth data. During the winters of 1999 and 2000, a set of carefully planned measurements were undertaken using 35 and 95 GHz polarimetric radars, resulting in over 300 data points for 1999 (total) and over 500 for 2000 (total). In addition, extensive ground truth data, including temperature, water content of snow pack, layer thickness, density, and snow/air interface roughness were collected. Numerous photographs of snow slices were also taken to assist in the characterization of the size and shape of snow particles. The data is now part of a web-accessible, large database of MMW clutter radar return at University of Michigan. In this section, we will describe the radar system used, the methods implemented in ground truth collection, and the measured data in terms of angular dependence, dynamic range, frequency dependence, etc.

4.2.1 Measurement Procedure

The backscatter measurements of snow in both winter seasons were made using the Digitizing Oscilloscope-based MMW radar systems developed by the University of Michigan [70]. The system is designed to transmit two consecutive pulses chirped over 500 MHz, one v-polarized and the other h-polarized, and detect simultaneously the **v** and **h** received components of the backscattered signal in response to each transmitted polarization. In fact it can acquire the full scattering matrix of a target (over 500 MHz bandwidth) within 2 μ seconds. Once calibrated, the new system can measure the radar return to an accuracy on the order of 1 dB in magnitude and 10° in phase. The cross polarization isolation of the system after calibration is on the order of 25 dB and 30 dB for the 35 and 95 GHz frontends, respectively [70]. Table 4.1 summarizes the system specifications of the 35 and 95 GHz systems.

Both the 35 and 95 GHz radars were colocated inside a specifically constructed shed and mounted on a portable gimbal as shown in Figure 4.1(a). The measurement site was at the Willow Run facility of the University of Michigan. The radars were oriented such that they could observe the same spot simultaneously. In Figure 4.1(b), the area to the left of the visible trace was snow-covered grass while the area to the right was a snow-covered asphalt pavement. Over the course of the winters of 1999 and 2000, several interesting dynamic and static conditions were observed. These

Table 4.1: Digitizing Oscilloscope Based System

RF Frontend	35 GHz	95 GHz
Maximum Bandwidth	0.5 GHz	0.5 GHz
Transmitter Beamwidth	4.2°	2.8°
sidelobe level	-20 dB	< -25dB
Polarization isolation	$>$ 25dB	$>$ 25dB
Polarizations trans.	v,h	v,h
Receiver Beamwidth	2.1°	1.4°
sidelobe level	-20 dB	< -25dB
Polarization isolation	$>$ 25dB	$>$ 25dB

included an actual snowfall event, static cold conditions, and melt-freeze cycles. During melt-freeze cycles, the snow conditions changed considerably. Typical snow particle shape and dimension are depicted in Figure 4.2(a). The particles are more discernible in Figure 4.2(b) where an image edge detection technique was applied. During these measurement periods, the following parameters were measured: the polarimetric radar backscatter at both 35 and 95 GHz, air temperature at breast height and near the surface of the snow (both in the shade), snow depth at several locations inside the enclosure, snow wetness and density using a microwave snow probe (Figure 4.3(a)), at different depths in the snow-pack, and the snow surface roughness using a laser profiler (Figure 4.3(b)). During static conditions, the backscatter was measured as a function of incidence angle 82° to 88° in 1° increments. When conditions were very dynamic, measurements were restricted to 84° and 86° incidence angles so that the variations could be monitored closely as a function of time.

The number of independent samples, a key parameter in determining the quality of the measured data, is the product of the number of independent spatial samples and the number of independent frequency samples for each spatial spot. The former is a variable, ranging from 10 to 20 in general, depending on the specific operation, while the later is 16, which is a function of the effective beamwidth and bandwidth of the radar, the incidence angle, and the specified range from radar to the target. In short, the total number of independent samples is somewhere between 160 and 240.

The measured data enable us to study the behavior of MMW backscatter from snow at near grazing incidence from different perspectives. First we will exhibit the collective behavior in terms of dynamic range as function of different physical parameters, then will present the angular dependency and diurnal pattern in the following subsections.

The dynamic range can be examined in different ways, for example, as function of sensor parameters such as incidence angle, or as function of physical parameters of the sensed scene, such as the thickness of the snow layer. We shall proceed in these two main directions.

First, dynamic range is examined as a function of the incidence angle. The dynamic range of the vertically copolarized backscatter from wet snow over asphalt at 35 GHz is plotted in Figure 4.4. It is seen that the signal level can vary substantially, as much as 20 dB for some incidence angles. Moreover, the mean signal level of each incidence angle decreases monotonically as incidence angle increases, conforming to our knowledge. The copolarized signal ratio $\sigma^0_{HH}/\sigma^0_{VV}$ is plotted in Figure 4.5 as a function of incidence angle. From this plot we can conclude that HH is consistently

(a) Shed constructed to host the 35GHz and 95GHz systems

(b) Measurement ground with pedestal for calibration

Figure 4.1: Outdoor Experimental Setup

(a)

(b)

Figure 4.2: Snow particles. (a) Photographic pictures of snow particles taken during measurements; (b) The same photograph after applying edge detection imaging technique.

(a) Probe

(b) Laser Profiler

Figure 4.3: Examples of ground truth collection. (a) Probe system to measure snow moisture and density; (b) Laser profiler system for snow surface roughness measurements.

lower than VV by varying signal levels (from 0 to 6 dB), except for one or two outliers. The cross-polarized to copolarized ratio, defined as $(\sigma_{hv}^0 + \sigma_{vh}^0)/(\sigma_{vv}^0 + \sigma_{hh}^0)$, is shown in Figure 4.6 and demonstrates a range from -13 dB to -6 dB, except for very small number of outliers.

At 95 GHz, similar observations can be applied to the dynamic range of the vertically copolarized backscatter as function of the incidence angle, as shown in Figure 4.7, and to the cross-polarized to copolarized ratio, as shown in Figure 4.9. However, The copolarized signal ratio $\sigma_{HH}^0/\sigma_{VV}^0$ plotted in Figure 4.8 differs appreciably from that of 35 GHz such that a significant portion (around 15 percent) of the data points shows a higher HH signal level than VV.

Next, for different snow layer thickness, the dynamic range of the vertically copolarized backscatter from wet snow at 86° incidence angle at 35 GHz is shown in Figure 4.10. For a particular day, qualitatively, it is seen that the backscatter signal level exhibits a "U" shape as a function of the snow layer depth. This is because that these wet snow measurements were corresponding to diurnal measurements, which led the backscatter signal level to drop when the snow began to melt, yet at that time the snow layer depth did not show any appreciable change, hence the right side of the "U" letter was formed. The left side of the "U" letter was formed similarly at the late stage of snow refreezing. The bottom of the "U"letter corresponded to the diurnal stage in between. On the other hand, quantitatively speaking, the backscatter signal level lies somewhere between -40 dB to -15 dB. Figure 4.11 shows the copolarized signal ratio $\sigma_{HH}^0/\sigma_{VV}^0$. It is obvious from this figure that HH is consistently lower than VV by varying signal levels (from 0 to 4 dB), except for two or three outliers. The cross-polarized to copolarized ratio, defined as $(\sigma_{hv}^0 + \sigma_{vh}^0)/(\sigma_{vv}^0 + \sigma_{hh}^0)$, is shown in Figure 4.12 and demonstrates a range from -13 dB to -6 dB, except for very small number of outliers.

Similar observations can be applied to the dynamic ranges of backscatter at 95 GHz as functions of the snow layer depth, as shown in Figure 4.13, 4.14 and 4.15, respectively.

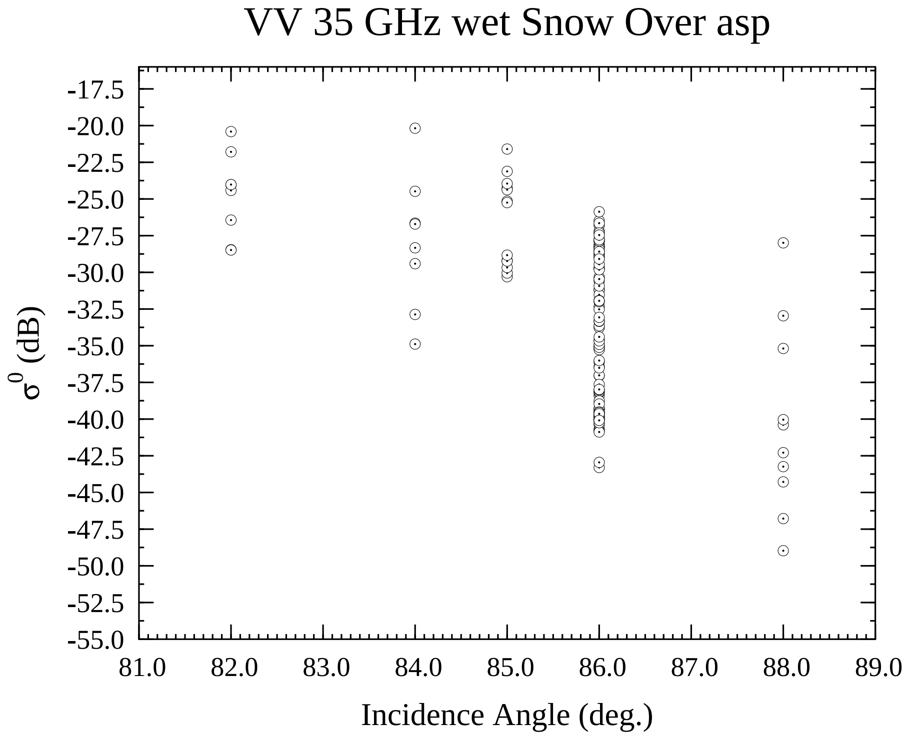

Figure 4.4: VV dynamic range vs. incidence angle at 35 GHz

4.2.2 Diurnal Response

Several diurnal measurements were conducted during the two winter measurement campaigns. One such measurement was made on February 9, 2000 for metamorphic snow. Starting from 8 am on that particular day, the air temperature at breast height rose gradually, from -1.2°C to reach 0°C (Figure 4.16) at $9:10$ am, when the snow pack thickness was 15.9 cm for snow above grass and 10.4 cm for snow above asphalt, respectively. The snow density was at a low value of 0.2 g/cc (Figure 4.17). No discernible snow wetness was detected by the snow probe placed 2 cm down the

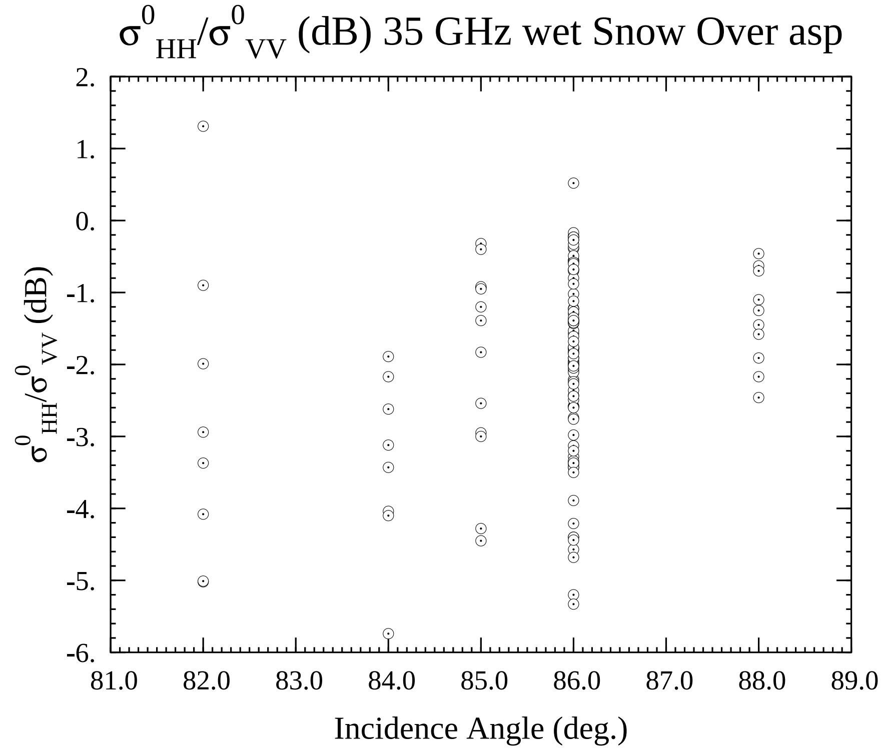

Figure 4.5: HH/VV dynamic range vs. incidence angle at 35 GHz

snow-air surface. From 10 am to 12 pm, while the temperature continued to rise to 4.7°C, the snow pack undertook some melting, as evident by the slow buildup of wetness to a m_v value of around 4.5% and the reduction in snow pack thickness, in particular for snow above grass. The backscattering response of snow above both grass and asphalt at both 35 GHz and 95 GHz showed significant drop, around 15 dB for all cases, accounting for the dynamic range of the whole day, as shown in Figure 4.19(a), Figure 4.19(b),Figure 4.20(a), and Figure 4.20(b), respectively. From then till 4 pm, temperature continued to rise at a slower pace to 6°C, resulting in a significant buildup of snow wetness and substantial drop of snow pack thickness above both grass and asphalt. The backscattering appeared to saturate. After 4 pm , the temperature dropped quickly, the snow pack thickness and snow wetness stabilized, the backscattering gradually recovered, though in different fashions for 35

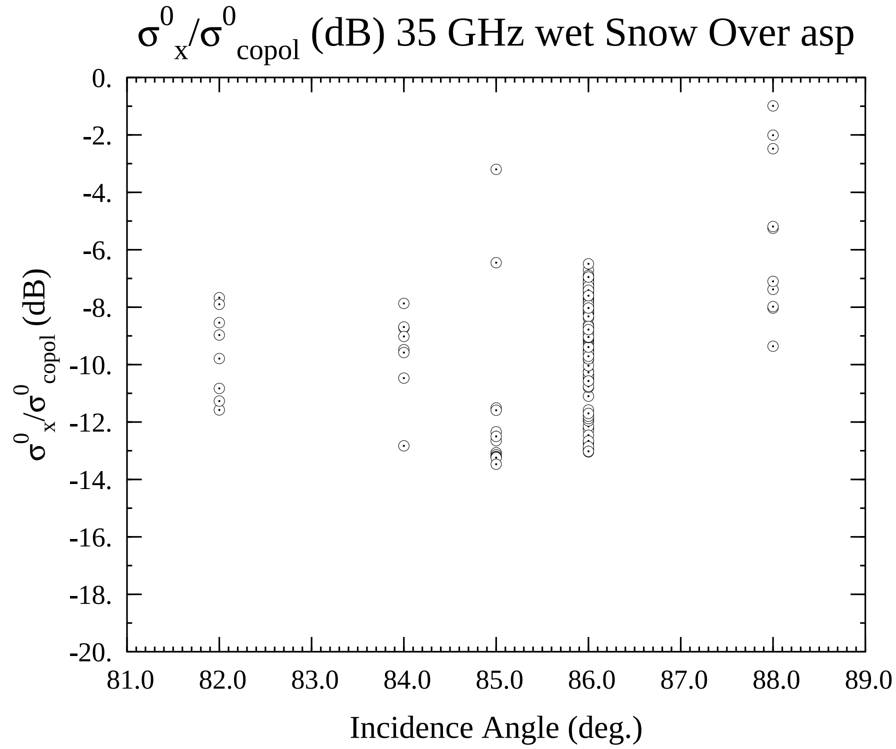

Figure 4.6: Cross-polarized/Copolarized dynamic range vs. incidence angle at 35 GHz

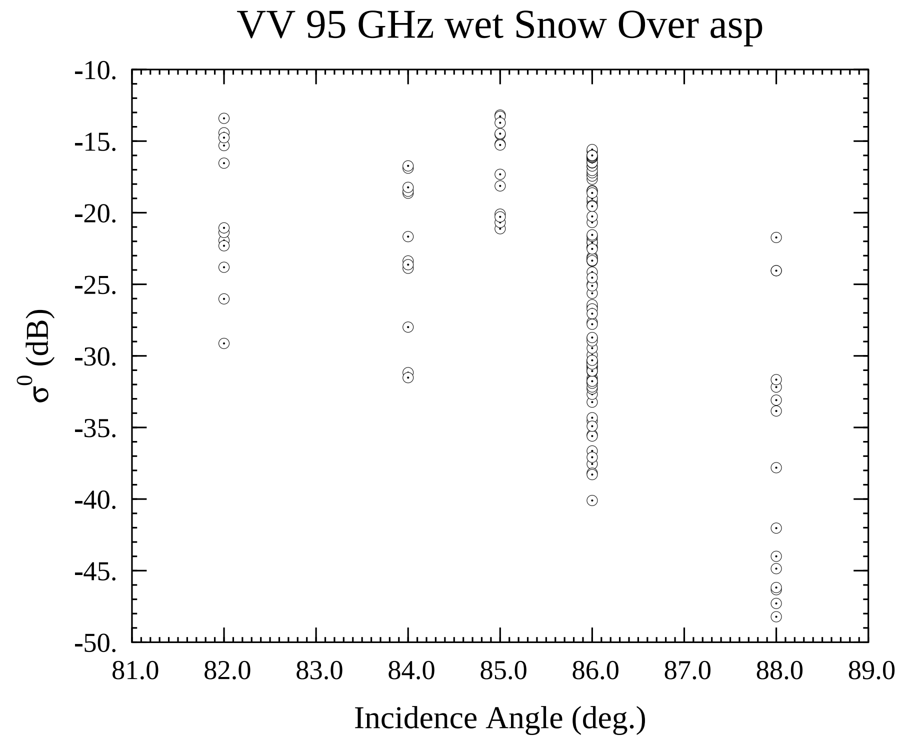

Figure 4.7: VV dynamic range vs. incidence angle at 95 GHz

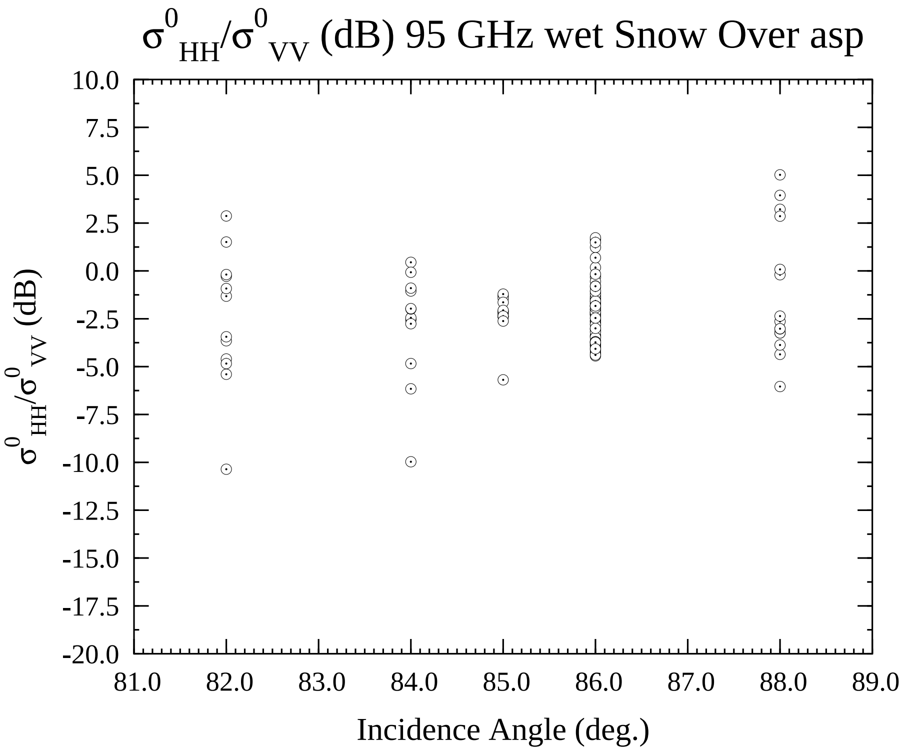

Figure 4.8: HH/VV dynamic range vs. incidence angle at 95 GHz

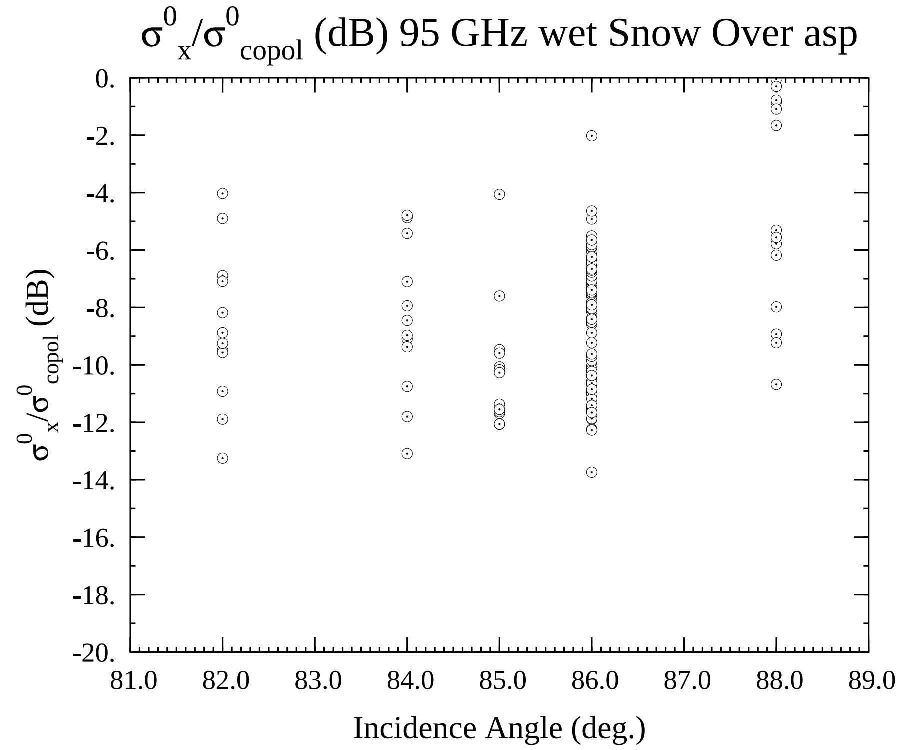

Figure 4.9: Cross-polarized/Copolarized dynamic range vs. incidence angle at 95 GHz

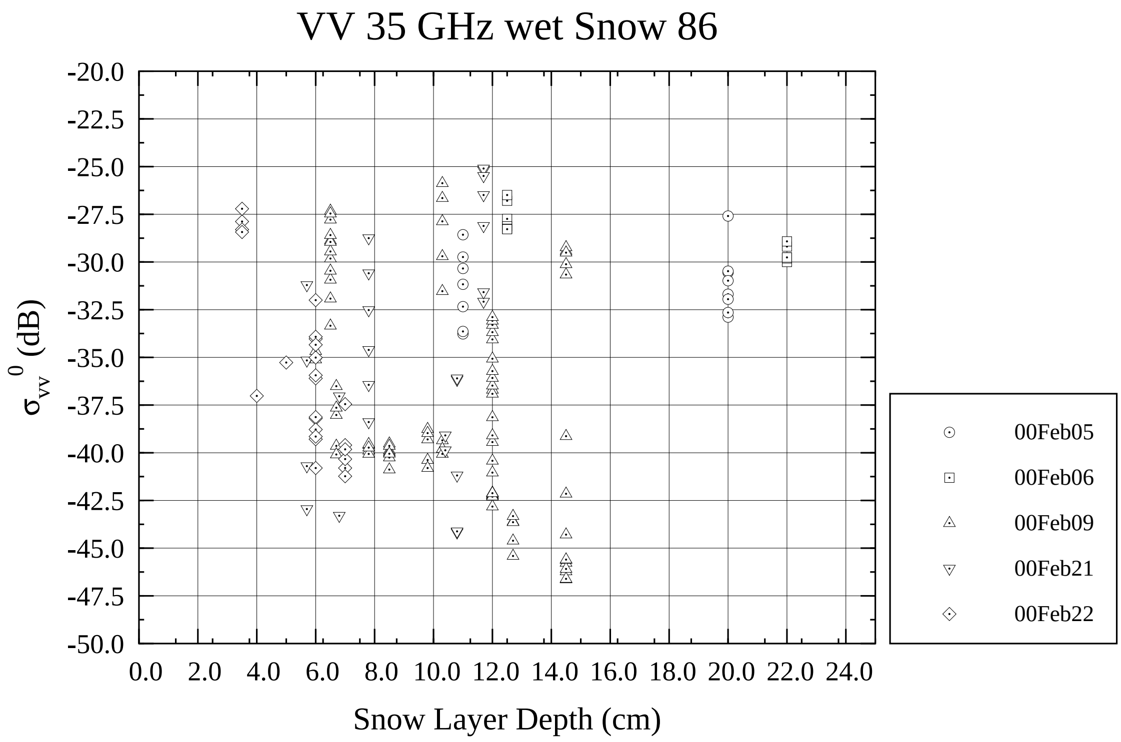

Figure 4.10: VV dynamic range vs. snow layer thickness at 86° incidence at 35 GHz

GHz and 95 GHz, the former showing a trend of continued recovery while the latter tending to saturate, in combination of a wider separation between the copolarized components and narrower copolarized to cross-polarized ratio. A typical surface roughness condition, taken at 12:21 pm as shown in Figure 4.18, reveals a rms height of 2 mm and correlation length of 5.2 cm.

4.2.3 Angular Response

As evident from the diurnal observations, the backscattering response changes markedly as a function of time, in particular from 10 am to 6 pm when the snow pack experiences a melting - freezing cycle when the temperature goes above 0°C at some time.

To obtain reliable angular measurements, it is crucial that the snow conditions remain stable over the duration of the measurement period. Bearing in mind that

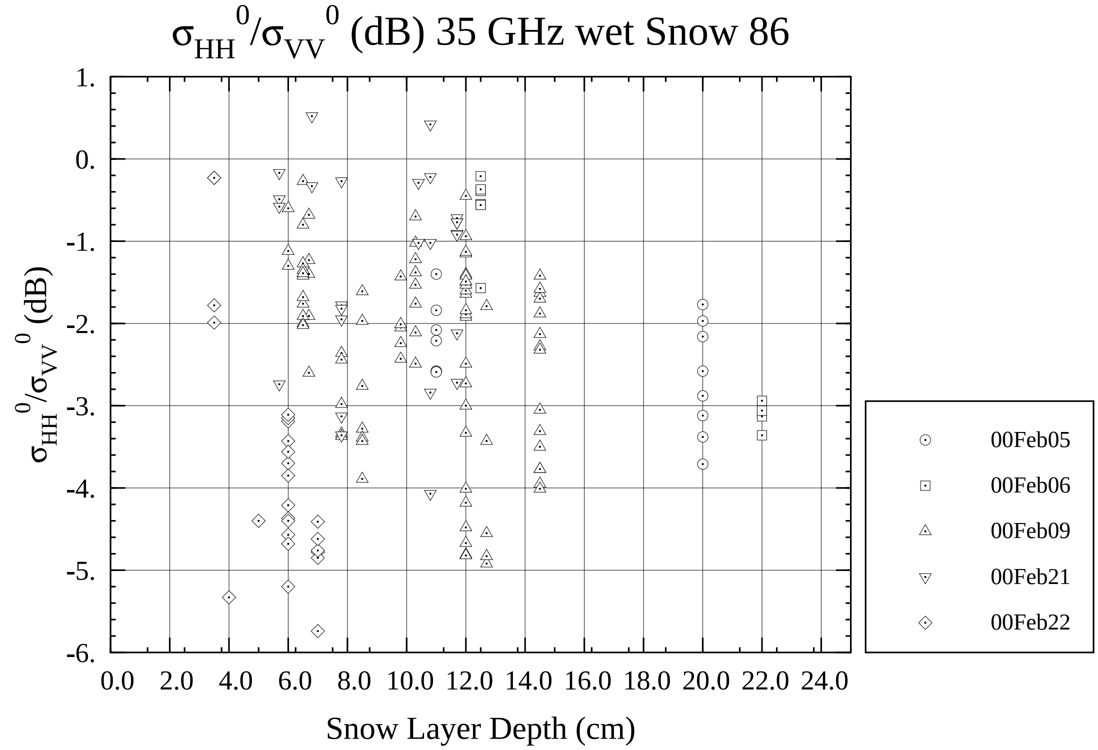

Figure 4.11: HH/VV dynamic range vs. snow layer thickness at 86° incidence at 35 GHz

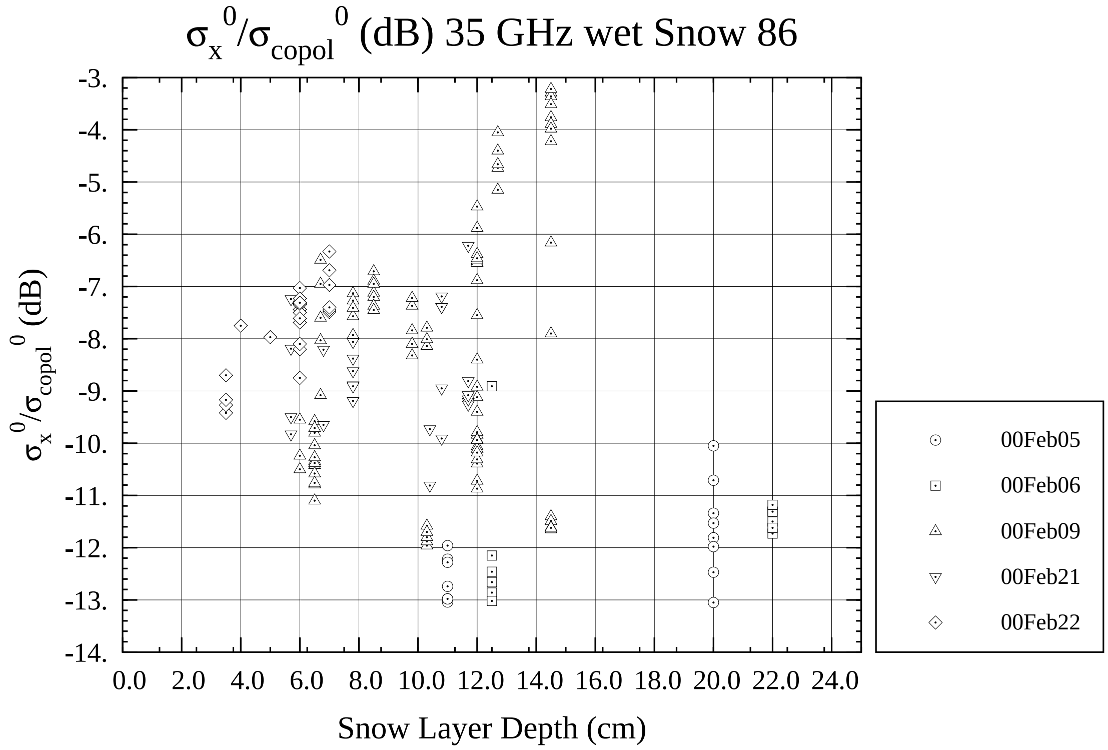

Figure 4.12: Cross-polarized/Copolarized dynamic range vs. snow layer thickness at 86° incidence at 35 GHz

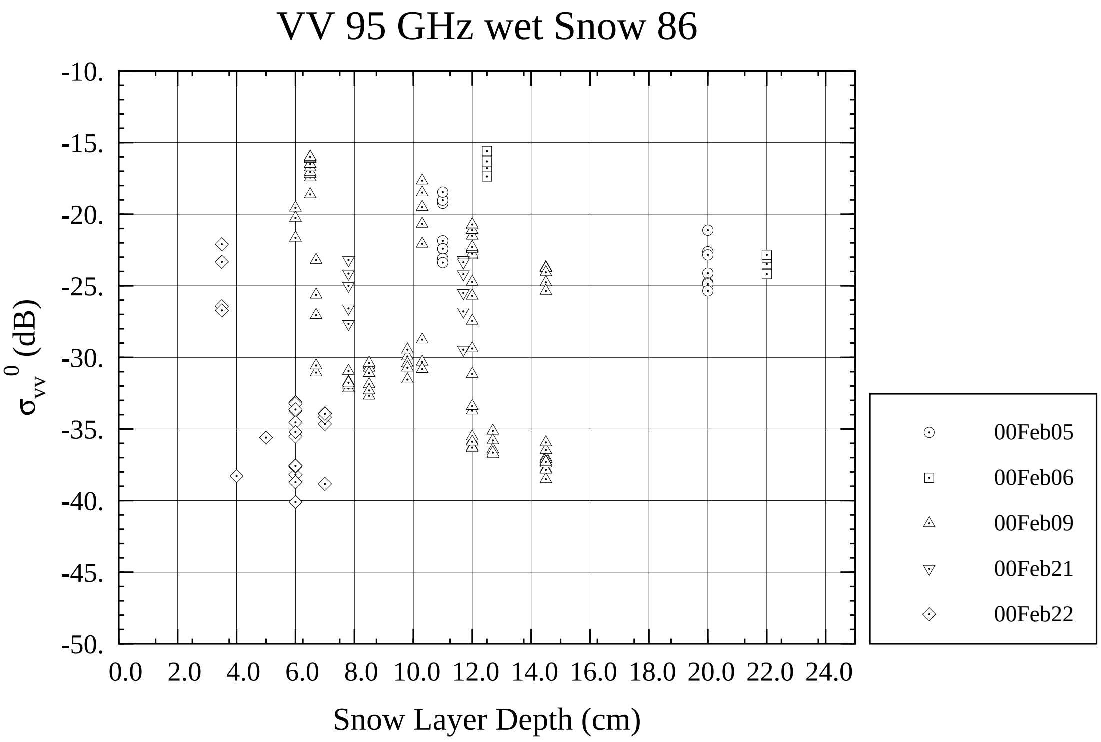

Figure 4.13: VV dynamic range vs. snow layer thickness at 86° incidence at 95 GHz

it takes time to adjust the incidence angle and antenna height above the ground between angular measurements, insuring stable conditions requires operation at below freezing temperatures, under low wind conditions (so as not to disturb snow surface roughness) and with no significant snowfall rate.

The measurements made on January 12, 1999 were conducted under such conditions. The measurements were started at 2:55pm and ended at 4:47 pm. During that period, the air temperature was measured several times and recorded to be around -5.5°C. The wind was mild and no snowfall occurred that afternoon. Based on several snow depth measurements, the depth was 36.5 cm.

The measurements were conducted over the angular range between 82° and 88°, for both 35 and 95 GHz. The results are shown in Figure 4.21(a) and Figure 4.21(b), respectively. All plots show the typical roll off of σ^0 with angle. We can readily

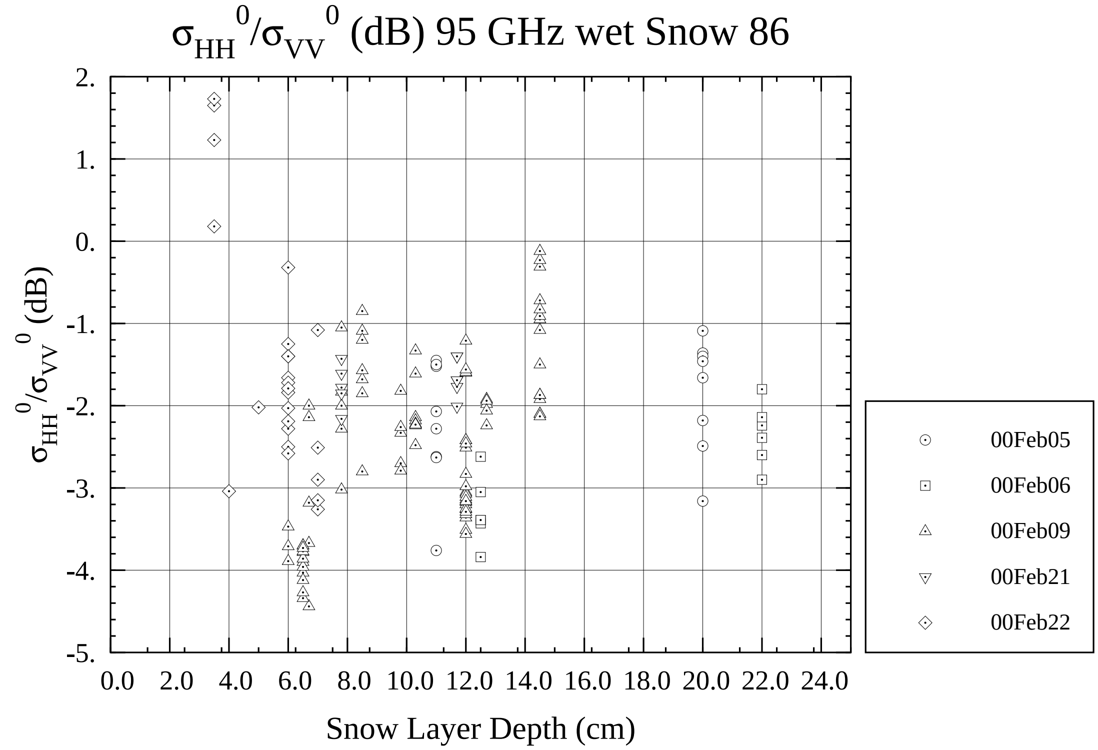

Figure 4.14: HH/VV dynamic range vs. snow layer thickness at 86° incidence at 95 GHz

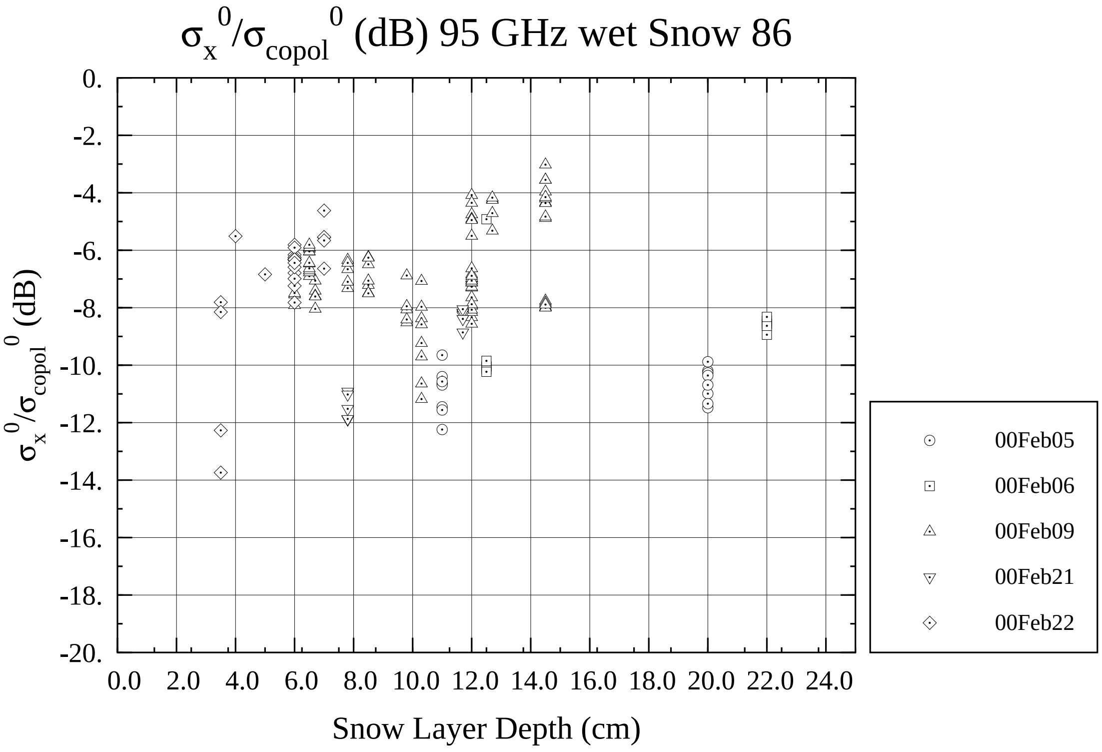

Figure 4.15: Cross-polarized/Copolarized dynamic range vs. snow layer thickness at 86° incidence at 95 GHz

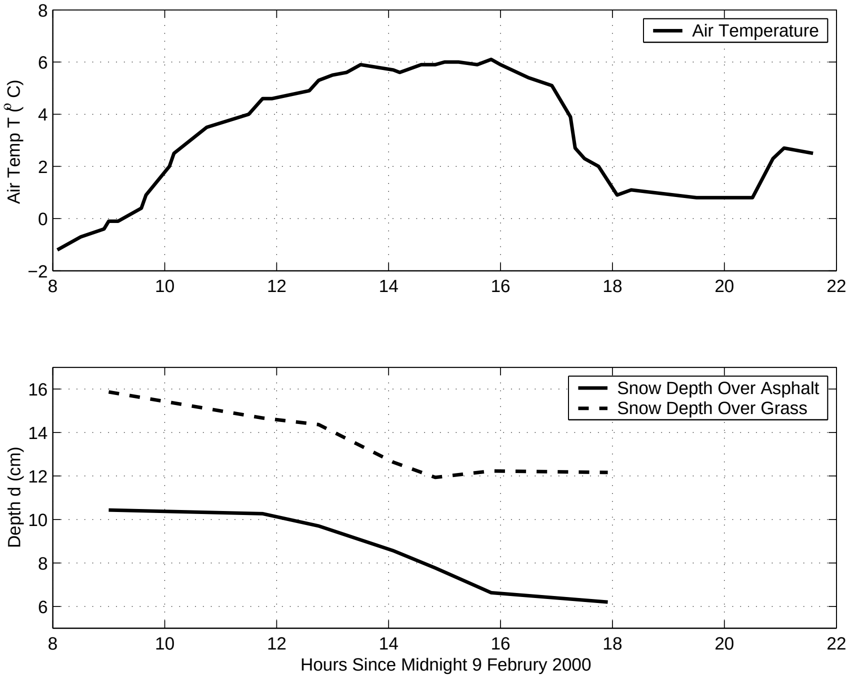

Figure 4.16: Air temperature and snow layer depth

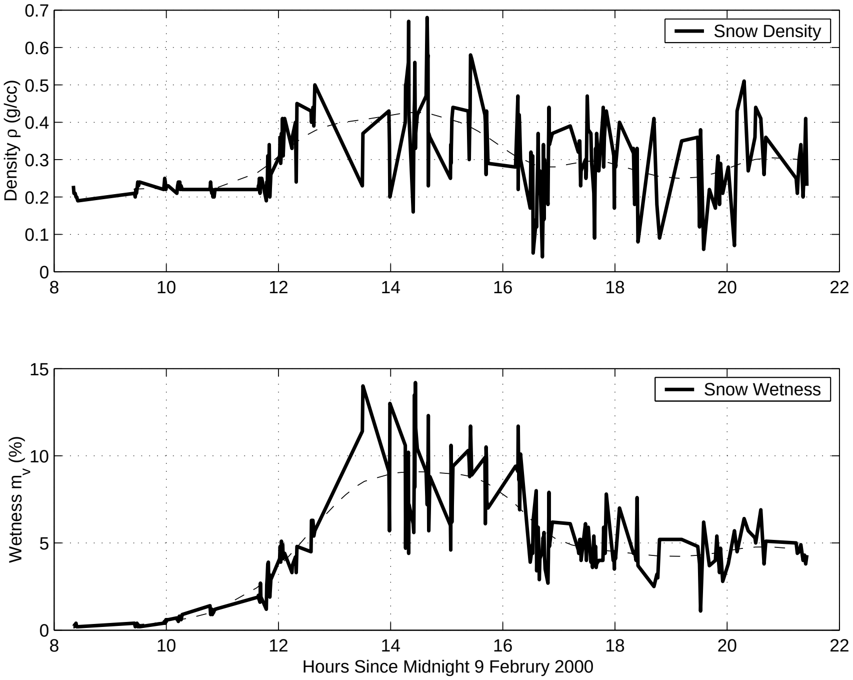

Figure 4.17: Snow density and wetness

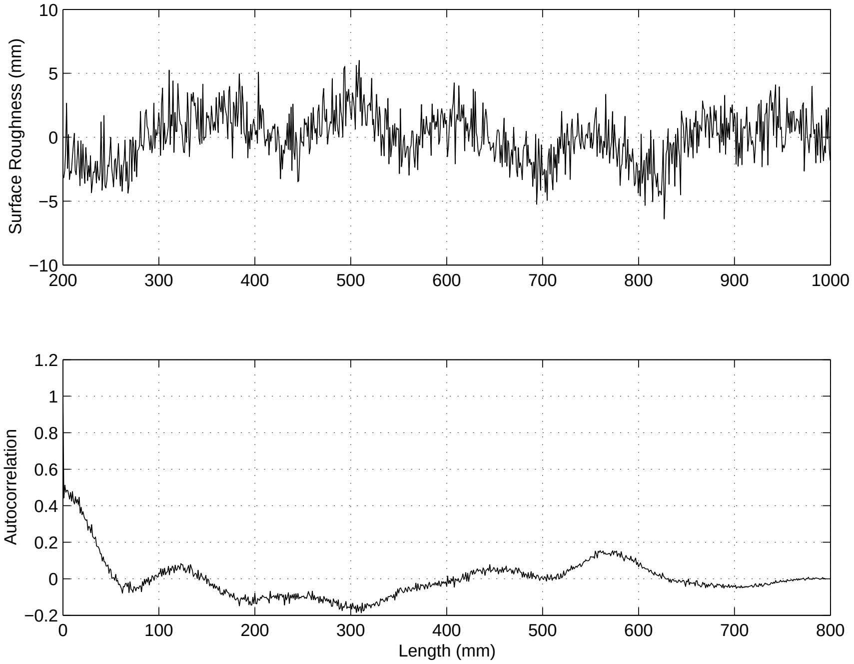

Figure 4.18: Snow surface roughness

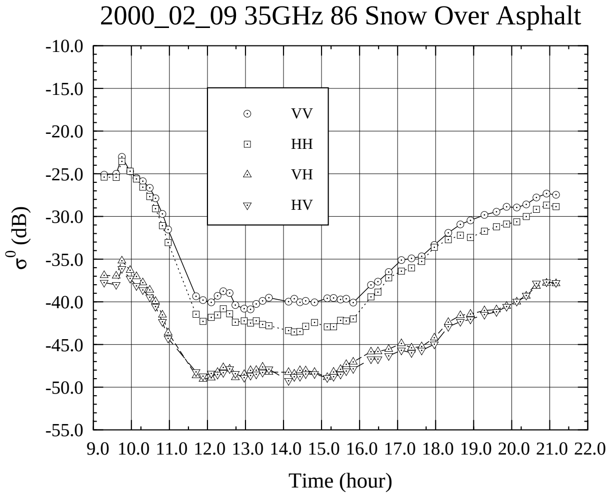

(a) Snow over asphalt 35GHz

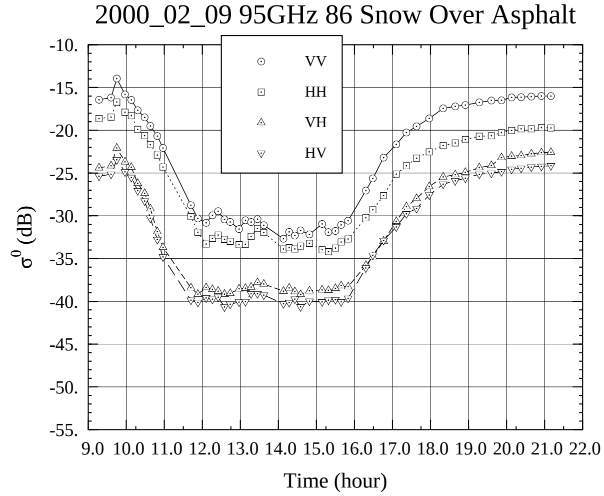

(b) Snow over asphalt 95GHz

Figure 4.19: Radar backscatter response of snow over asphalt measured at 86° incidence during the melt-freeze cycle. (a) 35 GHz. (b) 95 GHz

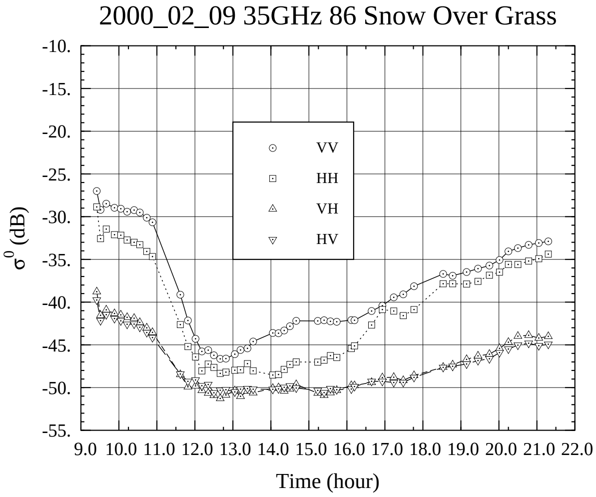

(a) Snow over grass 35GHz

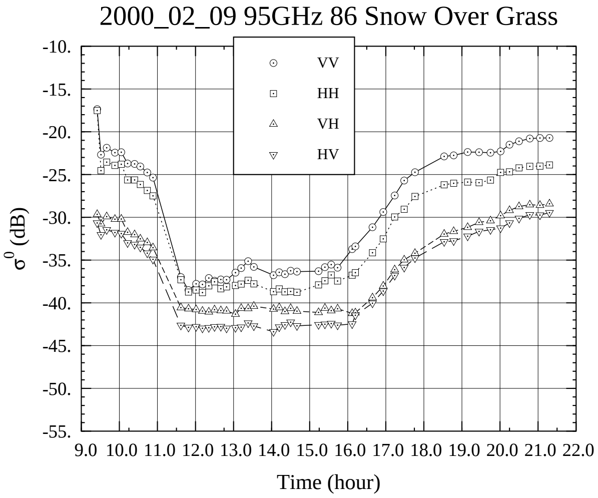

(b) Snow over grass 95GHz

Figure 4.20: Radar backscatter response of snow over grass measured at 86° incidence during the melt-freeze cycle. (a) 35 GHz. (b) 95 GHz

observe three salient features: (1) the two cross-polarized components are almost identical at all angles for both figures, which is expected and which confirms the quality of the calibration procedure; (2) the fastest change in level occurs between 85° and 88°, and it is more pronounced at 95 GHz than at 35 GHz; and (3) the two copolarized components are essentially identical at 95 GHz, but not so at 35 GHz.

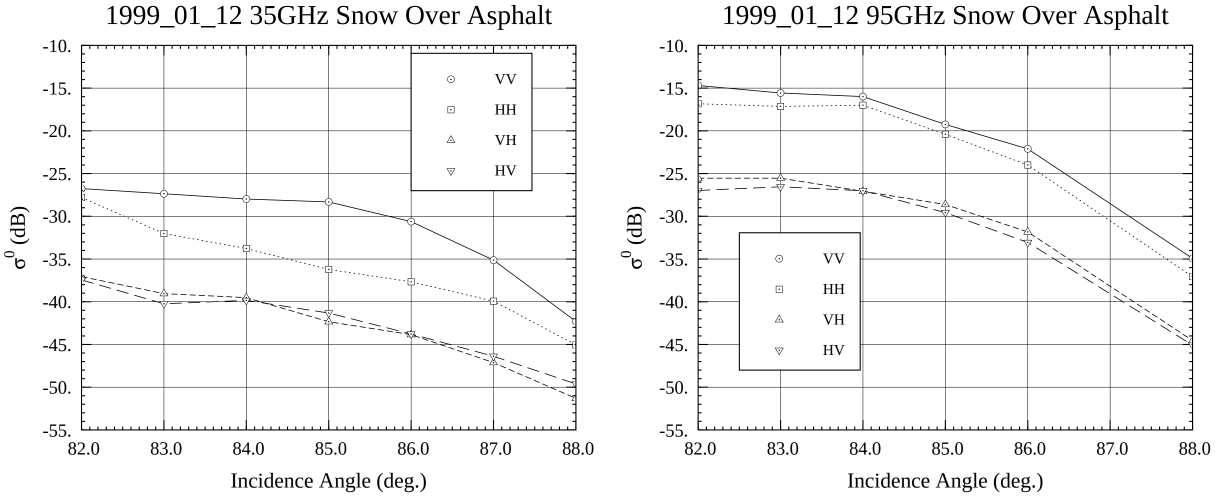

(a) 35 GHz

(b) 95 GHz

Figure 4.21: Radar backscatter response of snow over asphalt as function of incidence angle. (a) 35 GHz. (b) 95 GHz

4.3 Modeling of MMW Snow Angular Backscatter at Near Grazing Incidence

In general, the geometry of the snow layer backscatter problem is shown in Fig. 4.22, where both the snow-air surface and the snow-ground surface are rough. Yet to study the first order scattering mechanism of the snowpack, these surfaces are replaced by their mean surface as shown in the dotted line, leaving the rough surface effect for later consideration.

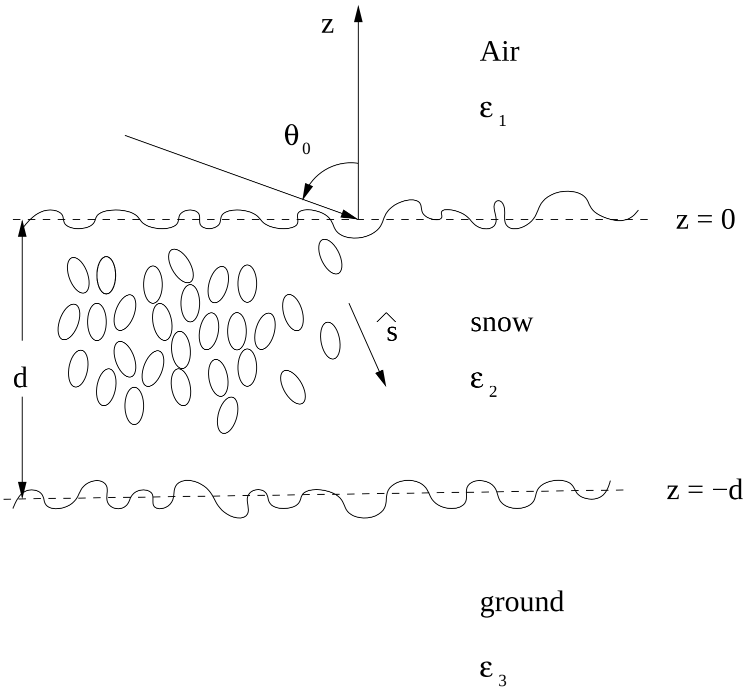

Figure 4.22: A plane wave incident upon a bounded layer of densely dispositioned spheroids with certain orientational distribution overlying a homogeneous half-space

As mentioned before, we have elected to use a hybrid technique between the conventional RT and the DMRT to model backscatter from snow. In this section, we will give a brief description of both the vector radiative transfer equation (VRTE) technique, since it serves as the general framework for our model, and of the numerical technique to solve VRTE. Next, the T-matrix technique will be used to calculate the phase matrix for a single scatterer which is assumed to be spheroidal in shape with dimensions comparable to wavelength, and the QCA will be used to calculate the volume extinction coefficient. Then, a novel technique will be described to reconcile the inconsistency of assumptions under CRT and QCA. At the end, the effect of surface roughness will be discussed.

4.3.1 VRTE Theory For Backscatter

For backscatter, the vector radiative transfer equation assumes the following form [93]:

$$\frac{d\mathbf{I}(\hat{\mathbf{s}},z)}{ds} = -\boldsymbol{\kappa}_e(\hat{\mathbf{s}})\mathbf{I}(\hat{\mathbf{s}},z) + \iint_{4\pi} \mathbf{P}(\hat{\mathbf{s}},\hat{\mathbf{s}}')\mathbf{I}(\hat{\mathbf{s}}',z)d\Omega' \tag{4.1}$$

where $\mathbf{I}(\hat{\mathbf{s}},z)$ is the specific intensity at depth z along the direction $\hat{\mathbf{s}}$, which is defined in [60], $\mathbf{P}(\hat{\mathbf{s}},\hat{\mathbf{s}}')$ is the phase matrix giving the contributions from direction $\hat{\mathbf{s}}'$ into the direction $\hat{\mathbf{s}}$, $\boldsymbol{\kappa}_e(\hat{\mathbf{s}})$ is the extinction matrix along direction $\hat{\mathbf{s}}$ for Stokes parameters.

The boundary condition for the specific intensity at the air-snow interface (defined by $z = 0$ and $0 \leq \theta \leq 2\pi$) is [112]:

$$\mathbf{I}(\pi-\theta,\phi;z=0) = \overline{\overline{\mathbf{T}}}_{12}\mathbf{I}_{0i}(\pi-\theta_0,\phi_0) + \overline{\overline{\mathbf{R}}}_{21}\mathbf{I}(\theta,\phi;z=0) \tag{4.2}$$

where $\overline{\overline{\mathbf{T}}}_{12}$ and $\overline{\overline{\mathbf{R}}}_{21}$ are the transmissivity and reflectivity matrices of the upper boundary, respectively, and are given explicitly in [60].

At the snow-soil interface (defined by $z = -d$ for $0 \leq \theta \leq \pi/2$),

$$\mathbf{I}(\theta, \phi; z = -d) = \overline{\overline{\mathbf{R}}}_{23}\mathbf{I}(\pi - \theta, \phi; z = -d) \tag{4.3}$$

where $\overline{\overline{\mathbf{R}}}_{23}$ is the reflectivity matrix of the lower boundary.

The discrete ordinate method is widely used to obtain the numerical solutions to Eq. 4.1 with the boundary conditions Eq. 4.2 and 4.3 enforced. In this technique, the specific intensity $\mathbf{I}(\theta, \phi; z)$ and the phase matrix $\mathbf{P}(\theta, \phi; \theta', \phi')$ are expanded using Fourier series in azimuthal direction to eliminate the ϕ dependence in Eq. 4.1. The details of this technique can be found in [46] and [101]. Upon the solution to the Fourier expansion of the specific intensity $\mathbf{I}_2$ in medium 2 being obtained, the total incoherent specific intensity in medium 1 can be synthesized as:

$$\mathbf{I} = \overline{\overline{\mathbf{T}}}_{21} \sum_{m=0}^{m=\infty} (\mathbf{I}_2^{mc} \cos m\phi + \mathbf{I}_2^{ms} \sin m\phi) \tag{4.4}$$

where the superscritps mc and ms refer to the mth order harmonic coefficients with cosine or sine dependence in the azimuthal directions, respectively.

For V-polarized incident wave, the backscattering coefficients due to the snow volume scattering for vv and hv can be obtained as [60]:

$$\begin{aligned} \sigma_{vv} &= 4\pi \cos\theta_0 I_1 \\ \sigma_{hv} &= 4\pi \cos\theta_0 I_2 \end{aligned} \tag{4.5}$$

where I_1 and I_2 are the first and second components of the total incoherent specific intensity in medium 1, $\mathbf{I}$.

For H-polarized incident wave, the backscattering coefficients due to the snow volume scattering for vh and hh can be obtained similarly.

4.3.2 Phase Matrix and Volume Extinction Coefficient of Snow Layer

Determination of the Phase Matrix

At millimeter wavelengths, the dimension of the snow particle can be comparable to the wavelength. To solve the phase matrix for a single spheroidal scatterer, the T-matrix method is widely called for to provide an exact analytic solution. This method, based on the extended boundary condition (EBC), attempts to relate the scattered field from a scatterer to the incident wave [111].

The T-matrix in its general form is:

$$\overline{\overline{\mathbf{T}}} = -Rg\overline{\overline{\mathbf{Q}}}^{t}(\overline{\overline{\mathbf{Q}}}^{t})^{-1} \tag{4.6}$$

where the $\overline{\overline{\mathbf{Q}}}$ matrix and the regular $\overline{\overline{\mathbf{Q}}}$ matrix, Rg$\overline{\overline{\mathbf{Q}}}$, are defined in [93], and t denotes matrix transpose. The special properties of $\overline{\overline{\mathbf{Q}}}$ and Rg$\overline{\overline{\mathbf{Q}}}$ are also given in [93]

The scattering amplitude dyad $\overline{\overline{\mathbf{F}}}(\theta_s, \phi_s; \theta_i, \phi_i)$ is related to $\overline{\overline{\mathbf{T}}}$ by:

$$\begin{aligned}\overline{\overline{\mathbf{F}}}(\theta_s, \phi_s; \quad & \theta_i, \phi_i) = \frac{4\pi}{k} \sum_{n,m,n',m'} (-1)^{m'} i^{n'-n-1} \\ & \{[T^{(11)}_{mnm'n'} \gamma_{mn} \overline{C}_{mn}(\theta_s, \phi_s) + T^{(21)}_{mnm'n'} i\gamma_{mn} \overline{B}_{mn}(\theta_s, \phi_s)] \gamma_{-m'n'} \overline{C}_{-m'n'}(\theta_i, \phi_i) + \\ & [T^{(12)}_{mnm'n'} \gamma_{mn} \overline{C}_{mn}(\theta_s, \phi_s) + T^{(22)}_{mnm'n'} i\gamma_{mn} \overline{B}_{mn}(\theta_s, \phi_s)] \\ & \gamma_{-m'n'} \overline{B}_{-m'n'}(\theta_i, \phi_i)/i\}\end{aligned} \tag{4.7}$$

where the vector spheric harmonics $\overline{B}_{mn}$ and $\overline{C}_{mn}$, as well as the quantity γ_{mn} are also defined in [93], and $T^{(u,v)}_{mnm'n'}$, $u, v = 1, 2$ are the entries to the T-matrix.

Upon determining $\overline{\overline{\mathbf{T}}}$, the scattering cross section of a spheroid scatterer for a given incident polarization, $\hat{p}$, is:

$$\sigma_{sp}(\theta_i, \phi_i) = \int_{4\pi} d\Omega_s [|f_{vp}(\theta_s, \phi_s; \theta_i, \phi_i)|^2 + |f_{hp}(\theta_s, \phi_s; \theta_i, \phi_i)|^2] \tag{4.8}$$

where f_{qp} is related to $\overline{\overline{\mathbf{F}}}$ as:

$$f_{qp} = \hat{q} \cdot \overline{\overline{\mathbf{F}}} \cdot \hat{p} \tag{4.9}$$

For a rotated spheroidal scatterer, its T-matrix determination is much more computationally involved, which is

$$\overline{\overline{\mathbf{T}}} = \overline{\overline{\mathbf{D}}}\,\hat{\overline{\overline{\mathbf{T}}}}\,\overline{\overline{\mathbf{D}}}^{-1} \tag{4.10}$$

where $\hat{\overline{\overline{\mathbf{T}}}}$ is the T-matrix for a spheroid scatterer without rotation, $\overline{\overline{\mathbf{D}}}$ is the rotation matrix which is given by:

$$\begin{pmatrix} \overline{\overline{\boldsymbol{\Delta}}} & 0 \\ 0 & \overline{\overline{\boldsymbol{\Delta}}} \end{pmatrix}$$

and the entry for matrix $\overline{\overline{\boldsymbol{\Delta}}}$ is:

$$(\overline{\overline{\boldsymbol{\Delta}}})_{mnm'n'} = \delta_{nn'}\Delta^{(n)}_{mm'} \tag{4.11}$$

where

$$\Delta^{(n)}_{mm'}(\alpha\beta\gamma) = e^{\{im'\gamma\}} d^{(n)}_{m'm}(\beta) e^{\{im\alpha\}} \tag{4.12}$$

and

$$d^{(n)}_{m'm}(\beta) = [\frac{(n+m')!(n-m')!}{(n+m)!(n-m)!}]^{1/2} (\cos\frac{\beta}{2})^{m'+m} (\sin\frac{\beta}{2})^{m'-m} P^{m'-m, m'+m}_{n-m'}(\cos\beta) \tag{4.13}$$

where $P^{(j,k)}_n(x)$ is the Jacobi polynomial of order n and degree (j,k) [1].

Given the volume fraction of the identical scatterers, and the joint *pdf*, $p(\alpha, \beta, \gamma)$, of the Eulerian angles α, β and γ, the phase matrix element P_{qp}, in its conventional form is given by [93]:

$$P_{qp}(\theta_s, \phi_s; \theta_i, \phi_i) = n_0 \int_0^{2\pi} d\alpha \int_0^{\pi} d\beta \int_0^{2\pi} d\gamma\, p(\alpha, \beta, \gamma)\, | f_{qp}(\theta_s, \phi_s; \theta_i, \phi_i) |^2 \tag{4.14}$$

Notice in the above simple and conventional treatment of the phase matrix, it is assumed that the scattered fields from distinct scatterers are statistically independent. This assumption, while useful for sparse medium, may not be valid for a dense medium such as snow, where the interaction among scatterers need to be considered. In subsection 4.3.3, a mechanism is introduced to compensate for the absense of interaction among scatterers.

Volume Extinction Coefficient $\boldsymbol{\kappa}_e$ of Snow

Since the snow layer is a dense nontenuous medium, the interaction between snow particles must be taken into account. By representing the interdependency of snow particles through what is called the pair distribution function, QCA is one of the recent approaches used to determine the effective propagation constant, hence the extinction coefficient $\boldsymbol{\kappa}_e$ [92]. If the pair distribution function is chosen as a simple hole-correction function, then this approach collapses to one that assumes independent scatterers. One salient feature of QCA is that it predicts a rise, a top-off, and a fall-off of the extinction rate when the volume fraction of the scatterers monotonically increases, as opposed to the monotonic increase predicted by the conventional approach assuming independent scatterers. This prediction is verified experimentally [47] and brings popularity to QCA. For dry snow, we find QCA to be an appealing approach when used in combination with the assumption of spherical scatterers with an effective size.

The assumed snow shape has a significant impact on the resultant volume extinction coefficient $\boldsymbol{\kappa}_e$ [89]. For reasons listed in the next chapter, it is both natural and pertinent to approximate the ice particles as spheroids with some orientational distribution. However, this treatment is conceptually simple yet computationally demanding. It is because of that, that in QCA, even if the spheroidal scatterers are assumed to be identical in shape and size, it is necessary to average over the orientation Eulerian angles (α, β, γ) on both sides of the simplest form of QCA, that is, the multiple scatterer equation shown in Eq. 4.17, hence on $\overline{\overline{\mathbf{T}}}$ matrix of single spheroidal scatterer. As evident in Eq. 4.10, the orientation information is embedded in $\overline{\overline{\mathbf{D}}}$ matrix and $\overline{\overline{\mathbf{D}}}^{-1}$ matrix. Since $\overline{\overline{\mathbf{D}}}$ and $\overline{\overline{\mathbf{D}}}^{-1}$ are seperated by $\hat{\overline{\overline{\mathbf{T}}}}$, and $\hat{\overline{\overline{\mathbf{T}}}}$ is not diagonal, the involved calculation for the averaging can be considerable, a major reason in [89] that orientational distribution is ignored in assuming particles as vertically aligned spheroids to determine $\boldsymbol{\kappa}_e$.

To attain the advantages in assuming spheroidal particles meanwhile alleviate the computational demand, we can adopt a novel intuitive strategy that dichotomizes the treatments of the shapes of snow particles in calculating the volume extinction coefficient $\boldsymbol{\kappa}_e$ and phase matrix $\mathbf{P}$. Specifically, we propose to treat the snow particles as spheres with certain effective sizes in calculating $\boldsymbol{\kappa}_e$ and as spheroids in calculating $\mathbf{P}$. The former is because the snow particles, though non-spherical in nature, tend to follow a uniform distribution in orientation, which leads to an extinction coefficient independent of polarization, an inherent property of the spherical scatterers. The latter is because that the scattering pattern depends on size and orientation, something can not be simply averaged out. This point is evident through a collective examination of Eq. 4.14, 4.10 and 4.7.

To summerize, we intend to use QCA to calculate the volume extincition coefficient $\boldsymbol{\kappa}_e$, and propose to treat the snow particles as spheres with effective sizes in such calculation for good reason. However, QCA takes into account the interaction among scatterers, while in calculating the phase matrix $\mathbf{P}$ in subsection 4.3.2, such interaction is ignored. It thus calls for some mechanism to reconcile these disparate assumptions. Such reconcilation mechanism is investigated in the next section.

4.3.3 Albedo Matching As a Reconcilation Mechanism

The disparate assumptions embedded in the treatment of $\boldsymbol{\kappa}_e$ and $\mathbf{P}$ need to be reconciled. As we shall see, failing to reconcile these assumptions may lead to severe performance degradation. However, this much needed reconcilation is either ignored in the remote sensing community [60] [58] or treated with many limitations [37] [29]. In this section, we propose a new approach based on albedo matching to provide such reconcilation. This technique is generic, hence the limitations inherent in [37] and [29] are avoided. It will be presented in detail after a brief review of the amplitude and phase correction method (for a dense medium) introduced by Fung, *etal.* [37].

Fung *et al.* [37] has attacked the inconsistency problem from a different angle. Their approach starts directly with the phase matrix, considers the array factor in the field formation, and comes up with what they call the amplitude and phase correction factor. Yet, their approach has certain drawbacks: 1) the interaction among scatterers is not treated in the strict sense; 2) a free variable to scale the rms variation of a scatterer's position to its mean position has to be introduced; 3) their approach is difficult to extend to cases of nonspherical scatterers with size and orientation distributions; 4) their approach requires the calculation of the erf function with complex argument, which is prone to numerical instability; and 5) most importantly, their amplitude and phase correction factor is zero for forward scattering, which implies a zero value for the phase matrix, counter-intuitive to the conventional understanding that in general, phase matrix shows a peak at the forward scattering. Comparison between the normalized VV component of the phase matrix using Fung's approach and using conventional approach for a spheric scatterer is shown in Figure 4.23. The diameter of the sphere is 0.4 mm, $f = 35$ GHz, $\theta_i = 52^\circ, \phi_i = 0, \phi_s = 0$, and the parameterization follows Fung's convention [29]

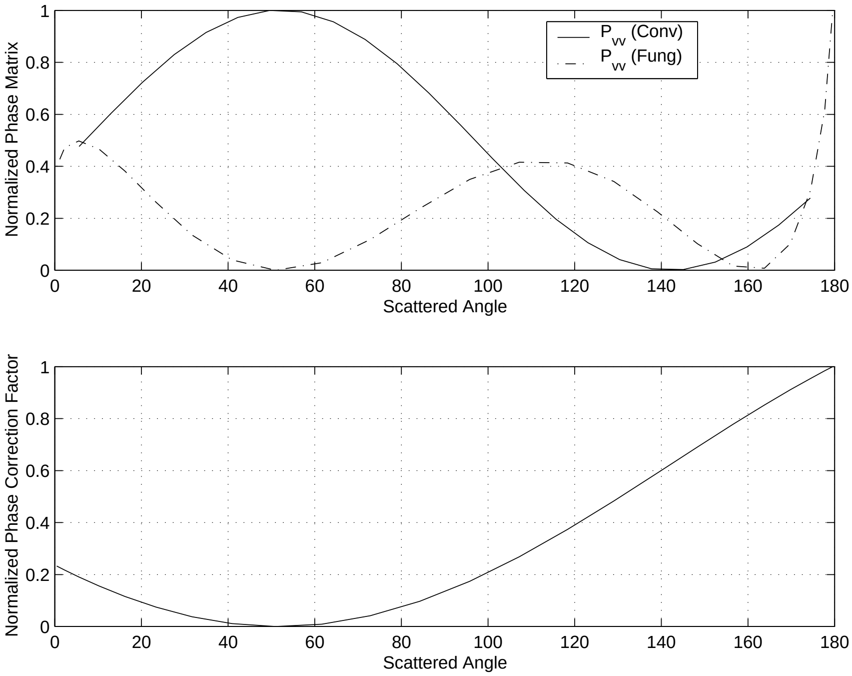

Figure 4.23: Comparison of P_{vv} between Fung's approach and the conventional approach for a sphere.

such that $s = 0.55d, l = 0.11d, \sigma = s(d - 2a)$, where a is the radius of the sphere.

We propose a new method to reconcile this inconsistency by albedo matching. This method begins with the recognition that we have two total scattering coefficients, one results from the calculation of $\mathbf{P}$ under independent scatterers assumption in the conventional RT, and the other is from QCA. Let us denote them by κ_s^{CRT} and κ_s^{QCA}, respectively. Then, the determination of their values proceeds as follows. For $\kappa_s(\hat{\mathbf{s}})^{CRT}$, which represents the total scattering at direction $\hat{\mathbf{s}}$ under independent scatterers assumption, is [93]

$$\kappa_s(\hat{\mathbf{s}})^{CRT} = \iint\limits_{4\pi} \left(\langle P_{pp}(\hat{\mathbf{s}}, \hat{\mathbf{s}}')\rangle + \langle P_{qp}(\hat{\mathbf{s}}, \hat{\mathbf{s}}')\rangle\right) d\Omega', \tag{4.15}$$

for p polarization, where $p, q = v, h$. We use $\langle\cdot\rangle$ to denote the averaged phase matrix over scatterer size and orientation distributions. The resultant $\kappa_s(\hat{\mathbf{s}})$ gives the κ_s^{CRT} for direction $\hat{\mathbf{s}}$. For κ_s^{QCA}, it is obtained through $\kappa_s^{QCA} = \kappa_e^{QCA}$ - κ_a, where κ_a

is the absorption coefficient and κ_e^{QCA} is the extinction coefficient calculated using QCA [93]. One should pay close attention that κ_e^{CRT} and κ_e^{QCA} so far obtained are not necessarily equal to each other, they are the results of different calculations under different assumptions.

The second step of the proposed method is to realize that for the same medium, the collective scattering for a specific direction should be uniquely determined statistically (in the averaging sense), hence we need to choose either κ_s^{CRT} or κ_s^{QCA} as the true value for total scattering coefficient. Most likely, κ_s^{QCA} is the correct one, because it takes into account the interaction among scatterers, a mechanism critical for a dense medium like snow.

Having made the decision, we need to rectify κ_s^{CRT} to match κ_s^{QCA}. The method we propose is to scale κ_s^{CRT} by a scaling factor

$$\alpha_s = \frac{\kappa_s^{QCA}}{\kappa_s^{CRT}} \tag{4.16}$$

for reasons that follow soon. In view of Eq. 4.15, this approach is equivalent to rescaling the phase matrix in CRT by α_s.

This approach can be justified as follows. For a dense medium, the effect of the interaction among scatterers on the collective scattering pattern can be thought of as a blurring function which convolves with the scattering pattern of a single scatterer, in exactly the same way what the spreading function does to the radar imaging of a region of interest. Put mathematically, the starting point of QCA is the multiple scatterer equation [93]:

$$\overline{w}^{(l)} = \sum_{j=1,j\neq l}^{N} \overline{\overline{\sigma}}(k\overline{r_l r_j})\overline{\overline{T}}^{(j)}\overline{w}^{(j)} + Rg\overline{\overline{\sigma}}(k\overline{r}_l)\overline{a}_{inc} \tag{4.17}$$

where $\overline{w}^{(l)}$ is the exciting field coefficient of the lth particle, and $\overline{\overline{\sigma}}$ involves the free space dyadic Green's function. Since the free space dyadic Green's function is invariant to spatial translation, it follows that the right side of the equation represents exactly the convolution function.

Now that the collective scattering pattern of a dense medium is a convolution operator on the single-scatterer scattering pattern, and convolution simply implies a spatial invariant linear system, a rescaling of such a linear system is fully justified.

So far we have completed the treatment of the snow volume scattering by introducing two novel techniques. First, we used different shape treatments in calculating the volume extinction coefficient $\boldsymbol{\kappa}_e$ and the phase matrix $\mathbf{P}$ to facilitate computation. Second, we introduced the albedo matching method to reconcile the inconsistency of the assumptions underlying the calculations of the volume extinction coefficient $\boldsymbol{\kappa}_e$ and phase matrix $\mathbf{P}$.

4.3.4 Snow-Air Rough Surface Scattering

The impact of surface roughness for VRTE is twofold: first, the specific intensity transmission coefficient is attenuated by a correction factor as compared with that of a specular surface; secondly, the specific intensity reflection coefficient is also attenuated when we set up boundary conditions. Furthermore, surface roughness entails direct surface backscatter and shadowing effect, which will be discussed briefly as follows.

Surface backscatter

For a surface with a large rms slope, the Kirchhoff stationary-phase approximation can be used to analyze surface scattering [93]. Moreover, if the second moment statistics of the surface roughness can be modeled by a Gaussian correlation function, then the dependence of the copolarized backscattering coefficient on incidence angle is proportional to [108]

$$\frac{1}{\cos^4\theta} e^{\{-\frac{\tan^2\theta}{4(\frac{\sigma_s}{\rho_l})^2}\}} \tag{4.18}$$

This factor drops rapidly with increasing θ. For example, assuming $\sigma_s/\rho_l = 0.1$, it is 240 dB lower for incidence at 60° than at 40°, a tremendous signal level drop. At 80° incidence, the consequential drop is extremely large. Hence it follows that at near grazing incidence the direct surface backscatter is negligible as compared to volume backscatter.

Shadowing correction

At near grazing incidence, roughness of the snow-air surface induces a shadowing effect that cannot be ignored. This is because at such incidence, the shadow of the illuminated area forms a large portion of the projected footprint. To account for the shadow effect, a shadowing function for the high-frequency geometrical optics limit is introduced as [69]:

$$S = \frac{1}{\frac{2}{\sqrt{\pi}}\tan\theta\frac{\sigma_s}{\rho_l}e^{(}-\frac{\rho_l^2}{4\sigma_s^2\tan^2\theta}) + erf(\frac{\rho_l}{2\sigma_s\tan\theta})} \tag{4.19}$$

where ρ_l is the correlation length and σ_s is the rms surface roughness. Their ratio σ_s/ρ_l defines the rms slope.

The final shadow-corrected backscattering coefficient σ^0_{sc} is:

$$\sigma^0_{sc} = \sigma^0 S \tag{4.20}$$

where σ^0 is the backscattering coefficient without shadowing.

4.4 Comparison between Model and Measurements of Dry Snow

In this section, we shall discuss progressively the effect upon the backscattering coefficients from snow of the newly proposed albedo matching technique, the shape of snow particle and its orientation, shadowing and roughness. Such discussion is through comparison between model prediction and measurements for angular patterns.

The angular measurements made on January 12, 1999 will be used because it represents typical angular patterns of backscattering from snowpack over asphalt at both 35 GHz and 95 GHz, as shown in Figure 4.21(a) and Figure 4.21(b), respectively. The measurements were started at 2:55pm and ended at 4:47 pm. During that period, the air temperature was measured several times and recorded to be around −5.5°C. The wind was mild and no snowfall occured that afternoon. Based on several snow depth measurements, the depth was 36.5 cm. Wetness reading was around 0 to 0.3% by volume, a reading that tempts us to choose $m_v = 0$ in the treatment. However, because MMW backscatter of snow is very sensitive to m_v, even when its value is very small, and because in the process of ground truth collection, snow pack was found not completely dry, we choose the average value of 0.1% as model input.

In Figure 4.24, comparison is made between measurement and simulation based on Kuga's approach for angular backscatter response at 35 GHz. We notice that the predicted copolarized levels are about 8 dB higher than the measurements, while the predicted cross-polarized level is about 8 dB lower, which indicates strong volume backscattering. Overestimation of the copolarized levels is the result of overestimating the phase matrix.

To correct this overestimation, the Next the proposed albedo matching technique is applied, and the result is shown in Figure 4.25, where roughness and shadow are still not considered yet. It is clear that the predicted copolarized signal levels are just about 3 dB higher than the measured data, which represents a significant improvement over Kuga's approach.

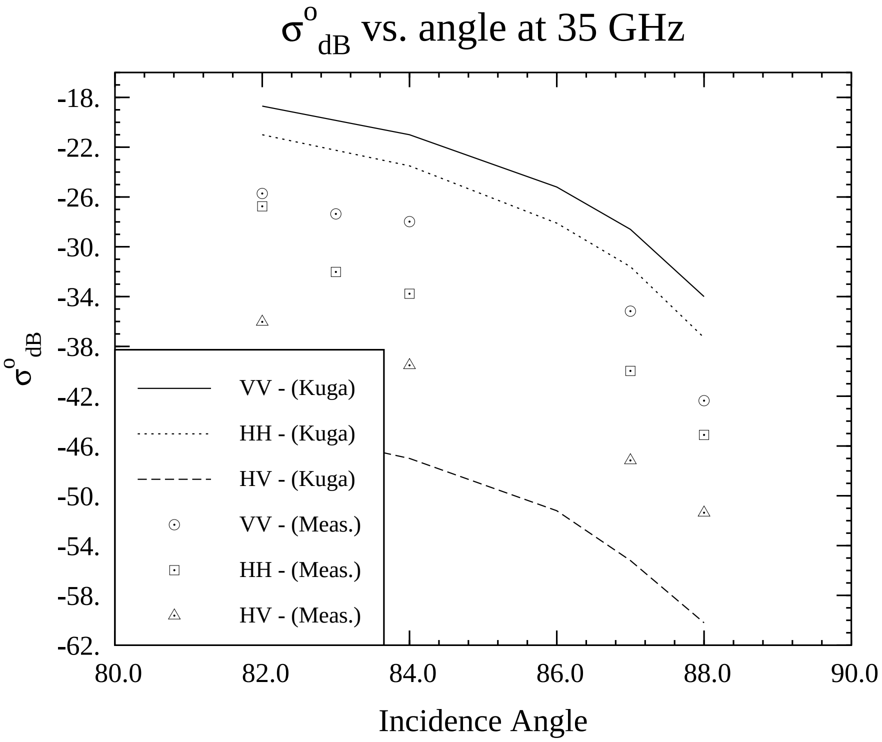

Figure 4.24: Comparison between measurement and simulation (Kuga) of angular backscatter response at 35 GHz. Dot denotes σ°_{vv}, square σ°_{hh} and upward triangle σ°_{vh} measurements. In simulation, snow particles are assumed to be independent spheres with average diameter 0.4mm in phase matrix calculation. Air-snow surface is assumed to be a specular plane.

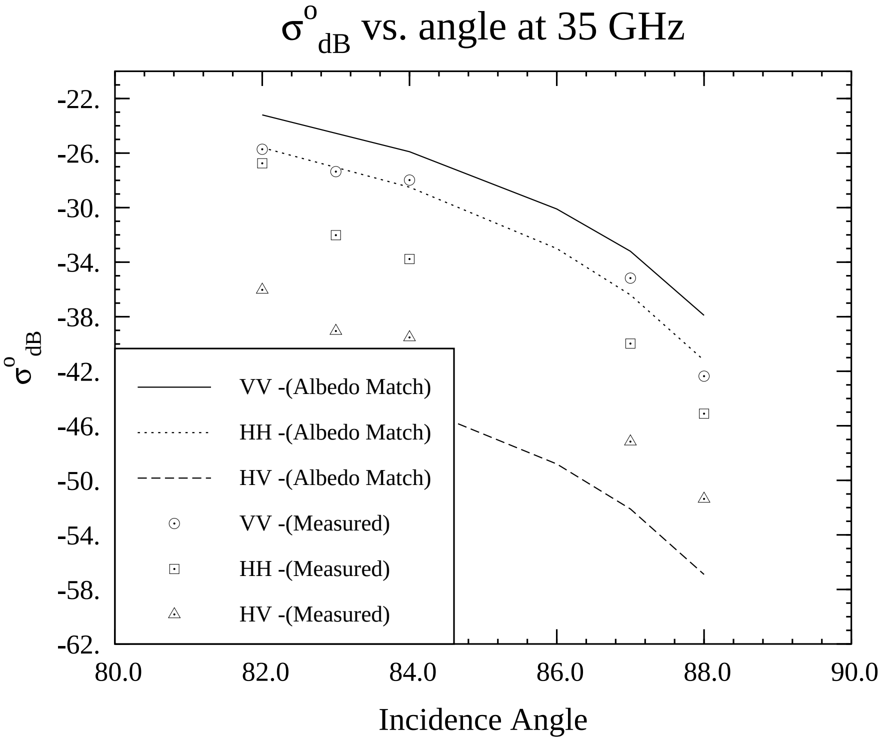

Figure 4.25: Same as in Fig. 4.24 except albedo matching is performed.

The result shows significant improvement for the predicted copolarized levels, even though only albedo matching is applied.

In Figure 4.26, a comparison is made between the propased albedo matching technique and Fung's amplitude and phase correction approach. In the simulation, for albedo matching technique, all parameters are the same as in Fig. 4.24; for Fung's approach, the parameterization follows Fung's convention [29] such that $s = 0.55d, l = 0.11d, \sigma = s(d - 2a)$, where a is the radius of the sphere. From the figure, it is clear that both techniques capture the angular dependence of the radar backscatter in the same fashion, except that Fung's approach tends to overestimate more by $1 \sim 2$ dB.

The effect of surface roughness on backscatter is illustrated in Figure 4.27, where a rms height of 2 mm is assumed. It demonstrates further volume backscatter correc-

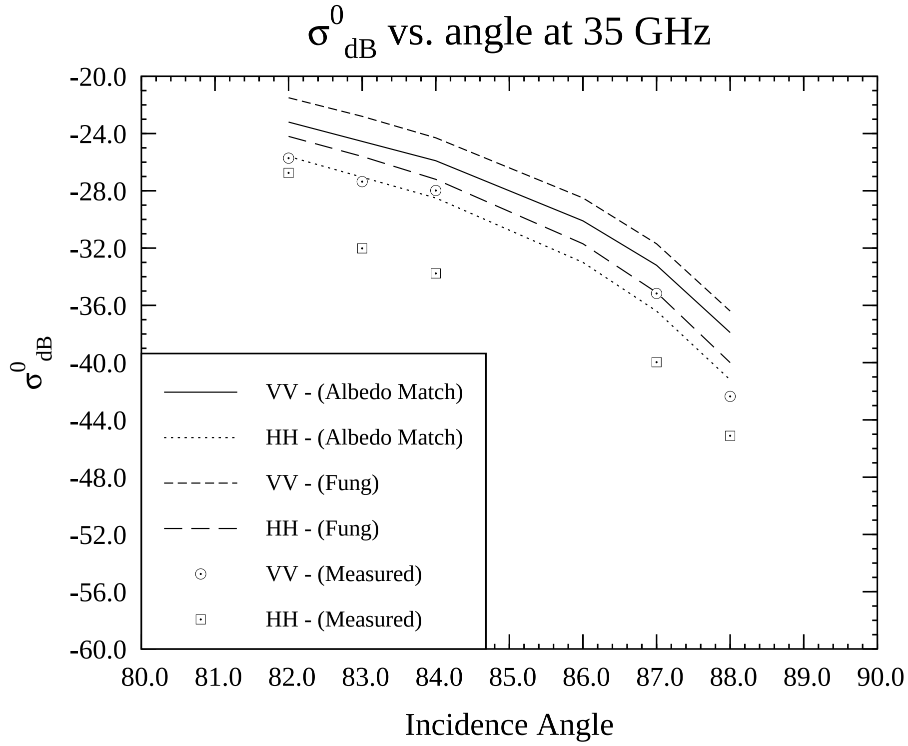

Figure 4.26: Comparison between proposed albedo matching and Fung's approach.

tion and a slight angular pattern correction. However, better capture of the angular characteristic of backscatter is realized when the shadow effect is incorporated in the model as shown in Figure 4.28, where a rms slope of 0.05 is assumed.

So far we have seen progressive improvement on the copolarized backscatter, but prediction of the cross-polarized component is not satisfactory as is evident when we compare Figure 4.24 to Figure 4.25.

The effect of snow particle shape on angular backscatter response at 35 GHz is shown in Figure 4.29, where snow particle is assumed to be a spheroid. Clearly, much better crosspolarized level is obtained.

Backscatter at 95 GHz shows similiar progress with each new treatment, and its counterpart to Figure 4.29 is shown in Figure 4.30.

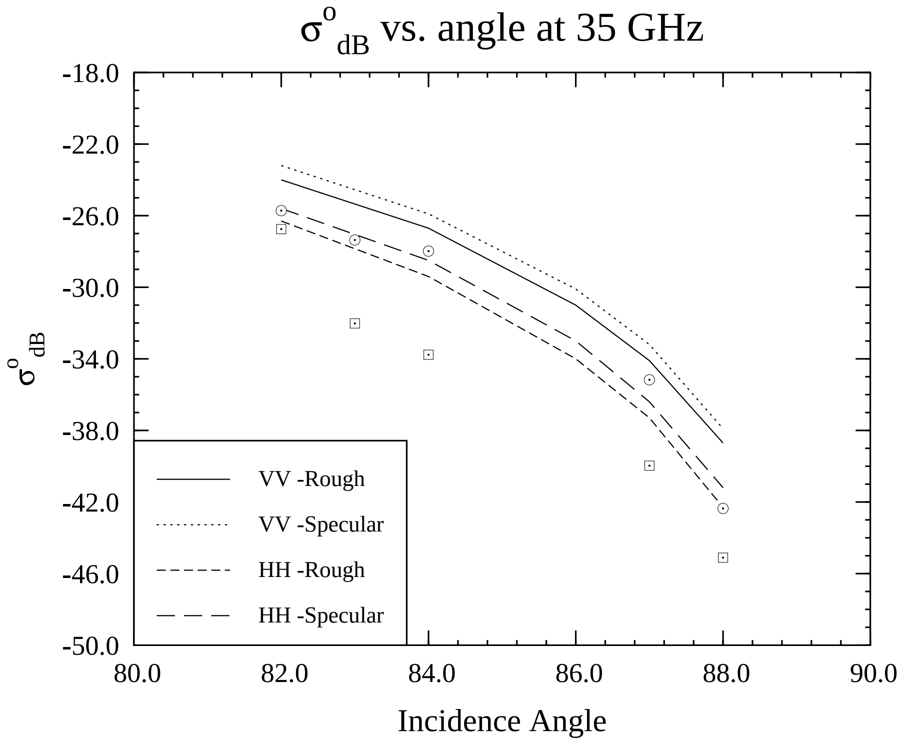

Figure 4.27: Effect of air-snow surface roughness on angular backscatter response at 35 GHz. Dot denotes σ°_{vv}, and square denotes σ°_{hh} measurements. In simulation, snow particle is assumed to be a sphere with average diameter 0.4mm. Albedo matching is performed, rms height is 2 mm. No shadowing effect is included.

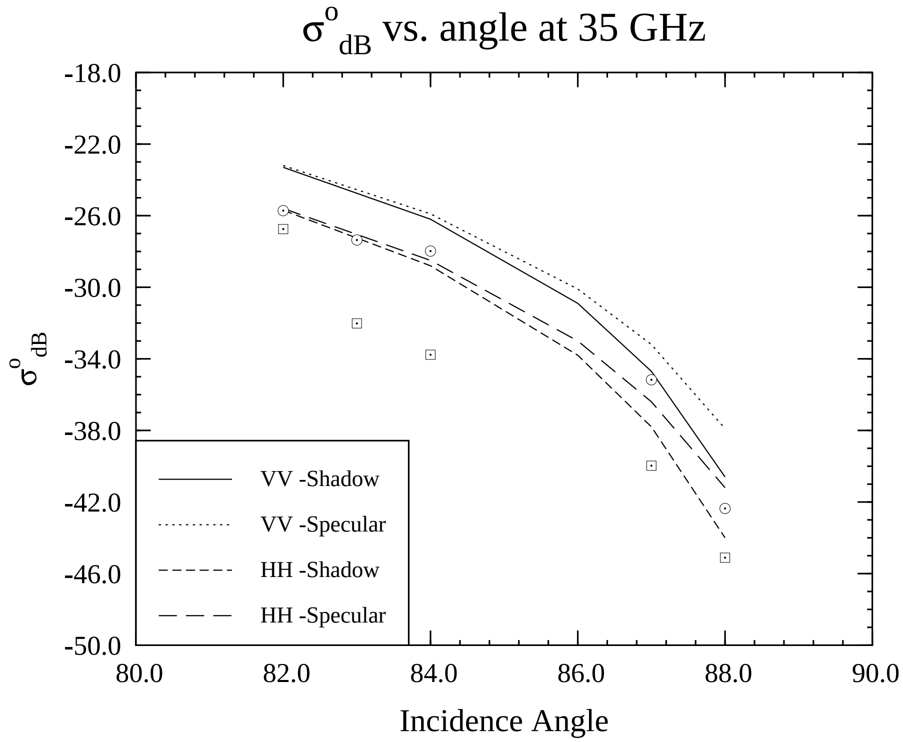

Figure 4.28: Effect of air-snow surface shadow on angular backscatter response at 35 GHz. Dot denotes σ°_{vv}, and square denotes σ°_{hh} measurements. In simulation, snow particle is assumed to be a sphere with average diameter 0.4mm. Albedo matching is performed, rms slope is 0.05. Only shadowing effect is included.

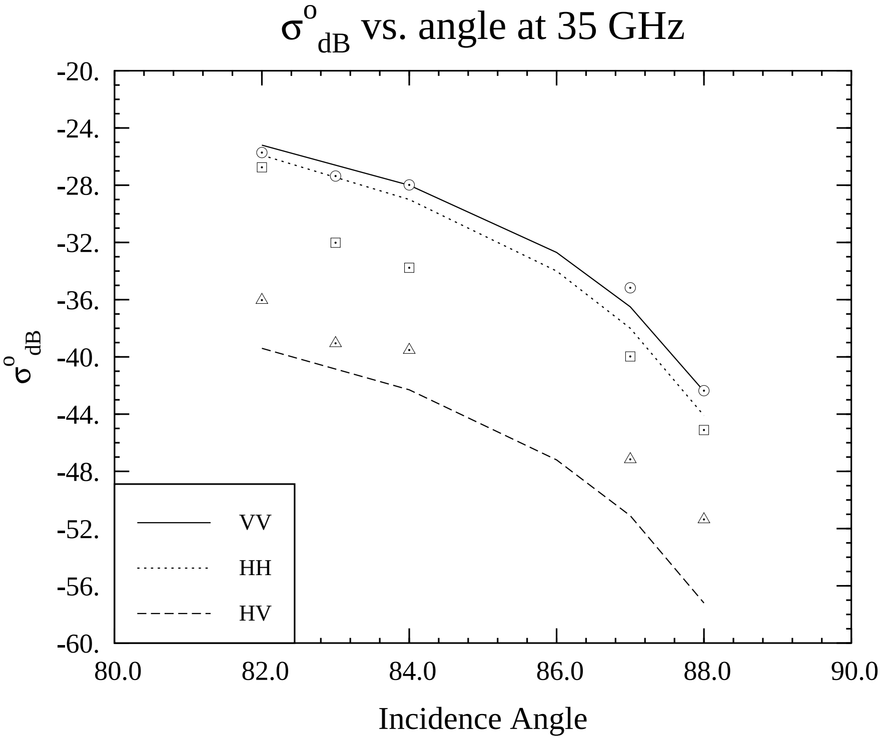

Figure 4.29: Effect of snow particle shape on angular backscatter response at 35 GHz. Dot denotes σ°_{vv}, square σ°_{hh} and upward triangle σ°_{vh} measurements. In simulation, snow particle is assumed to be a spheroid with average diameter 0.4mm on cross section and an elongation ratio of 1.1. Albedo matching is performed, rms slope is 0.05, rms height is 2 mm. Both shadowing and roughness effects are included.

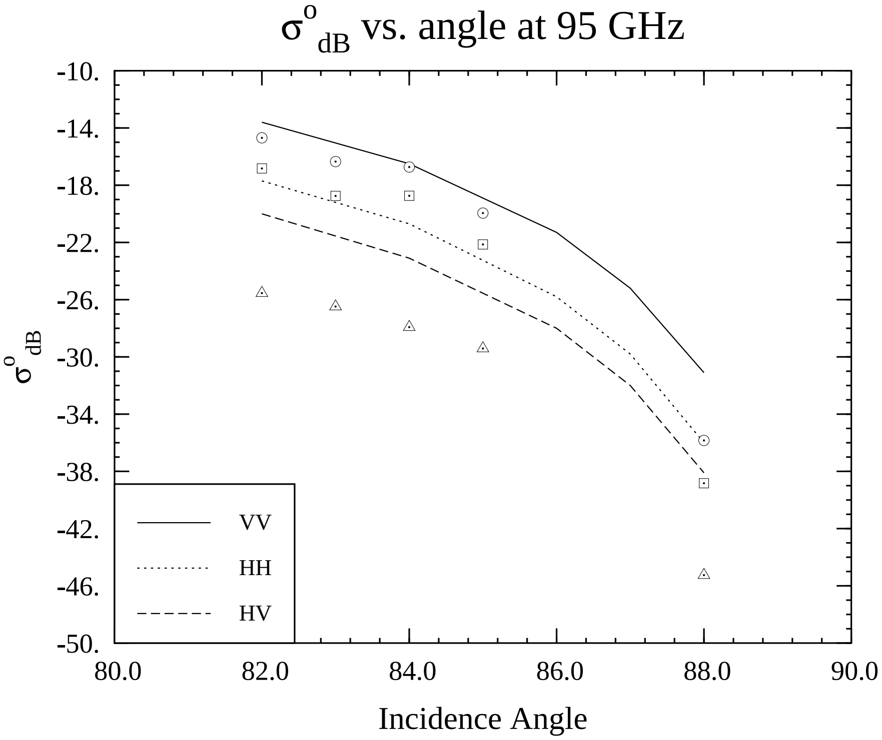

Figure 4.30: Effect of snow particle shape on angular backscatter response at 95 GHz. Dot denotes σ°_{vv}, square σ°_{hh} and upward triangle σ°_{vh} measurements. In simulation, snow particle is assumed to be a spheroid with average diameter 0.4mm on cross section and an elongation ratio of 1.1. Albedo matching is performed, rms slope is 0.05, rms height is 2 mm. Both shadowing and roughness effects are included.

4.5 Conclusion

This chapter describes the major measurement campaigns conducted in the winters of 1999 and 2000 to extend our understanding of snow backscatter to the near grazing incidence range. Carefully planned measurements were undertaken, resulting in over 300 data points for 1999 and over 500 for 2000, including measurements at both 35 and 95 GHz. In addition, extensive ground truth data, including temperature, water content in the snow pack, snow thickness, temperature and snow surface roughness, were collected. Numerous photographs of snow slices were also taken to assist characterization of snow particles in terms of shape and size.

Moreover, as the first part of the modeling efforts to interpret the angular backscattering behavior of snowpack over asphalt at both 35 GHz and 95 GHz, an albedo matching technique is proposed to reconcile the disparity inherent in QCA for $\boldsymbol{\kappa}_e$ calculation and in conventional determination of the phase matrix.

As a further consideration, the snow particle shape, which is a critical factor in the scattering behavior of snow at MMW band, is strategically assumed to be spherical with an effective size in determining $\boldsymbol{\kappa}_e$ using QCA to alleviate computational demand, while preserving the statistical independence of the extinction coefficient on polarization, and assuming the snow particle to be spheroidal in shape in calculating the phase matrix to differentiate scattering pattern and enhance the level of the crosspol.

The simulation results demonstrate that the proposed model successfully captures the backscatter angular response characteristic of the copolarized backscatters at both 35 and 95 GHz.

As mentioned before, the wet snow, which is frequently encountered in diurnal measurements, needs a treatment quite different from that of dry snow. This new treatment for wet snow in particular or for diurnal pattern in general is the subject of next chapter.

CHAPTER V

MMW Measurements and Modeling of Diurnal Backscattering of Snow At Near Grazing Incidence Incorporating Snow Thermodynamic Information

5.1 Introduction

During diurnal observations of MMW backscattering of snow, the governing thermodynamics process within the snowpack usually leads to appreciable changes in the vertical profile of the volumetric moisture content, m_v, and in shapes and sizes of ice particles [19], [8], and [72]. For metamorphic snow the ice particles are usually rounded yet not spherical. Chang *et al.* [11] [66] treated snow particles as oblate spheroids with identical distribution and shape, yet only considered dry snow. In [60], Kuga *et al.* treated snow particles as spheres with diameters following the Gaussian distribution with mean diameter of 1 mm and standard deviation of 0.2 mm throughout the duration of the diurnal cycle, a treatment did not truthfully reflect the dynamic change of the particle size. Recently, the effect of snow crystal shape and orientation on the scattering of passive microwave radiation were addressed in [32] and [33].

Adding to the complexity, the snowpack is a dense medium at MMW, which raises a major issue on how to determine the effective propagation constant of the snow medium. Recent techniques such as QCA and QCA-CP [93] render inappropriate results because of their very assumptions that fail to accommodate the cases where a thin water film surrounds the ice particle for slightly wet snow or for wet snow when irregularities exist in the water drop shape, resulting from filling the gaps between the ice particles [19].

It is well established that for a Rayleigh spheroid, a closed-form expression for the volume absorption coefficient exists [93]. The calculation of the volume scattering coefficient, however, needs to take an additional two-fold integration over the scattered directions. Not only does it require considerably more computation, but more importantly the awkward presence of this additional integration obscures insight into the effect of the geometrical or dielectric parameters on the scattering behavior. These drawbacks are overcome in this chapter by establishing the symmetry in the representations of the volume absorption and scattering coefficients.

Moreover, any modeling effort that attempts to incorporate the snowpack thermodynamics information calls for an explicit approach to describe the dynamics in the vertical moisture distribution of m_v, in the shape and size of the ice particles, and in the thickness of the snow layer should a multilayer treatment be adopted. The rigorous way, which starts from the governing thermodynamic differential equations, is formidably complex and hence unrealistic, mostly due to the complex topological nature of the snowpack and frequently encountered incomplete ground truth information required for parameterizing these differential equations [19]. However, a physical process, like the underlying thermodynamics process in the snowpack, does not elicit abrupt change in topological structure or hydrological properties [38]. This gradually evolving nature makes it a reasonable treatment to linearize the incremental changes in m_v, particle size, and snow layer thickness.

This chapter is organized as follows. Section 5.2 provides a brief description of the thermodynamics of the snowpack pertinent to diurnal observation, and highlights some key issues in the modeling effort. Section 5.3 establishes the symmetry in the representation of the volume absorption and scattering coefficients, in addition to pointing out numerically efficient ways to calculate the phase matrix averaged over orientation. Concerns over the determination of the effective refractive index for the snowpack and for the background are addressed in Section 5.4. In section 5.5, comparisons between measurements and model predictions are provided to justify the new treatments introduced in this chapter.

5.2 Thermodynamics Governing the Diurnal Cycle

Since metamorphic snow has undergone several cycles of the meting-freezing process, the ice particles usually tend to get "rounded off", resulting in shapes notably different from fresh snow. Yet the "round off" bears less in the sense that the ice particles are spherical than that the corners dominant in fresh snow fade off [19]. It is then quite natural to approximate the ice particles as spheroids with some orientational distribution, an assumption held reasonably well at millimeter wavelengths where penetration of the electromagnetic wave within the snow pack is very limited, hence renders the severe irregularities in shape such as hoar or column, which usually occur deep in the snow pack [19], invisible to the scatterometer.

When snow melts, the melting starts from the top of the snow layer and the rate of melting is governed by the energy flux at the upper surface of the snowpack. The mechanisms involved include radiation, sensible and latent heat transfer, and heat transfer from within the snowpack. In general, the radiation dominates while all the other mechanisms are of secondary importance [19]. However, the low thermal conductivity of snow elicits a vertical temperature gradient within the snowpack, which in turn gives rise to a nonuniform vertical distribution of moisture [38]. Unless the snowpack is sufficiently dry or wet, this moisture profile cannot be ignored in studying the snow diurnal behavior.

If the melting process is looked at more closely, when it starts, the smaller grains disappear first [19]. Yet as what will be shown soon, the phase matrix and extinction coefficient of a Rayleigh spheroid, just like Rayleigh sphere, is proportional to a^3 where a is the minimum dimension of the spheroid, suggesting that the disappearance of the smaller grains is of no appreciable significance to the collective scattering behavior of the snowpack. Consequently, we can approximate the snow particle distribution as uniform with a single size equal to the smallest dimension of the largest size spheroid.

Soon thereafter with the presence of liquid water in the snowpack, a rapid metamorphic change takes place. The disappearance of the smaller grains accelerates, thus leads to the rapid reduction of their contribution to the capillary attraction by which the water is held in the snow matrix. The water is released suddenly once the grains disappear and a drainage is formed. [19]. A rapid drop in the backscattering coefficient is usually observed [102] [66].

As the snowpack starts from top layer downward to freeze, which occurs when the short-wave radiation, primarily from the sun or diffused by particles in the sky, drops quickly late in the afternoon, the long-wave radiation from the earth comes in to counterbalance or even surpass the former, resulting in a reverse of direction in the energy flux at the upper surface of the snowpack. Consequently, the snow cools off, with gradual decrease in m_v and increase in particle size [19]. Yet the best indicator of the underlying thermodynamics is the temperature, which faithfully reflects the energy flux dynamics [38]. Temperature measured in the air near the snow surface would be ideal, yet it is very difficult to obtain, as pointed out by Geiger [38], mostly due to the difficulty encountered in separating the radiation and the energy flow. Still, temperature will be used as the primary indicator in assisting the identification of different thermodynamic processes.

In summary, the snowpack, undergoing a thermodynamic process, possesses different characteristics, in particular with regard to the dynamics of size, shape, density and m_v distribution. This realization calls for the need for any scattering model of snow to reflect as faithfully as possible these dynamics in parameters describing the snowpack.

A treatment of such thermodynamic process for a specific diurnal observation, based on the collected ground truth, will be detailed in Section 5.5.

5.3 Iterative RTE 1^{st} order solution for spheroidal particles with uniform distribution

5.3.1 General Expression for the Radar Scattering Coefficient

In the previous section, the need to treat the snowpack as representative of the underlying thermodynamics as faithfully as possible for any diurnal observations was established. If the snowpack is thick and sufficiently dry or wet, treating it as a semi-infinite medium is a reasonably pertinent choice. In other cases, such as when snow stars to melt or freeze, depending on the vertical temperature gradient, and correspondingly the m_v distribution, we need to treat the snowpack as a multilayer medium accordingly.

Unlike in the last chapter where the numerical technique was used to solve the RTE for dry snow case, in this chapter the iterative technique will be used instead to avoid any potential numerical instability problem that might arise in the numerical technique.

Meanwhile, in the calculations of the phase matrix and extinction matrix, we will, in light of the work of Kendra *et al.* [57] where they pointed out that CRT appears to give a reasonable prediction of the backscatter from a dense media, use CRT techniques instead, except that we will provide some improvement over or reformulation of the conventional treatment when approapriate.

For quick reference, we first consider the formula for the backscattering coefficients of 1) a semi-infinite layer; 2) a layer above a second semi-infinite layer.

Semi-infinite medium

For a semi-infinite medium, the 0^{th} order solution for the specific intensity at direction $\hat{s}$ at position z is:

$$\mathbf{I}(\hat{\mathbf{s}}, z) = -e^{(-\boldsymbol{\kappa}_e z/\mu_0)}\mathbf{I}(\hat{\mathbf{s}}, 0)\delta(\hat{\mathbf{s}} - \hat{\mathbf{s}}_0) \tag{5.1}$$

and the 1^{st} order solution is [46]:

$$\mathbf{I}_1(\hat{s}, z) = \frac{1}{\mu_s} e^{(-\boldsymbol{\kappa}_e z/\mu_s)} \int_{-\infty}^{z} d\tau \; e^{\boldsymbol{\kappa}_e \tau/\mu_s} \, \mathbf{P}(\hat{s}, \hat{s}_0) \, e^{-\boldsymbol{\kappa}_e \tau/\mu_0} \, \mathbf{I}_0(\hat{s}_0, 0) \tag{5.2}$$

where $\hat{s}_0$ is the incident direction within the medium, $\mu_s = \cos(\theta)$, θ is the propagation angle within the medium.

If we assume m_v to be homogeneous throughout the snow layer, and the orientational distribution of scatterer to be identical and independent, then the corresponding backscattering coefficients are given by:

$$\begin{aligned}
\sigma^0_{vv} &= 4\pi \cos\theta_i \frac{P_{vv}(-\hat{\mathbf{s}}_0, \hat{\mathbf{s}}_0)}{\kappa_{ev}(-\hat{\mathbf{s}}_0) + \kappa_{ev}(\hat{\mathbf{s}}_0)} T_{12v} T_{21v} \\
\sigma^0_{vh} &= 4\pi \cos\theta_i \frac{P_{vh}(-\hat{\mathbf{s}}_0, \hat{\mathbf{s}}_0)}{\kappa_{ev}(-\hat{\mathbf{s}}_0) + \kappa_{eh}(\hat{\mathbf{s}}_0)} T_{12v} T_{21h}
\end{aligned}$$

$$\begin{aligned} \sigma^0_{hv} &= 4\pi\cos\theta_i \frac{P_{hv}(-\hat{\mathbf{s}}_0,\hat{\mathbf{s}}_0)}{\kappa_{eh}(-\hat{\mathbf{s}}_0)+\kappa_{ev}(\hat{\mathbf{s}}_0)} T_{12h}T_{21v} \\ \sigma^0_{hh} &= 4\pi\cos\theta_i \frac{P_{hh}(-\hat{\mathbf{s}}_0,\hat{\mathbf{s}}_0)}{\kappa_{eh}(-\hat{\mathbf{s}}_0)+\kappa_{eh}(\hat{\mathbf{s}}_0)} T_{12h}T_{21h} \end{aligned} \tag{5.3}$$

where θ_i is the incidence angle, $T_{12p}, p = v, h$ is the transmissivity from medium 2 to medium 1 for polarization p, and $T_{21p}, p = v, h$, is the transmissivity for propagation from medium 1 to medium 2.

For a spherical scatterer, $P_{vh}(-\hat{\mathbf{s}}_0, \hat{\mathbf{s}}) = P_{hv}(-\hat{\mathbf{s}}_0, \hat{\mathbf{s}}) = 0$. Hence, $\sigma^0_{vh} = \sigma^0_{hv} = 0$ for the 1^{st} order solution.

The above formulas can be further simplified if the scatterer has axial symmetry, which would imply $\kappa_{ep}(\hat{s}) = \kappa_{ep}(-\hat{s})$, $p = v, h$. In that case,

$$\begin{aligned} \sigma^0_{vv} &= 2\pi\cos\theta_i \frac{P_{vv}(-\hat{\mathbf{s}}_0,\hat{\mathbf{s}}_0)}{\kappa_{ev}(\hat{\mathbf{s}}_0)} T_{12v}T_{21v} \\ \sigma^0_{vh} &= 2\pi\cos\theta_i \frac{P_{vh}(-\hat{\mathbf{s}}_0,\hat{\mathbf{s}}_0)}{\kappa_{eh}(\hat{\mathbf{s}}_0)} T_{12v}T_{21h} \\ &= \sigma^0_{hv} \\ \sigma^0_{hh} &= 2\pi\cos\theta_i \frac{P_{hh}(-\hat{\mathbf{s}}_0,\hat{\mathbf{s}}_0)}{\kappa_{eh}(\hat{\mathbf{s}}_0)} T_{12h}T_{21h} \end{aligned} \tag{5.4}$$

Homogeneous layer above a semi-infinite medium

For a layer of thickness d with flat boundary, the backscattering coefficients due to the bounded layer are [61]:

$$\begin{aligned} \sigma^0_{vv} &= 4\pi\cos\theta_i\; I_{vv,b}\; \frac{T_{12v}T_{21v}}{1-R_{21v}R_{23v}} \\ \sigma^0_{vh} &= 4\pi\cos\theta_i\; I_{vh,b}\; \frac{T_{12v}T_{21h}}{1-R_{21h}R_{23h}} \\ \sigma^0_{hv} &= 4\pi\cos\theta_i\; I_{hv,b}\; \frac{T_{12h}T_{21v}}{1-R_{21v}R_{23v}} \\ \sigma^0_{hh} &= 4\pi\cos\theta_i\; I_{hh,b}\; \frac{T_{12h}T_{21h}}{1-R_{21h}R_{23h}} \end{aligned} \tag{5.5}$$

where R_{21p}, $p = v, h$, refers to the reflectivity at the upper boundary of the bounded layer, R_{23p}, $p = v, h$, refers to the reflectivity at the lower boundary of the bounded layer, and

$$\begin{aligned} I_{pq,b} \;=\;& \frac{P_{pq}(-\hat{\mathbf{s}}_0,\hat{\mathbf{s}}_0)}{\kappa_{ep}(-\hat{\mathbf{s}}_0)+\kappa_{eq}(\hat{\mathbf{s}}_0)}(1-e^{(-(\kappa_{ep}(-\hat{\mathbf{s}}_0)+\kappa_{eq}(\hat{\mathbf{s}}_0))d/\cos\theta)}) \\ &+\frac{1}{\cos\theta}P_{pq}(-\hat{\mathbf{s}}_0,\hat{\mathbf{s}}_0)dR_{23p}e^{(-\kappa_{eq}(-\hat{\mathbf{s}}_0)d/\cos\theta)} \\ &+\frac{1}{\cos\theta}P_{pq}(-\hat{\mathbf{s}}_0,\hat{\mathbf{s}}_0)dR_{23q}e^{(-\kappa_{ep}(\hat{\mathbf{s}}_0)d/\cos\theta)} \\ &+P_{pq}(-\hat{\mathbf{s}}_0,\hat{\mathbf{s}}_0)R_{23p}R_{23q}e^{(-(\kappa_{ep}(-\hat{\mathbf{s}}_0)+\kappa_{eq}(\hat{\mathbf{s}}_0))d/\cos\theta)})\frac{1-e^{(-(\kappa_{ep}(-\hat{\mathbf{s}}_0)+\kappa_{eq}(\hat{\mathbf{s}}_0))d/\cos\theta)}}{\kappa_{ep}(-\hat{\mathbf{s}}_0)+\kappa_{eq}(\hat{\mathbf{s}}_0)} \end{aligned} \tag{5.6}$$

where $p, q = v, h$.

5.3.2 Establishing Symmetry Between $\kappa_{ap}(\hat{s})$ And $\kappa_{sp}(\hat{s})$

For a Rayleigh spheroid, the volume absorption coefficient $\kappa_{ap}(\hat{s})$ along the wave propagation direction $\hat{\mathbf{s}}$ enjoys a very simple expression [93], which is not the case for the volume scattering coefficient $\kappa_{sp}(\hat{s})$ in the conventional representation. As will be shown soon, the conventional $\kappa_{sp}(\hat{s})$ formula is not complete, which leads to two major drawbacks that can be overcome by treating $\kappa_{sp}(\hat{s})$ further. This new treatment is the subject of this subsection.

To start, a brief summary of the formulation for the volume absorption coefficient is provided, whose specific form will serve as a benchmark against which a new analogous expression for the volume scattering coefficient will be derived.

Volume Absorption Coefficient

The volume absorption coefficient for a medium of ice particles of spheroidal shape is given by [93],

$$\kappa_{ap}(\hat{s}) = n_0 \int_0^{2\pi} d\alpha \int_0^{\pi} d\beta \int_0^{2\pi} d\gamma p(\alpha,\beta,\gamma)\sigma_{ap}(\theta_i,\phi_i;\alpha,\beta,\gamma) \tag{5.7}$$

where, n_0 is the number density (number of particles per unit volume) of the ice particle, α, β and γ are the canonical Eulerian angles, $p(\alpha,\beta,\gamma)$ is the joint probability density function of the Eulerian angles, and $\sigma_{ap}(\theta_i, \phi_i; \alpha, \beta, \gamma)$ is the absorption cross section at the wave incident direction (θ_i, ϕ_i) of an individual particle which is given by:

$$\sigma_{ap} = \nu_0 k \frac{\epsilon_s''}{\epsilon} [\frac{(\hat{p} \cdot \hat{x}_b)^2}{|1 + \nu_d A_a|^2} + \frac{(\hat{p} \cdot \hat{y}_b)^2}{|1 + \nu_d A_b|^2} + \frac{(\hat{p} \cdot \hat{z}_b)^2}{|1 + \nu_d A_c|^2}] \tag{5.8}$$

where ν_0 is the volume of the spheroidal scatterer, k is the wave number of the background, ϵ is the dielectric constant of the background, ϵ_s'' is the imaginary part of the dielectric constant ϵ_s of the spheroidal scatterer, $\hat{x}_b, \hat{y}_b$ and $\hat{z}_b$ are the natural axes of such spheroidal scatterer governing the surface equation:

$$\frac{x_b^2}{a^2} + \frac{y_b^2}{b^2} + \frac{z_b^2}{c^2} = 1 \tag{5.9}$$

and A_a, A_b, A_c are defined as:

$$\begin{aligned} A_a &= \int_0^\infty \frac{ds}{(s + a^2) R_s} \\ A_b &= \int_0^\infty \frac{ds}{(s + b^2) R_s} \\ A_c &= \int_0^\infty \frac{ds}{(s + c^2) R_s} \\ R_s &= [(s + a^2)(s + b^2)(s + c^2)]^{1/2} \end{aligned} \tag{5.10}$$

Volume Scattering Coefficient

For the same medium of ice particles of spheroidal shape, the volume scattering coefficient is given by [93]:

$$\kappa_{sp}(\hat{s}) = \iint_{4\pi} d\Omega_s (P_{pp}(\theta_s, \phi_s; \theta_i, \phi_i) + P_{qp}(\theta_s, \phi_s; \theta_i, \phi_i)) \tag{5.11}$$

where the phase matrix P_{qp} is given by:

$$P_{qp}(\theta_s, \phi_s; \theta_i, \phi_i) = n_0 \int_0^{2\pi} d\alpha \int_0^{\pi} d\beta \int_0^{2\pi} d\gamma p(\alpha, \beta, \gamma) |f_{qp}(\theta_s, \phi_s; \theta_i, \phi_i)|^2 \tag{5.12}$$

and $f_{qp}(\theta_s, \phi_s; \theta_i, \phi_i)$ is the scattering function for p-polarization of the incident wave and q-polarization for the scattered wave. Note that f_{qp} is related to the scattering function dyad $\overline{\overline{F}}$ by $f_{qp} = \hat{q} \cdot \overline{\overline{F}} \cdot \hat{p}$. The latter is

$$\overline{\overline{F}} = \frac{k^2}{4\pi}\nu_0\frac{\epsilon_s - \epsilon}{\epsilon}\{\frac{\hat{x}_b\hat{x}_b}{1+\nu_d A_a} + \frac{\hat{y}_b\hat{y}_b}{1+\nu_d A_b} + \frac{\hat{z}_b\hat{z}_b}{1+\nu_d A_c}\} \tag{5.13}$$

However, the representation for $\kappa_{sp}(\hat{s})$ using Eq. 5.11 is not complete in the sense that, of the two constituent parts of $\kappa_{ep}(\hat{s})$, the volume absorption coefficient $\kappa_{ap}(\hat{s})$ requires averaging over orientation, which is done via a three-fold integration over the Eulerian angles, while the scattering coefficient $\kappa_{sp}(\hat{s})$ demands averaging over both orientation and scattering directions, which is via a five-fold integration. Such lack of symmetry bears two major drawbacks for $\kappa_{sp}(\hat{s})$:

1. It is more computationally intensive;
2. More importantly, it conceals the interplay among the geometrical and dielectric variables.

Fortunately these drawbacks are artificial and can be overcome by carrying out Eq. 5.11 further so as to achieve a formulation similar to Eq. 5.7 for $\kappa_{sp}(\hat{s})$. To do so, we interchange the integration over the Eulerian angles and the scattered direction, and take advantage of the structure of the scattering function dyad $\overline{\overline{F}}$ for a Rayleigh ellipsoid. The idea is to seek an efficient factorization of the integrand such that the terms related to the scattered direction will be singled out and grouped together so as to perform integration over the scattered direction only on these terms. This approach we propose here is a new extension to Whitt's polarization tensor method [113], where his focus was on the efficient calculation of the averaging process when calculating the phase matrix, which we will elaborate a bit more on in the next subsection.

This proposed mathematically-involved process is best illustrated by explaining the vv-polarized volume scattering coefficient κ_{sv}.

We will start by considering P_{vv}. Let

$$\begin{aligned} A_x &= \frac{k^2}{4\pi}\nu_0\frac{\epsilon_s-\epsilon}{\epsilon}\frac{(\hat{x}_b\cdot\hat{v}_i)}{1+\nu_d A_a} \\ A_y &= \frac{k^2}{4\pi}\nu_0\frac{\epsilon_s-\epsilon}{\epsilon}\frac{(\hat{y}_b\cdot\hat{v}_i)}{1+\nu_d A_b} \\ A_z &= \frac{k^2}{4\pi}\nu_0\frac{\epsilon_s-\epsilon}{\epsilon}\frac{(\hat{z}_b\cdot\hat{v}_i)}{1+\nu_d A_c} \end{aligned} \tag{5.14}$$

It follows from Eq. 5.13 and 5.14 that

$$\begin{aligned} |\, f_{vv}(\theta_s,\phi_s;\theta_i,\phi_i)\,|^2 &= f_{vv}(\theta_s,\phi_s;\theta_i,\phi_i)f^*_{vv}(\theta_s,\phi_s;\theta_i,\phi_i) \\ &= [(\hat{v}_s\cdot\hat{x}_b)A_x+(\hat{v}_s\cdot\hat{y}_b)A_y+(\hat{v}_s\cdot\hat{z}_b)A_z]\times \\ &\quad [(\hat{v}_s\cdot\hat{x}_b)A^*_x+(\hat{v}_s\cdot\hat{y}_b)A^*_y+(\hat{v}_s\cdot\hat{z}_b)A^*_z] \end{aligned} \tag{5.15}$$

Noting that the inner product can also be written as $(\overline{u}\cdot\overline{v}=\overline{u}^t\overline{v})$, where $\overline{u}$ and $\overline{v}$ are arbitrary column vectors and the superscript denotes transpose, it follows from Eq. 5.15 that

$$|\, f_{vv}(\theta_s,\phi_s;\theta_i,\phi_i)\,|^2=\begin{bmatrix} A_x & A_y & A_z \end{bmatrix}\begin{bmatrix} \hat{x}^t_b \\ \hat{y}^t_b \\ \hat{z}^t_b \end{bmatrix}(\hat{v}_s\hat{v}^t_s)\begin{bmatrix} \hat{x}_b & \hat{y}_b & \hat{z}_b \end{bmatrix}\begin{bmatrix} A^*_x \\ A^*_y \\ A^*_z \end{bmatrix} \tag{5.16}$$

The above equation contains three types of variables: 1) those related only to orientation, such as $\hat{x}_b$, $\hat{y}_b$ and $\hat{z}_b$; 2) those related to the geometry, the dielectric property of the scatterer and its orientation, and the incidence direction, such as A_x, A_y and A_z; 3) those related only to scattered direction, such as the term $(\hat{v}_s\hat{v}^t_s)$, a 3×3 matrix well factored out in this equation. It follows that when integration over the scattered direction is applied on the right hand side of Eq. 5.16, it is applied directly on the $(\hat{v}_s\hat{v}^t_s)$ term.

Using $\hat{v}^t_s=[\cos\theta_s\cos\phi_s,\cos\theta_s\sin\phi_s,-\sin\theta_s]$, the following integration is readily carried out:

$$\iint_{4\pi} d\Omega_s(\hat{v}_s\hat{v}_s^t) = \pi \begin{pmatrix} \frac{2}{3} & 0 & 0 \\ 0 & \frac{2}{3} & 0 \\ 0 & 0 & \frac{8}{3} \end{pmatrix} \tag{5.17}$$

Similarly, using $\hat{h}_s^t = [-\sin\phi_s, \cos\phi_s, 0]$,

$$\iint_{4\pi} d\Omega_s(\hat{h}_s\hat{h}_s^t) = \pi \begin{pmatrix} 2 & 0 & 0 \\ 0 & 2 & 0 \\ 0 & 0 & 0 \end{pmatrix} \tag{5.18}$$

Upon combining Eq. 5.11 and 5.12 and interchanging the integration order over the Eulerian angle and the scattered direction, and utilizing Eq. 5.17 and 5.18 yields

$$\begin{aligned}
\kappa_{sp}(\hat{s}) &= \iint_{4\pi} d\Omega_s n_0 \int_0^{2\pi} d\alpha \int_0^{\pi} d\beta \int_0^{2\pi} d\gamma p(\alpha,\beta,\gamma) \begin{bmatrix} A_x & A_y & A_z \end{bmatrix} \begin{bmatrix} \hat{x}_b^t \\ \hat{y}_b^t \\ \hat{z}_b^t \end{bmatrix} \\
&\quad (\hat{v}_s\hat{v}_s^t + \hat{h}_s\hat{h}_s^t) \begin{bmatrix} \hat{x}_b & \hat{y}_b & \hat{z}_b \end{bmatrix} \begin{bmatrix} A_x^* \\ A_y^* \\ A_z^* \end{bmatrix} \\
&= n_0 \int_0^{2\pi} d\alpha \int_0^{\pi} d\beta \int_0^{2\pi} d\gamma p(\alpha,\beta,\gamma) \begin{bmatrix} A_x & A_y & A_z \end{bmatrix} \begin{bmatrix} \hat{x}_b^t \\ \hat{y}_b^t \\ \hat{z}_b^t \end{bmatrix} \\
&\quad \iint_{4\pi} d\Omega_s(\hat{v}_s\hat{v}_s^t + \hat{h}_s\hat{h}_s^t) \begin{bmatrix} \hat{x}_b & \hat{y}_b & \hat{z}_b \end{bmatrix} \begin{bmatrix} A_x^* \\ A_y^* \\ A_z^* \end{bmatrix} \\
&= n_0 \frac{8}{3}\pi \int_0^{2\pi} d\alpha \int_0^{\pi} d\beta \int_0^{2\pi} d\gamma p(\alpha,\beta,\gamma) \begin{bmatrix} A_x & A_y & A_z \end{bmatrix}
\end{aligned}$$

$$\begin{bmatrix} \hat{x}_b^t \\ \hat{y}_b^t \\ \hat{z}_b^t \end{bmatrix} \begin{bmatrix} \hat{x}_b & \hat{y}_b & \hat{z}_b \end{bmatrix} \begin{bmatrix} A_x^* \\ A_y^* \\ A_z^* \end{bmatrix} \tag{5.19}$$

Noting that the middle term $\begin{bmatrix} \hat{x}_b^t \\ \hat{y}_b^t \\ \hat{z}_b^t \end{bmatrix} \begin{bmatrix} \hat{x}_b & \hat{y}_b & \hat{z}_b \end{bmatrix}$ in the above equation is just the identity matrix, we can further simplify the above to

$$\begin{aligned} \kappa_{sp}(\hat{s}) &= n_0 \frac{8}{3}\pi \int_0^{2\pi} d\alpha \int_0^{\pi} d\beta \int_0^{2\pi} d\gamma p(\alpha,\beta,\gamma)(|A_x|^2 + |A_y|^2 + |A_z|^2) \\ &= n_0 \int_0^{2\pi} d\alpha \int_0^{\pi} d\beta \int_0^{2\pi} d\gamma p(\alpha,\beta,\gamma)\sigma_{sp}(\theta_i,\phi_i;\alpha,\beta,\gamma) \end{aligned} \tag{5.20}$$

where we define

$$\begin{aligned} \sigma_{sp} &= \frac{8}{3}\pi[|A_x|^2 + |A_y|^2 + |A_z|^2] \\ &= \nu_i \nu_0 \frac{k^4}{6\pi}|\frac{\epsilon_s - \epsilon}{\epsilon}|^2 [\frac{(\hat{p}\cdot\hat{x}_b)^2}{|1+\nu_d A_a|^2} + \frac{(\hat{p}\cdot\hat{y}_b)^2}{|1+\nu_d A_b|^2} + \frac{(\hat{p}\cdot\hat{z}_b)^2}{|1+\nu_d A_c|^2}] \end{aligned} \tag{5.21}$$

as the scattering cross section of an individual particle, in correspondence to Eq. 5.8. In the above equation, ν_i is the volumetric fraction.

Now we can fully appreciate the symmetry between $\kappa_{ap}(\hat{s})$ and $\kappa_{sp}(\hat{s})$ as represented by Eq. 5.7 and Eq. 5.20, respectively. Moreover, Eq. 5.20 leads to a much simpler, yet more revealing, expression for the extinction cross section:

$$\sigma_{ep} = (\nu_i k \frac{\epsilon_s''}{\epsilon} + \nu_i \nu_0 \frac{k^4}{6\pi}|\frac{\epsilon_s - \epsilon}{\epsilon}|^2)[\frac{(\hat{p}\cdot\hat{x}_b)^2}{|1+\nu_d A_a|^2} + \frac{(\hat{p}\cdot\hat{y}_b)^2}{|1+\nu_d A_b|^2} + \frac{(\hat{p}\cdot\hat{z}_b)^2}{|1+\nu_d A_c|^2}] \tag{5.22}$$

through which, the extinction coefficient is determined by:

$$\kappa_{ep}(\hat{s}) = n_0 \int_0^{2\pi} d\alpha \int_0^{\pi} d\beta \int_0^{2\pi} d\gamma p(\alpha,\beta,\gamma)\sigma_{ep}(\theta_i,\phi_i;\alpha,\beta,\gamma) \tag{5.23}$$

The volume scattering coefficient of a medium of Rayleigh spheres is special case of Eq. 5.20. For such medium, the scattering, absorption and extinction coefficients are directly proportional to the scattering, absorption and extinction cross sections, respectively, because there is no Eulerian angle dependence for a sphere. Upon using $A_a = A_b = A_c = \frac{2}{3a^3}$ in Eq. 5.21 and Eq. 5.20, it yields

$$\kappa_{sp}(\hat{s}) = \frac{8\pi}{3}\nu_0 k^4 a^6 \left| \frac{\epsilon_s - \epsilon}{\epsilon_s + 2\epsilon} \right|^2 \tag{5.24}$$

which is just the well known $\kappa_{sp}(\hat{s})$ formula for a medium containing Rayleigh spheres.

To illustrate the computational efficiency of our proposed method to calculate the volume extinction coefficient, on a Sun Sparc workstation with operating system Solaris 2.7.1, it takes 0.4 second for our formulation, while it takes much longer time for the original formulation depending on the discretization configuration if the discrete ordinate Gaussian quadrature method is used to perform the integration. For example, if we choose 14 discrete ordinates for θ_s and 37 discrete ordinates for ϕ_s in Eq. 5.11, then it takes around 3 minutes and 20 seconds for such calculation. Such computational advantage of our approach will be more pronounced shall the numerical technique is used for RTE when appropriate, since then the same computation needs to be repeated for each discretized incident wave direction.

5.3.3 Numerically Efficient Method to Calculate the Average Phase Matrix

In this section, we formulate the procedure to facilitate the averaging of the phase matrix over the Eulerian angles, in accordance with the polarization tensor method proposed by Whitt [113], yet in a more compact and convenient form.

We start by restructuring $f_{pq}(\theta_s, \phi_s; \theta_i, \phi_i)$. For simplicity, we first define some new terms as follows: $C_k = \frac{k^2}{4\pi}\nu_0 \frac{\epsilon_s - \epsilon}{\epsilon}$, $A_1 = 1 + \nu_d A_a, A_2 = 1 + \nu_d A_b$, and $A_3 = 1 + \nu_d A_c$. The scattering matrix for one particle oriented with angles α, β, γ in

Eq. 5.13 becomes:

$$\begin{aligned} f_{pq}(\theta_s,\phi_s;\theta_i,\phi_i) &= C_k(\frac{(\hat{p}\cdot\hat{x}_b)(\hat{x}_b\cdot\hat{q})}{A_1}+\frac{(\hat{p}\cdot\hat{y}_b)(\hat{y}_b\cdot\hat{q})}{A_2}+\frac{(\hat{p}\cdot\hat{z}_b)(\hat{z}_b\cdot\hat{q})}{A_3}) \\ &= C_k\hat{p}^t(\frac{\hat{x}_b\hat{x}_b^t}{A_1}+\frac{\hat{y}_b\hat{y}_b^t}{A_2}+\frac{\hat{z}_b\hat{z}_b^t}{A_3})\hat{q} \\ &= C_k\underline{Q}^t_{pq}\underline{R} \qquad (5.25) \end{aligned}$$

where

$$\underline{Q}^t_{pq} = \left[\begin{array}{ccccccccc} p_1q_1 & p_1q_2 & p_1q_3 & p_2q_1 & p_2q_2 & p_2q_3 & p_3q_1 & p_3q_2 & p_3q_3 \end{array}\right] \qquad (5.26)$$

and

$$\underline{R} = \left[\begin{array}{c} \frac{x_{b1}x_{b1}}{A_1}+\frac{y_{b1}y_{b1}}{A_2}+\frac{z_{b1}z_{b1}}{A_3} \\ \frac{x_{b1}x_{b2}}{A_1}+\frac{y_{b1}y_{b2}}{A_2}+\frac{z_{b1}z_{b2}}{A_3} \\ \frac{x_{b1}x_{b3}}{A_1}+\frac{y_{b1}y_{b3}}{A_2}+\frac{z_{b1}z_{b3}}{A_3} \\ \frac{x_{b2}x_{b1}}{A_1}+\frac{y_{b2}y_{b1}}{A_2}+\frac{z_{b2}z_{b1}}{A_3} \\ \frac{x_{b2}x_{b2}}{A_1}+\frac{y_{b2}y_{b2}}{A_2}+\frac{z_{b2}z_{b2}}{A_3} \\ \frac{x_{b2}x_{b3}}{A_1}+\frac{y_{b2}y_{b3}}{A_2}+\frac{z_{b2}z_{b3}}{A_3} \\ \frac{x_{b3}x_{b1}}{A_1}+\frac{y_{b3}y_{b1}}{A_2}+\frac{z_{b3}z_{b1}}{A_3} \\ \frac{x_{b3}x_{b2}}{A_1}+\frac{y_{b3}y_{b2}}{A_2}+\frac{z_{b3}z_{b2}}{A_3} \\ \frac{x_{b3}x_{b3}}{A_1}+\frac{y_{b3}y_{b3}}{A_2}+\frac{z_{b3}z_{b3}}{A_3} \end{array}\right]$$

In view of the above, it is obvious that $\underline{Q}_{pq}$ is solely related to polarization, while $\underline{R}$ contains information regarding orientation, geometry and dielectric property.

Taking advantage of the new representation for f_{pq} as in Eq. 5.25, we apply conjugate square to both sides of Eq. 5.13 to obtain:

$$|\,f_{pq}(\theta_s,\phi_s;\theta_i,\phi_i)\,|^2 = |\,C_k\,|^2\underline{Q}^t_{pq}\underline{RR}^\sharp\underline{Q}_{pq} \qquad (5.27)$$

where $\sharp$ denotes the conjugate transpose.

Using $|f_{pq}|^2$ in Eq. 5.27, to calculate the average phase matrix according to Eq. (5.12), orientational averaging will be carried out upon some as opposed to all terms of $\underline{RR}^\sharp$, giving rise to another dimension of saving computation. The reason is that, for the problem at hand, regardless of whether we are considering monostatic or bistatic scattering, we are interested in the case where $\phi_s = \pi + \phi_i$, which makes $\underline{Q}_{pq}$ a sparse vector as we shall soon see. Consequently, we only need to average over the terms in $\underline{RR}^\sharp$ as necessary.

For instance, substituting of Eq. (5.26) for v_s and v_i into $\underline{Q}_{pq}$ yields

$$\underline{Q}_{vv} = \begin{bmatrix} \cos\theta_s \cos\theta_i \cos\phi_s \cos\phi_i \\ \cos\theta_s \cos\theta_i \cos\phi_s \sin\phi_i \\ -\cos\theta_s \sin\theta_i \cos\phi_s \\ \cos\theta_s \cos\theta_i \sin\phi_s \cos\phi_i \\ \cos\theta_s \cos\theta_i \sin\phi_s \sin\phi_i \\ -\cos\theta_s \sin\theta_i \sin\phi_s \\ -\sin\theta_s \cos\theta_i \cos\phi_i \\ -\sin\theta_s \cos\theta_i \sin\phi_i \\ \sin\theta_s \sin\theta_i \end{bmatrix}$$

For the backscattering direction, $\theta_s = \pi - \theta_i, \phi_s = \pi + \phi_i$. Without loss of generality, let $\phi_i = 0$. Then,

$$\underline{Q}_{vv} = \begin{bmatrix} \cos\theta_i{}^2 \\ 0 \\ -\cos\theta_i \sin\theta_i \\ 0 \\ 0 \\ 0 \\ -\cos\theta_i \sin\theta_i \\ 0 \\ \sin\theta_i{}^2 \end{bmatrix}$$

indicating that only 10 terms of $\underline{RR}^\sharp$, rather than 81, need orientational averaging. This is because:

$$\begin{aligned} \underline{Q}_{vv}^t \underline{RR}^\sharp \underline{Q}_{vv} &= \cos\theta_i{}^4 |\,(\underline{RR}^\sharp)_{11}\,|^2 - 2\cos\theta_i{}^3 \sin\theta_i Re((\underline{RR}^\sharp)_{13} + (\underline{RR}^\sharp)_{17}) \\ &+ \cos\theta_i{}^2 \sin\theta_i{}^2 (|\,(\underline{RR}^\sharp)_{33}\,|^2 |\,(\underline{RR}^\sharp)_{77}\,|^2 + 2Re((\underline{RR}^\sharp)_{37} + (\underline{RR}^\sharp)_{19})) \\ &- 2\cos\theta_i \sin\theta_i{}^3 Re((\underline{RR}^\sharp)_{39} + (\underline{RR}^\sharp)_{79}) + \sin\theta_i{}^4 \end{aligned} \tag{5.28}$$

Similarly,

$$\underline{Q}_{hv}^t = \begin{bmatrix} 0 & 0 & 0 & -\cos\theta_i & 0 & \sin\theta_i & 0 & 0 & 0 \end{bmatrix}$$

$$\underline{Q}_{vh}^t = \begin{bmatrix} 0 & \cos\theta_i & 0 & 0 & 0 & 0 & 0 & -\sin\theta_i & 0 \end{bmatrix}$$

and

$$\underline{Q}_{hh}^t = \begin{bmatrix} 0 & 0 & 0 & 0 & -1 & 0 & 0 & 0 & 0 \end{bmatrix}$$

Orientational averaging is much simpler for $\kappa_{ep}(\hat{s})$, thanks to the previous manipulation. As evident in Eq. (5.23) and Eq. (5.22), the only 9 terms needing orientation averaging are the diagonal terms of $\underline{RR}^\sharp$.

For illustration purposes, the above newly derived results for the volume scattering coefficients and the average phase matrix are specified in the next section.

5.3.4 Numerical Illustration

In this illustration, the Eulerian angles are assumed to follow a uniform joint distribution. For $\underline{RR}^\sharp$ in Eq. 5.27, the following results are readily obtained:

$$\begin{aligned}
<(\underline{RR}^\sharp)_{11}> &= \frac{3|A_1|^2+4Re(A_1A_3^*)+8|A_3|^2}{15|A_1A_3|^2} \\
<(\underline{RR}^\sharp)_{13}> &= 0 \\
<(\underline{RR}^\sharp)_{17}> &= 0 \\
<(\underline{RR}^\sharp)_{19}> &= \frac{|A_1|^2+8Re(A_1A_3^*)+6|A_3|^2}{15|A_1A_3|^2} \\
<(\underline{RR}^\sharp)_{33}> &= \frac{|A_1-A_3|^2}{15|A_1A_3|^2} \\
<(\underline{RR}^\sharp)_{37}> &= \frac{|A_1-A_3|^2}{15|A_1A_3|^2} \\
<(\underline{RR}^\sharp)_{39}> &= 0 \qquad (5.29) \\
<(\underline{RR}^\sharp)_{77}> &= \frac{|A_1-A_3|^2}{15|A_1A_3|^2} \\
<(\underline{RR}^\sharp)_{79}> &= 0 \\
<(\underline{RR}^\sharp)_{99}> &= \frac{3|A_1|^2+4Re(A_1A_3^*)+8|A_3|^2}{15|A_1A_3|^2} \qquad (5.30)
\end{aligned}$$

Using the above results, for the monostatic case, the average phase matrix for VV is calculated through Eq. 5.12 and 5.27:

$$P_{vv}^m = |C_k|^2\frac{3|A_1|^2+4Re(A_1A_3^*)+8|A_3|^2}{15|A_1A_3|^2} \qquad (5.31)$$

Similarly, for other polarization combinations,

$$\begin{aligned}
P_{vh}^m &= \frac{|C_k|^2}{15}\left|\frac{1}{A_1}-\frac{1}{A_3}\right|^2 \\
P_{hv}^m &= \frac{|C_k|^2}{15}\left|\frac{1}{A_1}-\frac{1}{A_3}\right|^2
\end{aligned}$$

$$P_{hh}^{m} = |C_k|^2 \frac{3|A_1|^2 + 4Re(A_1 A_3^*) + 8|A_3|^2}{15|A_1 A_3|^2} \tag{5.32}$$

where the superscript m stands for monostatic.

For the bistatic case with the scattering direction being specified as $\theta_s = \pi - \theta_i, \phi_s = \pi + \phi_i$, the average phase matrix are:

$$\begin{aligned}
P_{vv}^{b} &= |C_k|^2 \frac{3|A_1|^2 + 4Re(A_1 A_3^*) + 8|A_3|^2}{15|A_1 A_3|^2} cos^2(\theta_i + \theta_s) \\
&\quad + \frac{|C_k|^2}{15} \left| \frac{1}{A_1} - \frac{1}{A_3} \right|^2 (cos^2\theta_i + cos^2\theta_s) \\
P_{vh}^{b} &= \frac{|C_k|^2}{15} \left| \frac{1}{A_1} - \frac{1}{A_3} \right|^2 \\
P_{hv}^{b} &= \frac{|C_k|^2}{15} \left| \frac{1}{A_1} - \frac{1}{A_3} \right|^2 \\
P_{hh}^{b} &= |C_k|^2 \frac{3|A_1|^2 + 4Re(A_1 A_3^*) + 8|A_3|^2}{15|A_1 A_3|^2}
\end{aligned} \tag{5.33}$$

where the superscript b stands for bistatic.

Moreover, the extinction coefficients in Eq. 5.23 have the following expression after integration over the Eulerian angles:

$$\begin{aligned}
\kappa_{ev} &= (\nu_i k \frac{\epsilon_s''}{\epsilon} + \nu_i \nu_0 \frac{k^4}{6\pi} \left| \frac{\epsilon_s - \epsilon}{\epsilon} \right|^2)(\frac{2}{3|1 + \nu_d A_a|^2} + \frac{1}{3|1 + \nu_d A_c|^2}) \\
\kappa_{eh} &= (\nu_i k \frac{\epsilon_s''}{\epsilon} + \nu_i \nu_0 \frac{k^4}{6\pi} \left| \frac{\epsilon_s - \epsilon}{\epsilon} \right|^2)(\frac{2}{3|1 + \nu_d A_a|^2} + \frac{1}{3|1 + \nu_d A_c|^2})
\end{aligned} \tag{5.34}$$

The above clearly shows that $\kappa_{ev} = \kappa_{eh}$, which is consistent with what our intuition would suggest for a medium of Rayleigh spheroidal particles with uniform orientation distribution.

The extinction coefficient κ_{ev} and the average phase matrix term P_{vv} for both monostatic and bistatic scattering as functions of m_v are shown in Figure 5.1 for a medium of snow particles assuming typical values of radius $a = 0.3$ mm and elongation ratio $l = 3$. From Figure 5.1 it is clear that κ_{ev} increases rapidly with m_v, while P_{vv} is a very gentle function of m_v.

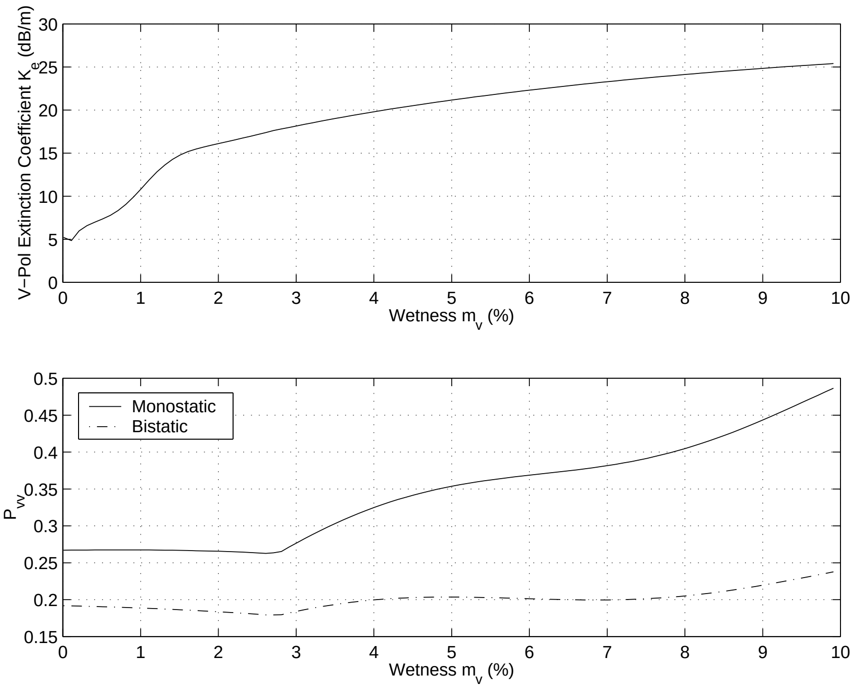

Figure 5.1: The extinction coefficient κ_{ev} and the average phase matrix term P_{vv} for both monostatic and bistatic scattering as functions of m_v. For the bistatic case, the scattering direction is specified as $\theta_s = \pi - \theta_i, \phi_s = \pi + \phi_i$. Snow particle has radius $a = 0.3$ mm and elongation ratio $l = 3$. In the calculation, f=35 GHz, $\theta_i = 86°$.

5.4 The Effective Index of Refraction of the Snow Layer and Background

The equivalent index of refraction n_2 of the snow layer will play a crucial role in the behavior of electromagnetic waves in the snow layer, as it will determine the principal propagation direction in the layer, the attenuation rate, as well as the reflectivity and transmissivity at the applicable boundaries. An accurate and universal model of n_2, a quite natural and logical requirement as it seems, remains an open question, largely due to the complicated nature of the geometry of the constituents, which include ice particles, water droplets and air bubbles, and their relative positions, as well as the electromagnetic interaction among them. Whatever model is chosen it has to conform to the following set of requirements: (1) the magnitude of the imaginary part of the calculated equivalent index of refraction n_2 must be a monotonously increasing function of m_v, which simply reflects the fact that higher extinction rates are associated with higher levels of water content; (2) good agreement between the calculated equivalent index of refraction n_2 and the applicable experimental data for extinction; and (3) the calculated equivalent index of refraction n_2 must exhibit a dependence on the geometry of the constituents. Condition (3) is based on the fact that the imaginary part of n_2 is associated with the extinction coefficient, which is at least dependent on the size of the snow particle [42].

Keeping this set of requirements in mind, we can evaluate the most popular models encountered in the literature, among which are (1) QCA [93], (2) Debye-like model [105], and (3) Modified Debye model [105]. We found, quite disappointingly, that none of these models satisfies the above three requirements simultaneously. For example, QCA violates requirement (1), showing the opposite trend with increasing m_v [60]; while neither the Debye-like model nor the modified Debye model include a dependence on the geometry of the snow [105]. A compromise has to be made here to choose a model. Considering that our intended task is to model the backscattering behavior of moderately wet snow, the QCA approach is not a favorable candidate because it has a tendency to mislead the calculation of the extinction rate. The Debye-like or modified Debye model, on the other hand, can provide us the correct trend with increasing m_v, while their lack of geometry dependence might not be that severe an issue. Consequently, they form the candidate model pool.

The Debye-like model is given as [105].

$$\begin{aligned} \epsilon'_{ws} &= A + \frac{B m_v^x}{1 + (f/f_0)^2} \\ \epsilon''_{ws} &= \frac{C (f/f_0) m_v^x}{1 + (f/f_0)^2} \end{aligned} \tag{5.35}$$

where $f_0 = 9.07$ GHz, which is an effective relaxation frequency of wet snow. In the ranges $3 \leq f \leq 37$ GHz, $0.09 \leq \rho_s \leq 0.38$ g cm^{-3}, and $1 \leq m_v \leq 12\%$, expressions for the parameters given above are:

$$\begin{aligned} A &= 1.0 + 1.83\rho_s + 0.02 m_v^{1.015} \\ B &= 0.073 \\ C &= 0.073 \\ x &= 1.31 \end{aligned} \tag{5.36}$$

The modified Debye model is applicable for cases where $m_v > 0.5\%$, which is somehow restrictive if dry snow is treated, hence it is discarded here.

The Debye model is then the only model remaining with which to calculate the equivalent index of refraction n_2. A typical dielectric constant by the Debye model as a function of the wetness m_v is depicted in Fig. 5.2 for $f = 35$ GHz and $\rho = 0.25$ g cm^{-3}.

What is equally important is to obtain an accurate expression for n_b, the effective

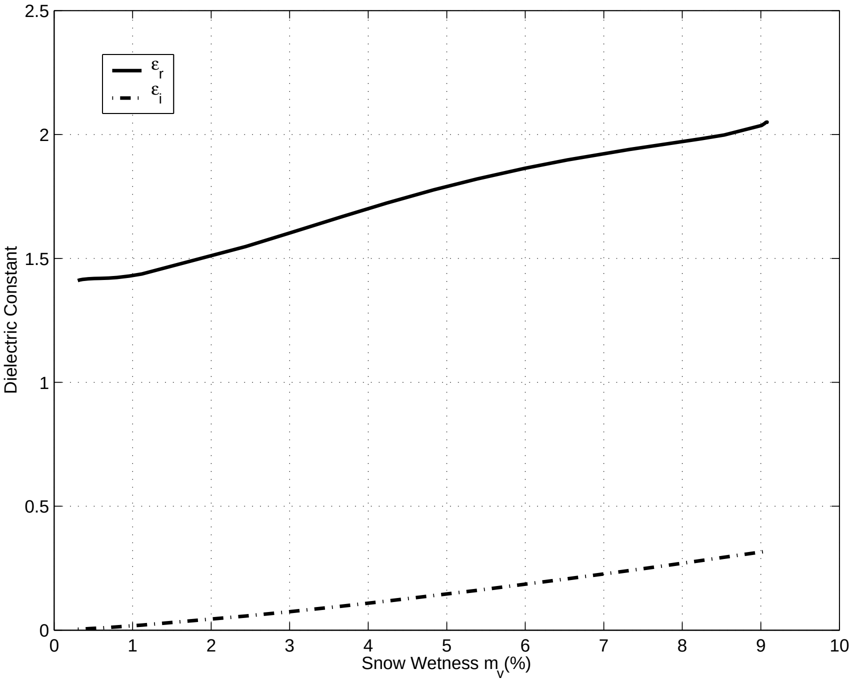

Figure 5.2: Dielectric constant as a function of the wetness m_v by Debye's model computed at $f = 35$ GHz and $\rho = 0.25 g/cm^3$.

index of refraction of the ice-particle background, which is needed to calculate $\kappa_{ep}(\hat{s})$ and the phase matrix P as shown in Eq. 5.34, 5.32 and 5.33. The determination of n_b depends on the way the background and scatterer are partitioned. For dry snow, this partition is trivial. Yet it is not the case for wet snow, where it presents a ramification of choices. For example, it is possible to treat the air as background while both the ice particle and the water droplet are scatterers, or to treat the mix of air and water droplet as background while the ice particle is the scatterer. In the first treatment, the geometrical complexity of the water droplet must be carefully addressed, which appears to be a quite challenging task, because according to [105], the water droplet tends to occupy the holes between the ice particles if the snow is wet enough (i.e., it is in the parnicular region), while it will simply surround the ice particle if the snow is relatively dry (or in the funicular region), where it is simply treated as the coating material to cover the ice particle for relatively dry snow [19]. On the other hand, as suggested by the literature, it is rarely treated as a separate scatterer even when the snow is in the funicular region, in part due to the difficulty encountered in treating the interaction among the water droplets, as well as between the water droplet and the ice particle, let alone the much unfriendly geometrical complexity. The modeling decision is then made to treat as background the mix of water droplet and the air. This being settled, another question is immediately raised as to which model is appropriate to determine the effective dielectric constant of the mixture. Among several model candidates, the PVS model is chosen in virtue of its good agreement with experimental data [105]. It is expressed as

$$\epsilon_{ws} = \epsilon_{ds} + \frac{m_v}{3}(\epsilon_w - \epsilon_{ds}) \sum_{u=a,b,c} [\frac{1}{1 + A_u(\frac{\epsilon_w}{\epsilon_{ws}} - 1)}] \tag{5.37}$$

where ϵ_w is the dielectric constant of liquid water.

5.5 Simulation vs. Measurement

Several diurnal measurements were conducted during the two winter measurement campaigns. One such measurement was made on February 9, 2000 for metamorphic snow. Starting from 8 am on that particular day, the air temperature at breast height rose gradually, from $-1.2°C$ to reach $0°C$ (Figure 5.3) at 9:10 am, when the snow pack thickness was 15.9 cm for snow above grass and 10.4 cm for snow above asphalt respectively.

The snow density was sitting at a low value of $0.2 g/cm^3$ (Figure 5.4). No discernible snow wetness was detected by the snow probe placed 1 inch down below the snow-air surface. From 10 am to 12 pm, while the temperature continued to rise to 4.7°C, the snow pack undertook some melting, as evident by the slow buildup of wetness to a m_v of around 4.5% and the reduction in snow pack thickness, in

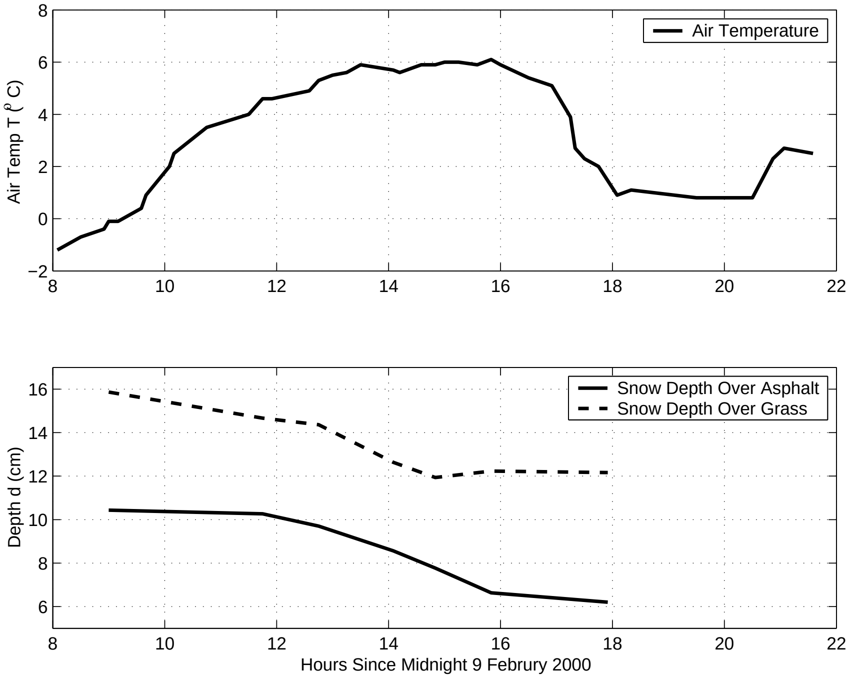

Figure 5.3: Snowpack depth and air temperature at breast height diurnal measurements on February 9, 2000

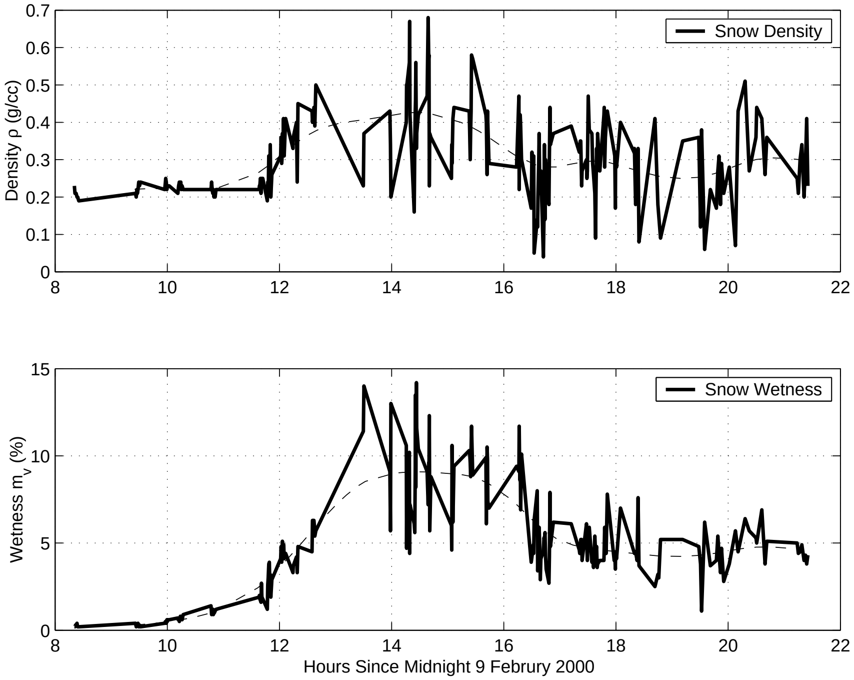

Figure 5.4: Snowpack wetness and snow density diurnal measurements on February 9, 2000

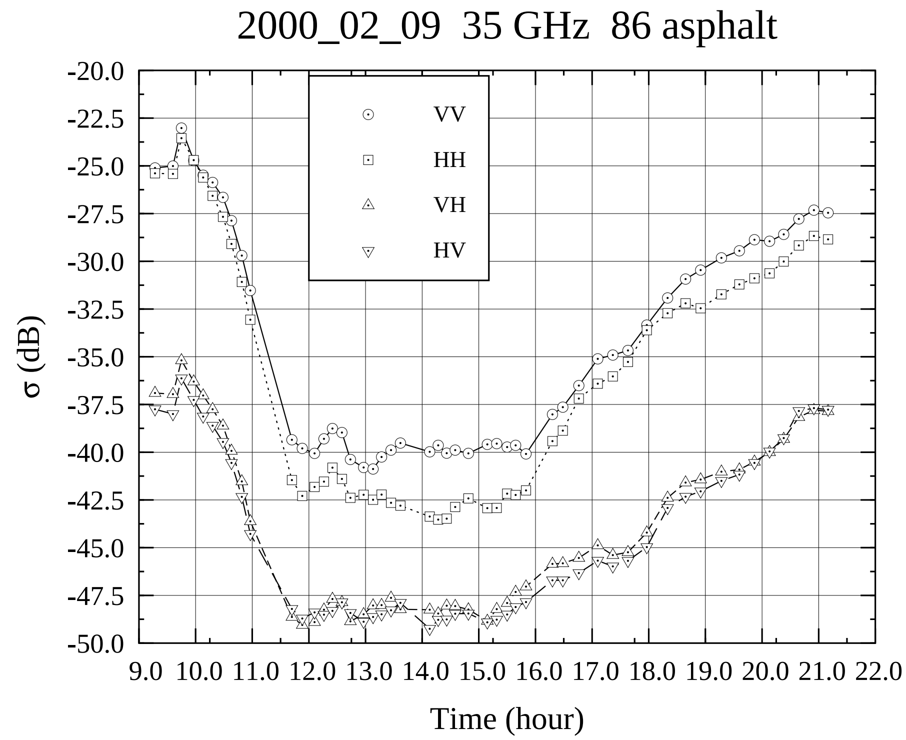

Figure 5.5: MMW backscattering diurnal measurements of snow over asphalt at incidence angle 86° at 35 GHz on February 9, 2000

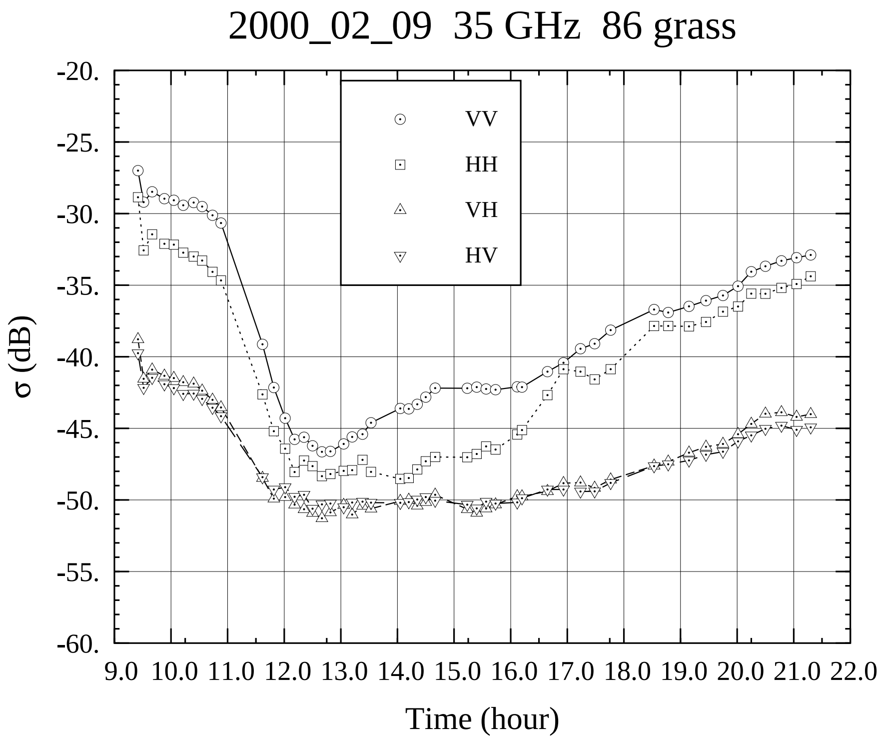

Figure 5.6: MMW backscattering diurnal measurements of snow over grass at incidence angle 86° at 35 GHz on February 9, 2000

particular for snow above grass. The backscattering by snow, above both grass and asphalt at 35 GHz, showed significant drop, around 15 dB for all cases, accounting for the dynamic range of the whole day, as shown in Figures 5.5 and 5.6. From then till 4 pm, temperature continued to rise at a slower pace to 6°C, resulting in a significant buildup of snow wetness and substantial drop of snow pack thickness above both grass and asphalt. The backscattering appeared to saturate. After 4 pm , the temperature dropped quickly, the snow pack thickness and snow wetness stabilized, the backscattering gradually recovered.

It appears that, without sample averaging, snow density and wetness appear to be highly random. Such randomness obscures the interpretation of the effect of snow attributes on the backscattering behavior. To overcome such a drawback, a smoothing procedure is adopted and the result is shown by the dotted line in Fig. 5.4.

As suggested in section 5.2, the evolution of the thermodynamics process within the snow-pack needs to be fully appreciated and accommodated in the treatment. The penalty in performance for not doing so can be quite severe. Let's take a close look at what will happen if the thermodynamics information is ignored in the modeling, which bears three implications: 1) the whole duration of the diurnal cycle is treated in the same way, except registering the difference in m_v and ρ as input variables to the model; 2) there is no multilayer treatment; 3) the size of the ice particles is fixed as opposed to being increasing at the freezing phase. The performances of this information-discarding model, as shown in Figure 5.7 for backscattering from snow over asphalt and in Figure 5.8 for backscattering from snow over grass, clearly demonstrate the lack of capacity to grasp the backscattering behavior. In short, the drawbacks lie, most evidently yet not exclusively, in three respects: 1) the failure to capture the abrupt drop in backscattering at the initial melting stage, especially for

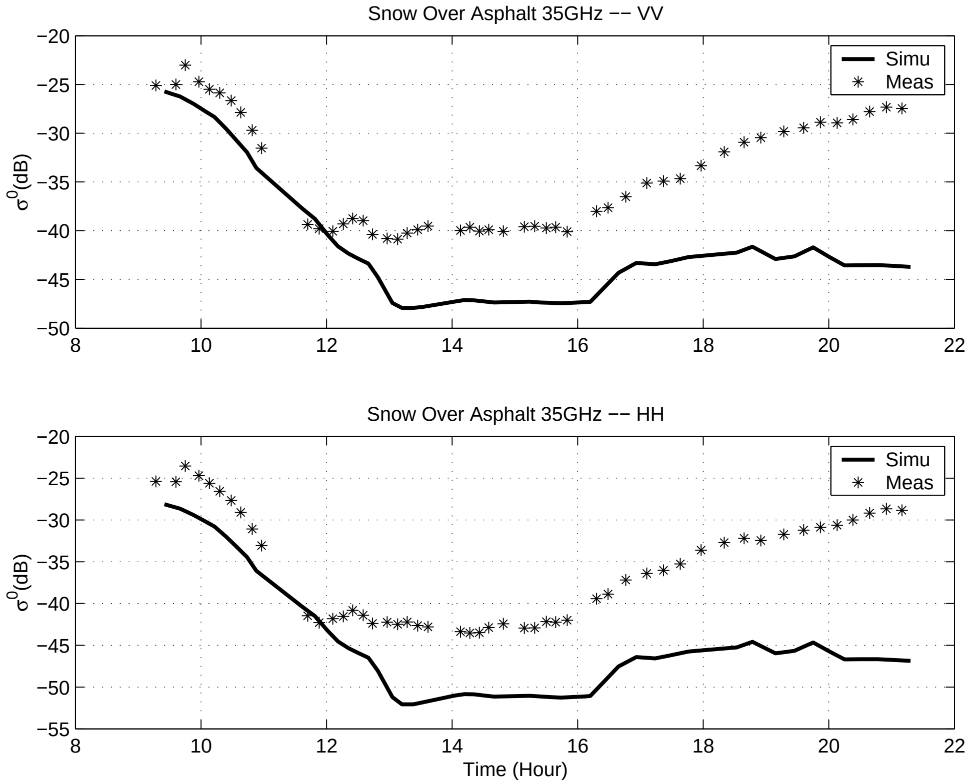

Figure 5.7: Simulation vs. measurement for snow over asphalt on February 9, 2000. Information regarding the underlying thermodynamic process within the snowpack is not incorporated in the model.

snow over grass; 2) the considerable underestimation of copolarized backscatter in the order of around 10dB for snow over asphalt; 3) most alarmingly, the incapability to capture the recovering of backscatter at the freezing stage for both copolarized backscatter from snow over both terrain conditions.

In incorporating the thermodynamic information, we need to divide the whole diurnal duration into several subregions. In the case of the measurements taken on February 9, 2000, the diurnal duration can be naturally divide into 5 subregions: 1) 9-10; 2) 10-12; 3) 12-16; 4) 16-18; 5) 18-20 as shown in Fig. 5.9. The characteristics for each subregion are as follows:

1) 9-10

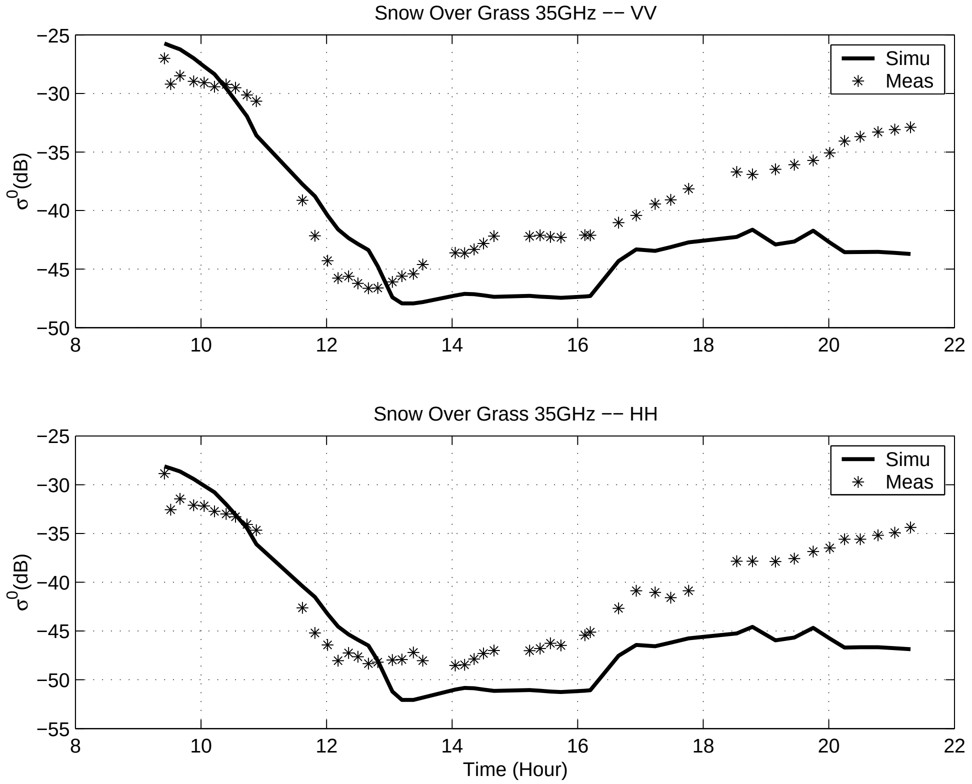

Figure 5.8: Simulation vs. measurement for snow over grass on February 9, 2000. Information regarding the underlying thermodynamic process within the snowpack is not incorporated in the model.

In this region, snow is relatively dry. The whole snow-pack can be treated as a single layer. Also, considering the snow depth is 15.9 cm over grass and 10.4 cm over asphalt, and the extinction coefficient is quite high at 35 GHz, it is reasonable to treat the snow-pack as semi-infinite.

2) 10-12

In this region, snow starts and continues to melt, resulting in an appreciable change in the m_v vertical distribution and in snow density ρ. For simplicity, the snowpack can be treated as a two-layer medium: a bounded layer of wet snow whose thickness increases as the snow melts over a semi-infinite layer of dry snow, each homogeneous in shape, size, m_v and ρ.

3) 12-16

In this region, snow is very wet, blocking any substantial electromagnetic wave penetration into the medium. The whole snow-pack can be treated as a single layer.

4) 16-18

In this region, snow starts and continues to cool off, resulting in a decrease in m_v and an increase in particle size. For simplicity, the snowpack again can be treated as a two-layer medium: a bounded layer of dry snow whose thickness increases as snow freezes over a semi-infinite layer of wet snow, each homogeneous in shape, size, m_v and ρ.

5) 18-22

In this region, snow continues to cool off at the lower bound. Yet the size growth stops in the upper layer, where the majority of backscattering is contributed. For simplicity, the snowpack can be treated as a two-layer medium: a bounded layer of dry snow over a semi-infinite layer of wet snow, each homogeneous in shape, size, m_v and ρ.

The corresponding geometry is best illustrated in Figure 5.9, where the extinction coefficient for each layer is also shown.

In summary, for each homogeneous layer, the scatterer is always assumed to be the ice particle with a dielectric constant $\epsilon_s = 3.15 - j0.001$ at 35 GHz. n2 and n_b are treated in accordance with the procedure described in section 5.4. Ice particles are assumed to be spheroidal, with an axial ratio of 3, the smallest radius being a. Moreover, the ice particles follow a uniform distribution in orientation, suggesting that the phase matrix and extinction coefficients can be determined by Eq. 5.32, 5.33 and 5.34, respectively.

It would be ideal if all the involved phsyical parameters could be readily available. Yet due to either economic or technical limitations in ground truth collection, some parameters are very difficult, if not impossible, to obtain directly from the ground truth. For instance, the average growth rate of the snow particle size at the initial stage of snow layer refreezing, or the true vertical distribution of m_v during the diurnal cycle. Inevitably some parameters have to be estimated from the measured data by some inversion technique. The parameters to be estimated pertinent to this study are particle size growth rate and the top layer growth rate.

The parameters, either obtained from the ground truth or from estimation, for each subregion for snow over asphalt are shown in Table 5.1, where the dynamics of the minor radius of ice particle, snow wetness and depth of the bounded snow upper layer are shown in three separate columns. It states that the minor radius of the ice particle a is always 0.3 mm for the whole melting process, yet for the upper dry snow layer when snow begins to freeze in region 4), this radius goes up to 0.4 mm linearly as shown in the linear relation $0.3 + \frac{t-16}{20}$, where we also use a minimum operation to upper bound the size such that it never exceeds 0.4 mm. In region 5), the radius

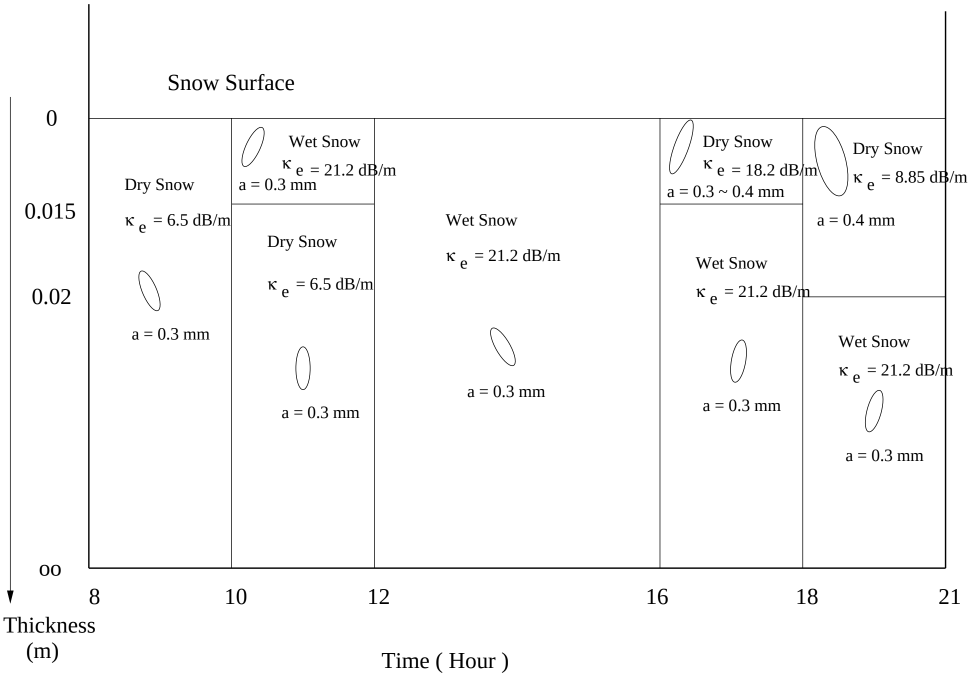

Figure 5.9: Illustration of subregions, snow layers and ice particle geometries for snow over asphalt on February 9, 2000. The extinction coefficient for each layer is also shown.

t	a(mm)	$m_v(\%)$	depth (m)
9-10	0.3	0.3	0
10-12	0.3	$\min(5, \frac{5}{1.8}(t-10))$	$\frac{0.015}{2}(t-10)$
12-16	0.3	5	semi-inf
16-18	$\min(0.4, 0.3 + \frac{t-16}{20})$	$\max(0.3, \frac{5}{5.5}(21.2-t))$	$\frac{0.02}{5.2}(t-16)$
18-22	0.4	$\max(0.3, \frac{5}{5.5}(21.2-t))$	$\frac{0.02}{5.2}(t-16)$

Table 5.1: Parameters For Snow Over Asphalt

stays at 0.4 mm as snow continues to freeze downward in the snowpack.

Likewise, all the linear growth and either upper or lower bound whenever applicable for snow wetness m_v and the thickness of the upper bounded snow layer follow the same interpretation.

The above parameters, along with the smoothed snow density ρ collected as shown in Fig. 5.4, are used to calculate the average phase matrix and the extinction coefficients given in Eq. 5.32, 5.33 and 5.34, respectively.

The predicted results are in good agreement for the copolarized measurements as shown in Figure 5.10. They capture the dynamics of the backscattering behavior, in particular the significant drop during early melting. Moreover, one should notice that the same physical parameters, either obtained from ground truth or from estimation, are used for both vertically and horizontally copolarized signal level predictions that demonstrate comparatively good performances.

Similarly, the parameters for each subregion for snow over grass are shown in Table 5.2. The predicted results are again in good agreement for the copolarized measurements as shown in Figure 5.11.

From the estimated parameters we notice that the snow particles are a bit larger

t	a(mm)	$m_v(\%)$	depth (m)
9-10	0.2	0.3	0
10-12	0.2	$\min(5, \frac{5}{2.2}(t-10))$	$\frac{0.015}{2}(t-10)$
12-16	0.2	5	semi-inf
16-18	$\min(0.25, 0.2+\frac{0.05}{2}(t-16))$	$\max(0.3, \frac{5}{5.5}(21.2-t))$	$\frac{0.02}{5.2}(t-16)$
18-22	0.25	$\max(0.3, \frac{5}{5.5}(21.2-t))$	$\frac{0.02}{5.2}(t-16)$

Table 5.2: Parameters For Snow Over Grass

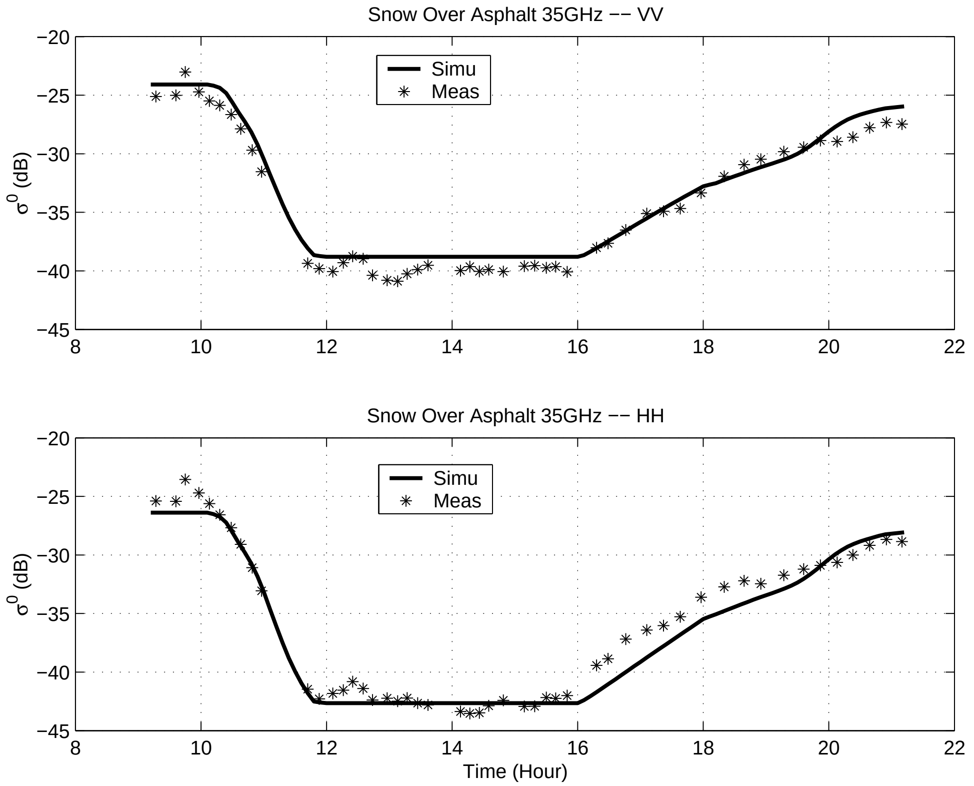

Figure 5.10: Simulation vs. measurement for snow over asphalt on February 9, 2000. Table 5.1 holds all the simulation parameters.

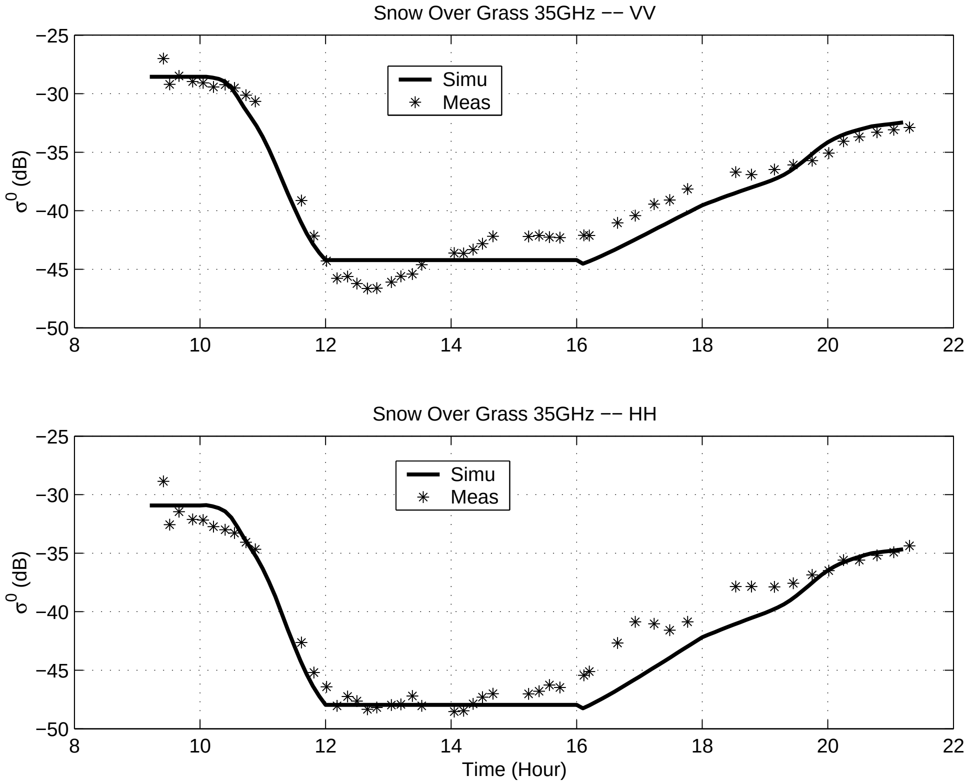

Figure 5.11: Simulation vs. measurement for snow over grass on February 9, 2000. Table 5.2 holds all the simulation parameters.

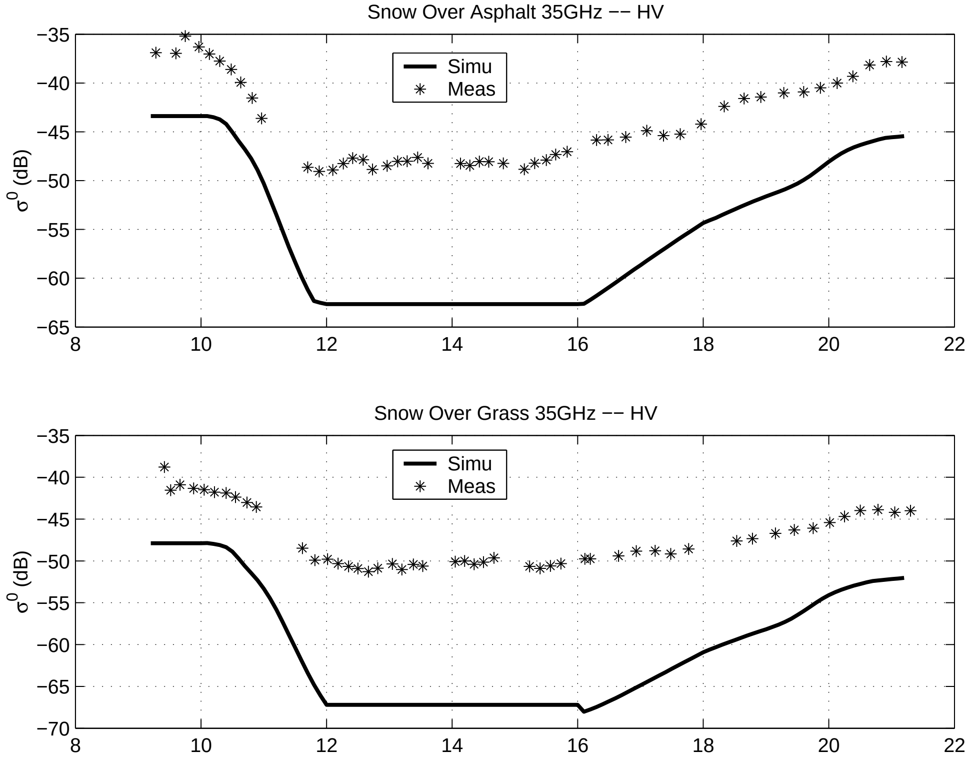

Figure 5.12: Simulation vs. measurement of cross-polarized backscatter for snow over both asphalt and grass on February 9, 2000. Table 5.2 and 5.1 hold all the simulation parameters.

for snow over asphalt than over grass, probably faithfully indicative of the consequence of different thermodynamic processes for the metamorphic snow packs over grass and asphalt.

The cross-polarized backscatter predicted by the model, in general, is 6-7 dB lower than the measurements for snow over both asphalt and grass, as shown in Figure 5.12. In the region 12-16, snow is very wet, causing the cross-polarized backscatter measurements to saturate. Consequently, we cannot make any legitimate conclusion except certain reasonable guess.

5.6 Conclusion

In this chapter, we studied the MMW diurnal backscattering behavior of snow over different terrain conditions at near grazing incidence. The underlying thermodynamic process of the snowpack was taken into account, which led to the division of several regions for diurnal observations based on ground truth measurements of m_v and air temperature at breast height. For each region, according to the unique dynamics in m_v, density ρ, particle size and so on, the snowpack was treated as either a semi-infinite layer or a two-layer medium. In the process of treating snow particles as spheroids, the symmetry between the volume absorption coefficient $\kappa_{ap}(\hat{s})$ and the volume scattering coefficient $\kappa_{sp}(\hat{s})$ was established. The model predictions demonstrate very good agreement with measurements.

CHAPTER VI

Forward Scattering At Near Grazing Incidence

For wireless communication systems, signal attenuation and interference caused by multipath ground reflection are of major concern. Signal attenuation imposes a stringent requirement on the SNR at the receiver end, and signal interference may add a further requirement on transmitter power and SNR. At the lower part of the microwave spectrum, such as the UHF band, both theoretical and semi-empirical communication models, up to 3D, have been developed for both rural and urban areas. Also reported in the literature are the blockage/shadowing and polarization measurements [54] and signal to interference ratio measurements [110]. In general, the critical channel characterization problem is to determine the so called scattering function which tries to capture the multipath and Doppler spreads in a compact form [79] [77]. Depending on the characteristics of the coherent field, the channel is classified into Rayleigh, Rician and Suzuki channels. More often than not, the channel is determined using either empirical data or by adopting much simplified theoretical models as opposed to advanced and slightly computationally demanding models such as IEM [52] [76].

On the other hand, although MMW communication systems possess some more advantageous features, such as wider bandwidth, than their lower frequency counter-parts, they have been rarely considered in the literature, let along the corresponding channel characterization problem at such frequencies.

For the remaining parts of this thesis, the problem of characterizing the forward scattered field will be approached along two different paths: (1) charactering through experiments the forward scattered field of soil and grass-covered surface; (2) extending the IEM model to incorporate antenna pattern from rough surface scattering. In Chapter VI, we will examine the advantage and disadvantages of two different measurement techniques and discuss recent measurements performed using both techniques. In Chapter VII, we will extend the IEM method to antenna pattern of the transmitter and receiver for the purpose of modeling the forward scattered field.

6.1 Introduction

The standard approach for measuring the height-interference diagram is shown in Figure 6.1, which we shall discuss in more detail in the next section. With the transmitter held in position, measurements of the received signal are made as a function of receiver height over the desired range.

Whereas the measurement arrangement in Figure 6.1 is straightforward, it would be highly convenient if the interference diagram can be deduced from radar backscattering measurements, as will be discussed later in section 6.3.

Our interest in studying the interference pattern at MMW wavelength stems from several considerations: (a) it has been examined before on a limited scale and only at 95 GHz [68], (b) millimeter-wave communication offers the advantage of narrower-beam antennas, when compared with antennas of the same size at lower frequencies, (c) wide bandwidths are easily obtained at MMW communication systems, and (d) adding a MMW communication system to a radar is rather straightforward and the additional cost is relatively low.

We shall investigate the relevant factors that collectively determine signal interference, which include: antenna look angle; carrier frequency (assuming narrow-band communication systems); polarization, antenna pattern; range to target; type of scatterers; and ground dielectric properties and geometrical conditions (smooth, rough, bare, vegetated, etc).

To fully appreciate the impacts of these factors, we shall proceed in a progressive fashion, starting from the simplest case and progressively adding more factors. As the terrain condition becomes more and more complex, so is the disturbance in the observed backscatter coherent interference pattern. As this trend continues, the interference pattern eventually collapses and becomes random-like. At that point, we are led to attack the forward interference pattern directly, which is the subject of the next chapter.

We start this examination process in section 6.2 with a brief study of the interference pattern for forward scattering under straightforward conditions so we may appreciate the character of the interference process, and to provide an illustration of how frequency diversity can be used to counter the loss in signal level during destructive interference.

Later as a side issue, we will demonstrate that this measurement technique holds the potential of assisting inversion of some critical physical parameters, such as the effective reflection coefficient of a surface.

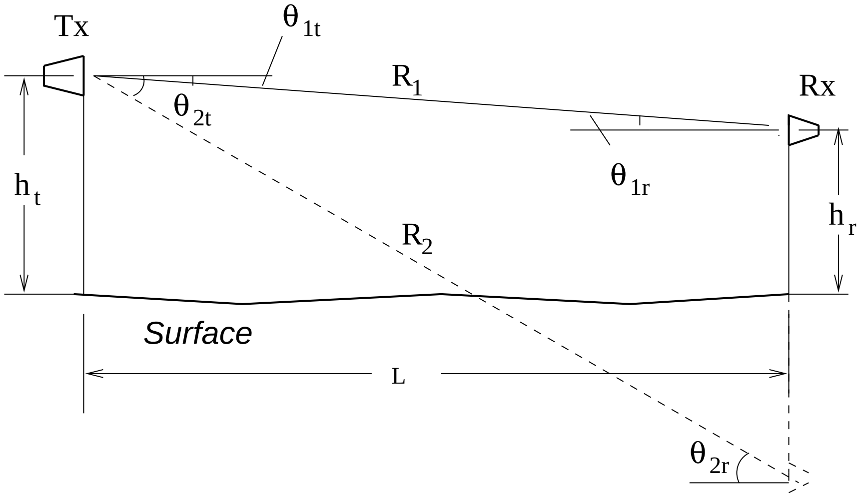

Figure 6.1: Geometry of the forward scattering with the horizontal distance between the transmitter and the receiver sufficiently large.

6.2 Forward Measurement Technique of Height Interference

The configuration for forward scattering is shown in Figure 6.1, where h_t is the height of the transmitter, h_r is the height of the receiver, and L is the horizontal distance between transmitter and receiver. In general, the electrical field at the receiver can be written as:

$$\bar{E} = \bar{E}_1 + \bar{E}_2 = (\frac{e^{-jkR_1}}{4\pi R_1} f_t(\theta_{1t}) f_r(\theta_{1r}) + \rho \frac{e^{-jkR_2}}{4\pi R_2} f_t(\theta_{2t}) f_r(\theta_{2r}))\bar{e}_0 \tag{6.1}$$

where k is the wave number, $\bar{e}_0$ is the transmitted field, R_1 and R_2 are the ranges from the transmitter to the receiver and the receiver's image, respectively, ρ is the Fresnel reflection coefficient, $f_t(\cdot)$ and $f_r(\cdot)$ are the antenna gains at the specified angles.

A typical interference pattern is shown in Figure 6.2. The vertical axis is $P_r = |\bar{E}|^2$, normalized to P_{r0}, the received free-space power level in the absence of interference,

$$P_{r0} = |\frac{e^{-jkR_1}}{4\pi R_1} f_t(\theta_{1t}) f_r(\theta_{1r}) \bar{e}_0|^2 \tag{6.2}$$

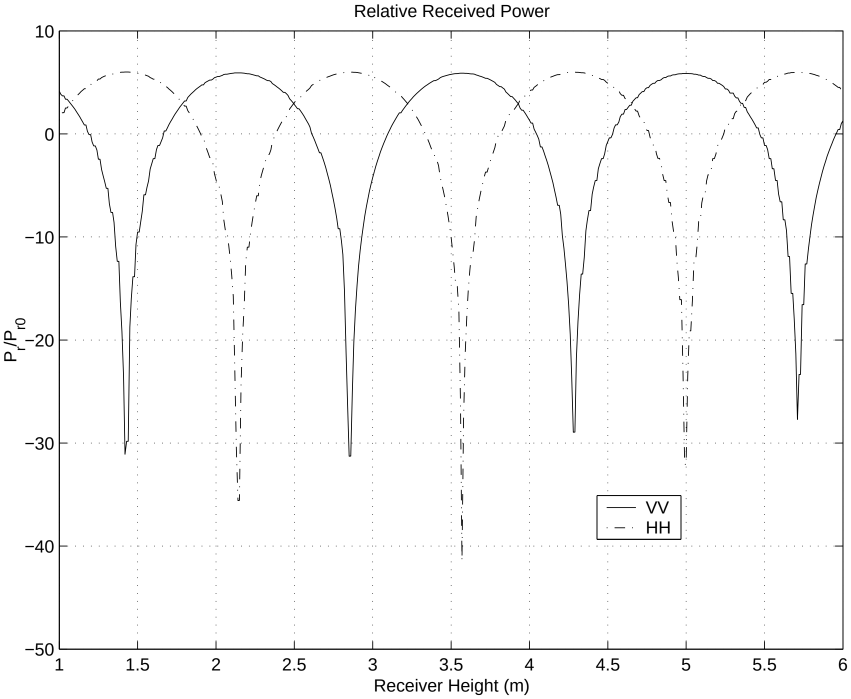

Figure 6.2: Forward interference pattern of the normalized received power P_r/P_{r0} as a function of the receiver height above a smooth surface. In this example, L=1000m, $h_t = 3m$, f=35GHz.

The 35-GHz interference pattern represents the variation of P_r/P_{r0} for a pair of wide-beam antennas such that all antenna pattern factors are approximately equal to 1. The calculations were performed for a stationary transmitter at a height of 3m as a function of receiver height over the range from 1m to 6m. The reflection coefficient was set equal to 1.

Constructive interference leads to twice the free-space electric field, or four times the free-space received power. These are the +6dB maxima. For this ideal case, the minima correspond to total cancellation, or $-\infty$ in dB. The opposite reflection coefficient signs for VV and HH leads to the flipping of the extrema (maxima and minima).

To examine the interference pattern at near grazing incidence, we first consider the case when L will be hypothetically allowed to approach infinity, which implicitly assumes that the sensitivity of the receiver is hypothetically high enough to receive this much attenuated signal. This treatment bears two implications: 1) the line-of-sight (LOS) signal and the interference signal reflected by the ground are well within the antenna beam, and therefore may have identical antenna gains, suggesting the treatment of the antennas as isotropic sources, and 2) the effective reflection coefficient from the ground approaches one, even if the surface is slightly rough. We can then write

$$\begin{aligned} R_1 &= \sqrt{L^2+(h_t-h_r)^2} \approx L(1+\frac{(h_t-h_r)^2}{2L^2}) when L \gg |h_t-h_r| \\ &= L(1+\frac{\delta_-^2}{2L^2}) \\ R_2 &= \sqrt{L^2+(h_t+h_r)^2} \approx L(1+\frac{(h_t+h_r)^2}{2L^2}) when L \gg |h_t-h_r| \\ &= L(1+\frac{\delta_+^2}{2L^2}) \qquad (6.3) \end{aligned}$$

where

$$\delta_- = h_t - h_r$$
$$\delta_+ = h_t + h_r \tag{6.4}$$

Hence,

$$\begin{aligned}\bar{E} &= \frac{1}{4\pi L}\left(e^{-jkL(1+\frac{\delta_-^2}{2L^2})} + e^{-jkL(1+\frac{\delta_+^2}{2L^2})}\right)\bar{e}_0 \\ &= \frac{1}{4\pi L}e^{-jkL(1+\frac{\delta_-^2}{2L^2})}\left(1 + e^{-j\frac{k}{2L}(\delta_+^2-\delta_-^2)}\right)\bar{e}_0\end{aligned} \tag{6.5}$$

To determine the interference pattern, which is governed by the factor

$$1 + e^{-j\frac{k}{2L}(\delta_+^2-\delta_-^2)} \tag{6.6}$$

we can adopt a rather intuitive figurative approach. Define

$$\theta = \frac{k(\delta_+^2 - \delta_-^2)}{2L} \tag{6.7}$$

which is a very small number because $k(\delta_+^2 - \delta_-^2) = 4kh_th_r$ is linear in h_r when L is sufficiently large. In the complex plane, the trajectory of $z = e^{-j\theta}$ is a tightly restricted arc on the unit circle as shown in the thick solid arc in Figure 6.3. Consequently, $1 + z$ is along the illustrated dotted arc.

Hence the interference term adds constructively to the LOS term since the very small angle θ implies that the interference term is approximately in phase with the LOS term.

However, in reality, due to SNR limitations, the receiver cannot be arbitrarily far away from the transmitter. The implied antenna pattern and near grazing effect, in addition to the scattering from the surface, make the interference pattern a rather complicated one.

A number of techniques can be used to combat the nulls encountered as the receiver height changes (Figure 6.2). Frequency diversity is a such technique. The basic idea is that if the transmitter can transmit signals using multiple carrier frequencies with the separation between center frequencies larger than the coherence

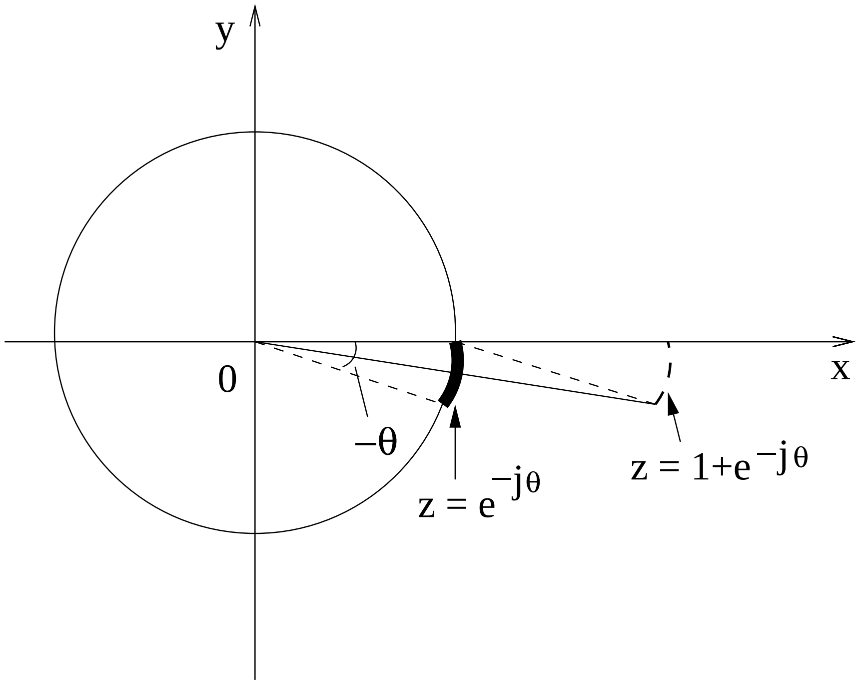

Figure 6.3: Signal space representation of the interference from ground in the complex plane

band of either channel, then at the receiver the received signals are independent, thereby permitting optimal diversity combining [79]. One simple technique is to always choose the received signal with the higher power (hence higher SNR). For example, if the carrier frequencies are $f_0 = 35$ GHz and $f_1 = f_0(1 + \delta)$, where δ is the frequency shift from f_0, and if the maximal power of the two is chosen at the receiver, then for a smooth surface, the interference patterns corresponding to different δ values are shown in Figure 6.4, from which we can determine the percentage of data points that fall below a preset power level as the received signal is processed using maximal frequency diversity combining. This process leads to Figure 6.5. Now the diversity gain can be readily calculated, which is defined as the difference in power levels with and without frequency diversity combining, above which a preset percentage of data points attain a specified power level. For example, if only $f_0 = 35$ GHz is used, then there is 1% of data points with $P_r/P_{r0} < -25$ dB, while 99% of data points with $P_r/P_{r0} \geq -25$ dB. On the other hand, if in addition we have another channel with frequency $f_1 = 1.05f_0$ to provide frequency diversity, then there is 1% of data points with $P_r/P_{r0} < -12$ dB, while 99% of data points with $P_r/P_{r0} \geq -12$ dB. Hence the diversity gain is 13.4 dB. The frequency diversity gains are summarized in Table 6.1.

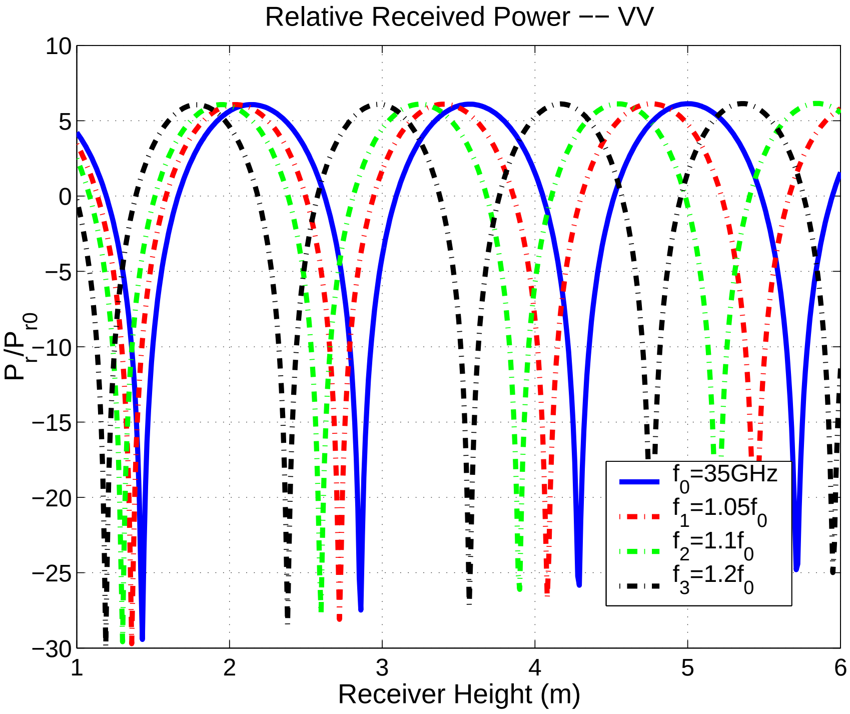

Figure 6.4: Forward interference pattern of the normalized received power P_r/P_{r0} for different carrier frequencies as a function of the receiver height above a smooth surface. In this example, $L = 1000$m, $h_t = 3$m.

By similar argument and treatment, we can also study the polarization gain by selecting the received polarized signal with the higher power (hence higher SNR). Thus for the same smooth surface, the interference patterns corresponding to different polarizations are shown in Figure 6.2, while the percentage of data points that fall below a preset power level as the received signal is processed using maximal

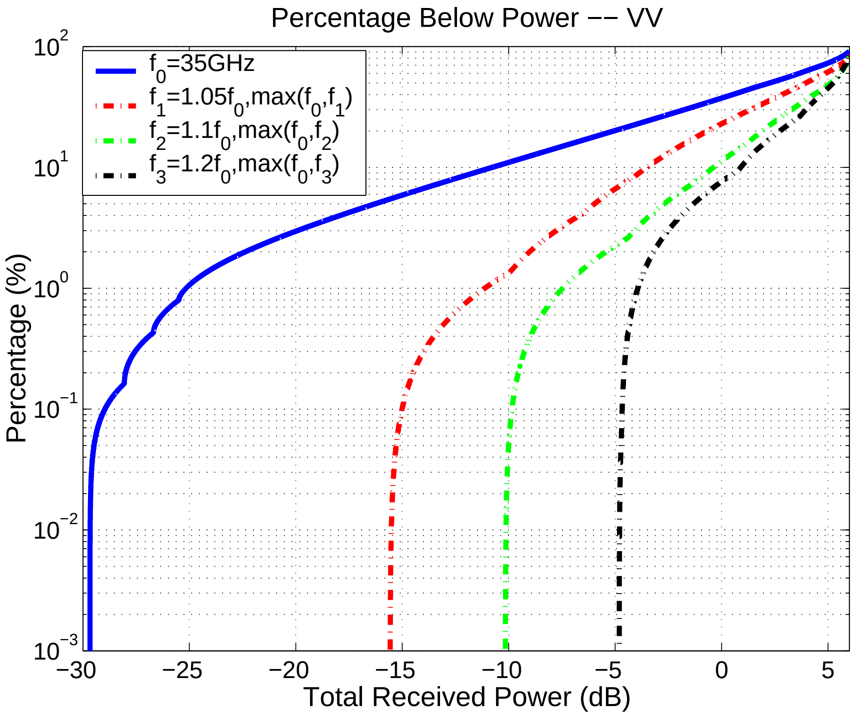

Figure 6.5: Percentage of data points below a preset power level as the received signal is processed using maximal frequency diversity combining. See Figure 6.4 for details.

Table 6.1: Frequency Diversity Gain

Percent	*Signal Level (dB)*				*Signal Gain (dB)*		
	f0	5%	10%	20%	5%	10%	20%
90	-11	-3.5	-0.8	1	7.5	10.2	12
99	-25.2	-11.8	-7.5	-4	13.4	17.7	21.2
99.9	-29	-15	-9.8	-4.5	14	19.2	24.5
99.99	-29.5	-15.5	-10.1	-4.8	14	19.4	24.7

polarization diversity combining is shown in Figure 6.6.

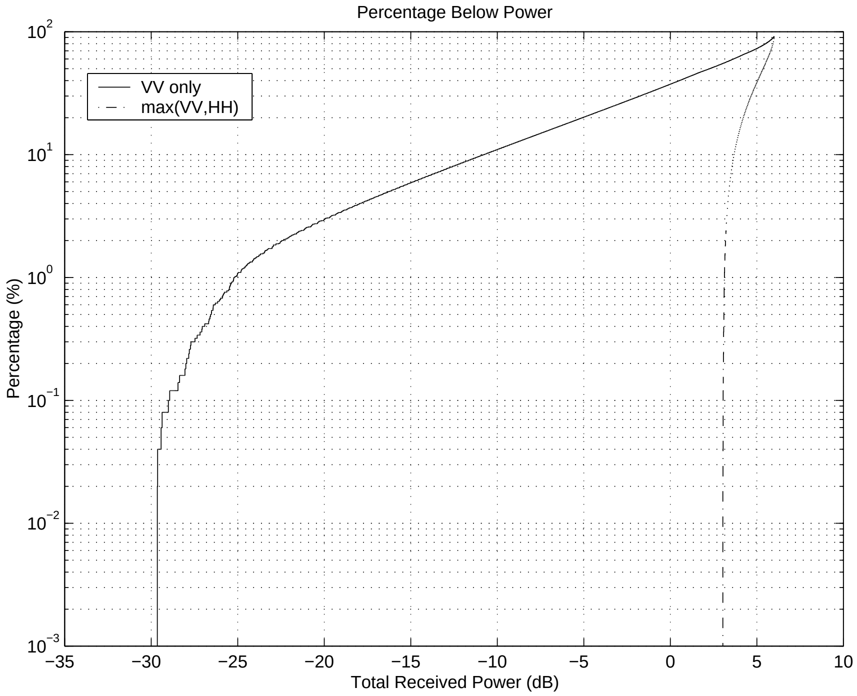

Figure 6.6: Percentage of data points below a preset power level as the received signal is processed using maximal polarization diversity combining. See Figure ?? for details.

6.3 Backward Measurement Technique

For remote sensing, one major concern is to extract physical properties of the sensed target. Preferably, such extraction can be based on monostatic measurements rather than bistatic measurements to avoid the difficulties encountered in the experimental arrangement for the latter. In this regard, Baker *et al.* [5] tried to extract bistatic cross section of a natural terrain from monostatic measurements with the aid of a corner reflector being placed in the far field at the desired bistatic direction. Sarabandi et al [82] attempted to extract the extinction coefficient from monostatic measurements by using a metallic plane being placed behind the target.

In this section we shall investigate the use of a radar operated in the backscattering mode to infer the forward interference pattern that would be observed by a communication system. The inference hence is in the statistical sense, which means that we need to infer both coherent and incoherent components of the forward scattered field from the backscatter response. Inference of the incoherent component has been studied by Crispin [21] and Kell [55]. We shall concentrate ourselves with the coherent component. We do so by measuring the backscatter from a metalic sphere above the terrain surface of interest as a function of the height of the sphere above the surface. Related work has been reported in the literature [39] [53] [67] [109], where [53] provides a numerical study of the accuracy of the so called four-ray model, and [39] [67] [109] focused on the calculation of the backscatter cross section, as opposed to the interference pattern which is our main concern. Our study of the interference pattern in this chapter progresses from a metallic sphere over a flat surface on to a rough surface, and then to a grass-covered surface. We also consider the role of the antenna pattern on the observed interference pattern.

We want to point out that this model can be used not only for the study of near grazing surface reflectivity for line-of-sight communication applications, but also for modeling the distorted radar signature of a target positioned above ground and measured at grazing incidence. In target embedding techniques, the radar return of a target, measured in free space, is embedded into a radar image of clutter only, and target detection techniques are evaluated this way.

6.3.1 Antenna Pattern Excluded

The geometry configuration of the backward scattering case with the assistance of a metallic sphere placed above a half space is shown in Figure 6.7.

Analytical solutions of the backscatter from such a simple setting are not readily

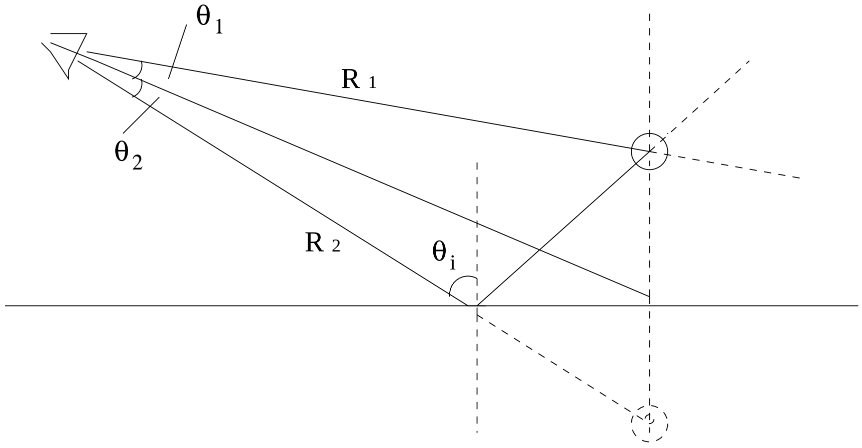

Figure 6.7: Geometry for backward scattering from a metallic sphere above a smooth surface

available due to the complexity of the half-space Green's function. Rather, we will adopt a widely applied simple four-ray approximate model. The accuracy of such a model was studied in [53], leading to the conclusion that the basic premise of the four-ray model holds well for scattering from an object above a half space, but since this model includes only single scattering effects, its accuracy depends on how significant the higher order effects are.

In this section, the antenna pattern is ignored. The surface is further assumed to be specular, leaving the more general rough case to be treated in a later section.

Based on the four-ray model, the four components contained in the backscattered field are shown symbolically in Figure 6.8 and written as:

$$\bar{E}_r = \bar{E}_1 + \bar{E}_2 + \bar{E}_3 + \bar{E}_4 \tag{6.8}$$

where

$$\begin{aligned} \bar{E}_1 &= \frac{e^{-jkR_1}}{4\pi R_1}\bar{\bar{S}}_1(-\theta_{10},\theta_{10})\frac{e^{-jkR_1}}{4\pi R_1}\cdot \hat{e}_1 \\ \bar{E}_2 &= \frac{e^{-jkR_1}}{4\pi R_1}\bar{\bar{S}}_1(-\theta_{10},\theta_{20})\frac{e^{-jkR_2}}{4\pi R_2}\cdot (\rho_h(\hat{e}_1\cdot\hat{h})\hat{h} + \rho_v(\hat{e}_1\cdot\hat{v})\hat{v}) \end{aligned} \tag{6.9}$$

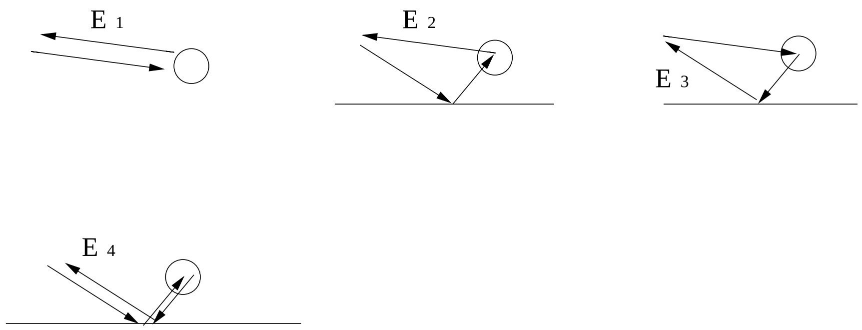

Figure 6.8: Field components for the backscattering

where ρ_h and ρ_v are the reflection coefficients for TE and TM polarizations, respectively, and $\hat{h}, \hat{v}$ represent the TE and TM unit vectors, respectively. The relevant angles are shown in Figure 6.9. For notational convenience, $\pi - \theta_{10}$ is short written as $-\theta_{10}$ in the sphere scattering functions, and $\pi - \theta_{20}$ is short written as $-\theta_{20}$. This short notation will be used throughout this chapter.

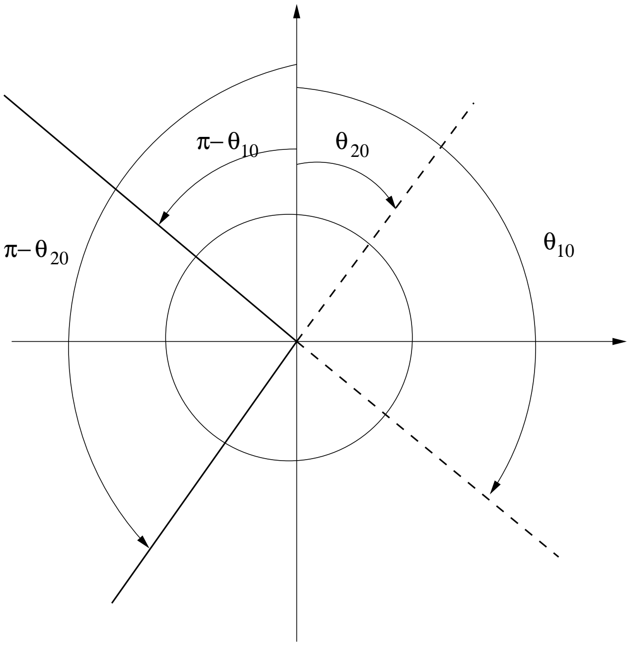

Figure 6.9: Convention of incident and scattered angles.

Similarly,

$$\begin{aligned}
\bar{E}_3 &= \frac{e^{-jkR_1}}{4\pi R_1}\bar{\bar{S}}_1(-\theta_{20},\theta_{10})\frac{e^{-jkR_2}}{4\pi R_2}\cdot(\rho_h(\hat{e}_1\cdot\hat{h})\hat{h}+\rho_v(\hat{e}_1\cdot\hat{v})\hat{v}) \\
\bar{E}_4 &= \frac{e^{-jkR_2}}{4\pi R_2}\bar{\bar{S}}_1(-\theta_{20},\theta_{20})\frac{e^{-jkR_2}}{4\pi R_2}\cdot(\rho_h^2(\hat{e}_1\cdot\hat{h})\hat{h}+\rho_v^2(\hat{e}_1\cdot\hat{v})\hat{v}) \qquad (6.10)
\end{aligned}$$

When writing out the field equations, we have incorporated the following facts: 1)the specular surface does not generate a cross-polarized field; 2) the incident wave and the scattered wave of interest, as shown in Figure 6.8, are approximately coplanar; hence, there is no depolarization effect either.

Finally, the power can be written as:

$$|\bar{E}_r| = |\bar{E}_1+\bar{E}_2+\bar{E}_3+\bar{E}_4|^2 \qquad (6.11)$$

A typical interference pattern for the backscattered field is shown in Figure 6.10. Again, the opposite reflection coefficient signs for VV and HH lead to the flipping of extrema (maxima and minima). A more resounding feature is that both VV and HH attain a 8 dB gain at maxima, rather than the 6 dB gain maximally attainable for the forward interference case. This is because there are 4 terms in this backscattering configuration in contrast to 2 terms in the forward scattering case; all 4 terms can possibly act in phase and hence add constructively. The maximum interference gain is 12 dB, which occurs when the magnitude of the reflection coefficient is 1 and all four terms add constructively to provide a four-fold increase in field or 16 times in power.

6.3.2 Backscatter Interference For a Rough Surface, with Antenna Pattern Included

The geometry illustrated in Figure 6.11 depicts a radar observing a point target above a rough surface interface.

In this case, the received field $\bar{E}_r$ contains five components:

$$\bar{E}_r = \bar{E}_1+\bar{E}_2+\bar{E}_3+\bar{E}_4+\bar{E}_5 \qquad (6.12)$$

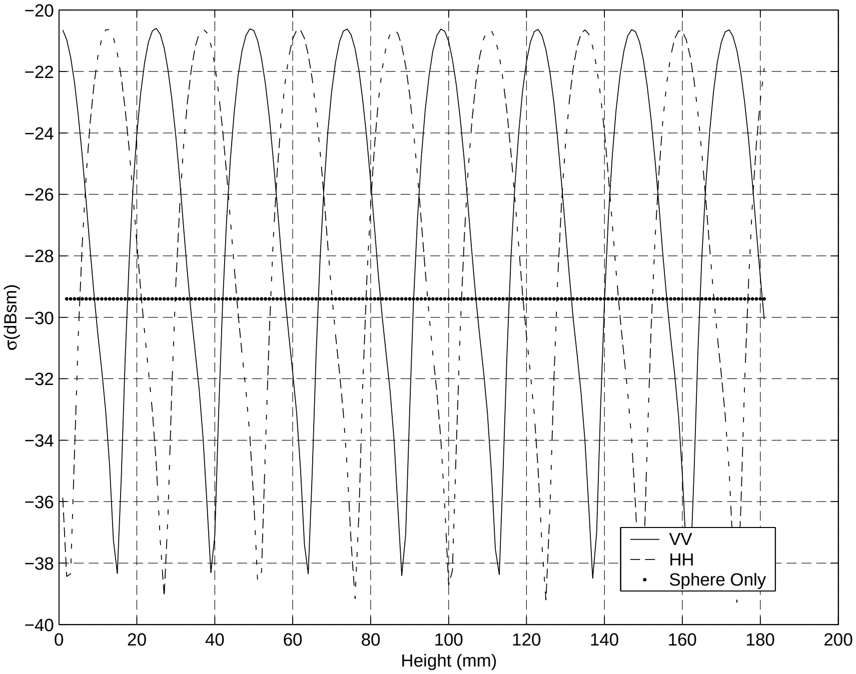

Figure 6.10: Backscatter interference pattern of the $\sigma(dBsm)$ as a function of the receiver height above a smooth surface with antenna pattern excluded. The dots shown are the backscatter $\sigma(dBsm)$ from the sphere itself, which serves as a base for calculating the interference gain/loss. In this example, L=8.5m,$\epsilon = 3$, metallic sphere radius is 1.9 cm, and antenna height is 1.5 m.

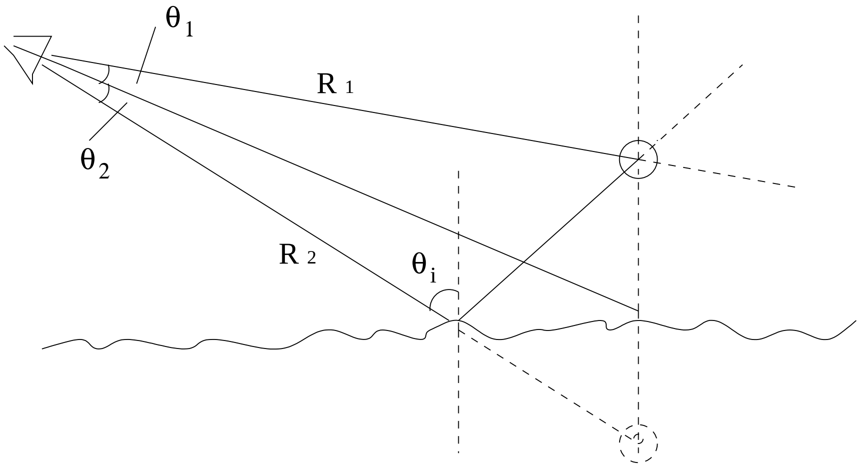

Figure 6.11: Geometry of the backward scattering from a metallic sphere over a rough surface with antenna pattern

where each component is shown symbolically in Figure 6.12. The direct backscattering component, $\bar{E}_5$, is ignored in the treatment because we are interested in near grazing incidence, in which case the direct ground backscatter is very small compared with the other components. Hence, we can again describe the received field $\bar{E}_r$ by the four-ray model.

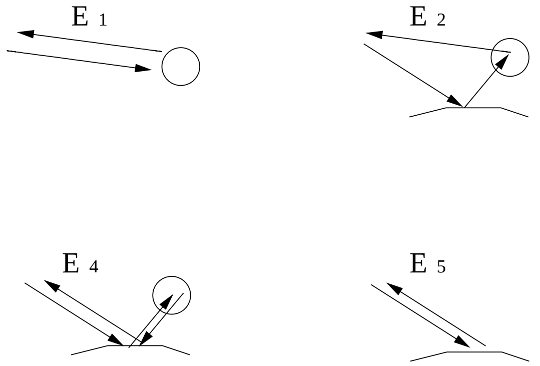

Figure 6.12: Components of the backscattering field

Fields $\bar{E}_2$ to $\bar{E}_4$ involve scattering from the surface. If the surface is rough, fields $\bar{E}_2$ to $\bar{E}_4$ are all random variables. To keep the model tractable in calculating the average received power density, we need a surface scattering model that is easy to handle in order to get the higher-order moments of the scattering statistics. The Kirchhoff model appears to be a good candidate, even though its region of validity may not be strictly applicable to certain surface conditions. We will also modify this model accordingly to alleviate mathematical complexity.

The direct backscatter from the sphere can be written as:

$$\bar{E}_1 = f_r(\theta_{1r}) \frac{e^{-jkR_1}}{4\pi R_1} \bar{\bar{S}}_1(-\theta_{10}, \theta_{10}) f_t(\theta_{1t}) \frac{e^{-jkR_1}}{4\pi R_1} \cdot \hat{e}_1 \tag{6.13}$$

where $f_t(\theta)$ and $f_r(\theta)$ are antenna pattern gains of the transmitter and receiver, respectively. $\bar{\bar{S}}_1(\theta_1, \theta_2)$ is the bistatic scattering matrix of the sphere, and $\hat{e}_1$ is the field of the incident wave.

For the surface-involved terms, we introduce certain symbols to simplify the expressions:

$$\begin{aligned}
\bar{E}_2 &= f_r(\theta_{1r})\frac{e^{-jkR_1}}{4\pi R_1}\bar{\bar{S}}_1(-\theta_{10},\theta_{20})\cdot\bar{E}_{s1}(\bar{r}_s,A_0)\frac{e^{-jkR_2}}{4\pi R_2}\\
\bar{E}_3 &= \frac{e^{-jkR_1}}{4\pi R_1}\bar{\bar{S}}_1(-\theta_{20},\theta_{10})\cdot\bar{E}_{s2}(A_0,\bar{r}_s)f_t(\theta_{1t})\frac{e^{-jkR_2}}{4\pi R_2}\\
\bar{E}_4 &= \frac{e^{-jkR_1}}{4\pi R_1}\bar{E}_{s2}(A_0,\bar{r}_s)\cdot\bar{\bar{S}}_1(-\theta_{10},\theta_{20})\cdot\bar{E}_{s1}(\bar{r}_s,A_0)\frac{e^{-jkR_2}}{4\pi R_2} \qquad (6.14)
\end{aligned}$$

where $\bar{E}_{s1}(\bar{r}_s, A_0)$ refers to the total field at the sphere after scattering by A_0, the region illuminated by the incidence wave and $\bar{E}_{s2}(A_0, \bar{r}_s)$ refers to the total field at the receiver scattered by A_0 after reflection by the sphere. Both scattered fields are calculated similarly [93]:

$$\bar{E}_s(\bar{r}) = ikE_0(\bar{\bar{I}} - \hat{k}_s\hat{k}_s)\cdot\int_{A_0} d\bar{r}'\bar{F}(\alpha,\beta)f_a(\theta')e^{i(\bar{k}_i-\bar{k}_s)\cdot\bar{r}'} \qquad (6.15)$$

where we introduce the antenna pattern $f_a(\theta')$ to recognize the effect of the non-uniform wavefront due to the antenna pattern.

It is well known that higher-order scattering terms are dominated by the lower order ones. To simplify the calculation, only the first-order term in Eq. 6.15 is retained. Further simplification is introduced when calculating the power density, where there are 16 terms involved, and the most computationally intensive term requires 4-fold integration on A_0, or 8-fold integration on coordinates. Since the directivity of the antenna is very high, we can assume a pencil-beam antenna whose antenna pattern is represented approximately by a Kronecker delta function, i.e.,

$$f_a(\theta') = f_a(\theta')\delta(\bar{r}' - \bar{r}_{spec}) \qquad (6.16)$$

where $\bar{r}_{spec}$ is the imagined specular point on the surface for coherent waves. Using Eq. 6.16 in Eq. 6.12-6.15, the field expression given by Eq. 6.12 is greatly simplified to:

$$E_r = E_0(1 + A_2 e^{-j\beta h(\bar{r}_{spec})} + A_3 e^{-j\beta h(\bar{r}_{spec})} + A_4 e^{-j2\beta h(\bar{r}_{spec})}) \tag{6.17}$$

where $\beta = 2k\cos\theta_i$,

$$\begin{aligned}
E_0 &= f_t(\theta_1)f_r(\theta_1)(\frac{e^{(-jkR_1)}}{4\pi R_1})^2 S_1(-\theta_{10},\theta_{10}) \\
A_2 &= \frac{f_t(\theta_2)}{f_t(\theta_1)}\rho e^{-jk(R_2-R_1)}\frac{R_1}{R_2}\frac{S_1(-\theta_{10},\theta_{20})}{S_1(-\theta_{10},\theta_{10})} \\
A_3 &= \frac{f_r(\theta_2)}{f_r(\theta_1)}\rho e^{-jk(R_2-R_1)}\frac{R_1}{R_2}\frac{S_1(-\theta_{20},\theta_{10})}{S_1(-\theta_{10},\theta_{10})} \\
A_4 &= \frac{f_t(\theta_2)f_r(\theta_2)}{f_t(\theta_1)f_r(\theta_1)}\rho^2(e^{-jk(R_2-R_1)}\frac{R_1}{R_2})^2\frac{S_1(-\theta_{20},\theta_{20})}{S_1(-\theta_{10},\theta_{10})}
\end{aligned} \tag{6.18}$$

and ρ is the Fresnel reflection coefficient.

If we assume that the surface height $h(\bar{r})$ follows a normal distribution, then

$$< e^{t\ h(\bar{r}')} >= e^{-\frac{t^2 s^2}{2}} \tag{6.19}$$

where s^2 is the variance of $h(\bar{r})$. Now taking the ensemble average on both sides of Eq. 6.17, and making use of Eq. 6.19, we obtain the coherent field as:

$$< E_r >= E_0(1 + A_2 e^{-j\frac{\beta^2 s^2}{2}} + A_3 e^{-j\frac{\beta^2 s^2}{2}} + A_4 e^{-j2\beta^2 s^2}) \tag{6.20}$$

We observe that this treatment eliminates the need for correlation information, and introduces an effective reflection coefficient ρ_{eff} as:

$$\rho_{eff} = \rho\, e^{(-\frac{\beta^2 s^2}{2})} \tag{6.21}$$

which is identical to that of physical optics (PO) [103]. For the power density calculation, after some algebra, we conclude that:

$$\begin{aligned}
< |\bar{E}|^2 > \;=\;& |E_0|^2(1 + |A_2|^2 + |A_3|^2 + |A_4|^2 + 2Re(A_2)e^{-\frac{\beta^2 s^2}{2}} \\
& + 2Re(A_3)e^{-\frac{\beta^2 s^2}{2}} + 2Re(A_4)e^{-\frac{4\beta^2 s^2}{2}} + 2Re(A_2 A_3^*) \\
& + 2Re(A_2 A_4^*)e^{-\frac{\beta^2 s^2}{2}} + 2Re(A_3 A_4^*)e^{-\frac{\beta^2 s^2}{2}})
\end{aligned}$$

$$\begin{aligned} = \;& |E|^2_{spec} - 2|E_0|^2[Re(A_2 + A_3 + A_2A_4^* + A_3A_4^*))(1 - e^{-\frac{\beta^2 s^2}{2}}) \\ & +2Re(A_4)(1 - e^{-2\beta^2 s^2})] \end{aligned} \tag{6.22}$$

where $|E|^2_{spec}$ denotes the power density for the specular surface case, superscript $*$ denotes conjugate.

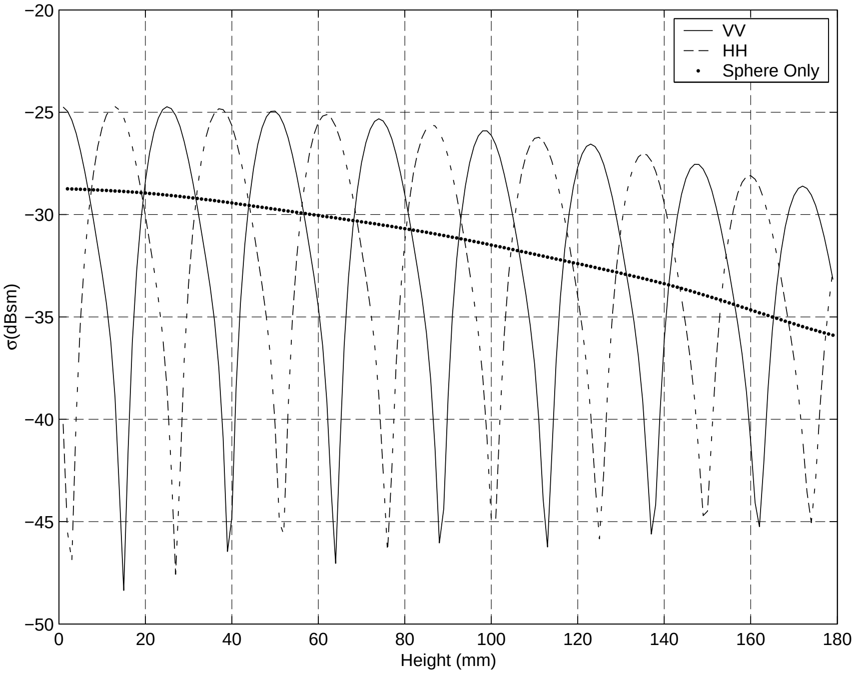

Figure 6.13: Backscatter interference pattern of the $\sigma(dBsm)$ with antenna pattern included as a function of the receiver height above a rough surface with rms height s=1cm. The dots shown are the backscatter $\sigma(dBsm)$ from the sphere itself, which serves as a base for calculating the interference gain/loss. In this example, L=8.5m,$\epsilon = 3$, metallic sphere radius is 1.9cm, and antenna height is 1.5m.

The antenna pattern tends to attenuate the interference pattern and the roughness tends to attenuate the gain, as shown in Figure 6.13. It is seen that the backscatter $\sigma(dBsm)$ from the sphere itself decreases gradually as the sphere moves higher and thus further away from the boresight direction of the antennas. For a radar system with a beamwidth of 1.4°, σ experiences a 7 dB drop as the sphere moves up 18 cm from the boresight direction. Meanwhile, due to the roughness of the surface, the effective reflection coefficient ρ_{eff}, as given in Eq. 6.21, is also smaller in magnitude. Hence, the interference gain drops to 3 dB as compared to 8 dB for a smooth surface (as was shown in Figure 6.10).

6.4 Equivalence Between Monostatic and Bistatic Scattering

The main purpose of using the backscatter technique is to infer the forward scattered field from the measured backscattered field for practical considerations. This section addresses this inference issue by establishing the equivalence between monostatic and bistatic scattering for the coherent components. The conditions for this equivalence relation to hold are also provided.

We shall start with the simple flat-surface case and then progress to the more-complicated rough-surface case.

6.4.1 Case 1. Smooth Surface

In this case, there is no direct surface backscattering, that is, $\bar{E}_5 = 0$. For the sake of clarity, we rewrite the other four components as follows:

$$\begin{aligned}
E_{1pq} &= (\frac{e^{-jkR_1}}{4\pi R_1})^2 f_t(\theta_{1t}) f_r(\theta_{1r}) S_{pq}(-\theta_{10}, \theta_{10}) \\
E_{2pq} &= \frac{e^{-jkR_1}}{4\pi R_1} \frac{e^{-jkR_2}}{4\pi R_2} f_t(\theta_{2t}) f_r(\theta_{1r}) \rho S_{pq}(-\theta_{20}, \theta_{10}) \\
E_{3pq} &= \frac{e^{-jkR_1}}{4\pi R_1} \frac{e^{-jkR_2}}{4\pi R_2} f_t(\theta_{1t}) f_r(\theta_{2r}) \rho S_{pq}(-\theta_{10}, \theta_{20}) \\
E_{4pq} &= (\frac{e^{-jkR_2}}{4\pi R_2})^2 f_t(\theta_{2t}) f_r(\theta_{2r}) \rho^2 S_{pq}(-\theta_{20}, \theta_{20}) \qquad (6.23)
\end{aligned}$$

where the subscripts p,q denote polarization configurations. The ability to factor the summation

$$E_{pq,b} = E_{1pq} + E_{2pq} + E_{3pq} + E_{4pq} \qquad (6.24)$$

is the key to establishing the equivalence.

We assume we can factor the summation as:

$$\begin{aligned} E_{1pq}+E_{2pq}+E_{3pq}+E_{4pq} &= (\frac{e^{-jkR_1}}{4\pi R_1}f_r(\theta_{1r})h_1+\frac{e^{-jkR_2}}{4\pi R_2}\rho f_r(\theta_{2r})h_2) \\ & (\frac{e^{-jkR_1}}{4\pi R_1}f_t(\theta_{1t})h_3+\frac{e^{-jkR_2}}{4\pi R_2}\rho f_t(\theta_{2t})h_4) \qquad (6.25) \end{aligned}$$

where $h_1 \sim h_4$ are unknown functions to be determined. The solutions for $h_1 \sim h_4$ do not exist in general, except for some special cases that meet the following conditions:

$$\begin{aligned} h_1h_3 &= S_{pq}(-\theta_{10},\theta_{10}) \\ h_1h_4 &= S_{pq}(-\theta_{20},\theta_{10}) \\ h_2h_3 &= S_{pq}(-\theta_{10},\theta_{20}) \\ h_2h_4 &= S_{pq}(-\theta_{20},\theta_{20}) \qquad (6.26) \end{aligned}$$

The fact that the scatterer is a sphere implies:

$$h_1h_3 = h_2h_4 \qquad (6.27)$$

For the copolarized fields, which are our main concern, the reciprocity theorem implies:

$$h_1h_4 = h_2h_3 \qquad (6.28)$$

In view of the above, the following condition must hold:

$$h_1^2 = h_2^2 \;\Rightarrow\; h_1 = \pm h_2 \;\Rightarrow\; h_3 = \pm h_4 \qquad (6.29)$$

where the positive or negative signs are assumed simultaneously. Then the following must hold:

$$S_{pp}(-\theta_{10},\theta_{10}) = \pm S_{pp}(-\theta_{20},\theta_{10}) \qquad (6.30)$$

If we concentrate on the absolute value, then the above result states: the bistatic scattering magnitude must be sufficiently close to that of the monostatic magnitude.

For a spherical scatterer, this condition can be satisfied when the scattering direction is within 20 degrees of the incidence direction, that is, the bistatic range can be up to 20 degrees.

So, if the biscattering direction is not far away from the backscattering direction (say, within ±20° range), then we have

$$S_{pp}(-\theta_{10},\theta_{10}) \approx S_{pp}(-\theta_{20},\theta_{10}) \tag{6.31}$$

Note that we have eliminated the minus sign due to the fact that these two terms tend to be equal in both magnitude and phase [9].

Hence we can rewrite the backscatter field as:

$$\begin{aligned} E_{pp,b} &= E_{1pp}+E_{2pp}+E_{3pp}+E_{4pp} \\ &= \left(\frac{e^{-jkR_1}}{4\pi R_1} f_r(\theta_{1r}) + \frac{e^{-jkR_2}}{4\pi R_2}\rho f_r(\theta_{2r})\right) \\ &\quad \left(\frac{e^{-jkR_1}}{4\pi R_1} f_t(\theta_{1t}) + \frac{e^{-jkR_2}}{4\pi R_2}\rho f_t(\theta_{2t})\right) S_{pp}(-\theta_{10},\theta_{10}) \\ &= f_r(\theta_{1r}) f_t(\theta_{1t}) \left(\frac{e^{-jkR_1}}{4\pi R_1}\right)^2 S_{pp}(-\theta_{10},\theta_{10}) \left(1+e^{-jk(R_2-R_1)}\frac{R_1}{R_2}\frac{f_r(\theta_{2r})}{f_r(\theta_{1r})}\rho\right) \\ &\quad \left(1+e^{-jk(R_2-R_1)}\frac{R_1}{R_2}\frac{f_t(\theta_{2t})}{f_t(\theta_{1t})}\rho\right) \end{aligned} \tag{6.32}$$

The forward scattering field is:

$$E_{pp,f} = f_r(\theta_{1r}) f_t(\theta_{1t}) \frac{e^{-jkR_1}}{4\pi R_1}\left(1+e^{-jk(R_2-R_1)}\frac{R_1}{R_2}\frac{f_r(\theta_{2r})f_t(\theta_{2t})}{f_r(\theta_{1r})f_t(\theta_{1t})}\rho\right) \tag{6.33}$$

When the transmitter and receiver are both far enough away from the sphere, the difference between θ_{1r} and θ_{2r} is very small, and so is that between θ_{1t} and θ_{2t}. The antenna pattern will satisfy $\frac{f_r(\theta_{2r})}{f_r(\theta_{1r})} \approx 1$ and $\frac{f_t(\theta_{2t})}{f_t(\theta_{1t})} \approx 1$. Consequently, we have the following:

$$E_{1pp}+E_{2pp}+E_{3pp}+E_{4pp} = f_r(\theta_{1r}) f_t(\theta_{1t}) \left(\frac{e^{-jkR_1}}{4\pi R_1}\right)^2 S_{pp}(-\theta_{10},\theta_{10}) \left(1+e^{-jk(R_2-R_1)}\frac{R_1}{R_2}\rho\right)^2 \tag{6.34}$$

and

$$E_{ppf} = f_r(\theta_{1r})f_t(\theta_{1t})\frac{e^{-jkR_1}}{4\pi R_1}(1 + e^{-jk(R_2-R_1)}\frac{R_1}{R_2}\rho) \tag{6.35}$$

which suggests the following relation between monostatic and bistatic scattering:

$$E_{pp,b} = \frac{S_{pp}(-\theta_{10}, \theta_{10})}{f_r(\theta_{1r})f_t(\theta_{1t})}E^2_{pp,f} \tag{6.36}$$

which indicates that the backward scattered field is proportional to the square of the forward scattered field, within a factor determined by the backscatter of a metallic sphere, antenna pattern and simple geometry.

6.4.2 Case 2. Rough Surface

Following the assumptions underlying Eq. (6.31), we can similarly factor Eq. (6.17) as:

$$\begin{aligned} E_{pp} &= (1 + e^{-jk(R_2-R_1)}\frac{R_1}{R_2}\frac{f_r(\theta_{2r})}{f_r(\theta_{1r})}\tilde{\rho}) \\ &\quad (1 + e^{-jk(R_2-R_1)}\frac{R_1}{R_2}\frac{f_t(\theta_{2t})}{f_t(\theta_{1t})}\tilde{\rho}) \end{aligned} \tag{6.37}$$

where $\tilde{\rho} = \rho e^{-j\beta h(\bar{r}_{spec})}$ is the effective reflection coefficient for a rough surface.

Taking into consideration the far field effect, the relation between monostatic and bistatic scattering is identical to that of a smooth surface, namely:

$$E_{pp,b} = \frac{S_{pp}(-\theta_{10}, \theta_{10})}{f_r(\theta_{1r})f_t(\theta_{1t})}E^2_{pp,f} \tag{6.38}$$

6.5 Experimental Results For The Backscatter Case

In the previous sections, to keep the model tractable, we made some simplifications. The four-ray model is used to calculate the backscatter fields. The validity of this model needs to be checked against measured data.

The setup for the backscatter measurements is shown in Figure 6.14. We shall start with the specular surface case. Given this configuration, to account for the

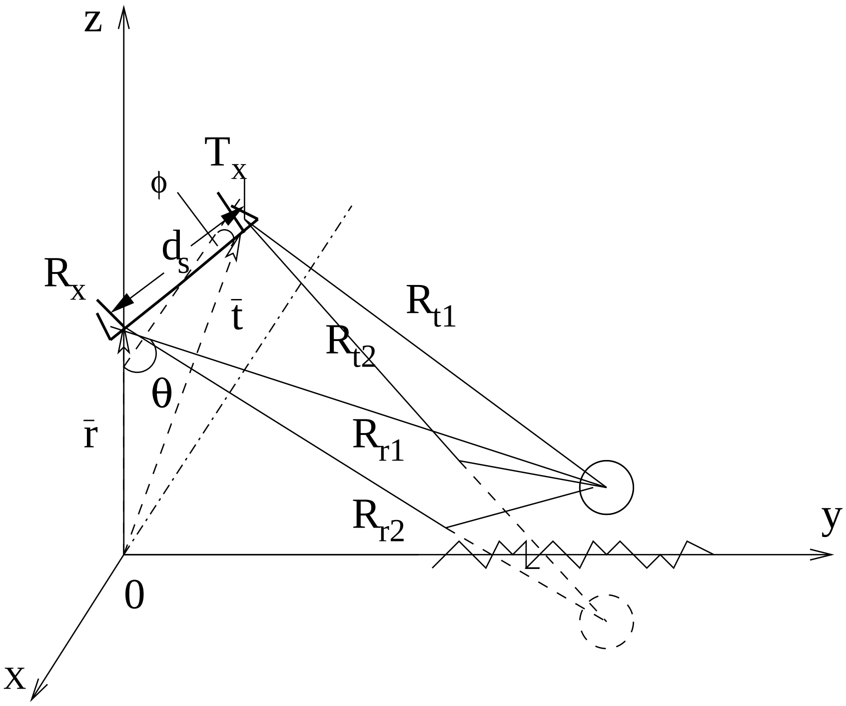

Figure 6.14: Geometry of the forward and backward scattering with antenna pattern for a rough surface

physical distance between the transmitter and receiver, the field components are modified slightly to:

$$
\begin{aligned}
\bar{E}_1 &= \frac{e^{-jkR_{t1}}}{4\pi R_{t1}} \frac{e^{-jkR_{r1}}}{4\pi R_{r1}} \bar{\bar{S}}_1(\tilde{\theta}_{t1}, \tilde{\theta}_{r1}) f_t(\theta_{t1}) f_r(\theta_{r1}) \cdot \hat{e}_1 \\
\bar{E}_2 &= \frac{e^{-jkR_{t2}}}{4\pi R_{t2}} \frac{e^{-jkR_{r1}}}{4\pi R_{r1}} \bar{\bar{S}}_1(\tilde{\theta}_{t2}, \tilde{\theta}_{r1}) \rho_t f_t(\theta_{t2}) f_r(\theta_{r1}) \cdot \hat{e}_1 \\
\bar{E}_3 &= \frac{e^{-jkR_{t1}}}{4\pi R_{t1}} \frac{e^{-jkR_{r2}}}{4\pi R_{r2}} \bar{\bar{S}}_1(\tilde{\theta}_{t1}, \tilde{\theta}_{r2}) \rho_r f_t(\theta_{t1}) f_r(\theta_{r2}) \cdot \hat{e}_1 \\
\bar{E}_4 &= \frac{e^{-jkR_{t2}}}{4\pi R_{t2}} \frac{e^{-jkR_{r2}}}{4\pi R_{r2}} \bar{\bar{S}}_1(\tilde{\theta}_{t2}, \tilde{\theta}_{r2}) \rho_t \rho_r f_t(\theta_{t2}) f_r(\theta_{r2}) \cdot \hat{e}_1 \qquad (6.39)
\end{aligned}
$$

where the relevant items are defined in terms of the following quantities:

(1) the position vectors of receiver $\bar{r}$ and transmitter $\bar{t}$ are given by:

$$
\begin{aligned}
\bar{r} &= [d_s/2(\cos\phi - 1), -d_s/2\sin\phi, H_r] \\
\bar{t} &= [-d_s/2(\cos\phi + 1), d_s/2\sin\phi, H_r] \qquad (6.40)
\end{aligned}
$$

where d_s is the center-to-center distance from transmitter to receiver.

(2) H_r is the height of the antenna, and ϕ is the azimuth angle generated between the transmitter and the receiver in Fig. 6.14.

The normalized direction vector of the transmitting antenna, which is the propagation vector, is given by:

$$\hat{k} = [\sin\theta\sin\phi, \sin\theta\cos\phi, -\cos\theta] \tag{6.41}$$

where θ is the look angle. The position vectors of the sphere $\bar{s}$ and sphere image $\tilde{s}$ are :

$$\begin{aligned} \bar{s} &= [0, L, h_s] \\ \tilde{s} &= [0, L, -h_s] \end{aligned} \tag{6.42}$$

Let *dist* denote the distance operator. Then

$$\begin{aligned} R_{t1} &= dist(\bar{t}, \bar{s}) \\ R_{t2} &= dist(\bar{t}, \tilde{s}) \\ R_{r1} &= dist(\bar{r}, \bar{s}) \\ R_{r2} &= dist(\bar{r}, \tilde{s}) \end{aligned} \tag{6.43}$$

and

$$\begin{aligned} \tilde{\theta}_{t1} &= \angle(\hat{z}, \bar{t}\bar{s}) \\ \tilde{\theta}_{t2} &= \pi - \angle(\hat{z}, \bar{t}\tilde{s}) \\ \tilde{\theta}_{r1} &= \angle(\hat{z}, \bar{s}\bar{r}) \\ \tilde{\theta}_{r2} &= \angle(\hat{z}, \tilde{s}\bar{r}) \\ \theta_{\rho t} &= \tilde{\theta}_{t2} \\ \theta_{\rho r} &= \tilde{\theta}_{r2} \end{aligned} \tag{6.44}$$

We note that $\bar{t}\bar{s}$ is the vector from $\bar{t}$ to $\bar{s}$, or $\bar{s} - \bar{t}$.

6.5.1 Perfectly Conducting Smooth Surface

The above formulation was verified by checking against measurements of a metallic sphere over an aluminum plate. The size of the sheet was 2.4 m × 1.2 m × 3.2 mm. Absorbers were placed in front of the sheet to eliminate diffraction from the front edge. The relevant parameters are: $\theta = 80^\circ, \phi = 0.5^\circ, L = 8.5m, H_r = 1.50m$, f = 35 GHz. The measurements and simulations of VV and HH are shown in Figure 6.15(a) and Figure 6.15(b), respectively. It is seen that the measured pattern is in close agreement with the pattern calculated based on theory.

Moreover, as mentioned before, this measurement technique holds the potential of assisting inversion of some critical physical parameters, such as the effective reflection coefficient. For instance, an inversion of the TM reflection coefficient based on the measured data gives a value of 0.96, very close to the theoretic value of 1 for a metallic sheet.

6.5.2 Smooth Sand Surface Case

The next experiment was to measure a refined sand surface(US Silica ASTM 50-70) of uniform size distribution filling a wooden box of size 1.8 m × 1.05 m × 12.7 cm. Yet due to the limited available sand, the box had to be filled with styrofoam on the bottom first. The thickness of the sand layer was 2 cm. The footprint of the radar signal of the receiver with beamwidth 2.8° is comparable to the size of the box, while that of the transmitter with beamwidth 4.2°, is larger.

Measurements were taken of a sphere over the smooth sand surface. The results are shown in Figure 6.16(a) and Figure 6.16(b), respectively, along with the simulation based on the known dielectric constant for sand, which is 2.6. Both plots show that the simple four-ray model approximately captures the scattering process

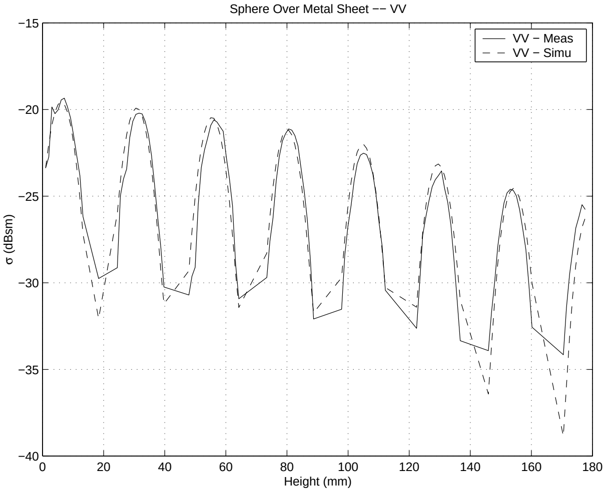

(a) VV

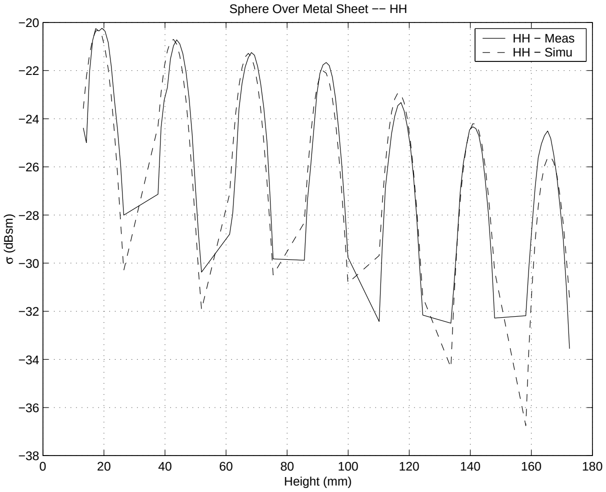

(b) HH

Figure 6.15: Agreement between four-ray model and measurements of backscatter radar cross section $\sigma(dBsm)$ interference pattern for a metallic sphere over an aluminum plate. In this example, antenna height is 1.5 m, distance to sphere is 8.5 m, surface reflection coefficient is 1, and incidence angle is 80°.

under consideration, although the deviation shown may be attributable to volume scattering and the limited thickness of the sand.

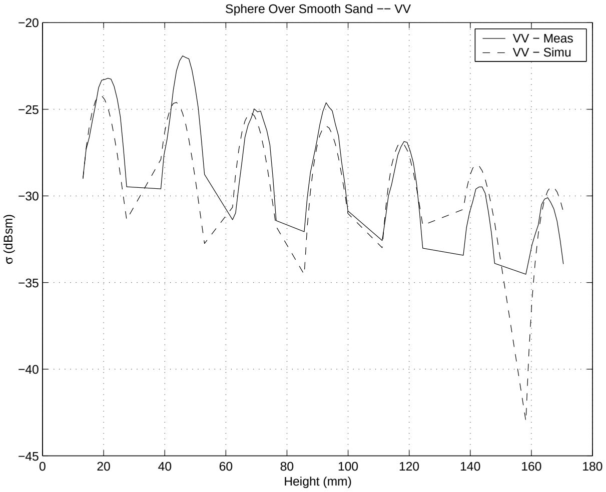

(a) VV

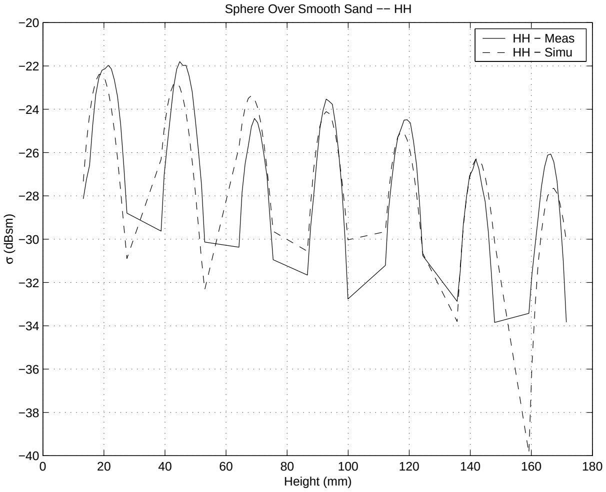

(b) HH

Figure 6.16: Agreement between four-ray model assuming perfect dielectric constant of the medium (sand) and measurements of backscatter radar cross section $\sigma(dBsm)$ interference pattern for a metallic sphere over a smooth sand surface. In this example, antenna height is 1.5 m, L=8.5 m, incidence angle is 80°, $\epsilon = 2.6 - j0.1$

6.5.3 Rough Soil Surface Case

To investigate the interference pattern for a rough surface, fifty independent samples are obtained for each height of the sphere above a slightly wet rough soil surface. The rms height of the rough surface is 1 cm.

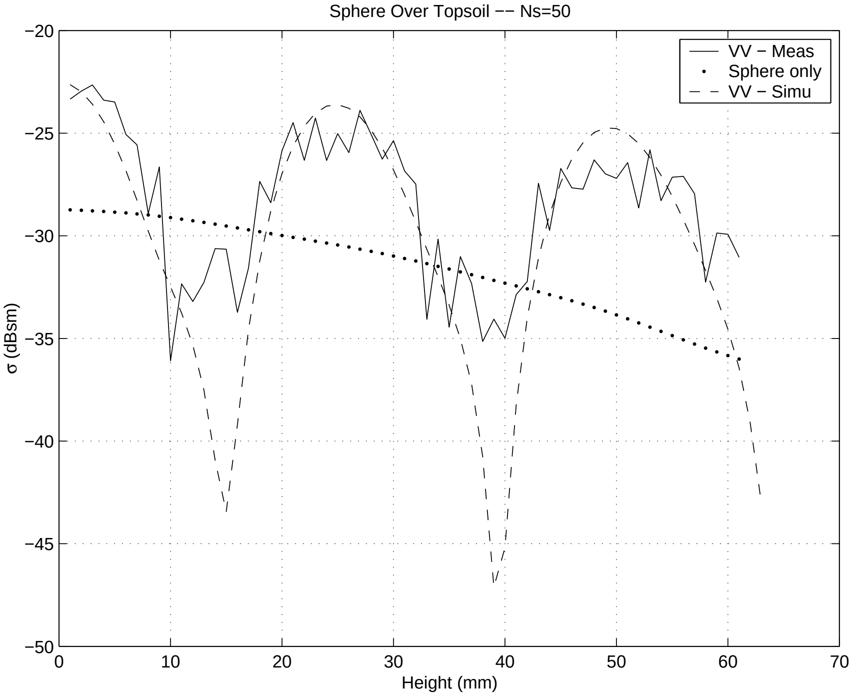

Figure 6.17: Agreement between four-ray model assuming an effective reflection coefficient and measurements of backscatter radar cross section $\sigma(dBsm)$ interference pattern for a metallic sphere over a rough soil surface with rms height of 1cm. In this example, antenna height is 1.5 m, L=8.5 m, incidence angle is 80°, and the effective reflection coefficient along boresight direction is 0.7. The number of independent samples used to calculate the coherent field is 50.

The coherent fields of the measurements are shown in Figure 6.17. It clearly shows an interference pattern (large scale) with local random variations due to the incoherent component. The four-ray model given by Eq. 6.39 and Eq. 6.21 is applied, assuming an effective reflection coefficient of 0.7 at the boresight direction. Good agreement between simulation and measurements is obtained, which suggests that the valid region of the simple four-ray model can be extended to a relatively complicated setting such as a rough surface with rms height of 1 cm, or $ks = 2\pi s/\lambda = 7.3$. Nevertheless, the local variations raise the concern whether it is possible for the coherent field to be so dominated by the incoherent component as the roughness increases that the interference pattern becomes no longer discernible? If this is the case, then the backscatter technique will fail to provide any inference of the forward scattered field.

The answer to the above question depends on the ratio between the coherent and incoherent power, which is equivalent to SNR in communication, and the number of independent samples N. A detailed theoretical analysis of this topic is given in Section 6.6.

6.5.4 Grass-Covered Surface Case

Grass-covered surfaces represent a more complicated situation. Similar to the topsoil case, 50 independent samples were obtained for each sphere position. The coherent field is shown in Figure 6.18. It is very difficult to tell whether or not the measured variation contains a periodic interference pattern. Figure 6.19 shows that the averaged incoherent component of the received power is the dominant component since its average value is about 7 dB higher than the coherent component. A simulated interference pattern is plotted against the measurements to illustrate to what degree the interference pattern is destroyed.

The measurements were repeated to obtain 100 and 200 independent samples, so as to reduce the effect of the incoherent component. Neither dataset provided a discernible interference pattern, however.

The above observations elicit the following questions: given a SNR, how many

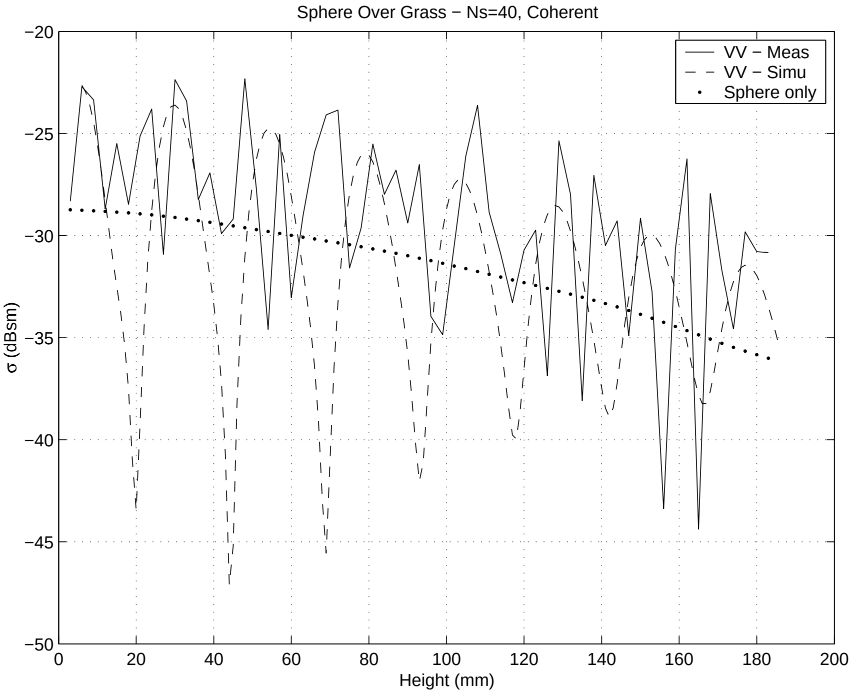

Figure 6.18: Coherent component of VV backscattered field from a metallic sphere over grass covered surface. 40 independent samples are used to calculate the coherent field.

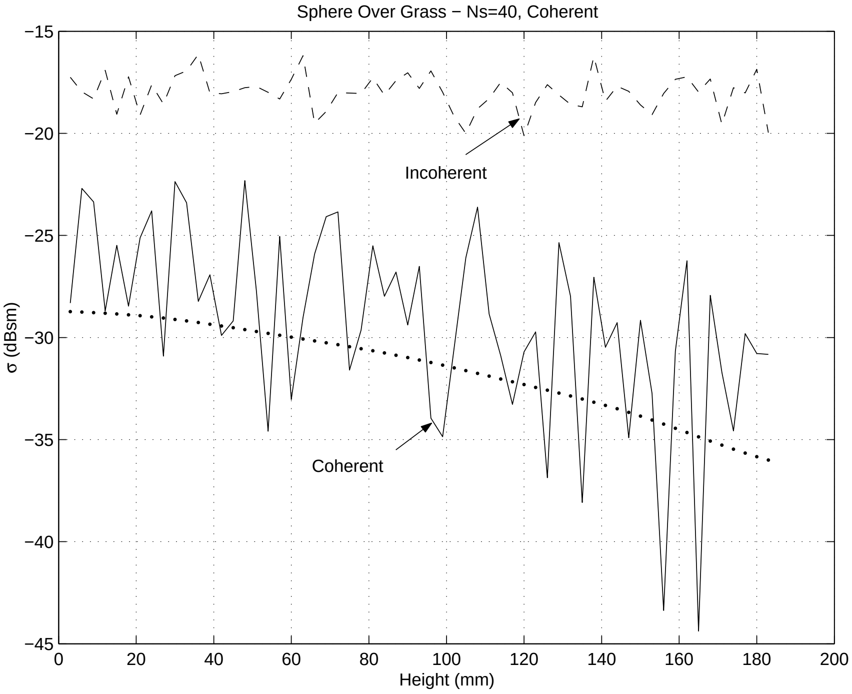

Figure 6.19: Comparison between the measured coherent and average incoherent components of VV backscattered field from a metallic sphere over a grass-covered surface. 40 independent samples are used for all calculations.

independent samples would be needed to establish a clear interference pattern?

Or more specifically, since the interference pattern describes the behavior of the magnitude of the coherent field, the question is: how well can it be estimated for a given SNR and a specified number of independent samples N?

6.6 Estimation of Backscatter Parameters

The measured backscattered field can be written as:

$$x_n = x + v_n \tag{6.45}$$

where x is the coherent field, $v_n \sim N(0, \sigma^2 I_2)$ represents the incoherent component, σ^2 is the incoherent power of either the real or imagery part of the field, I_2 is the 2×2 identity matrix to recognize the complex field.

To estimate $|x|$ and σ^2, two methods can be used:

<u>Method 1</u>: Maximum likelihood (ML)

Define $\mu = |x|$. It is well known that $r = |x_n|$ follows a Rice distribution [103]:

$$p(r) = \frac{r}{\sigma^2} e^{(} - \frac{1}{2\sigma^2}(r^2 + \mu^2)) I_0(\frac{r\mu}{\sigma^2}) \tag{6.46}$$

where $I_0(\cdot)$ is the modified Bessel function of 0-th order.

When N independent samples are available, the likelihood is

$$J = p(r_1, r_2, ..., r_N) = \prod_{i=1}^{N} p(r_i) \tag{6.47}$$

The ML method seeks such μ and σ that maximize J, or equivalently, $\ln J$:

$$\ln J = \sum_{i=1}^{N} \ln r_i - 2N \ln \sigma - \frac{N\mu^2}{2\sigma^2} - \sum_{i=1}^{N} \frac{r_i^2}{2\sigma^2} + \sum_{i=1}^{N} \ln[I_0(\frac{r_i \mu}{\sigma^2})] \tag{6.48}$$

Solution for (μ, σ) may be obtained by solving:

$$\begin{aligned} \frac{\delta}{\delta\mu} \ln J(\mu,\sigma) &= 0 \\ \frac{\delta}{\delta\sigma} \ln J(\mu,\sigma) &= 0 \end{aligned} \qquad (6.49)$$

Because lnJ is highly nonlinear in structure, it is very difficult, if not impossible, to obtain a closed-form solution for Eq. 6.49. Nevertheless, we can still take advantage of the following relation:

$$\frac{1}{N}\sum_{r=1}^{N} r_i^2 = \mu^2 + 2\sigma^2 = E(r^2) \qquad (6.50)$$

Hence if we define $\gamma = \frac{\mu^2}{2\sigma^2}, y = \frac{r}{E(r^2)}$, the pdf can be written as:

$$p_y(y|\gamma) = 2(1+\gamma)ye^(- [(1+\gamma)y^2 + \gamma])I_0(2y\sqrt{\gamma(1+\gamma)}) \qquad (6.51)$$

which depends only on a single parameter, γ. A ML solution for γ requires:

$$\frac{1}{1+\gamma} + \frac{1+2\gamma}{N\sqrt{\gamma(1+\gamma)}} \sum_{i=1}^{N} \frac{y_i I_1(y_i')}{I_0(y_i')} = 1 + \frac{1}{N}\sum_{i=1}^{N} y_i^2 \qquad (6.52)$$

where $y_i' = 2y_i\sqrt{\gamma(1+\gamma)}$, and $I_1(\cdot)$ is the modified Bessel function of 1st order. It comes as no surprise that a closed form analytic solution for γ is still beyond our reach. Hence, we have to resort to a numerical solution.

After the magnitude of γ is determined numerically using Eq. 6.52, the result can be used in conjunction with Eq. 6.50 to solve for μ and σ.

The ML estimator performance has two important attributes:

a) The ML estimator is biased, since the Rice distribution does not belong to the exponential family [87].

b) The ML estimator is not a uniformly minimum variance estimator(UMVUE), again due to the fact that the Rice distribution is not in the exponential family [87].

Method 2: Coherent averaging to estimate σ and μ.

The coherent backscattered field after averaging over N independent samples is:

$$\bar{x} = x + \frac{1}{N}\sum_{n=1}^{N} v_n = x + \bar{v} \qquad (6.53)$$

where $\bar{v} \sim N(0, \frac{1}{N}\sigma^2 I_2)$.

Let $\hat{\mu} = E(|\bar{x}|)$ be the estimator of $|x| = \mu$, which is a biased estimator because

$$E(|\bar{x}|) = \sqrt{\frac{\pi N}{8}} \frac{((\mu^2 + 2\sigma^2/N)I_0(\frac{\mu^2 N}{4\sigma^2}) + \mu^2 I_1(\frac{\mu^2 N}{4\sigma^2}))e^{(} - \frac{\mu^2 N}{4\sigma^2})}{\sigma} \tag{6.54}$$

which is not equal to $|x|$ in general.

Now if we form the vector

$$\left[\begin{array}{cccccc} x_{1r} - \bar{x}_r & \ldots & x_{Nr} - \bar{x}_r & x_{1i} - \bar{x}_i & \ldots & x_{Ni} - \bar{x}_i \end{array} \right]$$

and construct

$$\hat{\sigma}^2 = \frac{1}{2N-1}[\sum_{n=1}^{N}(x_{nr} - \bar{x}_r)^2 + \sum_{n=1}^{N}(x_{ni} - \bar{x}_i)^2] \tag{6.55}$$

then we know $\hat{\sigma}^2$ is an unbiased estimate of σ^2. Meanwhile, $\hat{\sigma}^2$ follows a gamma distribution.

The estimation uncertainties are:

$$\begin{aligned} Var(\hat{\mu}) &= (\mu^2 + 2\frac{\sigma^2}{N}) - E^2(|\bar{x}|) + (E(|\bar{x}|) - \mu)^2 \\ Var(\hat{\sigma}^2) &= \frac{2\sigma^4}{2N-1} \end{aligned} \tag{6.56}$$

where Var stands for the variance.

To make use of SNR, which we define as $\gamma = \frac{\mu^2}{\sigma^2}$, we need to normalize the data samples with respect to σ. If we define $y = r/\sigma$, the new pdf is:

$$f_y(y) = \frac{2(1+\gamma)y}{\sqrt{2+\gamma}} e^{(} - [\frac{1+\gamma}{2+\gamma}y^2 + \gamma]) I_0(2y\sqrt{\frac{\gamma(1+\gamma)}{2+\gamma}}) \tag{6.57}$$

Let $\hat{\eta} = E(|y|)$ be the estimator of μ/σ. The mean and variance for this estimator $\hat{\eta}$ is given as:

$$\begin{aligned} E(\hat{\eta}) &= \sqrt{\frac{\pi N}{8}}((\gamma + 2/N)I_0(N\gamma/4) + \gamma I_1(N\gamma/4))e^{(} - N\gamma/4) \\ Var(\hat{\eta}) &= (\gamma + 2/N) - E^2(\hat{\eta}) + (E(\hat{\eta}) - \sqrt{\gamma})^2 \end{aligned} \tag{6.58}$$

However, the expression for the σ estimator is much simpler:

$$\begin{aligned} E(\hat{\sigma}^2) &= 1 \\ Var(\hat{\sigma}^2) &= \frac{2}{2N-1} \end{aligned} \tag{6.59}$$

The asymptotic behavior of the estimator $\hat{\eta}$ as the number of independent samples N goes to infinity merits some elaboration.

It is well known that for the modified Bessel function of p-th order, when the argument $z \to 0$,

$$I_p(z) \sim \frac{e^z}{\sqrt{2\pi z}}(1 - \frac{\mu - 1}{8z} + o(\frac{1}{z^2})) \tag{6.60}$$

where $\mu = 4p^2$.

Now when $N \to \infty$, we have the following:

$$\begin{aligned} E(\hat{\eta}) &\sim \sqrt{\frac{\pi N}{8}}((\gamma + 2/N)\frac{e^{(}N\gamma/4)}{\sqrt{2\pi N\gamma/4}} + \gamma\frac{e^{(}N\gamma/4)}{\sqrt{2\pi N\gamma/4}})e^{(} - N\gamma/4) \\ &\to \sqrt{\gamma} = \frac{\mu}{\sigma} \\ Var(\hat{\eta}) &\to 0 \end{aligned} \tag{6.61}$$

which simply states that "the estimator provides an unbiased estimation" is approximately true.

6.7 Forward Scattering Measurements

From the previous sections, it is seen that it is very difficult to measure the interference pattern of the coherent component from the backscatter measurements when the field is highly disturbed by a random scattering medium, even after performing coherent averaging with a large number of independent samples. Thus, it is difficult to infer the forward scattered field from backscattered measurements of a sphere over a volume scattering medium such as grass. Consequently, we need to resort to forward scattering measurements.

Yet what to measure? Another interference pattern as a function of the receiver height? For smooth and slightly rough surfaces, we can expect some well behaved interference pattern, which is helpful for diversity planning to combat signal nulls, nulls that are usually associated with substantially low SNR at the receiver. Yet this pattern becomes quite complicated when the surface is medium rough or covered with vegetation such as grass. In such cases, regardless of the receiver position, the received signal is the summation of multipath signals, and therefore subject to signal fading.

From diversity theory, if statistical information of each path is available, then the multipath signal can be processed in an optimal fashion to bridge the deep fading gap [77]. Hence it is more important to characterize the channel response statistics for any receiver position than to conduct the interference pattern measurement as a function of receiver height. Such channel characterization is therefore the topic of this section.

Since the channel response is the superposition of many scattered fields, we can start by studying the scattered fields thereafter. If the field is scattered from a homogeneous random medium, then it follows a complex Gaussian distribution, which is completely characterized by its mean and variance, or coherent and incoherent parts of the scattered field. The homogeneous random media we chose included a dry rough surface, a wet rough surface, and a grass-covered rough surface.

6.7.1 Measurements Description

The measurements were conducted using a 35 GHz network-analyzer based radar system developed by the University of Michigan. Its specifications are summarized in Table 6.2:

Table 6.2: Network-Analyzer Based System

RF Frontend	35 GHz
Maximum Bandwidth	2 GHz
Transmitter Beamwidth	4.2°
sidelobe level	-20 dB
Polarization isolation	> 25dB
Polarizations trans.	any
Receiver Beamwidth	2.1°
sidelobe level	-20 dB
Polarization isolation	> 25dB

The random medium (topsoil or grass) was placed on top of a turntable. The transmitter and receiver were well aligned to be coplanar. The geometry of the measurements is shown in Figure 6.20.

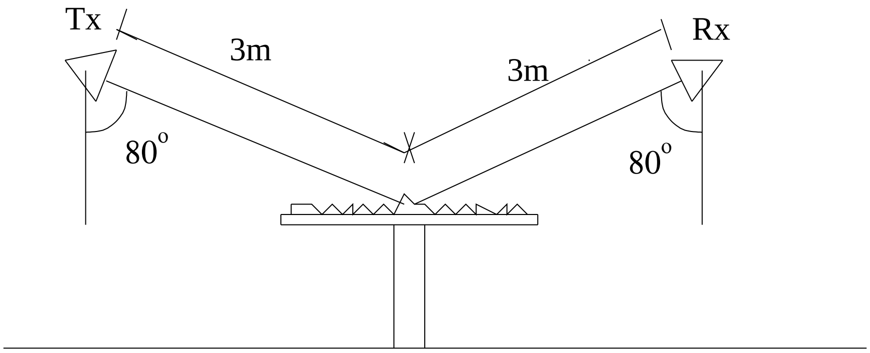

Figure 6.20: Setup for forward scattering measurements

6.7.2 Measurements

Figure 6.21 shows the coherent power and phase of the forward scattered field from a dry soil surface with a rms height of 8mm measured across the 35 GHz system bandwidth. It is seen that HH is higher than VV, which is as expected since the Fresnel coefficient for HH is higher than that for VV. Also the difference in phase angle is 180°, as expected. The incoherent power is shown in Figure 6.22. It is several dB higher than the coherent power level.

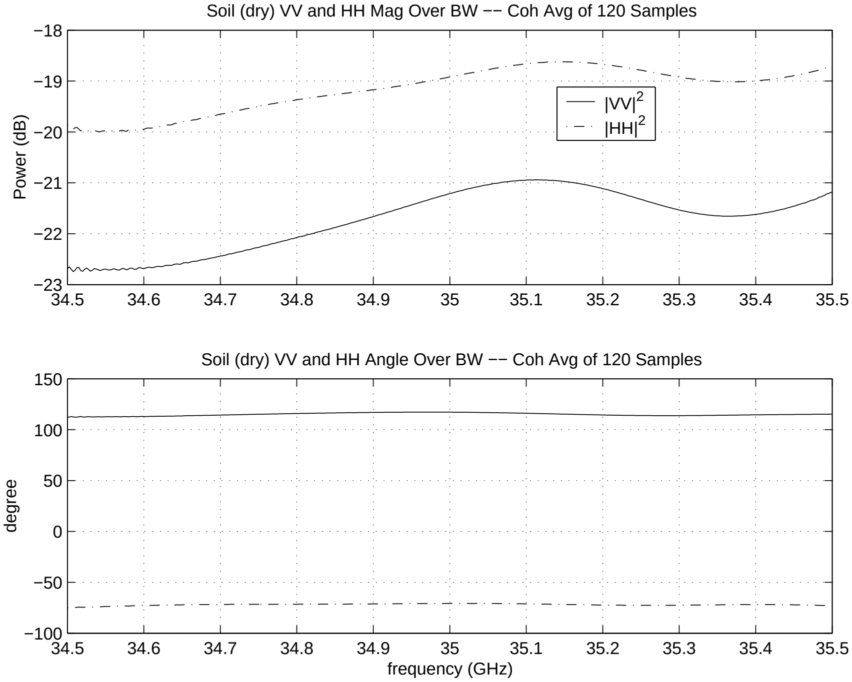

Figure 6.21: Coherent power and phase of the forward scattered field from a dry soil surface with a rms height of 8mm measured across the 35 GHz system bandwidth.

The same observations apply to measurements of the forward scattered field from wet soil, as shown in Figures 6.23 and 6.24. In addition, it shows 1dB increase in power level for both coherent and incoherent components, and slightly wider separation between the copolarized coherent powers due to the increased reflection coef-

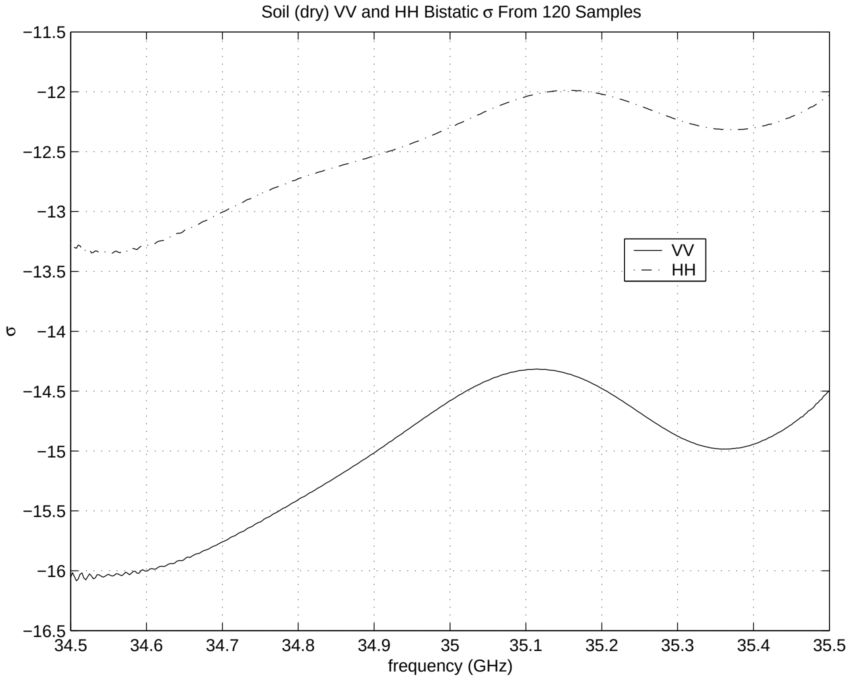

Figure 6.22: Incoherent power of the forward scattered field from a dry soil surface with a rms height of 8mm measured across the 35 GHz system bandwidth.

ficient.

The measurements for grass-covered soil are shown in Figures 6.25 and 6.26, respectively. The coherent components are contributed almost solely by the underlying soil surface, since for a thin and long structure like grass, which can be modeled as a straight line-dipole lying along the $\hat{z}$ axis, the scattered field is [88]:

$$S_{pq} = \frac{k_0^2}{4\pi} l\hat{p} \cdot P \cdot \hat{q} \frac{\sin U}{U} \tag{6.62}$$

where U is given by:

$$U = \frac{kl}{2}(\cos\theta_s - \cos\theta_i) \tag{6.63}$$

Hence when l is sufficiently large, the factor $\sin U/U$ approaches a delta function, which means that the scattered field is highly concentrated around the forward propagation direction. One should notice that when $\theta_s = \theta_i$, the factor $\sin U/U$

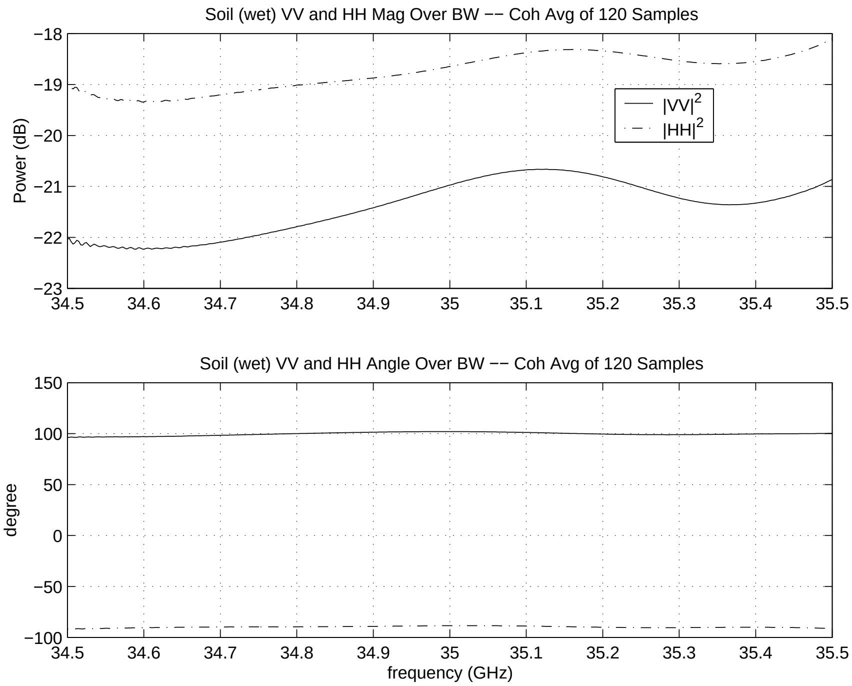

Figure 6.23: Coherent power and phase of the forward scattered field from a wet soil surface with a rms height of 8mm measured across the 35 GHz system bandwidth.

degenerates to a delta function also.

It is seen that the HH coherent power level is 8dB down from that for the dry soil surface, and the VV coherent power level is 11dB down from that of the dry soil surface. This suggests that the grass layer serves as a highly attenuating medium, with higher attenuation rate for VV due to the vertical structure of grass. Similar observations are applicable to the incoherent components.

Figure 6.27 shows the magnitude and power statistics of the incoherent scattered field. It is seen that the magnitude follows closely the Rayleigh distribution while the power follows closely the exponential distribution, suggesting a circularly symmetric complex Gaussian distribution.

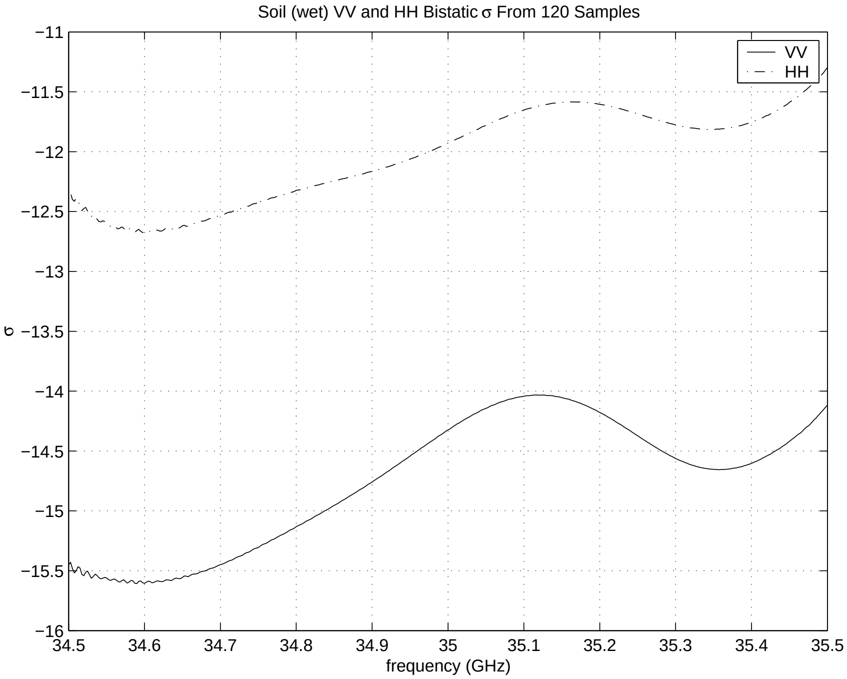

Figure 6.24: Incoherent power of the forward scattered field from a wet soil surface with a rms height of 8mm measured across the 35 GHz system bandwidth.

6.8 Relating Forward and Backward Scattered Incoherent Powers

In this section, we try to relate the forward and backward incoherent powers scattered from a volume scattering medium like grass with azimuthal symmetry. At near grazing incidence of 80°, we conjecture that the backscatter is dominated by the volume scattering from grass, hence it provides only information related to volume scattering for the forward scattering case. The relations are best illustrated in Figure 6.28.

We assume a simple scattering model for the forward scattering cross section of the grass-covered ground:

$$\sigma_t = \Gamma\sigma_g + \sigma_v \tag{6.64}$$

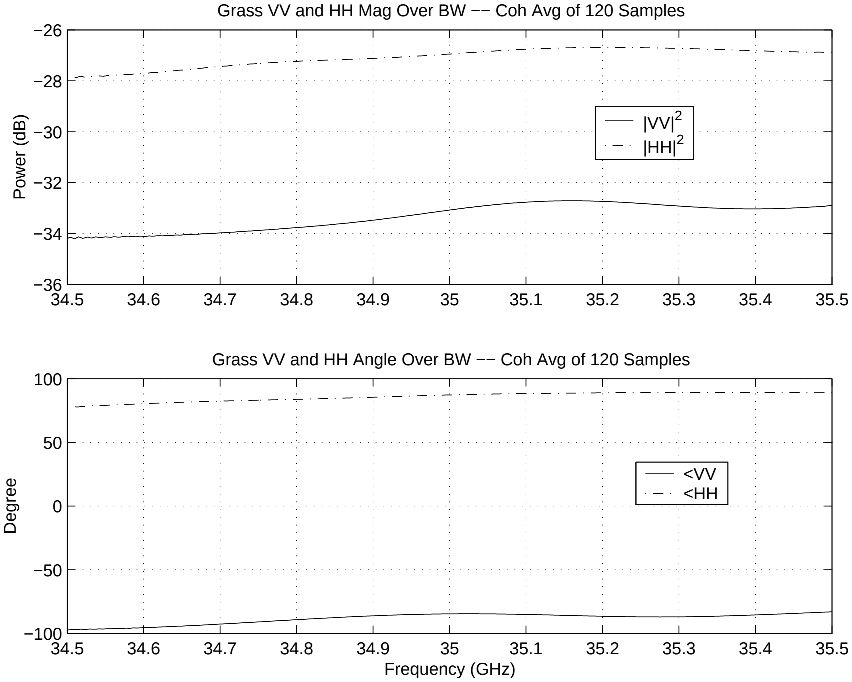

Figure 6.25: Coherent power and phase of the forward scattered field from a grass-covered surface with a rms height of 8mm measured across the 35 GHz system bandwidth.

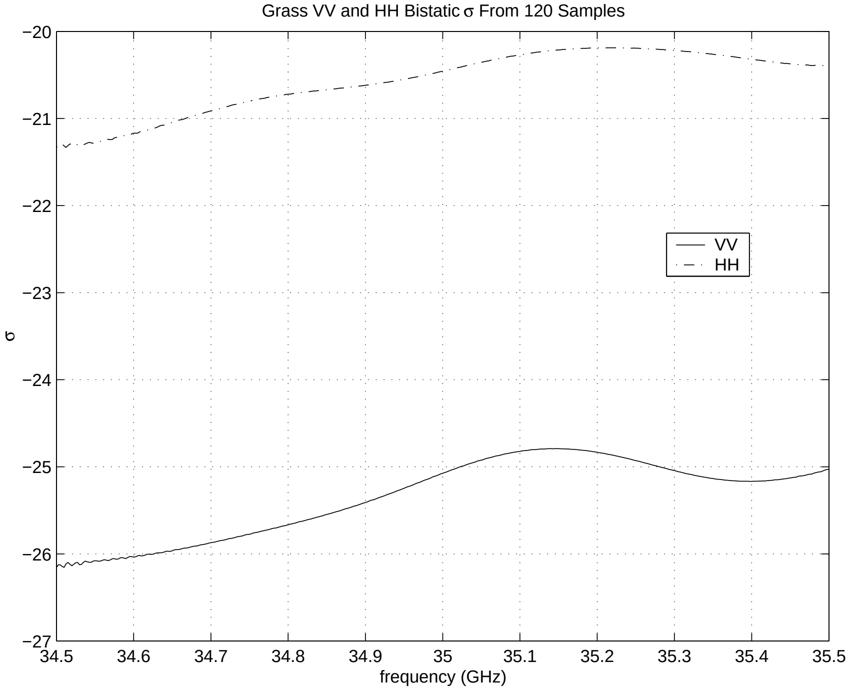

Figure 6.26: Incoherent power of the forward scattered field from a grass-covered surface with a rms height of 8mm measured across the 35 GHz system bandwidth.

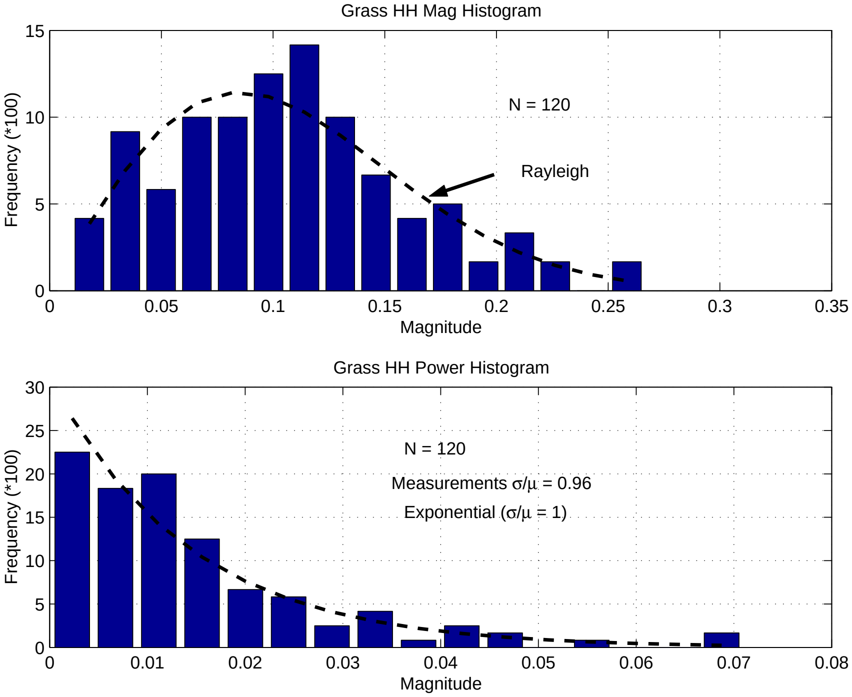

Figure 6.27: Magnitude and power distributions of the incoherent component of the forward scattered field from a grass-covered surface (bar graph). The number of independent samples is 120. They follow closely the Rayleigh and exponential distributions (broken lines), respectively.

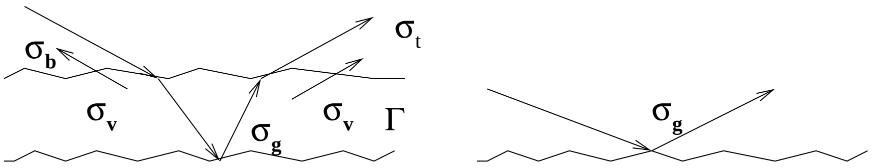

Figure 6.28: Forward cross sections for a grass-covered surface and for the surface only

Table 6.3: Forward Scattering Measurements Data

	Coherence		Incoherence	
	VV	HH	VV	HH
surface only	-21.21	-18.92	-14.58	-12.30
surface+grass	-33.08	-26.95	-25.08	-20.46
difference	11.87	8.03	11.50	8.16

which states that the total forward cross section σ_t is the sum of surface cross section σ_g being attenuated by the transmission coefficient Γ, and the volume cross section σ_v. Since cross section is proportional to incoherent power, we can rewrite Eq. 6.64 as:

$$P_t = \Gamma P_g + P_v \tag{6.65}$$

or

$$\frac{P_t}{P_g} = \Gamma + \frac{P_v}{P_g} \tag{6.66}$$

where P denotes incoherent power, and the subscripts bear the same meaning.

We shall try to determine the forward volume scattered incoherent power P_v. Assume both the coherent and incoherent powers are attenuated by the same rate. From the measured data we can tabulate the relevant values as shown in Table 6.3(all numbers are in dB):

Take VV for example. After substituting all the relevant numbers into Eq. 6.66, we have:

$$\begin{aligned} 10^{-10.5/10} &= 10^{-11.87/10} + \frac{P_v}{P_g} \\ \Rightarrow \frac{P_v}{P_g} &= 0.024 = -16.2dB \\ \Rightarrow P_v &= -14.58 - 16.2 = -30.78dB \end{aligned} \tag{6.67}$$

This result is very close to the measured backscatter incoherent power of $P_b = -30.92$ dB. The good agreement between model prediction and measurements justifies our conjecture.

6.9 Conclusion

In this chapter, an attempt was made to investigate the conditions under which the backscatter technique can be used to substitute for forward scattering to circumvent the difficulties encountered in the experimental setup for forward scattering. It is found that for a range of surface conditions from smooth to slightly rough even to medium rough, the backward scattered fields were predicted using a four-ray model to be in good agreement with the measurements, indicating the practicality of such substitution in light of the equivalence between forward and backward scattering established in section 6.4. However, when a volume scattering medium such as grass-covered surface is encountered, the four-ray model fails to predict the coherent field given the high disturbance inherent in such medium. Forward scattering technique is called for use in such cases. Study of MMW forward scattering from rough surface is the subject of next chapter.

As incoherent field is concerned, the backscatter measurements can provide good estimation of the volume scattering if the medium is azimuthally symmetric. However, the incoherent component from the surface is almost missed in the backscattering due to the near grazing incidence.

CHAPTER VII

Extension to the IEM Model to Incorporate Antenna Pattern For Rough Surface Scattering

7.1 Introduction

In studying rough surface scattering, the Kirchhoff model and the small perturbation model are among the most widely used models. Yet their efficiency is restricted to small roughness or long correlation length surfaces. For instance, to study the scattering of an incident plane wave with wavenumber k from a rough surface with rms height σ and correlation length l, the Kirchhoff model is used within the following restrictions: $k\sigma \leq 1.5$ and $kl > 6.28$, and the validity region of the small perturbation model (SPM) is $k\sigma < 0.3$ and $kl \leq 3$.

To circumvent these limitations, the integral equation model (IEM) was recently developed [34] and has become one of the most popular theoretical models for rough surface scattering [63] [62] [13] [10] [20] [81] [24]. The IEM attempts to bridge the gap between the validity regions of the Kirchhoff and the small perturbation model. Moreover, it also attempts to include multiple-scattering effects as second order. This model assumes a uniform plane wave incident upon the rough surface, then proceeds to determine the tangential electric and magnetic fields, which are then decomposed into a standard Kirchhoff and complementary components. Finally the Stratton-Chu integral is invoked in order to calculate the scattered far field from the rough surface. Further extensions to the IEM model can be found in [45] [14] [44] [2] [36]. All of the above variations found in the literature follow the original work in assuming a uniform plane wave incident upon the rough surface. A comparison of backscattering models for rough surfaces was provided in [13].

The IEM model is mostly used for the calculation of the backscatter or bistatic scattering coefficients. In either of these cases, theoretical results, which are based on the assumption of uniform plane wave incidence, are usually compared without any danger with the measurements where the antenna pattern of the scatterometers is accounted for by calibration. However, in the case of wireless communication, the antenna pattern must be incorporated into the theoretical formulation for rough surface scattering, because it is almost impossible to perform any calibration given the constantly changing distance between the transmitter and receiver, the terrain condition, and the incidence angles, just to name a few. It thus calls for modifications to the conventional IEM formulation to address this issue.

Given the importance of including the antenna pattern into the theoretical formulation for rough surface scattering, it might be assumed that at least some significant work has been done in this regard. Yet surprisingly, such work can hardly be found in the literature. The absence is mostly due to the detachment of the remote sensing and wireless communication community. For the former, studying of the backscatter or bistatic scattering coefficient from rough surface is of primary concern, where the conventional IEM formulation has brought many plausible successes in explaining radar calibrated measurements. For the latter, the critical channel characterization problem is to determine the so called scattering function which tries to capture the multipath and Doppler spreads in a compact form [79] [77].

Studying the coherent and incoherent scattered fields at any specific point from a rough surface, which is the main theme of this chapter, covers a wide range of realistic wireless communication settings and can serve as a starting point for developing more advanced models for more complicated terrain conditions such as vegetation-covered rough surface.

Specifically, we shall derive the theoretical formulation for rough surface scattering with the antenna pattern being taken into consideration. The derivation basically follows the method outlined in [34] IEM formulation with two exceptions: 1) the antenna pattern is incorporated wherever is appropriate; 2) to avoid unnecessary numerical integration, the Fresnel region argument is adopted to identify the effective illuminated area.

It is conceivable to keep the antenna pattern as generic as possible, except certain restrictions are in order: 1) the antenna pattern is axially symmetrical with regard to its boresight; 2) the antenna pattern affects the amplitude not the phase, which is usually the assumption made for exponential beam; 3) the antenna pattern has continuous first order partial derivatives with respect to its arguments.

This chapter is organized as follows. The IEM method will be recapitulated briefly to provide the necessary background; then we derive the theoretical formulation for rough surface scattering with the antenna pattern being taken into consideration; calculation of the antenna pattern and its first order derivatives with respect to it arguments are performed for two hypothetic antenna patterns, namely, sinc beam and exponential beam; then some simulation results will be presented for different settings. The last section concludes this chapter.

7.2 IEM Model

This section provides a brief summary of the IEM model as derived in [34], which provides the base for our new treatment as detailed in the next section.

Assuming a uniform plane wave incident upon a rough surface:

$$\bar{E}^i = \hat{p} E_0 e^{\{-j(\bar{k}_i \cdot \bar{r})\}} = \hat{p} E^i \tag{7.1}$$

where $\bar{k}_i = \hat{k}_i k$ is the wave propagation vector, and $\hat{p}$ is the unit polarization vector.

Let the incident and scattered directions be defined as shown in Fig. 7.1.

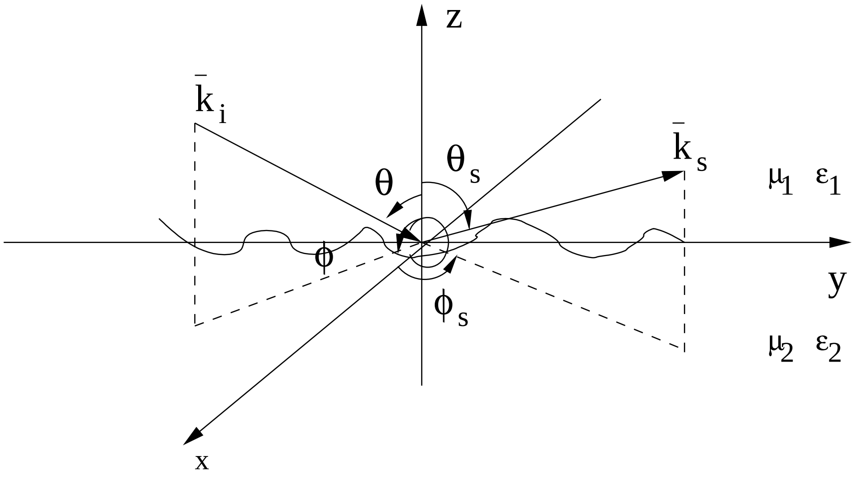

Figure 7.1: Geometry of rough surface scattering of an incident plane wave.

Then the propagation and polarization vectors are:

$$\begin{aligned}
\bar{k}_i &= k(\hat{x}\sin\theta\cos\phi + \hat{y}\sin\theta\sin\phi - \hat{z}\cos\theta) \\
&= \hat{x}k_x + \hat{y}k_y - \hat{z}k_z \\
\hat{h} &= -\hat{x}\sin\phi + \hat{y}\cos\phi \\
\hat{v} &= \hat{x}\cos\theta\cos\phi + \hat{y}\cos\theta\sin\phi + \hat{z}\sin\theta
\end{aligned} \tag{7.2}$$

for the incident wave and

$$\begin{aligned}
\bar{k}_s &= k(\hat{x}\sin\theta_s\cos\phi_s + \hat{y}\sin\theta_s\sin\phi_s + \hat{z}\cos\theta_s) \\
&= \hat{x}k_{sx} + \hat{y}k_{sy} + \hat{z}k_{sz} \\
\hat{h}_s &= \hat{x}\sin\phi_s - \hat{y}\cos\phi_s \\
\hat{v}_s &= -\hat{x}\cos\theta_s\cos\phi_s - \hat{y}\cos\theta_s\sin\phi_s + \hat{z}\sin\theta_s \qquad (7.3)
\end{aligned}$$

for the scattered wave.

The tangential fields over the surface contain the standard Kirchhoff term and a complementary term to represent the second-order multiple scattering:

$$\begin{aligned}
\hat{n}\times\bar{E} &= (\hat{n}\times\bar{E})_k + (\hat{n}\times\bar{E})_c \\
\hat{n}\times\bar{H} &= (\hat{n}\times\bar{H})_k + (\hat{n}\times\bar{H})_c \qquad (7.4)
\end{aligned}$$

where the subscripts k and c denote the Kirchhoff and the complementary components, respectively, and $\hat{n}$ is the surface vector with unit norm which is determined by:

$$\hat{n} = \frac{-Z_x\hat{x} - Z_y\hat{y} + \hat{z}}{D_1} \qquad (7.5)$$

with $D_1 = \sqrt{Z_x^2 + Z_y^2 + 1}$, and Z_x and Z_y are local slope terms:

$$\begin{aligned}
Z_x &= \frac{\partial z}{\partial x} \\
Z_y &= \frac{\partial z}{\partial y} \qquad (7.6)
\end{aligned}$$

where $z = z(x, y)$ is the surface height at point (x, y).

The Kirchhoff tangential fields can be approximated as:

$$\begin{aligned}
(\hat{n}\times\bar{E})_{kv} &\approx (1 - R_{||})\hat{n}\times\hat{v}E^i \\
\eta(\hat{n}\times\bar{H})_{kv} &\approx (1 + R_{||})\hat{n}\times(\hat{k}_i\times\hat{v})E^i
\end{aligned}$$

$$\begin{aligned}(\hat{n}\times\bar{E})_{kh} &\approx (1+R_{\perp})\hat{n}\times\hat{h}E^{i}\\ \eta(\hat{n}\times\bar{H})_{kh} &\approx (1-R_{\perp})\hat{n}\times(\hat{k}_i\times\hat{h})E^{i}\end{aligned} \tag{7.7}$$

where $R_{||}$ and $R_{\perp}$ are TM and TE Fresnel reflection coefficients, respectively.

The complementary tangential fields can be approximated similarly.

In accordance with the Stratton-Chu integral, the scattered far field in the medium above the rough surface can be written as

$$E^{s}_{qp} = C\int[\hat{q}\times\hat{k}_s\cdot(\hat{n}\times\bar{E}_p)+\eta\hat{q}\cdot(\hat{n}\times\bar{H}_p)]e^{\{j(\hat{k}_s\cdot\bar{r})\}}ds \tag{7.8}$$

where $C = -\frac{jk}{(4\pi)^2R_1R_2}e^{\{-jk(R_1+R_2)\}}$, R_1 and R_2 are the distances from the specular point on the surface to the transmitter and to the receiver, respectively, as shown in Figure 7.2.

Corresponding to the Kirchhoff and complementary components for the tangential fields, the scattered fields contain also two components:

$$E^{s}_{qp} = E^{k}_{qp} + E^{c}_{qp} \tag{7.9}$$

where

$$E^{k}_{qp} = CE_0\int f_{qp}e^{\{j(\bar{k}_s-\bar{k}_i)\cdot\bar{r}\}}ds \tag{7.10}$$

and

$$E^{c}_{qp} = \frac{CE_0}{8\pi^2}\int F_{qp}e^{\{ju(x-x^{'})+jv(y-y^{'})+j\bar{k}_s\cdot\bar{r}-j\bar{k}_i\cdot\bar{r}^{'}\}}dxdydx^{'}dy^{'}dudv \tag{7.11}$$

Making use of Eq. 7.4, 7.7 and 7.10, the Kirchhoff coefficients are determined as:

$$\begin{aligned}f_{vv} &\approx -[(1-R_{||})\hat{h}_s\cdot(\hat{n}\times\hat{v})+(1+R_{||})\hat{v}_s\cdot(\hat{n}\times\hat{h})]D_1\\ f_{hh} &\approx -[(1-R_{\perp})\hat{h}_s\cdot(\hat{n}\times\hat{v})+(1+R_{\perp})\hat{v}_s\cdot(\hat{n}\times\hat{h})]D_1\\ f_{hv} &\approx [(1-R)\hat{v}_s\cdot(\hat{n}\times\hat{v})-(1+R)\hat{h}_s\cdot(\hat{n}\times\hat{h})]D_1]\end{aligned} \tag{7.12}$$

where $R = \frac{R_{\|} - R_{\perp}}{2}$.

It follows that the Kirchhoff coefficients f_{qp} are linear functions of the surface norm $\hat{n}$, which is in turn linear functions of the local slope terms Z_x and Z_y; terms whose spatial dependence can be removed by performing integration by parts and ignoring the edge term in the conventional way. The final simplification for the local slope terms are found for the Kirchhoff coefficients f_{qp} to be

$$\begin{aligned} Z_x &= \frac{k_{sx} - k_x}{k_{sz} + k_z} \\ Z_y &= \frac{k_{sy}}{k_{sz} + k_z} \end{aligned} \tag{7.13}$$

These newly formed local slope terms Z_x, Z_y are used in Eq. 7.12 to simplify the Kirchhoff coefficients. For instance,

$$f_{vv} = \frac{2R_{\|}}{\cos\theta + \cos\theta_s}[\sin\theta\sin\theta_s - (1 + \cos\theta\cos\theta_s)\cos(\phi_s - \phi)] \tag{7.14}$$

The expressions for the complementary coefficients F_{qp} are more complex than for f_{qp}. For instance, consider F_{vv}:

$$\begin{aligned} F_{vv}(u,v) &= -[(1 - R_{\|})/q - (1 - R_{\|})\frac{\mu_r}{q_t}](1 + R_{\|})C_1 \\ &\quad +[(1 - R_{\|})/q - (1 + R_{\|})/q_t](1 - R_{\|})C_2 \\ &\quad +[(1 - R_{\|})/q - (1 + R_{\|})/(\epsilon_r q_t)](1 + R_{\|})C_3 \\ &\quad +[(1 + R_{\|})/q - (1 - R_{\|})\frac{\epsilon_r}{q_t}](1 - R_{\|})C_4 \\ &\quad +[(1 + R_{\|})/q - (1 - R_{\|})/q_t](1 + R_{\|})C_5 \\ &\quad +[(1 + R_{\|})/q - (1 - R_{\|})/(\mu_r q_t)](1 - R_{\|})C_6 \end{aligned} \tag{7.15}$$

where

$$C_1 = k\hat{h}_s \cdot \hat{n} \times (\hat{n}' \times \hat{h})D_1 D_1' \tag{7.16}$$

and $\bar{n}'$ is the local surface vector with unit norm at another point on the rough surface, $D_1' = \sqrt{Z_x'^2 + Z_y'^2 + 1}$, $q = \sqrt{k^2 - u^2 - v^2}$, $q_t = \sqrt{k_t^2 - u^2 - v^2}$, k_t is the wave number in the space below the rough surface, and $C_2 \sim C_6$ are defined in [34].

For the complementary coefficients F_{qp}, their local spatial dependencies can be similarly eliminated and the results are:

$$\begin{aligned} Z_x &= -\frac{k_{sx} + u}{k_{sz}} \\ Z_y &= -\frac{k_{sy} + v}{k_{sz}} \\ Z_x' &= \frac{k_x + u}{k_z} \\ Z_y' &= \frac{k_y + v}{k_z} \end{aligned} \tag{7.17}$$

These newly formed local slope terms Z_x, Z_y, Z_x' and Z_y' are used in the Eq. 7.15 to simplify $C_1 \sim C_6$ for the complementary coefficients F_{qp}. For instance,

$$\begin{aligned} C_1 &= k\hat{h}_s \cdot \hat{n} \times (\hat{n}' \times \hat{h}) D_1 D_1' \\ &= k\cos\phi_s\{\cos\phi - \frac{(k_{sx} + u)}{k_{sz}k_z}[(k_x + u)\cos\phi + (k_y + v)\sin\phi]\} \\ &\quad +k\sin\phi_s\{\sin\phi - \frac{(k_{sy} + v)}{k_{sz}k_z}[(k_x + u)\cos\phi + (k_y + v)\sin\phi]\} \end{aligned} \tag{7.18}$$

7.3 Modified IEM

In the previous section, the scattered far field from a rough surface incident upon by a uniform plane wave is decomposed into the standard Kirchhoff field and a complementary field. The determination of the Kirchhoff field is completed through the Kirchhoff coefficient f_{qp}, while the complementary field is completed through the complementary coefficient F_{qp}. In the case of nonuniform plane wave incidence due to the incorporation of the antenna pattern, the above structure still holds, except new expressions for both the Kirchhoff and complementary coefficients are expected.

7.3.1 The Kirchhoff Coefficients f_{qp}

Our starting point is to modify the Kirchhoff field equations Eq. 7.12 to incorporate the antenna pattern $g(x,y)$:

$$\begin{aligned} f_{vv} &\approx -[(1-R_{||})\hat{h}_s\cdot(\hat{n}\times\hat{v})+(1+R_{||})\hat{v}_s\cdot(\hat{n}\times\hat{h})]D_1 g(x,y) \\ f_{hh} &\approx -[(1-R_{\perp})\hat{h}_s\cdot(\hat{n}\times\hat{v})+(1+R_{\perp})\hat{v}_s\cdot(\hat{n}\times\hat{h})]D_1 g(x,y) \\ f_{hv} &\approx [(1-R)\hat{v}_s\cdot(\hat{n}\times\hat{v})-(1+R)\hat{h}_s\cdot(\hat{n}\times\hat{h})]D_1 g(x,y) \end{aligned} \tag{7.19}$$

Notice that the antenna pattern $g(x,y)$ is actually the product of the antenna patterns of the transmitter, $g^{Tx}(x,y)$, and of the receiver, $g^{Rx}(x,y)$.

Analogous to the conventional IEM formulation, we now seek to eliminate the local spatial dependencies of the local slope terms Z_x and Z_y. We shall start with Z_x term and consider the following integral containing it:

$$E^k_{qp} = CE_0\int Z_x g(x,y)e^{\{j[(k_{sx}-k_x)x+k_{sy}y+(k_{sz}+k_z)z]\}}dxdy \tag{7.20}$$

Upon applying integration by parts on the right side of the above equation, it yields:

$$\begin{aligned} E^k_{qp} = \; & CE_0\int dy\frac{g(x,y)}{j(k_{sz}-k_z)}e^{\{j[(k_{sx}-k_x)x+k_{sy}y+(k_{sz}+k_z)z]\}} \\ & -CE_0\int\frac{g_x(x,y)+j(k_{sx}-k_x)g(x,y)}{j(k_{sz}-k_z)} \\ & e^{\{j[(k_{sx}-k_x)x+k_{sy}y+(k_{sz}+k_z)z]\}}dxdy \end{aligned} \tag{7.21}$$

where $g_x(x,y)$ is the partial derivative of the antenna pattern $g(x,y)$ with respect to x. Similarly, $g_y(x,y)$ is the partial derivative with respect to y.

In Eq. 7.21, the first term is evaluated at the edge of the illuminated area in the $\hat{x}$ coordinate, hence is negligible [6]. Comparing the second term with the right side of Eq. 7.20 implies the new identity for Z_x:

$$Z_x g(x,y) = -\frac{g_x(x,y) + j(k_{sx} - k_x)g(x,y)}{j(k_{sz} - k_z)} \tag{7.22}$$

Attention should be paid that in the above relation, Z_x still carries local spatial dependency through antenna pattern $g(x,y)$ and its partial derivative $g_x(x,y)$, a drawback which will be remedied later on.

Similarly, we obtain for Z_y:

$$Z_y g(x,y) = -\frac{g_y(x,y) + jk_{sy}g(x,y)}{j(k_{sz} - k_z)} \tag{7.23}$$

Notice that f_{qp} is linear in Z_x and Z_y, we can apply the superposition principle to obtain a new expression for f_{qp}. Taking f_{vv} first.

$$f_{vv} = f_{vv,F}\; g(x,y) + f_{vv,D} \tag{7.24}$$

where $f_{vv,F}$ refers to the conventional IEM result for f_{vv} assuming uniform plane wave incidence, $f_{vv,D}$ is the correction factor. Eq. 7.24 demonstrates that the Kirchhoff coefficient f_{vv}, when antenna pattern is incorporated, is the discounted version of the conventional $f_{vv,F}$, plus a correction term $f_{vv,D}$. The correction term $f_{vv,D}$ is determined by:

$$\begin{aligned} f_{vv,D} \;=\; & \frac{(1 - R_{\|})}{j(k_{sz} - k_z)}[-g_y(x,y)\sin\theta\sin(\phi_s - \phi) \\ & +(\cos\theta g(x,y) - g_x(x,y)\sin\theta)\cos(\phi_s - \phi)] \\ & -\frac{(1 + R_{\|})}{j(k_{sz} - k_z)}[g(x,y)\cos\theta_s\cos(\phi_s - \phi) + g_x(x,y)\sin\theta_s] \end{aligned} \tag{7.25}$$

Similarly, the new expressions for f_{hh} and f_{hv} are as follows:

$$f_{hh} = f_{hh,F}\; g(x,y) + f_{hh,D} \tag{7.26}$$

where

$$\begin{aligned} f_{hh,D} &= \frac{(1-R_{\perp})}{j(k_{sz}-k_z)}[\cos\theta_s\cos(\phi_s-\phi)g(x,y)+g_x(x,y)\sin\theta_s] \\ &-\frac{(1+R_{\perp})}{j(k_{sz}-k_z)}[-g_y(x,y)\sin\theta\sin(\phi_s-\phi) \\ &+(g(x,y)\cos\theta-g_x(x,y)\sin\theta)\cos(\phi_s-\phi)] \end{aligned} \tag{7.27}$$

and

$$f_{hv} = f_{hv,F}\, g(x,y) + f_{hv,D} \tag{7.28}$$

where

$$\begin{aligned} f_{hv,D} &= \frac{(1-R)}{j(k_{sz}-k_z)}[-g_y(x,y)\sin\theta\cos\theta_s\cos(\phi_s-\phi) \\ &-(g(x,y)\cos\theta-g_x(x,y)\sin\theta)\cos\theta_s\sin(\phi_s-\phi)] \\ &-\frac{(1-R)}{j(k_{sz}-k_z)}g_y(x,y)\cos\theta\sin\theta_s+(1+R)g(x,y)\sin(\phi_s-\phi) \end{aligned} \tag{7.29}$$

7.3.2 The Complimentary Coefficient F_{qp}

Our starting point is to modify the Kirchhoff field equations Eq. 7.15 to incorporate the antenna pattern $g(x,y)$, which enters the equations through the primed system.

Similar to the treatment of the local slope terms for the Kirchhoff coefficients, upon applying integration by parts and eliminating the edge term, the new expressions for the local slope terms are found to be:

$$\begin{aligned} Z_x &= -\frac{u+k_{sx}}{k_{sz}} \\ Z_y &= -\frac{v+k_{sy}}{k_{sz}} \\ Z_x^{'} &= \frac{g_{x'}(x^{'},y^{'})+j(k_x+u)g(x^{'},y^{'})}{jk_z} \\ Z_y^{'} &= \frac{g_{y'}(x^{'},y^{'})+j(k_y+v)g(x^{'},y^{'})}{jk_z} \end{aligned} \tag{7.30}$$

which demonstrates that the Z_x and Z_y terms are identical to that of the conventional IEM, while $Z_x^{'}$ and $Z_y^{'}$ are modulated by the antenna pattern and its derivatives.

Consequently, although the general forms of the complementary coefficients F_{pq} remain unchanged, $C_1 \sim C_6$ in the F_{qp} expressions need to be recalculated. As an example, we consider C_1 as expressed in Eq. 7.16. Upon substituting all the new local slope terms into the surface vectors $\hat{n}$ and $\hat{n}^{'}$, it yields:

$$\begin{aligned} C_1 \;=\; & k[(\cos\phi - \frac{k_{sx}+u}{k_z k_{sz}}((k_x + g_x(x,y)k_z + u)\cos\phi \\ & +(k_y + g_y(x,y)k_z + u)\sin\phi))\cos\phi_s \\ & +(\sin\phi - \frac{k_{sy}+v}{k_z k_{sz}}((k_x + g_x(x,y)k_z + u)\cos\phi \\ & +(k_y + g_y(x,y)k_z + u)\sin\phi))\sin\phi_s] \end{aligned} \tag{7.31}$$

A comparison between the new expression for C_1 as in Eq. 7.31 and the conventional one as in Eq. 7.16 reveals that the modification is performed through substituting $k_x + g_x(x,y)k_z$ for k_x and $k_y + g_y(x,y)k_z$ for k_y, a natural consequence from the new form of $Z_x^{'}$ and $Z_y^{'}$ as in Eq. 7.30 and the fact that C_1 is linear in both the surface vectors $\hat{n}$ and $\hat{n}^{'}$. It is not difficult to verify that the same substitution rule applies to the recalculation of $C_2 \sim C_6$. For quick reference, all the C coefficients $C_1 \sim C_6$ are listed in the appendix.

So far we have completed the reformulation of the Kirchhoff and the complementary coefficients when antenna pattern is considered. Yet the antenna pattern is expressed in a generic form through $g(x,y), g_x(x,y)$ and $g_y(x,y)$. Specifications of such antenna pattern is provided in the next section.

7.4 Calculation of $g(x,y)$, $g_x(x,y)$ and $g_y(x,y)$

The geometry of the wireless communication system above a rough surface is shown in Fig. 7.2. It is obvious that the direct link field will be interfered by the scattered field from the rough surface. The latter is affected by the geometry setting, the dielectric constant of the rough surface, and the antenna patterns of the transmitter and receiver.

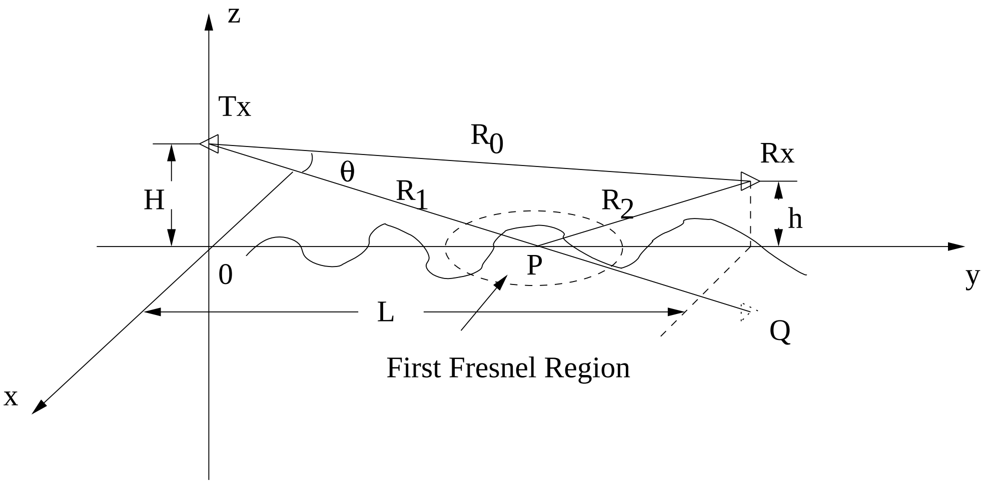

Figure 7.2: Geometry of a wireless line-of-sight communication system above rough surface.

As mentioned before, the antenna pattern $g(x,y)$ is the product of that of the transmitter and the receiver, i.e.,

$$g(x,y) = g^{Tx}(x,y)g^{Rx}(x,y) \tag{7.32}$$

with its two partial first order direvatives:

$$\begin{aligned} g_x(x,y) &= g_x^{Tx}(x,y)g^{Rx}(x,y) + g^{Tx}(x,y)g_x^{Rx}(x,y) \\ g_y(x,y) &= g_y^{Tx}(x,y)g^{Rx}(x,y) + g^{Tx}(x,y)g_y^{Rx}(x,y) \end{aligned} \tag{7.33}$$

We shall assume the antenna pattern $g^{Tx}(x,y)$ is a function of the angle between the direction from the transmitter to the specific point, P, and the direction of the boresight. The same assumption holds for the receiver antenna pattern $g^{Rx}(x,y)$. We shall calculate $g^{Tx}(x,y)$ and its partial direvatives as an illustration. For simplicity, we shall refer to this angle by antenna pattern angle hereafter. We further assume that the transmitter is always looking directly at the receiver, as shown in Fig. 7.2, where the shown item Q is the image of the receiver above the mean surface. Then the antenna pattern angle for arbitrary point P can be calculated with

$$\theta = \cos^{-1} < T_x\hat{R}_x, T_x\hat{P} > \tag{7.34}$$

where $< \cdot >$ denotes the inner product, $T_x\hat{R}_x$ refers to the unit vector pointing from T_x to R_x.

Now the coordinates for the transmitter, the receiver, and the image of receiver are:

$$\begin{aligned} T_x &: (0,0,H) \\ R_x &: (0,L,h) \\ Q &: (0,L,-h) \end{aligned} \tag{7.35}$$

For any arbitrary point on the rough surface, $P(x,y,z)$, the antenna pattern angle can be determined as follows:

$$\begin{aligned} \theta &= \theta(< \overline{T_xR_x}, \overline{T_xP} >) \\ &= \cos^{-1} < \frac{\overline{T_xR_x}}{|\overline{T_xR_x}|}, \frac{\overline{T_xP}}{|\overline{T_xP}|} > \\ &= \cos^{-1} < \frac{(0,L,h-H)}{\sqrt{L^2+(h-H)^2}}, \frac{(x,y,z-H)}{\sqrt{x^2+y^2+(z-H)^2}} > \\ &\approx \cos^{-1} < \frac{(0,L,h-H)}{\sqrt{L^2+(h-H)^2}}, \frac{(x,y,-H)}{\sqrt{x^2+y^2+H^2}} > \\ &= \cos^{-1}(\frac{yL-H(h-H)}{\sqrt{L^2+(h-H)^2}\sqrt{x^2+y^2+H^2}}) \end{aligned} \tag{7.36}$$

In the above we have forced $z = 0$ in calcuating the antenna pattern angle because the distance between the transmitter and the receiver is assumed to be sufficiently large and the roughness is never comparable.

In what follows, the antenna pattern $g^{Tx}(x, y)$ and its derivatives $g_x^{Tx}(x, y)$ and $g_y^{Tx}(x, y)$ are specified for the specular point for reasons will be soon clear. The coordinate for the specular point is:

$$\begin{aligned} x_{sp} &= 0 \\ y_{sp} &= \frac{H}{H+h}L \end{aligned} \tag{7.37}$$

Two antenna patterns are considered here: one follows a sinc pattern and the other represents an exponential beam.

7.4.1 Case1: Sinc Antenna Pattern

In this case, the antenna pattern is given by:

$$g^{Tx}(x, y) = sinc(\beta_0 \theta) \tag{7.38}$$

It immediately follows that when specified to the specular point:

$$\begin{aligned} g^{Tx,sp} &= sinc(\beta_0 \cos^{-1}(\gamma)) \\ g_x^{Tx,sp} &= 0 \\ g_y^{Tx,sp} &= -\frac{(h+H)[\beta_0 \cos^{-1}(\gamma) \cos(\beta_0 \cos^{-1}(\gamma)) - \sin(\beta_0 \cos^{-1}(\gamma))]}{\beta_0 H \sqrt{[(h+H)^2 + L^2][1 + \frac{L^2}{(h+H)^2}]}(\cos^{-1}(\gamma))^2} \end{aligned} \tag{7.39}$$

where the superscript *sp* denotes specular point, and

$$\gamma = \frac{H - h + \frac{L^2}{h+H}}{\sqrt{[(h-H)^2 + L^2][1 + \frac{L^2}{(h+H)^2}]}} \tag{7.40}$$

7.4.2 Case2: Exponential Beam Antenna Pattern

In this case, the antenna pattern is given by:

$$g^{Tx}(x,y) = e^{\{-\beta_0 \theta\}} \tag{7.41}$$

It immediately follows that when specified to the specular point:

$$\begin{aligned} g^{Tx,sp} &= e^{\{-\beta_0 \cos^{-1}(\gamma)\}} \\ g^{Tx,sp}_x &= 0 \\ g^{Tx,sp}_y &= \frac{(h+H)\beta_0 e^{\{-\beta_0 \cos^{-1}(\gamma)\}}}{H\sqrt{[(h+H)^2+L^2][1+\frac{L^2}{(h+H)^2}]}} \end{aligned} \tag{7.42}$$

where

$$\gamma = \frac{H-h+\frac{L^2}{h+H}}{\sqrt{[(h-H)^2+L^2][1+\frac{L^2}{(h+H)^2}]}} \tag{7.43}$$

7.5 Calculation of the Coherent and Incoherent Scattered Field

When calculating the scattered field from a rough surface, the conventional way is to perform the integral in the Stratton-Chu representation over the illuminated area. Yet when the incident wave does not illuminate the rough surface even obliquely, as in the communication case where the transmitter is directed towards the receiver, only part of the energy through antenna pattern reaches the rough surface and gets scattered. In this case, there is an ambiguity in how to determine the region over which the integral is performed. Be it called the effective scattering region of the rough surface, the determination of which is critical in the sense that an underestimate of this effective scattering region will render the calculated scattered field inaccurate, while an overestimate of it will significantly increase the computational burden.

One approach is to follow the Fresnel zone argument. For a point source above a specular plane, on which the locus of all points whose secondary radiation arrives with a constant phase difference δ with respect to the direct radiation at the observation point forms an ellipse. A family of ellipses will result as δ is allowed to be increased in steps of half wavelength. The first three ellipses in such family are shown in dotted line in Fig. 7.3. The first zone is encompassed by the first ellipse, while successive zones are bounded by two neighboring ellipses and have opposite average phases. As a result, the secondary fields from adjacent zones, such as from the second and third zones, or from the forth and fifth zones, will tend to cancel. Consequently, the first Fresnel zone makes the most significant contribution of the field at the observation point [6].

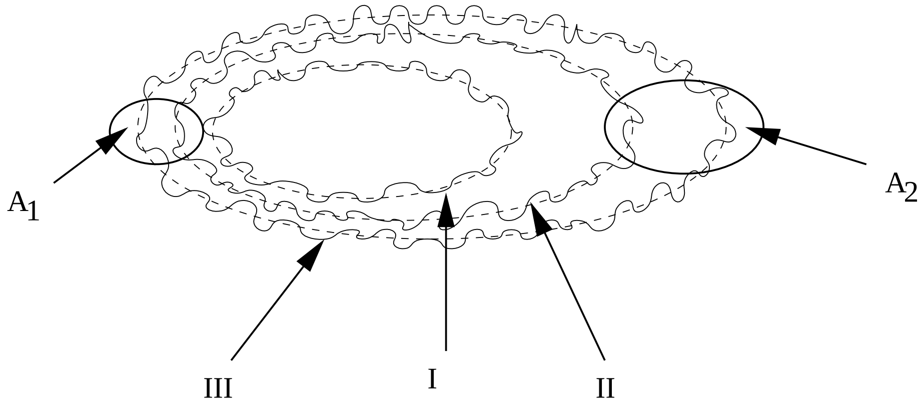

Figure 7.3: The Fresnel zones on a scattering rough surface.

We argue that the same conclusion holds for millimeter-wave scattering from a rough surface even if there exists an antenna pattern as opposed to the isotropical pattern by a point source. First of all, we should recall that the equal phase curve is an ellipse on a specular surface. When the surface becomes rough, it induces some distortion to the ellipses, as shown in Fig. 7.3. Yet the average distance between neighboring ellipses is very small because the net traveling distances from the source to the observation point through the points on the distorted ellipses differ from each other by only half wavelength. As a result, the contributions of the scattered field from adjacent zones still tend to cancel each other in a patchwise way, for instance, as from patches A_1 and A_2 as shown in Fig. 7.3. These patches are small enough not to allow any appreciable change in the antenna pattern, hence the cancellation mechanism still holds at the presence of antenna pattern. Consequently, again the first Fresnel zone makes the most significant contribution to the scattered field at the observation point.

Based on the observation that the first Fresnel zone contains the specular point and that the antenna pattern does not change appreciably within this zone, it is reasonable to let the antenna pattern and its partial derivatives be specified at the specular point, which is done in the last section.

Having determined the effective scattering region to be the first Fresnel zone on a rough surface, we are in a position to calculate the coherent and incoherent components of the scattered field.

7.5.1 Scattered Coherent Field

The field at the receiver is the summation of direct field and the field being scattered by the rough surface. That is,

$$\bar{E}_{qp} = \bar{E}_{qp,1} + \bar{E}_{qp,2} \tag{7.44}$$

where only the second term is random, hence taking ensemble averaging of both sides leads to:

$$< \bar{E_{qp}} >= \bar{E}_{qp,1} + < \bar{E}_{qp,2} > \tag{7.45}$$

According to Eq. 7.9, the second term can be decomposed into the Kirchhoff term and complementary term:

$$< \bar{E}_{qp,2} >=< \bar{E}^{k}_{qp,2} > + < \bar{E}^{c}_{qp,2} > \tag{7.46}$$

with each term being determined as follows. For the Kirchhoff term,

$$\begin{aligned}
E^{k}_{qp} &= CE_0 \int f_{qp} e^{\{j(\bar{k}_s - vki)\cdot\bar{r}\}} ds \\
&\Rightarrow \\
< E^{k}_{qp} > &= CE_0 \int f_{qp} e^{\{j[(k_{sx}-k_x)x+(k_{sy}-k_y)y]\}} < e^{\{j(k_{sz}+k_z)\}} > dxdy \\
&= CE_0 \int f_{qp} e^{\{j[(k_{sx}-k_x)x+(k_{sy}-k_y)y]\}} e^{\{-\frac{(k_{sz}+k_z)^2}{2}\sigma^2\}} dxdy \\
&\approx CE_0 f_{qp} e^{\{-\frac{(k_{sz}+k_z)^2}{2}\sigma^2\}} \int f_{qp} e^{\{j[(k_{sx}-k_x)x+(k_{sy}-k_y)y]\}} dxdy \\
&= 4\pi^2 CE_0 f_{qp} e^{\{-\frac{(k_{sz}+k_z)^2}{2}\sigma^2\}} \delta(k_{sx}-k_x)\delta(k_{sy}-k_y) \qquad (7.47)
\end{aligned}$$

In the above, we have assumed that the rough surface follows a normal distribution.

Similarly for the complementary term,

$$\begin{aligned}
E^{c}_{qp} &= \frac{CE_0}{8\pi^2} \int F_{qp} e^{\{ju(x-x^{'})+jv(y-y^{'})+j\bar{k}_s\cdot\bar{r}-j\bar{k}_i\cdot\bar{r}^{'}\}} \\
&\quad dxdydx^{'}dy^{'}dudv \\
&\Rightarrow \\
< E^{c}_{qp} > &= \frac{CE_0}{8\pi^2} \int F_{qp} e^{\{ju(x-x^{'})+jv(y-y^{'})+jk_{sx}x+jk_{sy}y-jk_x x^{'}-jk_y y^{'}\}} \\
&\quad < e^{\{jk_{sz}z+jk_z z^{'}\}} > dxdydx^{'}dy^{'}dudv \qquad (7.48)
\end{aligned}$$

where $\delta(\cdot)$ is the Kronecker delta function.

It is well known that the linear combination $w = k_{sz}z + k_z z^{'}$ follows a normal distribution with

$$\begin{aligned}
E\{w\} &= 0 \\
Var\{w\} &= k_{sz}^2\sigma^2 + k_z^2\sigma^2 + 2k_{sz}k_z\rho(x-x^{'}, y-y^{'})\sigma^2 \qquad (7.49)
\end{aligned}$$

Hence

$$
\begin{aligned}
< E^c_{qp} > &\approx \frac{CE_0}{8\pi^2} F_{qp} e^{\{-\frac{(k_{sz}^2+k_z^2)}{2}\sigma^2\}} \\
&\int e^{\{ju(x-x^{'})+jv(y-y^{'})+jk_{sx}x+jk_{sy}y\}} \\
&e^{\{-jk_x x^{'}-jk_y y^{'}-k_{sz}k_z\sigma^2\rho(x-x^{'},y-y^{'})\}} dxdydx^{'}dy^{'}dudv \\
&= \frac{CE_0}{8\pi^2} F_{qp} e^{\{-\frac{(k_{sz}+k_z)^2}{2}\sigma^2\}} 4\pi^2 \delta(k_{sx}-k_x)\delta(k_{sy}-k_y) \qquad (7.50)
\end{aligned}
$$

In view of Eq. 7.46, 7.47 and 7.50, the coherent scattered field is

$$
< E_{qp} >= 4\pi^2 C E_0 e^{\{-\frac{(k_{sz}+k_z)^2}{2}\sigma^2\}} (f_{qp} + \frac{F_{qp}}{8\pi^2}) \delta(k_{sx}-k_x)\delta(k_{sy}-k_y) \qquad (7.51)
$$

7.5.2 Incoherent Power of The Scattered Field

In the conventional IEM derivation of the incoherent power of the scattered field, the Kirchhoff and complementary coefficients f_{qp} and F_{qp} are kept in generic form. The extended IEM formulation, reported in Section 7.3, modifies only f_{qp} and F_{qp} to incorporate the antenna pattern. Therefore, we can adopt the conventional expression for the incoherent power of the scattered field, except that f_{qp} and F_{qp} should be changed accordingly.

From [34], the incoherent power due to single scattering is given by:

$$
P^s_{qp} = \frac{E_0^2 A_0}{4\pi R_2^2} \frac{k^2}{2} e^{\{-\sigma^2(k_z^2+k_{sz}^2)\}} \sum_{n=1}^{infty} \sigma^{2n} |I^n_{qp}|^2 \frac{W^n(k_{sx}-k_x, k_{sy}-k_y)}{n!} \qquad (7.52)
$$

where A_0 is the area of the effective scattering region on the rough surface, and

$$
I^n_{qp} = (k_{sz}+k_z)^n f_{qp} e^{\{-\sigma^2 k_z k_{sz}\}} + \frac{(k_{sz}^n F_{qp}(-k_x,-k_y) + (k_z)^n F_{qp}(-k_{sx},-k_{sy})}{2} \qquad (7.53)
$$

and $W^n(k_{sx}-k_x, k_{sy}-k_y)$ is the roughness spectrum of the surface related to the nth power of the surface correlation function. For a Gaussian correlation function, we have:

$$
W^n(k_{sx}-k_x, k_{sy}-k_y) = \frac{l^2}{2n} e^{\{-\frac{[(k_{sx}-k_x)^2+(k_{sy}-k_y)^2]l^2}{4n}\}} \qquad (7.54)
$$

where l is the correlation length of the rough surface.

The incoherent power due to multiple scattering is given in [34].

In the above, f_{qp} should be calculated using Eq. 7.24 $\sim$ 7.29, and F_{qp} should be calculated using the procedure described in section 7.3.2.

7.6 Numerical Illustrations

In this section, when the modified IEM method is used to study a rough surface, the impacts of polarization, antenna pattern, beamwidth, surface roughness are examined by simulations. Unless stated otherwise, the frequency is 35 GHz.

First, the relative magnitudes of the coherent components of the calculated fields scattered from a rough surface using the modefied IEM method (E-IEM) and the physical optical method (PO) are compared, as shown in Figure 7.4 using the magnitude ratio. It is seen that the magnitude from E-IEM is several folds larger than that from PO at small horizontal distance between the transmitter and receiver, then decreases monotonically with increasing distance, eventually becomes smaller than that from PO. Since larger distance is translated into larger incidence angle (from the view of the specular point on the rough surface), the above states that at small incidence angle, the magnitude from E-IEM is larger than that from PO, then it decreases monotonically with increasing incidence angle.

Second, the coherent component of VV total field is compared to the free space line-of-sight component, as shown in Figure 7.5. It is seen that the interference due to the field scattered from the rough surface ranges from 2 to 10 dB, depends on the horizontal distance between the transmitter and receiver.

Third, the coherent components of the copolarized VV and HH total fields are compared in Figure 7.6. As expected, they are out of phase.

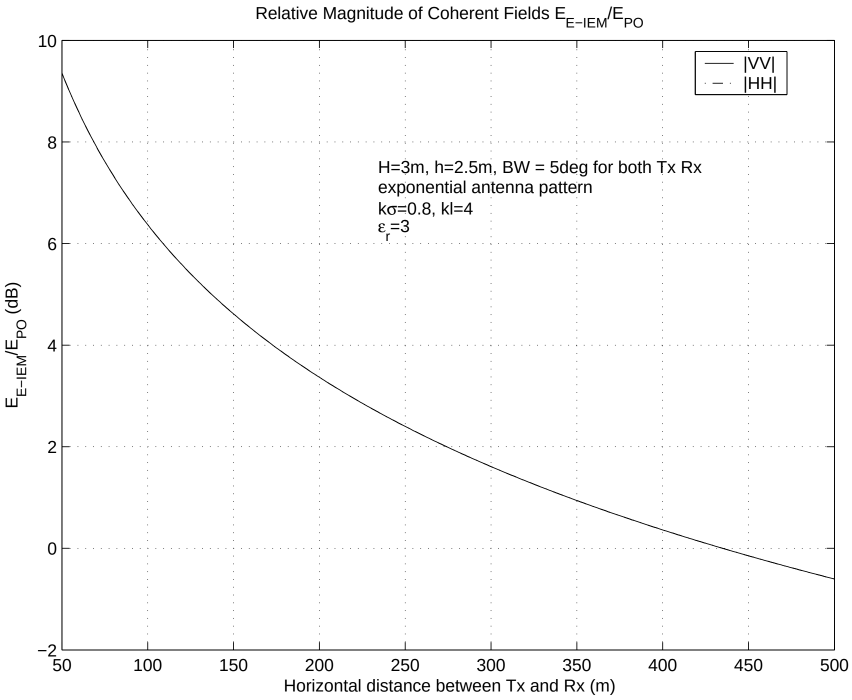

Figure 7.4: Comparison between E-IEM and PO. In the simulation, H=3m,h=2.5m, beadwidth is 5° for both transmitter and receiver, both assume exponential antenna pattern, $k\sigma = 0.8, kl = 4, \epsilon_r = 3$.

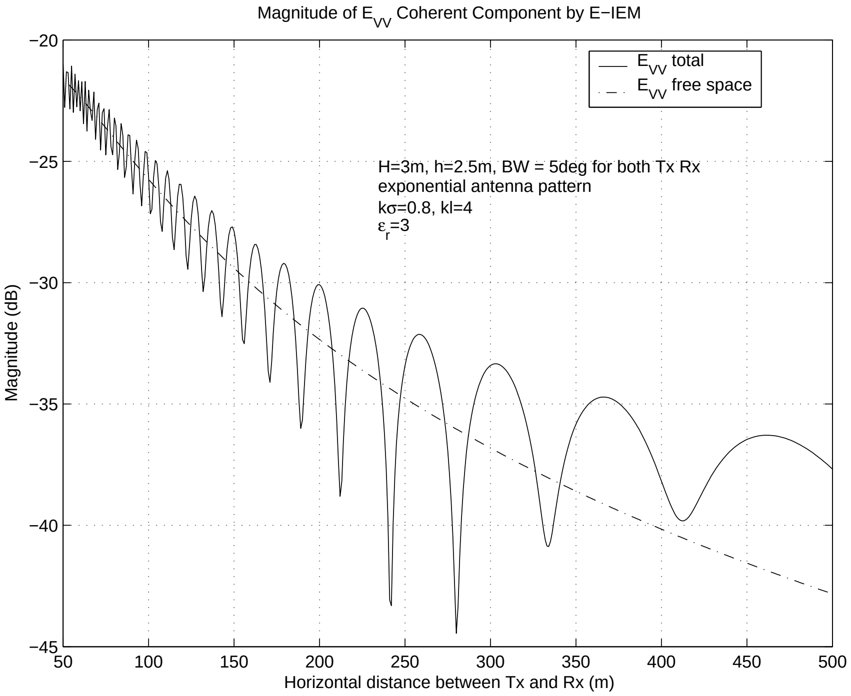

Figure 7.5: Comparison between total and free space fields. All simulation parameters are the same as in Figure 7.4.

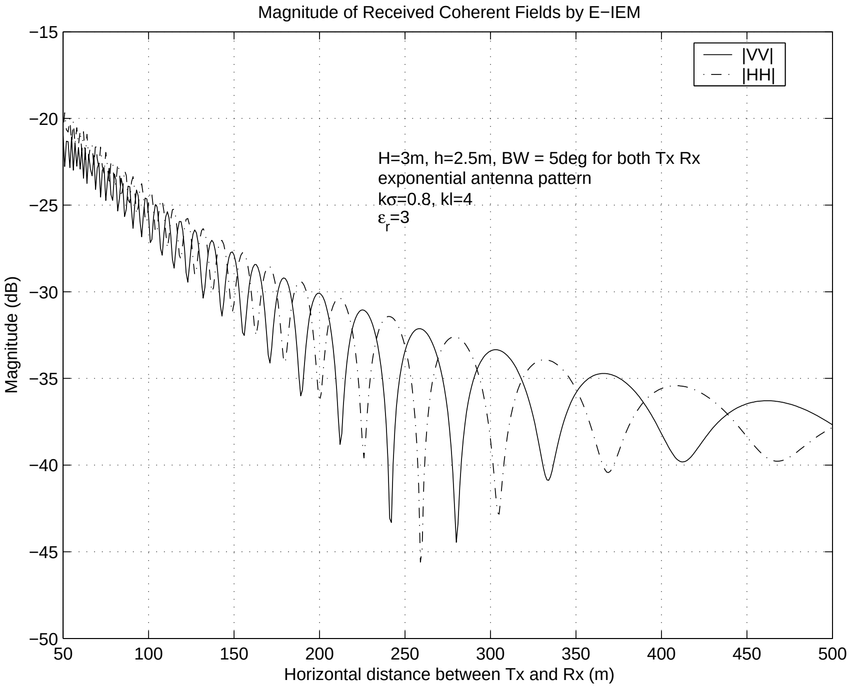

Figure 7.6: Comparison between VV and HH. All simulation parameters are the same as in Figure 7.4.

Forth, the effect of assuming different antenna patterns, namely, exponential and sinc patterns, on the coherent component of the scattered field is examined in Figure 7.7. It is seen that except at small horizontal distance, where sinc pattern induces a sharp drop in signal level, for medium and large distances, both antenna patterns show a resemblance of impacts.

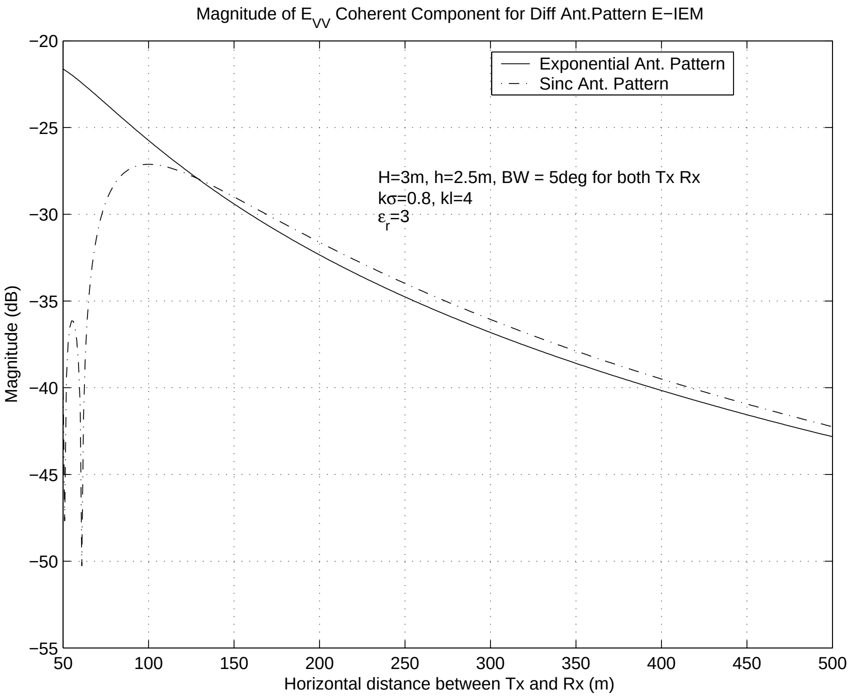

Figure 7.7: Comparison between exponential pattern and sinc pattern. All simulation parameters are the same as in Figure 7.4, except the antenna pattern is replaced with what is appropriate.

Fifth, the effect of antenna beamwidth on the coherent component of the scattered field is examined in Figure 7.8. It shows that the impact of antenna beamwidth is considerable when the beamwidth is very small, yet tends to saturate quickly as the beamwidth increases.

Finally, the effect of surface roughness on the coherent component of the scattered field is examined in Figure 7.9. It is seen that at near grazing incidence, roughness

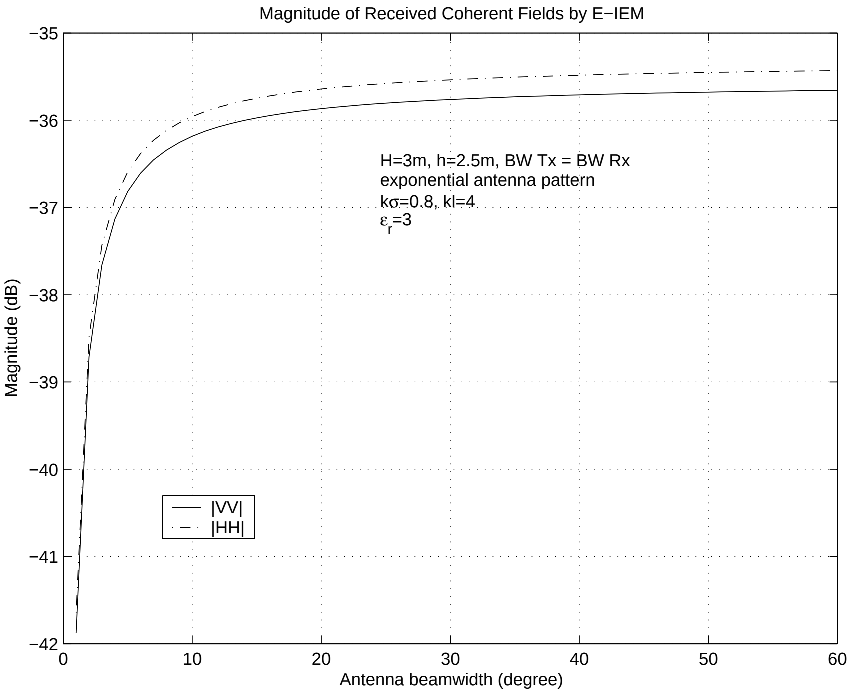

Figure 7.8: Effect of antenna beamwidth. All simulation parameters are the same as in Figure 7.4, except the horizontal distance $L = 300$m.

plays an negligible role.

7.7 Conclusion

Although IEM has shown to be suitable for studying scattering from a broad range of different rough surfaces, it ignored the antenna pattern. Yet in the case of wireless communication, the antenna pattern must be incorporated into the theoretical formulation. Such formulation was developed in this chapter. The impacts of polarization, antenna pattern, beamwidth, surface roughness upon the scattered field from a rough surface were examined by simulations.

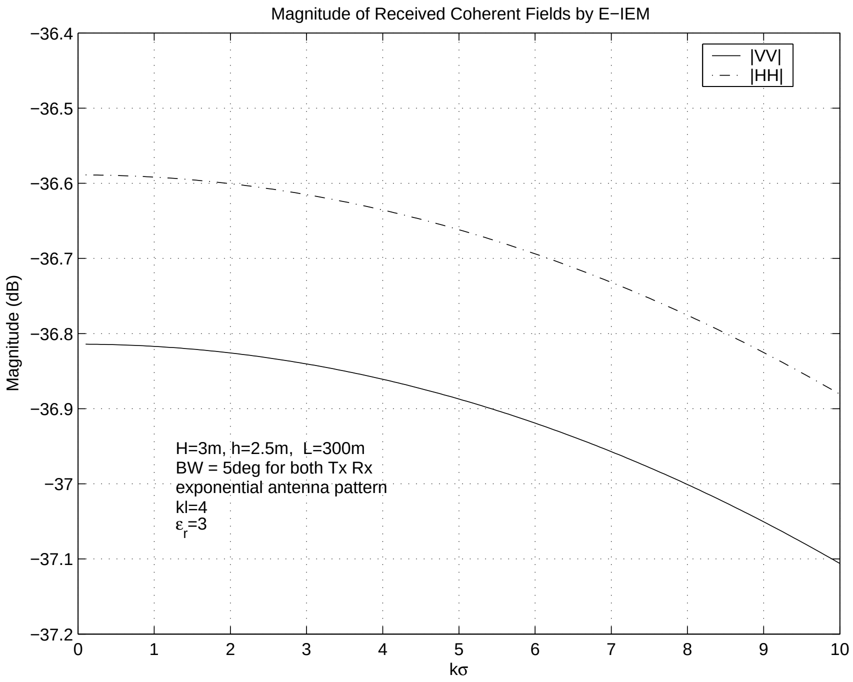

Figure 7.9: Effect of rough surface rms height. All simulation parameters are the same as in Figure 7.4, except the horizontal distance $L = 300$m.

CHAPTER VIII

Conclusions and Directions for Future Work

In Chapter II, the topic of sensitivity to soil moisture for vegetation-covered land by active and passive sensors at L band was revisited. At such a low microwave frequency, for the usually encountered vegetation covers such as grass and soybean, which are electrically small in dimension, the conventional RTE was used to study the scattering mechanisms.

In Chapter III the radar response of a soybean canopy was examined. The scattering mechanism becomes more complex for a soybean canopy at C band. Since the main concern was to develop an inversion algorithm for extracting water content, biomass, rough surface rms height and soil moisture from the L, C bands measu rements of soybean at 45° incidence, both the high order scattering approach and the antenna array-like approach were ruled out due to the complexity and the limited measurement data available for inversion, respectively. Rather, assuming the adoption of the conventional RTE technique, effort was focused on the characterization of the dependence of the volume extinction coefficient κ_e and the phase matrix $\mathbf{P}$, two critical input parameters to RTE, upon the water content to the biomass. Chapter III addressed all the relevant issues and provided discussions of the inversion results.

When the sensor frequency moves from the microwave to the millimeter-wave regime, the scattering mechanism becomes even substantially more complicated, mainly due to the dense medium nature of many natural media such as snow. For dry snow, the conventional RTE was used, in conjunction with QCA, for studying the backscatter due to the relative simplicity of the air-ice mixture approach. Moreover, the different characterizations of the propagation properties of the dry snow media provided by CRT and QCA were reconciliated and addressed in Chapter IV, along with the modeling performance. Further discussion was also provided on the impact of snow particle shape and surface roughness upon the backscatter.

Yet when snow becomes wet, as frequently encountered in diurnal observations, the QCA approach for determining the volume extinction coefficient κ_e collapses due to the severe violation of its assumptions. Encouraged by the success of conventional RTE when applied to other dense media [56], the conventional RTE was adopted for wet snow. This treatment was addressed in Chapter V where the thermodynamic information was incorporated in the application of the model to explain diurnal observations.

Pure incoherent power treatment is insufficient when it comes to the characterization of a communication channel, where the interference statistics assume a considerably important role. In such cases, the necessary electric-field based study was given in Chapter VI. At 35 GHz, a simple Kirchhoff model was used for scattering from rough surfaces. Based on it, a four-ray model was constructed to help interpret the observed backward interference pattern. Moreover, to infer the forward scattering behavior from the backward one, an equivalence relation between forward and backward scattering was established. However, when the surface is very rough, or covered by some vegetation such as grass, the backward interference pattern tends to disintegrate, even for a moderate number of independent samples. This calls for techniques that can address both the coherent and incoherent components of the scattered field from a rough surface directly. IEM is one such candidate, but it cannot be applied directly in its current form because it assumes uniform plane wave incidence. Such an approximation may not be valid or appropriate for calculating the forward scattered field. Hence, the IEM formulation was revisited in Chapter VII wherein the antenna electric-field pattern was incorporated in the calculation of the field intercepted by the receive antenna.

8.1 Summary of Accomplishments

1. Evaluation of the sensitivity to soil moisture for both active and passive sensors at L band. This evaluation brought to a conclusion a long disputed issue. Implementation of the MIMICS model was extended to passive case.

2. Development of an inversion algorithm for extracting water content, biomass, rough surface rms height and soil moisture from the L, C bands measurements of soybean at 45° incidence.

3. Characterization and extensive measurements of MMW backscatter from snow at near grazing incidence.

4. Development of MMW snow backscatter model for angular pattern at near grazing incidence.

5. Development of MMW snow backscatter model for diurnal pattern at near grazing incidence.

6. Characterization and measurements of backscatter interference pattern at 35 GHz over different terrain.

7. Development of model to interpret the observed interference pattern.
8. Establishment of the equivalence between backscatter and forward scattering interference pattern.
9. Extension of the conventional IEM model for rough surface scattering to incorporate antenna pattern.

8.2 Directions for Future Work

The directions for future work envisioned by the author are:

1. Extend the analysis of sensitivity to soil moisture to other frequencies, such as C band.
2. Extend the inversion algorithm from a scalar version to a vector version. Incorporate the dynamics of underlying soil surface roughness.
3. Characterize the shape, size and orientation of snow particle more accurately through ground truth collection.
4. Use more advanced surface/volume scattering model to improve the predictive power for cross-polarized backscatter for MMW snow diurnal measurements. For instance, use the modified IEM model developed in Chapter VII to calculate the rough air-snow interface scattering.
5. Develop more advanced model for scattering from vegetation covered terrain in the interference study. Use the modified IEM model developed in Chapter VII rather than the Kirchhoff model to calculate the scattered field from the rough surface in the four-ray model.

6. Study more realistic antenna pattern other than the hypothetic exponential beam or sinc pattern in the modified IEM model.

APPENDICES

APPENDIX A

C coefficients of F_{qp} for the modified IEM

$$\begin{aligned}
C_1 \;=\;& k[(\cos\phi - \frac{k_{sx}+u}{k_z k_{sz}}((k_x + g_x(x,y)k_z + u)\cos\phi \\
&+(k_y + g_y(x,y)k_z + u)\sin\phi))\cos\phi_s \\
&+(\sin\phi - \frac{k_{sy}+v}{k_z k_{sz}}((k_x + g_x(x,y)k_z + u)\cos\phi \\
&+(k_y + g_y(x,y)k_z + u)\sin\phi))\sin\phi_s]
\end{aligned} \tag{A.1}$$

$$\begin{aligned}
C_2 \;=\;& -\cos\phi_s[\frac{\cos\phi\cos\theta}{k_{sz}}(k_{sx}+u)u + \frac{\sin\phi\cos\theta}{k_{sz}}(k_{sx}+u)v \\
&+\frac{\sin\phi\cos\theta}{k_z}(k_x + g_x(x,y)k_z + u)v - \frac{\cos\phi\cos\theta}{k_z}(k_y + g_y(x,y)k_z + v)v \\
&+\frac{\sin\theta}{k_{sz}k_z}((k_{sx}+u)(k_x + g_x(x,y)k_z + u)u \\
&+(k_{sx}+u)(k_y + g_y(x,y)k_z + v)v)] \\
&-\sin\phi_s[\frac{\cos\phi\cos\theta}{k_{sz}}(k_{sy}+v)u + \frac{\sin\phi\cos\theta}{k_{sz}}(k_{sy}+v)v \\
&-\frac{\sin\phi\cos\theta}{k_z}(k_x + g_x(x,y)k_z + u)u + \frac{\cos\phi\cos\theta}{k_z}(k_y + g_y(x,y)k_z + v)u \\
&+\frac{\sin\theta}{k_{sz}k_z}((k_{sy}+v)(k_y + g_y(x,y)k_z + v)v \\
&+(k_x + g_x(x,y)k_z + u)(k_{sy}+v)u)]
\end{aligned} \tag{A.2}$$

$$\begin{aligned}
C_3 \;=\;& -(u\cos\phi_s + v\cos\phi_s) \\
&[\sin\theta - ((k_x + g_x(x,y)k_z + u)\cos\phi\cos\theta)/k_z \\
&-((k_y + g_y(x,y)k_z + v)\sin\phi\cos\theta/k_z]
\end{aligned} \tag{A.3}$$

$$\begin{aligned}
C_4 &= k[\cos\phi_s \cos\theta_s(\cos\phi\cos\theta(1-(k_{sy}+v)(k_y+g_y(x,y)k_z+v)/(k_{sz}k_z)) \\
&+\sin\phi\cos\theta((k_x+g_x(x,y)k_z+u)(k_{sy}+v)/(k_{sz}k_z)) \\
&+\sin\theta(k_x+g_x(x,y)k_z+u)/k_z) \\
&+\sin\phi_s\cos\theta_s(\cos\phi\cos\theta(k_{sx}+u)(k_y+g_y(x,y)k_z+v)/(k_{sz}k_z)) \\
&+\sin\phi\cos\theta(1-(k_{sx}+u)(k_x+g_x(x,y)k_z+u)/(k_{sz}k_z)) \\
&+\sin\theta(k_y+g_y(x,y)k_z+v)/k_z) \\
&+\frac{\sin\theta_s}{k_{sz}k_z}(\cos\phi\cos\theta(k_{sx}+u)k_z+\sin\phi\cos\theta(k_{sy}+v)k_z \\
&+\sin\theta((k_{sx}+u)(k_x+g_x(x,y)k_z+u) \\
&+(k_{sy}+v)(k_y+g_y(x,y)k_z+v)))]
\end{aligned} \tag{A.4}$$

$$\begin{aligned}
C_5 &= \cos\phi_s\cos\theta_s(\frac{\cos\phi}{k_{sz}}(k_{sy}+v)v-\frac{\cos\phi}{k_z}(k_x+g_x(x,y)k_z+u)u \\
&-\frac{\sin\phi}{k_z}(k_y+g_y(x,y)k_z+v)u-\frac{\sin\phi}{k_{sz}}(k_{sy}+v)u) \\
&-\sin\phi_s\cos\theta_s(\frac{\cos\phi}{k_z}(k_x+g_x(x,y)k_z+u)v+\frac{\cos\phi}{k_{sz}}(k_{sx}+u)v \\
&+\frac{\sin\phi}{k_z}(k_y+g_y(x,y)k_z+v)v-\frac{\sin\phi}{k_{sz}}(k_{sx}+u)u) \\
&-\frac{\sin\theta_s}{k_{sz}k_z}(\cos\phi((k_{sx}+u)(k_x+g_x(x,y)k_z+u)u \\
&+(k_x+g_x(x,y)k_z+u)(k_{sy}+v)v) \\
&+\sin\phi(u(k_{sx}+u)(k_y+g_y(x,y)k_z+v) \\
&+v(k_{sy}+v)(k_y+g_y(x,y)k_z+v)))
\end{aligned} \tag{A.5}$$

$$\begin{aligned}
C_6 &= \frac{1}{k_z}((k_x+g_x(x,y)k_z+u)\sin\phi-(k_y+g_y(x,y)k_z+v)\cos\phi) \\
&(v\cos\phi_s\cos\theta_s-u\sin\phi_s\cos\theta_s+\sin\theta_s(k_{sx}v-k_{sy}u)/k_{sz})
\end{aligned} \tag{A.6}$$

BIBLIOGRAPHY

BIBLIOGRAPHY

[1] M. Abramowitz and J.A. Stegun. *Handbook of Mathematical Functions.* Dover Publications, 1965.

[2] J.L. Alvarez-Perez. An extension of the iem/iemm surface scattering model. *Waves Random Media*, 11:307–329, 2001.

[3] E.P.W. Attema and F.T. Ulaby. Vegetation modeled as a water cloud. *Radio Sci.*, 13:357–364, 1978.

[4] M. Autret, R. Bernard, and D. Vidal-Madjor. Theoretical study of the sensitivity of the microwave backscattering coefficient to the soil surface parameters. *International Journal of Remote Sensing*, pages 171–179, Jan. 1989.

[5] J.M. Baker, J.B. Mead, and R.E. McIntosh. Forward scatter polarimetric measurements of terrain at 35 and 225 ghz. *IGARSS*, 4:2080 –2083, 1998.

[6] P. Beckmann. *The scattering of electromagnetic waves from rough surfaces.* Macmillan, New York, 1963.

[7] P. Bertuzzi, A. Chanzy, D. Vidal-Madjar, and M. Autret. Use of a microwave backscatter model for retrieving soil moisture over bare soil. *Internaitonal Journal of Remote Sensing*, pages 2653–2668, Sept. 1992.

[8] C.F. Bohren and S.B. Singham. Backscattering by nonspherical particles - a review of methods and suggested new approaches. *J. Geophys Res-Atmos*, 96(D3):5269–5277, March 1991.

[9] Craig F. Bohren and Donald R. Huffman. *Absorbtion and Scattering of Light by Small Particles.* Wiley-Interscience, New York, 1983.

[10] C. Bourlier, G. Berginc, and J. Saillard. Monostatic and bistatic statistical shadowing functions from a one-dimensional stationary randomly rough surface: Ii. multiple scattering. *Wave Random Media*, 12(2):175–200, Apr. 2002.

[11] P.S. Chang, J.B. Mead, E.J. Knapp, G.A. Sadowy, R.E. Davis, and R.E. McIntosh. Polarimetric backscatter from fresh and metamorphic snowcover at millimeter wavelengths. *IEEE Transactions on Antennas and Propagation*, 44(1):58–73, Jan. 1996.

[12] N.S. Chauhan, D.M. Le Vine, and R.H. Lang. Discrete scatter model for microwave radar and radiometer response to corn: Comparison of theory and data. *IEEE Transactions on Geoscience and Remote Sensing*, 32(2):416–426, Mar 1994.

[13] K.S. Chen and A.K. Fung. A comparison of backscattering models for rough surfaces. *IEEE Transactions on Geoscience and Remote Sensing*, 33(1):195–200, Jan. 1995.

[14] K.S. Chen, T.D. Wu, M.K. Tsay, and A.K. Fung. Note on the multiple scattering in an iem model. *IEEE Transactions on Geoscience and Remote Sensing*, 38(1):249–256, Jan. 2000.

[15] T. Chiu and K. Sarabandi. Electromagnetic scattering interaction between leaves and thin branches. *IGARSS*, 1:300–302, 1998.

[16] T. Chiu and K. Sarabandi. Electromagnetic scattering interaction between a dielectric cylinder and a slightly rough surface. *IEEE Transactions on Antennas and Propagation*, 47(5):902–913, 1999.

[17] Tsen-Chieh Chiu. *Electromagnetic Scattering from Rough Surfaces Covered With Short Branching Vegetation.* PhD dissertation, University of Michigan, Ann Arbor, 1998.

[18] B.J. Choudhury, T.J. Schmugge, A. Chang, and R.W. Newton. Effect of surface roughness on the microwave emission from soils. *J. Geophys. Res.*, 84:5699–5706, 1979.

[19] S.C. Colbeck, editor. *Dynamics of Snow and Ice Masses.* Academic Press, New York, 1980.

[20] B.G. Colpitts. The integral equation model and surface roughness signatures in soil moisture and tillage type determination. *IEEE Transactions on Geoscience and Remote Sensing*, 36(3):833–837, May 1998.

[21] J.W. Crispin and K.M. Siegel. *Methods of Radar Cross Section Analysis.* Academic, New York, 1968.

[22] R.D. DeRoo, Y. Du, and F.T. Ulaby. Observations of mmw backscatter from snow near grazing incidence. *IEEE International Symposium Antennas and Propagation Society*, 1:44–47, 1999.

[23] R.D. DeRoo, Y. Du, F.T. Ulaby, and M.C. Dobson. A semi-empirical backscattering model at l-band and c-band for a soybean canopy with soil moisture inversion. *IEEE Transactions on Geoscience and Remote Sensing*, 39(4):864–872, April 2001.

[24] D. Didascalou, J. Maurer, and W. Wiesbeck. A novel stochastic rough-surface scattering representation for ray-optical wave propagation modelling. *Vehicular Technology Conference*, 3:1785 –1788, 2001.

[25] M.C. Dobson and F.T. Ulaby. Active microwave soil moisture research. *IEEE Trans. Geosci. Remote Sensing*, GE-24(1):23–36, Jan. 1986.

[26] M.C. Dobson and F.T. Ulaby. Preliminary evaluatin of the sir-b response to soil moisture, surface roughness, and crop canopy cover. *IEEE Trans. Geosci. Remote Sensing*, GE-24(4):517–526, July 1986.

[27] Y. Du, F.T. Ulaby, and M.C. Dobson. Sensitivity to soil moisture by active and passive microwave sensors. *University of Michigan Technical Report 032601-1*, Sept. 1998.

[28] Y. Du, F.T. Ulaby, and M.C. Dobson. Sensitivity to soil moisture by active and passive microwave sensors. *IEEE Transactions on Geoscience and Remote Sensing*, 38(1):105–114, Jan. 2000.

[29] H.T. Ewe, H.T. Chuah, and A.K. Fung. Backscatter model for a dense discrete medium: analysis and numerical results. *Remote Sensing of Environment*, 65(2):195–203, Aug 1998.

[30] P. Ferrazzoli, S. Paloscia, P. Pampaloni, G. Schiavon, D. Solimini, and P. Coppo. Sensitivity of mcirowave measurments to vegetation biomass and soil moisture content: A case study. *IEEE Trans. Geosci. Remote Sensing*, pages 750–756, July 1992.

[31] P. Ferrazzoli, S. Paloscia, P. Pampaloni, G. Shiavon, S. Sigismondi, and D. Solimini. The potential of multifrequency polarimetric SAR in assessing agricultural and arboreous biomass. *IEEE Transactions on Geoscience and Remote Sensing*, 35(1):5–17, January 1997.

[32] J.L. Foster, J.S. Barton, A.T.C. Chang, and D.K. Hall. Snow crystal orientation effects on the scattering of passive microwave radiation. *IEEE Transactions on Geoscience and Remote Sensing*, 38(5):2430–2434, Sept. 2000.

[33] J.L. Foster, D.K. Hall, A.T.C. Chang, A. Rango, W. Wergin, and E. Erbe. Effects of snow crystal shape on the scattering of passive microwave radiation. *IEEE Transactions on Geoscience and Remote Sensing*, 37(2):1165–1168, March 1999.

[34] A.K. Fung. *Microwave scattering and emission models and their applications.* Artech House, Boston, 1994.

[35] A.K. Fung and H.J. Eom. A comparison between active and passive sensing of soil moisture from vegetated terrains. *IEEE Trans. Geosci. Remote Sensing*, 5:768–775, Sept. 1985.

[36] A.K. Fung, W.Y. Liu, K.S. Chen, and M.K. Tsay. An improved iem model for bistatic scattering from rough surfaces. *J Electromagnet Wave*, 16(5):689–702, 2002.

[37] A.K. Fung, S. Tjuatja, J.W. Bredow, and H.T. Chuah. Dense medium phase and amplitude correction theory for spatially and electrically dense media. *IGARSS*, 2:1336–1338, 1995.

[38] R. Geiger. *The Climate Near The Ground.* Harvard University Press, Cambridge, 1965.

[39] L.X. Guo and K. Cheyoung. Light-scattering models for a spherical particle above a slightly dielectric rough surface. *Microwave and Optical Technology Letters*, 33(2):142–146, Apr. 2002.

[40] M. Hallikainen, K. Tigerstedt, V.S. Jaaskelainen, J. Pulliainen, and J. Koskinen. Microwave radiometer response to snow in the 6.8 to 94 ghz range for various land-cover categories. *IGARSS*, 3:1786–1788, 1999.

[41] Marti T. Hallikainen, Fawwaz T. Ulaby, M. Craig Dobson, Mohammed A. El-Rayes, and L. Wu. Microwave dielectric behaviour of wet soil, Part I: Empircal models and experimental observations. *IEEE Transactions on Geoscience and Remote Sensing*, 23(1):25–34, January 1985.

[42] M.T. Hallikainen, F.T. Ulaby, and T.E. Vandeventer. Extinction behavior of dry snow in the 18-ghz and 90-ghz range. *IEEE Transactions on Geoscience and Remote Sensing*, 25(6):737–745, Nov. 1987.

[43] J. J. Hanway and C. R. Weber. Dry matter accumulation in soybean (*Glycine max* (l) Merrill) plants as influenced by N, P, and K fertilization. *Agronomy Journal*, 63:263–266, March–April 1971.

[44] C.Y. Hsieh. Polarimetric bistatic scattering from random rough surfaces along azimuth angles. *Microwave and Millimeter Wave Technology*, pages 591 –594, 2000.

[45] C.Y. Hsieh, A.K. Fung, G. Nesti, A.J. Sieber, and P. Coppo. Further study of the iem surface scattering model. *IEEE Transactions on Geoscience and Remote Sensing*, 35(4):901–909, July 1997.

[46] A. Ishimaru. *Wave propagation and scattering in random media I.* Academic Press, New York, 1978.

[47] A. Ishimaru and Y. Kuga. Attenuation constant of coherent field in a dense distribution of particles. *J.Opt.Soc.Amer.*, 72:1317–1320, 1982.

[48] T.J. Jackson. Measuring surface soil moisture using passive microwave remote sensing. *Hydrol. Processes*, (7):139–152, 1993.

[49] T.J. Jackson and T.J. Schmugge. Vegetation effects on the microwave emission of soils. *Remote Sensing Environ.*, (36):203–212, 1991.

[50] T.J. Jackson and D.E. Le Vine. Mapping surface soil moisture using an aircraft-based passive microwave instrument: algorithm and example. *J. Hydrol.*, (184):85–99, 1996.

[51] T.J. Jackson, D.M. Le Vine, A.J. Griffis, D.C. Goodrich, T.J.Schmugge, C.T.Swift, and P.E. O'Neill. Soil moisture and rainfall estimation over a semi-arid environment with the estar microwave radiometer. *IEEE Trans. Geosci. Remote Sensing*, (31):836–841, 1993.

[52] W.C. Jakes. *Microwave mobile communications.* Wiley, New York, 1974.

[53] J.T. Johnson. A study of the four-path model for scattering from an object above a half space. *Microwave and Optical Technology Letters*, 30(2):130–134, July 2001.

[54] A. Kara and H.L. Bertoni. Blockage/shadowing and polarization measurements at 2.45 ghz for interference evaluation between bluetooth and ieee 802.11 wlan. *IEEE International Sym, Antennas and Propagation Society*, 3:376–379, 2001.

[55] R.E. Kell. On the derivation of the bistatic rcs from monostatic measurements. *Proc.IEEE*, 52:983–988, Aug. 1965.

[56] J.R. Kendra and K. Sarabandi. Hybrid experimental/theoretical scattering model for dense random media. *IEEE Transactions on Geoscience and Remote Sensing*, 37(1):21–35, Jan 1999.

[57] J.R. Kendra and K. Sarabandi. Hybrid experimental/theoretical scattering model for dense random media. *IEEE Transactions on Geoscience and Remote Sensing*, 37(1):21–35, Jan 1999.

[58] J.R. Kendra, K. Sarabandi, and F.T. Ulaby. Radar measurements of snow: Experiment and analysis. *IEEE Transactions on Geoscience and Remote Sensing*, 36(3):864–879, May 1998.

[59] N. Kruopis, J. Praks, A.N. Arslan, H.M. Alasalmi, J.T. Koskinen, and M.T. Hallikainen. Passive microwave measurements of snow-covered forest areas in emac'95. *IEEE Transactions on Geoscience and Remote Sensing*, 37(6):2699–2705, Nov. 1999.

[60] Y. Kuga, F.T. Ulaby, T. Haddock, and R.D. DeRoo. Millimeter-wave radar scattering from snow. i. radiative transfer model. *Radio Science*, 26(2):329–341, March-April 1991.

[61] E.S. Li and K. Sarabandi. Low grazing incidence millimeter-wave scattering models and measurements for various road surfaces. *IEEE Trans on Antennas and Propagation*, 47(5):851–861, May 1999.

[62] E.S. Li and K. Sarabandi. Low grazing incidence millimeter-wave scattering models and measurements for various from road surfaces. *IEEE Transactions on Antennas and Propagation*, 47:851–861, 1999.

[63] H.J. Mametsa, F. Koudogbo, and P.F. Combes. Application of iem and radiative transfer formulations for bistatic scattering of rough surfaces. *IGARSS*, 1:662–664, 2002.

[64] Kyle C. McDonald, M. Craig Dobson, and Fawwaz T. Ulaby. Using MIMICS to model L-band multiangle and multitemporal backscatter from a walnut orchard. *IEEE Transactions on Geoscience and Remote Sensing*, 28(4):477–491, July 1990.

[65] James B. Mead, Paul S. Chang, Stephen P. Lohmeier, Philip M. Langlois, and Robert E. McIntosh. Polarimetric observations and theory of millimeter-wave backscatter from snow cover. *IEEE Transactions on Antennas and Propagation*, 41(1):38–45, January 1993.

[66] J.B. Mead, P.S. Chang, S.P. Lohmeier, P.M. Langlois, and R. McIntosh. Polarimetric observations and theory of millimeter-wave backscatter from snow cover. *IEEE Trans on Antennas and Propagation*, 41(1):38–46, Jan. 1993.

[67] K.B. Nahm and W.L. Wolfe. Ligh-scattering models for spheres on a conducting plane - comparison with experiment. *Applied Optics*, 26(15):2995–2999, Aug. 1987.

[68] R.M. Narayanan, D.D. Cox, J.M. Ralston, and M.R. Christian. Millimeter-wave specular and diffuse multipath components of terrain. *IEEE Transactions on Antennas and Propagation*, 44(5):627–645, May 1996.

[69] R.M. Narayanan and R.E. McIntosh. Millimeter-wave backscatter characteristics of multilayered snow surfaces. *IEEE Trans. Geosci. Remote Sensing*, 38(5):693–703, May 1990.

[70] A.Y. Nashashibi, K. Sarabandi, P. Frantzis, R.D.DeRoo, and F.T.Ulaby. An ultrafast wide-band millimeter-wave (mmw) polarimetric radar for remote sensing applications. *IEEE Transactions on Geoscience and Remote Sensing*, 40(8):1777–1786, Aug. 2002.

[71] A. Geoffrey Norman, editor. *Soybean Physiology, Agronomy, and Utilization*, chapter 2, pages 17–44. Academic Press, New York, 1978.

[72] S.G. Obrien and G.H. Goedecke. Scattering of millimeter wave by snow crystals and equivalent homogeneous symmetric particles. *Applied Optics*, 27(12):2439–2444, June 1988.

[73] Y. Oh, K. Sarabandi, and F. T. Ulaby. An empirical model and an inversion technique for radar scattering from bare soil surfaces. *IEEE Trans. Geosci. Remote Sensing*, pages 370–382, 1992.

[74] Yisok Oh, Kamal Sarabandi, and Fawwaz T. Ulaby. An empirical model and an inversion technique for radar scattering from bare soil surfaces. *IEEE Transactions on Geoscience and Remote Sensing*, 30(2):370–381, March 1992.

[75] Yisok Oh, Kamal Sarabandi, and Fawwaz T. Ulaby. An inversion algorithm for retrieving soil moisture and surface roughness from polarimetric radar observation. In *Digest*, volume 3 of *IEEE International Geoscience and Remote Sensing Symposium (IGARSS '94)*, pages 1582–1584, Pasadena, CA, 8–12 August 1994.

[76] J.D. Parsons. *The mobile radio propagation channel.* John Wiley, New York, 2000.

[77] M. Poatzold. *Mobile fading channels.* J. Wiley, New York, 2002.

[78] William H. Press, Saul A. Teukolsky, William T. Vetterling, and Brian P. Flannery. *Numerical Recipes in Fortran: The Art of Scientific Computing.* University Press, Cambridge, second edition, 1992.

[79] J.G. Proakis. *Digital communications.* McGraw-Hill, New York, 1995.

[80] S.S. Saatchi, D.M. LeVine, and R.H. Lang. Microwave backscattering and emission model for grass canopies. *IEEE Trans. Geosci. Remote Sensing*, pages 177–186, Jan. 1994.

[81] K. Sarabandi and T.C. Chiu. Electromagnetic scattering from slightly rough surfaces with inhomogeneous dielectric profiles. *IEEE Transactions on Antennas and Propagation*, 45(9):1419–1430, Sept. 1997.

[82] K. Sarabandi and A. Nashashibi. A novel bistatic scattering matrix measurement technique using a monostatic radar. *IEEE Transactions on Antennas and Propagation*, 44(1):41–50, Jan. 1996.

[83] K. Sarabandi and P.F. Polatin. Electromagnetic scattering from two adjacent objects. *IEEE Transactions on Antennas and Propagation*, 42(4):510–517, Apr 1994.

[84] T. Schmugge, P.E. O'Neill, and J.R. Wang. Passive microwave soil moisture research. *IEEE Trans. Geosci. Remote Sensing*, GE-24(1):12–22, Jan. 1986.

[85] T. B. A. Senior, K. Sarabandi, and F. T. Ulaby. Measuring and modeling the backscatter cross section of a leaf. *Radio Science*, 22(6):1109–1116, November 1987.

[86] J.C. Shi, J. Wang, A.Y. Hsu, P.E. O'Neill, and E.T. Engman. Estimation of bare surface soil moisture and surface roughness parameter using l-band sar image data. *IEEE Trans. Geosci. Remote Sensing*, pages 1254–1266, Sept. 1997.

[87] M.D. Srinath, P.K.R. Karan, and R. Viswanathan. *Introduction to Statistical Signal Processing with Applications.* Prentice-Hall, New Jersey, 1996.

[88] J.M. Stiles and K. Sarabandi. Modeling microwave propagation in a grass vegetation layer. *IGARSS*, 3:1571–1573, 1998.

[89] L. Tsang, K.H. Ding, and S.E. Shih. Monte carlo simulations of scattering of electromagnetic waves from dense distributions of nonspherical particles. *IGARSS*, 2:919–921, 1997.

[90] L. Tsang and A. Ishimaru. Radiative wave equations for vector electromagnetic propagation in dense nontenuous media. *Journal of Electromagnetic Waves and Applications*, 1(1):59–72, 1987.

[91] L. Tsang and J.A. Kong. Scattering of electromagnetic-waves from a dense medium consisting of correlated mie scatterers with size distributions and applications to dry snow. *J. Electromagnet Wave*, 6(3):265–286, 1992.

[92] L. Tsang and J.A. Kong. Scattering of electromagnetic waves from a dense medium consisting of correlated mie scatterers with size distributions and applications to dry snow. *J. of Electromagnetic Waves and Applications*, 6(8):265–286, 1992.

[93] L. Tsang, J.A. Kong, and R.T. Shin. *Theory of Microwave Remote Sensing.* Wiley-Interscience, New York, 1985.

[94] L. Tsang, J.A. Long, and R.T. Shin. *Theory of Microwave Remote Sensing.* New York: Wiley,, 1985.

[95] Fawwaz T. Ulaby, Pascale C. Dubois, and Jakob van Zyl. Radar mapping of surface soil moisture. *Journal of Hydrology*, 184:57–84, 1996.

[96] Fawwaz T. Ulaby, Richard K. Moore, and Adrian K. Fung. *Microwave Remote Sensing: Active and Passive*, volume 2. Addison-Wesley, Reading, MA, 1982.

[97] Fawwaz T. Ulaby, Kamal Sarabandi, Kyle C. McDonald, Michael Whitt, and M. Craig Dobson. Michigan Microwave Canopy Scattering Model. *International Journal of Remote Sensing*, 11(7):1223–1253, 1990.

[98] Fawwaz T. Ulaby and Edward A. Wilson. Microwave attenuation properties of vegetation canopies. *IEEE Transactions on Geoscience and Remote Sensing*, 23(5):746–753, November 1985.

[99] F.T. Ulaby and M.C. Dobson. *Handbook of Radar Scattering Statistics for Terrain.* Dedham, MA: Artech House, 1989.

[100] F.T. Ulaby, P.C. Dubois, and J. van Zyl. Radar mapping of surface soil moisture. *Journal of Hydrology*, (184):57–84, 1996.

[101] F.T. Ulaby and C. Elachi, editors. *Radar Polarimetry for Geoscience Applications.* Artech House, Norwood, MA, 1990.

[102] F.T. Ulaby, T.F. Haddock, R.T. Austin, and Y. Kuga. Millimeter-wave radar scattering from snow. 2. comparison of theory with experimental observations. *Radio Science*, 26(2):343–351, Mar-Apr 1991.

[103] F.T. Ulaby, R.K. Moore, and A.K. Fung. *Microwave Remote Sensing: Active and Passive*, volume 2. Dedham, MA: Artech House, 1982.

[104] F.T. Ulaby, R.K. Moore, and A.K. Fung. *Microwave Remote Sensing: Active and Passive*, volume 3. Dedham, MA: Artech House, 1986.

[105] F.T. Ulaby, R.K. Moore, and A.K. Fung. *Microwave Remote Sensing: Active and Passive III.* Artech House, MA, 1986.

[106] F.T. Ulaby, K. Sarabandi, K. McDonald, M. Whitt, and M.C. Dobson. Michigan microwave canopy scattering model. *Int. J. Remote Sensing*, 11:1223–1253, 1990.

[107] F.T. Ulaby, P. Siqueira, A. Nashashibi, and K. Sarabandi. Semi-empirical model for radar backscatter from snow at 35 and 95 ghz. *IEEE Transactions on Geoscience and Remote Sensing*, 34(5):1059–1065, Sept. 1996.

[108] F.T. Ulaby, P. Siqueira, A. Nashashibi, and K. Sarabandi. Semi-empirical model for radar backscatter from snow at 35 and 95 ghz. *IEEE Trans. Geosci. Remote Sensing*, 34(5), Sept. 1996.

[109] G. Videen, M.G. Turner, V.J. Iafelice, W.S. Bickel, and W.L. Wolfe. Scattering from a small sphere near a surface. *J Opt Soc AM A*, 10(1):118–126, Jan. 1993.

[110] L.C. Wang and C.W. Wang. A near real-time signal to interference ratio measurement technique in a frequency-selective multipath fading channel for the wcdma system. *Vehicular Technology Conference*, 2:752–756, 2001.

[111] P.C. Waterman. Symmetry, unitarity, and geometry in electromagnetic scattering. *Physical Review D*, 3(4):825–839, Feb. 1971.

[112] B. Wen, L. Tsang, D.P. Winebrenner, and A. Ishimaru. Dense medium radiative transfer theory: comparison with experiment and application to microwave remote sensing and polarimetry. *IEEE Trans. Geosci. Remote Sensing*, 28(1):46–59, Jan. 1990.

[113] M. Whitt. *Microwave Scattering from Periodic Row-Structured Vegetation.* PhD dissertation, University of Michigan, Ann Arbor, 1991.

[114] J.P. Wigneron, J.C. Calvet, Y. Kerr, A. Chanzy, and A. Lopes. Microwave emission of vegetation sensitivity to leaf characteristics. *IEEE Trans. Geosci. Remote Sensing*, pages 716–726, May 1993.

[115] S.H. Yueh, J.A. Kong, J.K. Jao, R.T. Shin, and T. Le Toan. Branching model for vegetation. *IEEE Trans Geosci Remote Sens*, 30(2):390–402, Mar 1992.